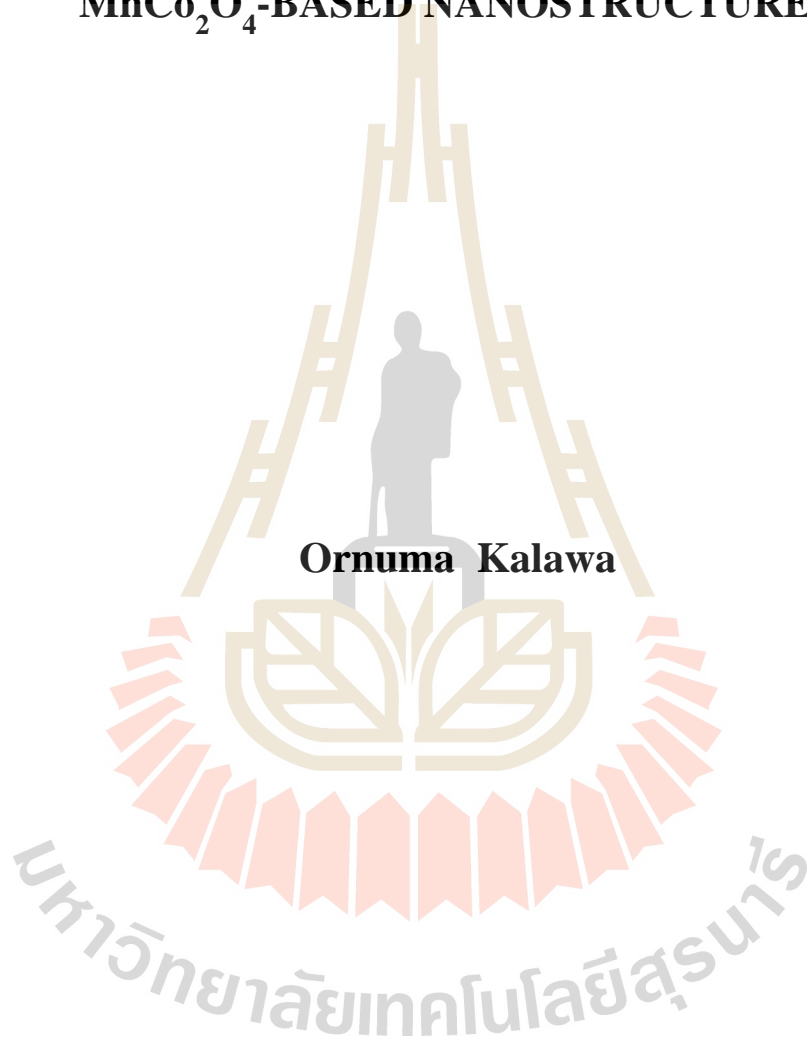


**FABRICATION, STRUCTURE, AND
ELECTROCHEMICAL PROPERTIES OF
MnCo₂O₄-BASED NANOSTRUCTURES**



Ornuma Kalawa

A Thesis Submitted in Partial Fulfillment of the Requirements for the

Degree of Doctor of Philosophy in Physics

Suranaree University of Technology

Academic Year 2019

การประดิษฐ์ โครงสร้าง และสมบัติทางไฟฟ้าเคมีของโครงสร้างนาโนกลุ่ม
แมงกานีสโคบอลต์ออกไซด์



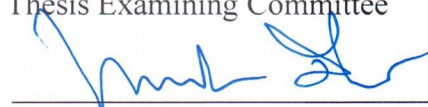
นางสาวอรอุมา กาพหว่า

วิทยานิพนธ์นี้เป็นส่วนหนึ่งของการศึกษาตามหลักสูตรปริญญาวิทยาศาสตรดุษฎีบัณฑิต
สาขาวิชาฟิสิกส์
มหาวิทยาลัยเทคโนโลยีสุรนารี
ปีการศึกษา 2562

**FABRICATION, STRUCTURE, AND ELECTROCHEMICAL
PROPERTIES OF $MnCo_2O_4$ -BASED NANOSTRUCTURES**

Suranaree University of Technology has approved this thesis submitted in partial fulfillment of the requirements for the Degree of Doctor of Philosophy.

Thesis Examining Committee



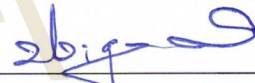
(Asst. Prof. Dr. Panomsak Meemon)

Chairperson



(Prof. Dr. Santi Maensiri)

Member (Thesis Advisor)



(Assoc. Prof. Dr. Prayoon Songsiriritthigul)

Member



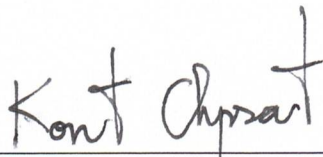
(Assoc. Prof. Dr. Nonglak Meethong)

Member



(Dr. Narong Chanlek)

Member



(Assoc. Prof. Flt. Lt. Dr. Kontorn Chamniprasart)

Vice Rector for Academic Affairs
and Internationalization



(Assoc. Prof. Dr. Worawat Meevasana)

Dean of Institute of Science

อรอุมา กาพหว่า : การประดิษฐ์ โครงสร้าง และสมบัติทางไฟฟ้าเคมีของโครงสร้างนาโน
กลุ่มแมงกานีสโคบอลต์ออกไซด์ (FABRICATION, STRUCTURE, AND
ELECTROCHEMICAL PROPERTIES OF $MnCo_2O_4$ -BASED
NANOSTRUCTURE). อาจารย์ที่ปรึกษา : ศาสตราจารย์ ดร.สันติ แม่นศิริ, 230 หน้า.

อนุภาคนาโนกลุ่มแมงกานีสโคบอลต์ออกไซด์/เส้นใยนาโนกลุ่มแมงกานีสโคบอลต์ออกไซด์
/สมบัติเชิงเคมีไฟฟ้า/ตัวเก็บประจุยิ่งยวด

ในงานวิจัยนี้ได้ทำการเตรียมอนุภาคนาโนของกลุ่มแมงกานีสโคบอลต์ออกไซด์ ($MnCo_2O_4$ และ $Mn_{1-x}M_xCo_2O_4$) เมื่อ $M = Ni$ และ Zn ($0.0 \leq x \leq 0.2$) โดยวิธีสารละลายพอลิเมอร์อย่างง่าย และเส้นใยนาโนของกลุ่มแมงกานีสโคบอลต์ออกไซด์ ($MnCo_2O_4$ และ $Mn_{1-x}M_xCo_2O_4$) เมื่อ $M = Ni$ และ Zn ($0.0 \leq x \leq 0.2$) เตรียมโดยเทคนิคอิเล็กโทรสปินนิง สารตัวอย่างที่เตรียมได้ถูกนำไปตรวจสอบโดยใช้เทคนิคการเลี้ยวเบนของรังสีเอกซ์ (XRD) กล้องจุลทรรศน์แบบส่องผ่าน (TEM) กล้องจุลทรรศน์แบบส่องกราดชนิดฟิลด์อิมเมชัน (FESEM) เทคนิคสเปกโทรสโกปีการดูดกลืนรังสีเอกซ์ (XAS) เทคนิคสเปกโทรสโกปีโฟโตอิเล็กตรอนด้วยรังสีเอกซ์ (XPS) และวัดพื้นที่ผิวจำเพาะด้วยเทคนิค Brunauer-emmett-teller (BET) นอกจากนี้ได้ศึกษาผลของอุณหภูมิในการเผาและปริมาณการแทนที่ของ Ni และ Zn ไอออนในโครงสร้างนาโนแมงกานีสโคบอลต์ออกไซด์ที่มีต่อสมบัติเชิงไฟฟ้าเคมีของขั้วไฟฟ้าที่เตรียมได้จากวัสดุกลุ่มนาโนแมงกานีสโคบอลต์ออกไซด์ ซึ่งสมบัติเชิงไฟฟ้าเคมีได้ถูกศึกษาโดยเทคนิค Cyclic voltammetry (CV) Galvanostatic charge/discharge (GCD) และอิเล็กโทรเคมีคัลอิมพีแดนซ์สเปกโทรสโกปี (EIS)

จากผลการทดลองพบว่าอนุภาคนาโนกลุ่ม $MnCo_2O_4$ และเส้นใยนาโนกลุ่ม $MnCo_2O_4$ มีโครงสร้างแบบลูกบาศก์ มีขนาดอนุภาค 30 ถึง 200 นาโนเมตรและขนาดเส้นผ่าศูนย์กลาง 200-400 นาโนเมตร ตามลำดับ จากการศึกษาด้วยเทคนิค XANES และ XPS สามารถระบุสถานะเลขออกซิเดชันของ Mn^{3+}/Mn^{4+} และ Co^{2+}/Co^{3+} ในทุกตัวอย่าง และ Ni^{2+} และ Zn^{2+} พบในตัวอย่าง $MnCo_2O_4$ เจือด้วย Ni และ Zn ตามลำดับ จากการศึกษาสมบัติเชิงเคมีไฟฟ้าของขั้วไฟฟ้าที่ประดิษฐ์ได้ในสารละลายอิเล็กโทรไลต์โพแทสเซียมไฮดรอกไซด์ ความเข้มข้น 6 โมลาร์ โดยใช้ระบบสามขั้วไฟฟ้า พบว่ามีการเก็บประจุโดยกระบวนการแบบประจุแฝง (pseudocapacitive) ของอนุภาคนาโนของโลหะ และโลหะออกไซด์ในแต่ละขั้วไฟฟ้า ในอนุภาคนาโนกลุ่ม $Mn_{1-x}M_xCo_2O_4$ เมื่อ $M = Ni$ และ Zn พบว่าขั้วไฟฟ้าเตรียมจาก $Mn_{0.85}Ni_{0.15}Co_2O_4$ ให้ค่าความจุไฟฟ้าจำเพาะ 378 F/g ที่ความหนาแน่นกระแส 1 A/g เนื่องจากตัวอย่างนี้มีขนาดของพื้นที่ผิวจำเพาะที่ใหญ่กว่าตัวอย่างอื่น ๆ

ซึ่งจะทำให้มีพื้นที่ผิวสัมผัสระหว่างอิเล็กโทรไลต์กับขั้วไฟฟ้าสำหรับการเกิดปฏิกิริยารีดออกซ์เพิ่มมากขึ้น และขั้วไฟฟ้าที่เตรียมจากเส้นใยนาโน $Mn_{0.85}Ni_{0.15}Co_2O_4$ ให้ค่าความจุไฟฟ้าจำเพาะ 280 F/g ที่ความหนาแน่นกระแส 1 A/g สมบัติที่น่าสนใจอีกประการคือวัสดุเหล่านี้สามารถรักษาความสามารถของการคายประจุได้มากกว่าร้อยละ 70 หลังการทดสอบการคายประจุจำนวน 1000 รอบ



สาขาวิชาฟิสิกส์
ปีการศึกษา 2562

ลายมือชื่อนักศึกษา อรุณ ทรัพย์
ลายมือชื่ออาจารย์ที่ปรึกษา ศ.ดร.ป.ป.

ORNUMA KALAWA : FABRICATION, STRUCTURE, AND
ELECTROCHEMICAL PROPERTIES OF MnCo_2O_4 -BASED
NANOSTRUCTURES. THESIS ADVISOR : PROF. SANTI MAENSIRI,
D.Phil. 230 PP.

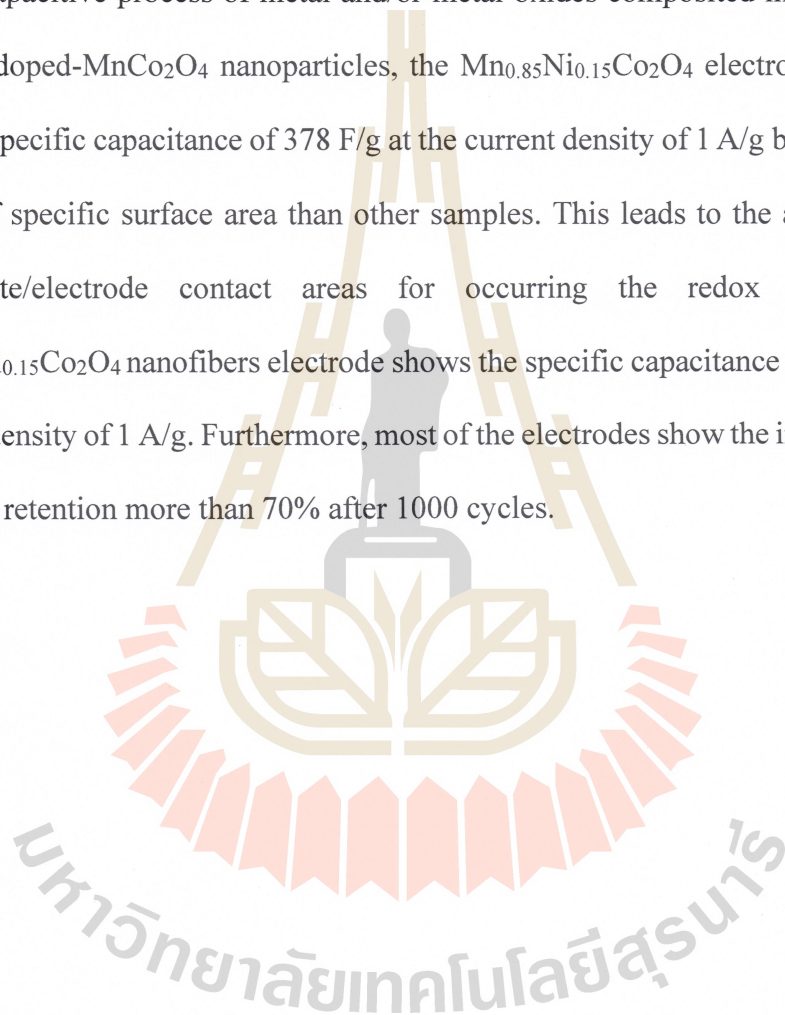
MnCo_2O_4 -BASED NANOPARTICLES/ MnCo_2O_4 -BASED NANOFIBERS
/ELECTROCHEMICAL PROPERTIES/SUPERCAPACITOR

In this work, the pure MnCo_2O_4 and $\text{Mn}_{1-x}\text{M}_x\text{Co}_2\text{O}_4$ where $\text{M} = \text{Ni}$ and Zn ($0.0 \leq x \leq 0.2$) nanoparticles were prepared by a facile a simple polymer solution method, while the pure MnCo_2O_4 and $\text{Mn}_{1-x}\text{M}_x\text{Co}_2\text{O}_4$ nanofibers where $\text{M} = \text{Ni}$ and Zn ($0.0 \leq x \leq 0.2$) were fabricated by electrospinning technique. The obtained samples were characterized by X-ray diffraction (XRD), transmission electron microscopy (TEM), field emission scanning electron microscopy (FESEM), X-ray absorption near edge structure (XANES), X-ray photoelectron spectroscopy (XPS), and Brunauer-Emmett-Teller (BET) techniques. The effects of calcination temperature and Ni and Zn ions substitution in MnCo_2O_4 nanostructures on the electrochemical properties of the MnCo_2O_4 nanostructures were investigated. The electrochemical performance was examined by cyclic voltammetry (CV), galvanostatic current charge-discharge and electrochemical impedance spectroscopy (EIS).

The XRD and TEM results reveal that the MnCo_2O_4 -based nanoparticles and MnCo_2O_4 -based nanofibers have a cubic structure with particle sizes of between 30 to 200 nm and diameters of 200-400 nm, respectively. The XANES and XPS have confirmed the mixed valence state of $\text{Mn}^{3+}/\text{Mn}^{4+}$ and $\text{Co}^{2+}/\text{Co}^{3+}$ in all samples.

Moreover, Ni^{2+} and Zn^{2+} were observed in the Ni-doped MnCo_2O_4 and Zn-doped MnCo_2O_4 nanostructures.

The electrochemical properties were performed on all samples by using a three-electrode cell system in 6.0 M KOH electrolyte. All the electrodes stored the charge by pseudocapacitive process of metal and/or metal oxides composited in each electrode. For the doped- MnCo_2O_4 nanoparticles, the $\text{Mn}_{0.85}\text{Ni}_{0.15}\text{Co}_2\text{O}_4$ electrode provides the highest specific capacitance of 378 F/g at the current density of 1 A/g because it has the larger of specific surface area than other samples. This leads to the augmentation of electrolyte/electrode contact areas for occurring the redox reactions. The $\text{Mn}_{0.85}\text{Ni}_{0.15}\text{Co}_2\text{O}_4$ nanofibers electrode shows the specific capacitance of 208 F/g at the current density of 1 A/g. Furthermore, most of the electrodes show the imposing cycling capacity retention more than 70% after 1000 cycles.



School of Physics

Academic Year 2019

Student's Signature

Ornoma Kalawa

Advisor's Signature

[Signature]

ACKNOWLEDGEMENTS

The achievement of this research required a lot of guidance and assistance from many people, who deserve my deepest gratitude. I would first like to express my gratitude to my thesis advisor, Prof. Dr. Santi Maensiri for giving me precious guidance, wonderful opportunity, great encouragement, and continuous support of this research. Besides my thesis advisor, I am extremely grateful to the Science Achievement Scholarship of Thailand (SAST) for the unstinting support of my Ph.D. study.

I am especially grateful to all the thesis examination committee members, Asst. Dr. Panomsak Meemon, Asst. Dr. Nonglak Meethong, Assoc. Prof. Dr. Prayoon Songsiriritthigul, and Dr. Narong Chanlek for serving on my Ph.D. in reading the thesis and providing me with useful comments. I would like to expand my gratitude to all AMP group members who have guided me during this research. In addition, I sincerely thank to the personnel of the School of Physics, Suranaree University of Technology for their unfailing assistance and the Synchrotron Light Research Institute (Public Organization) for XANES and XPS facilities.

Finally, I am deeply appreciative of getting continuous support and good encouragement from my parents, my sisters, brother-in-law, and my husband during my Ph.D. study, thesis researching, and thesis writing. This attainment might not have been possible without them.

Ornuma Kalawa

CONTENTS

	Page
ABSTRACT IN THAI.....	I
ABSTRAC IN ENGLISH.....	III
ACKNOWLEDGEMENTS.....	V
CONTENTS.....	VI
LIST OF TABLES.....	X
LIST OF FIGURES.....	XIII
LIST OF ABBREVIATIONS.....	XXV
CHAPTER	
I INTRODUCTION.....	1
1.1 Background and motivation.....	1
1.2 Research objective.....	3
1.3 Scope and limitations.....	4
1.4 Location of research.....	4
1.5 Expected results.....	5
1.6 Outline of thesis.....	5
II LITERATURE REVIEWS.....	7
2.1 Electrochemical capacitors.....	7
2.1.1 Electrostatic double-layer capacitor (EDLCs).....	8
2.1.2 Pseudocapacitors.....	9
2.1.3 Hybrid-capacitors.....	11

CONTENTS (Continued)

	Page
2.2 Manganese cobalt spinel oxides.....	12
2.3 Electrochemical properties of MnCo ₂ O ₄	13
III RESEARCH METHODOLOGY.....	16
3.1 Materials and apparatus.....	16
3.1.1 Materials.....	16
3.1.2 Apparatus.....	17
3.2 Materials fabrication.....	17
3.2.1 Precursor preparation.....	17
3.2.2 Synthesis of MnCo ₂ O ₄ -based nanoparticles.....	18
3.2.3 Fabrication of MnCo ₂ O ₄ -based nanofibers.....	18
3.3 Material characterization.....	24
3.3.1 X-Ray diffraction (XRD).....	24
3.3.2 Scanning electron microscopy.....	25
3.3.3 Transmission electron microscopy.....	27
3.3.4 Brunauer-Emmett-Teller (BET) and Barrett-Joyner-Halenda (BJH).....	28
3.3.5 X-ray absorption spectroscopy (XAS).....	31
3.3.6 X-ray photoelectron spectroscopy (XPS).....	33
3.4 Electrochemical measurements.....	34
3.4.1 Electrode preparation.....	35
3.4.2 Electrochemical cell setup.....	35

CONTENTS (Continued)

	Page
3.4.3 Cyclic voltammetry.....	37
3.4.4 Galvanostatic charge/discharge testing (GCD).....	38
3.4.5 Electrochemical impedance spectroscopy (EIS).....	39
IV RESULTS AND DISCUSSION.....	42
4.1 MnCo ₂ O ₄ nanoparticles.....	43
4.1.1 Structural and morphology characterization.....	43
4.1.2 Electrochemical properties.....	60
4.2 Ni-doped MnCo ₂ O ₄ nanoparticles.....	70
4.2.1 Structural and morphology characterization.....	70
4.2.2 Electrochemical properties.....	90
4.3 Zn-doped MnCo ₂ O ₄ nanoparticles.....	97
4.3.1 Structural and morphology characterization.....	97
4.3.2 Electrochemical properties.....	117
4.4 MnCo ₂ O ₄ nanofibers.....	123
4.4.1 Structural and morphology characterization.....	123
4.4.2 Electrochemical properties.....	140
4.5 Ni-doped MnCo ₂ O ₄ nanofibers.....	147
4.5.1 Structural and morphology characterization.....	147
4.5.2 Electrochemical properties.....	167
4.6 Zn-doped MnCo ₂ O ₄ nanofibers.....	173
4.6.1 Structural and morphology characterization.....	173

CONTENTS (Continued)

	Page
4.6.2 Electrochemical properties.....	192
4.7 Conclusion of the effects of calcination temperature on the electrochemical properties of MnCo ₂ O ₄ nanostructures.....	199
4.8 Conclusion of the effects of the nanostructures and various dopants concentration on electrochemical properties.....	201
V CONCLUSIONS AND SUGGESTIONS.....	207
5.1 The structure and morphology characterization.....	207
5.2 The Electrochemical properties.....	208
5.3 Suggestions.....	209
REFERENCES.....	213
APPENDIX.....	228
CURRICULUM VITAE.....	230

LIST OF TABLES

Table	Page
2.1	Summary of the various metal oxide electrodes.....11
2.2	Comparison of MnCo ₂ O ₄ -based performance for supercapacitor.....15
3.1	List of starting raw materials for preparation of the precursor solution of MnCo ₂ O ₄ nanostructure.....19
3.2	List of starting raw materials for preparation of the precursor solution of Mn _{1-x} Ni _x Co ₂ O nanostructures.....20
3.3	List of starting raw materials for preparation of the precursor solution of Mn _{1-x} Zn _x Co ₂ O ₄ nanostructures.....21
4.1	Summary of crystallite sizes (<i>D</i>) from XRD, <i>d</i> -spacing (<i>d</i>), and lattice constant (<i>a</i>) of MnCo ₂ O ₄ nanoparticles at different calcined temperatures.....45
4.2	Edge energy and oxidation state of the standard samples and MnCo ₂ O ₄ nanoparticles.....51
4.3	Structural parameters of spinel MnCo ₂ O ₄57
4.4	Comparison of supercapacitor performance of the MnCo ₂ O ₄ -based Electrode materials.....69
4.5	Summary of crystallite sizes (<i>D</i>) from XRD, <i>d</i> -spacing (<i>d</i>), and lattice Constant (<i>a</i>) of Mn _{1-x} Ni _x Co ₂ O ₄ (<i>x</i> = 0.00, 0.05, 0.10, 0.15, and 0.20) nanoparticles.....71
4.6	Edge energy and Oxidation state of the standard samples and Ni-doped MnCo ₂ O ₄ nanoparticles.....79

LIST OF TABLES (Continued)

Table	Page
4.7 XPS data of the Ni-doped MnCo ₂ O ₄ nanoparticles.....	85
4.8 Physical properties of spinel Mn _{1-x} Ni _x Co ₂ O ₄ (x = 0.00, 0.05, 0.10, 0.15, and 0.20).....	89
4.9 Summary of crystallite sizes (D) from XRD, d-spacing (d), and lattice constant (a) of Mn _{1-x} Zn _x Co ₂ O ₄ (x = 0.00, 0.05, 0.10, 0.15, and 0.20) nanoparticles.....	98
4.10 Edge energy and Oxidation state of the standard samples and Mn _{1-x} Zn _x Co ₂ O ₄ (x = 0.00, 0.05, 0.10, 0.15, and 0.20) nanoparticle.....	105
4.11 XPS data of the Mn _{1-x} Zn _x Co ₂ O ₄ (x = 0.00, 0.05, 0.10, 0.15, and 0.20) nanoparticles.....	112
4.12 Physical properties of spinel Mn _{1-x} Zn _x Co ₂ O ₄ (x = 0.00, 0.05, 0.10, 0.15, and 0.20) nanoparticles.....	116
4.13 Summary of crystallite sizes (D) from XRD, d-spacing (d), and lattice constant (a) of MnCo ₂ O ₄ nanofibers at different calcined temperatures.....	124
4.14 Edge energy and oxidation state of the standard samples and MnCo ₂ O ₄ nanofibers.....	130
4.15 XPS data of the MnCo ₂ O ₄ nanofibers.....	136
4.16 Structural parameters of spinel MnCo ₂ O ₄	140
4.17 Summary of crystallite sizes (D) from XRD, d-spacing (d), and lattice constant (a) of Mn _{1-x} Ni _x Co ₂ O (x = 0.00, 0.05, 0.10, 0.15, and 0.20) nanofibers.....	148

LIST OF TABLES (Continued)

Table	Page
4.18	Edge energy and oxidation state of the standard samples and $Mn_{1-x}Ni_xCo_2O$ ($x = 0.00, 0.05, 0.10, 0.15,$ and 0.20) nanofibers.....155
4.19	XPS data of the $Mn_{1-x}Ni_xCo_2O$ ($x = 0.00, 0.05, 0.10, 0.15,$ and 0.20) nanofibers.....162
4.20	Physical properties of spinel $Mn_{1-x}Ni_xCo_2O$ ($x = 0.00, 0.05, 0.10, 0.15,$ and 0.20) nanofibers.....166
4.21	Summary of crystallite sizes (D) from XRD, d -spacing (d), and lattice constant (a) of $Mn_{1-x}Zn_xCo_2O$ ($x = 0.00, 0.05, 0.10, 0.15,$ and 0.20) nanofibers.....174
4.22	Edge energy and Oxidation state of the standard samples and $Mn_{1-x}Zn_xCo_2O$ ($x = 0.00, 0.05, 0.10, 0.15,$ and 0.20) nanofibers.....181
4.23	XPS data of the $Mn_{1-x}Zn_xCo_2O$ ($x = 0.00, 0.05, 0.10, 0.15,$ and 0.20) nanofibers.....188
4.24	Physical properties of spinel $Mn_{1-x}Zn_xCo_2O$ ($x = 0.00, 0.05, 0.10, 0.15,$ and 0.20) nanofibers.....192
4.25	The maximum specific capacitance of $MnCo_2O_4$ -based NPs and $MnCo_2O_4$ -based NFs electrodes at current densities of $1A/g$ and BET specific surface area, Total pore volume, and Mean pore diameter.....205
4.26	Comparison of supercapacitor performance of the $MnCo_2O_4$ based materials reported earlier.....206

LIST OF FIGURES

Figure	Page
2.1 Ragone plot represents an energy density and power density of energy storage devices (Kim <i>et al.</i> , 2015).....	8
2.2 A schematic of charged electrochemical double-layer capacitor (Zhong <i>et al.</i> , 2015).....	9
2.3 A schematic of charged pseudocapacitors (Zhong <i>et al.</i> , 2015).....	10
2.4 Schematic of an a hybrid-capacitor (Zhong <i>et al.</i> , 2015).....	12
2.5 Crystal Structure of AB ₂ O ₄ cubic spinel (Issa <i>et al.</i> , 2013).....	13
3.1 Diagram showing the electrospinning system.....	19
3.2 A schematic of the preparation and characterization of MnCo ₂ O ₄ -based nanoparticles.....	22
3.3 A schematic of the preparation and characterization of MnCo ₂ O ₄ -based nanofibers.....	23
3.4 Diagram showing geometrical condition for diffraction from lattice planes.....	24
3.5 Schematic diagram of the core components of an SEM microscope (Inkson, 2016).....	26
3.6 Schematic of core components of a TEM microscope (Inkson, 2016).....	28
3.7 Categories of gas adsorption loops (IUPAC) (Donohue and Aranovich, 1998).....	31

LIST OF FIGURES (Continued)

Figure	Page
3.8	Rough schematic of XPS physics “Photoelectric Effect”. (Image from Wikimedia commons, public domain).....34
3.9	Three-electrode electrochemical cell setup consist of reference electrode (Ag/AgCl), counter electrode (Platinum wire), and working electrode.....36
3.10	Electrochemical measurements set up contains with the three-electrode system, computer, and potentiostat/galvanostat.....36
3.11	Cyclic voltammograms showing rectangular features for an EDLC system, and oxidation peaks for a redox active pseudocapacitor.....38
3.12	Nyquist plot of EDLC a) Ideal, b) Ordinary, and c) Basic equivalent circuit of EDLC.....41
4.1	XRD patterns of precursor and MnCo ₂ O ₄ nanoparticles calcined for 2 h in atmosphere at different calcined temperatures.....43
4.2	FESEM images of MnCo ₂ O ₄ nanoparticles calcined for 2 h in atmosphere at (a) 500 °C, (b) 600 °C, (c) 700 °C, and (d) 800 °C46
4.3	TEM images with corresponding SAED of MnCo ₂ O ₄ nanoparticles calcined for 2 h in atmosphere at (a,b) 500 °C, (c,d) 600 °C, (e,f) 700 °C, and (g,h) 800 °C.....47
4.4	Normalized XANE spectra and their corresponding first-derivative at Co K-edge of MnCo ₂ O ₄ nanoparticles.....49
4.5	Normalized XANE spectra and their corresponding first-derivative at Mn K-edge of MnCo ₂ O ₄ nanoparticles.....50
4.6	XPS spectra at Co 2p of the MnCo ₂ O ₄ nanoparticles.....53

LIST OF FIGURES (Continued)

Figure	Page
4.7	XPS spectra at Mn 2p of the MnCo ₂ O ₄ nanoparticles.....54
4.8	XPS spectra at O 1s of the MnCo ₂ O ₄ nanoparticles.....55
4.9	Nitrogen adsorption/desorption isotherms and pore size distribution (inset) of MnCo ₂ O ₄ nanoparticles calcined at (a) 500 °C, (b) 600 °C, (c) 700 °C, and (d) 800 °C.....58
4.10	CV curves at various scan rates of MnCo ₂ O ₄ nanoparticles calcined at.....62
4.11	Comparison of the specific capacitance at various calcination temperature of MnCo ₂ O ₄ nanoparticles as a function of scan rate.....63
4.12	Galvanostatic charge-discharge curves at various current densities of MnCo ₂ O ₄ nanoparticles calcined at (a) 500 °C, (b) 600 °C, (c) 700 °C, and (d) 800 °C.....65
4.13	Comparison of the specific capacitance at various calcination temperature of MnCo ₂ O ₄ nanoparticles as a current density.....66
4.14	Capacity retention (%) at various calcination temperature of MnCo ₂ O ₄ electrodes after 1000 cycles at a current density of 2 A/g.....66
4.15	The EIS curves of the MnCo ₂ O ₄ at various calcination.....68
4.16	(a) XRD patterns of Mn _{1-x} Ni _x Co ₂ O ₄ (x = 0.00, 0.05, 0.10, 0.15, and 0.20) nanoparticles and (b) relative shift in (311) peak of MnCo ₂ O ₄ with respect to Ni-doping.....70
4.17	FESEM images of Mn _{1-x} Ni _x Co ₂ O ₄ nanoparticles: (a) x = 0.00, (b) x = 0.05, (c) x = 0.10, (d) x = 0.15, and (e) x = 0.20.....73

LIST OF FIGURES (Continued)

Figure	Page
4.18	TEM images with corresponding SAED of $Mn_{1-x}Ni_xCo_2O_4$ nanoparticles and particle size distribution: (a) $x = 0.00$, (b) $x = 0.05$, (c) $x = 0.10$, (d) $x = 0.15$, and (e) $x = 0.20$74
4.19	(a) Normalized XANE spectra (<i>Inset</i> of a present edge shift of samples) and (b) their Corresponding first-derivative of Ni-doped $MnCo_2O_4$ nanoparticles at Co K-edge.....76
4.20	(a) Normalized XANE spectra and (b) their Corresponding first-derivative of Ni-doped $MnCo_2O_4$ nanoparticles at Mn K-edge.....77
4.21	(a) Normalized XANE spectra and (b) their Corresponding first-derivative of Ni-doped $MnCo_2O_4$ nanoparticles at Ni K-edge.....78
4.22	XPS spectra at Co 2p of the $Mn_{1-x}Ni_xCo_2O_4$ ($x = 0.00, 0.05, 0.10, 0.15,$ and 0.20) nanoparticles.....81
4.23	XPS spectra at Mn 2p of the Ni-doped $MnCo_2O_4$ nanoparticles.....82
4.24	XPS spectra at Ni 2p of the Ni-doped $MnCo_2O_4$ nanoparticles.....83
4.25	XPS spectra at O1s of the Ni-doped $MnCo_2O_4$ nanoparticles.....84
4.26	Nitrogen adsorption/desorption isotherms and pore size distribution (<i>inset</i>) of $Mn_{1-x}Ni_xCo_2O_4$ nanoparticles: (a) $x = 0.00$, (b) $x = 0.05$, (c) $x = 0.10$, (d) $x = 0.15$, and (e) $x = 0.20$87
4.27	CV curves at various scan rates of $Mn_{1-x}Ni_xCo_2O_4$ nanoparticles: (a) $x = 0.00$, (b) $x = 0.05$, (c) $x = 0.10$, (d) $x = 0.15$, and (e) $x = 0.20$. (f) specific capacitance as a function of scan rates.....92

LIST OF FIGURES (Continued)

Figure	Page
4.28 Galvanostatic charge-discharge curves at various current densities of $Mn_{1-x}Ni_xCo_2O_4$ nanoparticles: (a) $x = 0.00$, (b) $x = 0.05$, (c) $x = 0.10$, (d) $x = 0.15$, and (e) $x = 0.20$. (f) specific capacitance as a function of current density.....	94
4.29 Capacity retention (%) of $Mn_{1-x}Ni_xCo_2O_4$ ($x = 0.00, 0.05, 0.10, 0.15$, and 0.20) electrodes after 1000 cycles at a current density of 2 A/g.....	95
4.30 The Nyquist plot of $Mn_{1-x}Ni_xCo_2O_4$ ($x = 0.00, 0.05, 0.10, 0.15$, and 0.20) electrodes.....	96
4.31 (a) XRD patterns of $Mn_{1-x}Zn_xCo_2O_4$ ($x = 0.00, 0.05, 0.10, 0.15$, and 0.20) nanoparticles and (b) relative shift in (311) peak of $MnCo_2O_4$ with respect to Zn-doping.....	98
4.32 FESEM images of $Mn_{1-x}Zn_xCo_2O_4$ nanoparticles: (a) $x = 0.00$, (b) $x = 0.05$, (c) $x = 0.10$, (d) $x = 0.15$, and (e) $x = 0.20$	100
4.33 TEM images with corresponding SAED of $Mn_{1-x}Zn_xCo_2O_4$ nanoparticles: (a,b) $x = 0.00$, (c,d) $x = 0.05$, (e,f) $x = 0.10$, (g,h) $x = 0.15$, and (i,j) $x = 0.20$	101
4.34 Normalized XANE spectra and of $Mn_{1-x}Zn_xCo_2O_4$ ($x = 0.00, 0.05, 0.10, 0.15$, and 0.20) nanoparticles at Co K-edge.....	103
4.35 Normalized XANE spectra and of $Mn_{1-x}Zn_xCo_2O_4$ ($x = 0.00, 0.05, 0.10, 0.15$, and 0.20) nanoparticles at Mn K-edge.....	103

LIST OF FIGURES (Continued)

Figure	Page
4.36	Normalized XANE spectra and of $Mn_{1-x}Zn_xCo_2O_4$ ($x = 0.00, 0.05, 0.10, 0.15,$ and 0.20) nanoparticles at Zn K-edge.....104
4.37	XPS survey spectrum of the $Mn_{1-x}Zn_xCo_2O_4$ ($x = 0.00, 0.05, 0.10, 0.15,$ and 0.20) nanoparticles.....107
4.38	XPS spectra at Co 2p of the $Mn_{1-x}Zn_xCo_2O_4$ ($x = 0.00, 0.05, 0.10, 0.15,$ and 0.20) nanoparticles.....108
4.39	XPS spectra at Mn 2p of the $Mn_{1-x}Zn_xCo_2O_4$ ($x = 0.00, 0.05, 0.10, 0.15,$ and 0.20) nanoparticles.....109
4.40	XPS spectra at Zn 2p of the $Mn_{1-x}Zn_xCo_2O_4$ ($x = 0.05, 0.10, 0.15,$ and 0.20) nanoparticles.....110
4.41	XPS spectra at O1s of the $Mn_{1-x}Zn_xCo_2O_4$ ($x = 0.00, 0.05, 0.10, 0.15,$ and 0.20) nanoparticles.....111
4.42	Nitrogen adsorption/desorption isotherms and pore size distribution (inset) of $Mn_{1-x}Zn_xCo_2O_4$ ($x = 0.00, 0.05, 0.10, 0.15,$ and 0.20) nanoparticles.....114
4.43	CV curves at various scan rates of $Mn_{1-x}Zn_xCo_2O_4$ nanoparticles: (a) $x = 0.00,$ (b) $x = 0.05,$ (c) $x = 0.10,$ (d) $x = 0.15,$ and (e) $x = 0.20$118
4.44	Galvanostatic charge-discharge curves at various current densities of $Mn_{1-x}Zn_xCo_2O_4$ nanoparticles: (a) $x = 0.00,$ (b) $x = 0.05,$ (c) $x = 0.10,$ (d) $x = 0.15,$ and (e) $x = 0.20$120
4.45	Capacity retention (%) of $Mn_{1-x}Zn_xCo_2O_4$ ($x = 0.00, 0.05, 0.10, 0.15,$ and 0.20) electrodes after 1000 cycles at a current density of 2 A/g.....121

LIST OF FIGURES (Continued)

Figure	Page
4.46	The Nyquist plots of the $Mn_{1-x}Zn_xCo_2O_4$ ($x = 0.00, 0.05, 0.10, 0.15,$ and 0.20) NPs electrodes.....122
4.47	XRD patterns of precursor and $MnCo_2O_4$ nanofibers calcined for 3 h in atmosphere at different temperatures.....124
4.48	The picture and FESEM images of as-electrospun fibers.....126
4.49	FESEM images with EDS spectra of $MnCo_2O_4$ nanofibers calcined for 3 h in atmosphere at (a) $700\text{ }^\circ\text{C}$, (b) $800\text{ }^\circ\text{C}$, and (c) $900\text{ }^\circ\text{C}$126
4.50	TEM images with corresponding SAED of $MnCo_2O_4$ nanofibers calcined for 3 h in atmosphere at (a,b) as-electrospun fibers, (c,d) $700\text{ }^\circ\text{C}$, (e,f) $800\text{ }^\circ\text{C}$ and (g,h) $900\text{ }^\circ\text{C}$127
4.51	Normalized XANE spectra at Co K-edge of $MnCo_2O_4$ nanofibers.....129
4.52	Normalized XANE spectra at Mn K-edge of $MnCo_2O_4$ nanofibers.....129
4.53	XPS survey spectrum of the $MnCo_2O_4$ nanofibers.....132
4.54	XPS spectra at Co 2p of the $MnCo_2O_4$ nanofibers.....133
4.55	XPS spectra at Mn 2p of the $MnCo_2O_4$ nanofibers.....134
4.56	XPS spectra at O 1s of the $MnCo_2O_4$ nanofibers.....135
4.57	Nitrogen adsorption/desorption isotherms and pore size distribution (inset) of $MnCo_2O_4$ nanofibers calcined at (a) $700\text{ }^\circ\text{C}$, (b) $800\text{ }^\circ\text{C}$, and (c) $900\text{ }^\circ\text{C}$138
4.58	CV curves at various scan rates of $MnCo_2O_4$ nanofibers calcined at (a) $700\text{ }^\circ\text{C}$, (b) $800\text{ }^\circ\text{C}$, and (c) $900\text{ }^\circ\text{C}$141

LIST OF FIGURES (Continued)

Figure	Page
4.59 Galvanostatic charge-discharge curves at various current densities of MnCo ₂ O ₄ nanofibers calcined at (a) 700 °C, (b) 800 °C, and (c) 900 °C.....	144
4.60 Comparison of the specific capacitance as a current density of MnCo ₂ O ₄ nanofibers at various calcination temperature.....	145
4.61 Capacity retention (%) at various calcination temperature of MnCo ₂ O ₄ electrodes after 1000 cycles at a current density of 2 A/g.....	145
4.62 The Nyquist plots of the of MnCo ₂ O ₄ NFs electrodes at various calcination temperature.....	146
4.63 (a) XRD patterns of Mn _{1-x} Ni _x Co ₂ O ₄ (x = 0.00, 0.05, 0.10, 0.15, and 0.20) nanofibers and (b) relative shift in (311) peak of MnCo ₂ O ₄ with respect to Ni-doping.....	148
4.64 FESEM images and EDS spectrums of Mn _{1-x} Ni _x Co ₂ O ₄ nanofibers: (a) x = 0.00, (b) x = 0.05, (c) x = 0.10, (d) x = 0.15, and (e) x = 0.20.....	150
4.65 TEM images with corresponding HRTEM and SAED of Mn _{1-x} Ni _x Co ₂ O ₄ nanofibers: (a,b) x = 0.00, (c,d) x = 0.05, (e,f) x = 0.10, (g,h) x = 0.15, and (i,j) x = 0.20.....	151
4.66 Normalized XANE spectra at Co K-edge of Mn _{1-x} Ni _x Co ₂ O ₄ (x = 0.00, 0.05, 0.10, 0.15, and 0.20) nanofibers.....	153
4.67 Normalized XANE spectra at Mn K-edge of Mn _{1-x} Ni _x Co ₂ O ₄ (x = 0.00, 0.05, 0.10, 0.15, and 0.20) nanofibers.....	153

LIST OF FIGURES (Continued)

Figure	Page
4.68	Normalized XANE spectra at Ni K-edge of $Mn_{1-x}Ni_xCo_2O_4$ ($x = 0.00, 0.05, 0.10, 0.15,$ and 0.20) nanofibers.....154
4.69	XPS survey spectrum of the $Mn_{1-x}Ni_xCo_2O_4$ ($x = 0.00, 0.05, 0.10, 0.15,$ and 0.20) nanofibers.....157
4.70	XPS spectra at Co 2p of the $Mn_{1-x}Ni_xCo_2O_4$ ($x = 0.00, 0.05, 0.10, 0.15,$ and 0.20) nanofibers.....158
4.71	XPS spectra at Mn 2p of the $Mn_{1-x}Ni_xCo_2O_4$ ($x = 0.00, 0.05, 0.10, 0.15,$ and 0.20) nanofibers.....159
4.72	XPS spectra at Ni 2p of the $Mn_{1-x}Ni_xCo_2O_4$ ($x = 0.05, 0.10, 0.15,$ and 0.20) nanofibers.....160
4.73	XPS spectra at O 1s of the $Mn_{1-x}Ni_xCo_2O_4$ ($x = 0.00, 0.05, 0.10, 0.15,$ and 0.20) nanofiber.....161
4.74	Nitrogen adsorption/desorption isotherms and pore size distribution (inset) of $Mn_{1-x}Ni_xCo_2O_4$ ($x = 0.00, 0.05, 0.10, 0.15,$ and 0.20) nanofibers...164
4.75	CV curves at various scan rates of $Mn_{1-x}Ni_xCo_2O_4$ nanofibers: (a) $x = 0.00,$ (b) $x = 0.05,$ (c) $x = 0.10,$ (d) $x = 0.15,$ and (e) $x = 0.20$168
4.76	Galvanostatic charge-discharge curves at various current densities of $Mn_{1-x}Ni_xCo_2O_4$ nanofibers: (a) $x = 0.00,$ (b) $x = 0.05,$ (c) $x = 0.10,$ (d) $x = 0.15,$ and (e) $x = 0.20$170
4.77	Comparison of the specific capacitance at various a current density of $Mn_{1-x}Ni_xCo_2O_4$ ($x = 0.00, 0.05, 0.10, 0.15,$ and 0.20) nanofibers.....171

LIST OF FIGURES (Continued)

Figure	Page
4.78	Capacity retention (%) of $Mn_{1-x}Ni_xCo_2O_4$ ($x = 0.00, 0.05, 0.10, 0.15,$ and 0.20) nanofibers and after 1000 cycles at a current density of 2 A/g.....171
4.79	The Nyquist plots of the of $Mn_{1-x}Ni_xCo_2O_4$ ($x = 0.00, 0.05, 0.10, 0.15,$ and 0.20) NFs electrodes at various calcination temperature.....172
4.80	(a) XRD patterns of $Mn_{1-x}Ni_xCo_2O_4$ ($x = 0.00, 0.05, 0.10, 0.15,$ and 0.20) nanofibers and (b) relative shift in (311) peak of $MnCo_2O_4$ with respect to Zn-doping.....174
4.81	FESEM images of $Mn_{1-x}Zn_xCo_2O_4$ nanofibers: (a) $x = 0.00,$ (b) $x = 0.05,$ (c) $x = 0.10,$ (d) $x = 0.15,$ and (e) $x = 0.20$176
4.82	TEM images with corresponding SAED of $Mn_{1-x}Zn_xCo_2O_4$ nanofibers: (a,b) $x = 0.00,$ (c,d) $x = 0.05,$ (e,f) $x = 0.10,$ (g,h) $x = 0.15,$ and (i,j) $x = 0.20$177
4.83	Normalized XANE spectra and of $Mn_{1-x}Zn_xCo_2O_4$ ($x = 0.00, 0.05, 0.10, 0.15,$ and 0.20) nanofibers at Co K-edge.....179
4.84	Normalized XANE spectra and of $Mn_{1-x}Zn_xCo_2O_4$ ($x = 0.00, 0.05, 0.10, 0.15,$ and 0.20) nanofibers at Mn K-edge.....179
4.85	Normalized XANE spectra and of $Mn_{1-x}Zn_xCo_2O_4$ ($x = 0.00, 0.05, 0.10, 0.15,$ and 0.20) nanofibers at Zn K-edge.....180
4.86	XPS survey spectrum of the $Mn_{1-x}Zn_xCo_2O_4$ ($x = 0.00, 0.05, 0.10, 0.15,$ and 0.20) nanofibers.....183

LIST OF FIGURES (Continued)

Figure	Page
4.87 XPS spectra at Co 2p of the $Mn_{1-x}Zn_xCo_2O_4$ ($x = 0.00, 0.05, 0.10, 0.15,$ and 0.20) nanofibers.....	184
4.88 XPS spectra at Mn 2p of the $Mn_{1-x}Zn_xCo_2O_4$ ($x = 0.00, 0.05, 0.10, 0.15,$ and 0.20) nanofibers.....	185
4.89 XPS spectra at Zn 2p of the $Mn_{1-x}Zn_xCo_2O_4$ ($x = 0.05, 0.10, 0.15,$ and 0.20) nanofibers.....	186
4.90 XPS spectra at O 1s of the $Mn_{1-x}Zn_xCo_2O_4$ ($x = 0.00, 0.05, 0.10, 0.15,$ and 0.20) nanofibers.....	187
4.91 Nitrogen adsorption/desorption isotherms and pore size distribution (inset) of $Mn_{1-x}Zn_xCo_2O_4$ ($x = 0.00, 0.05, 0.10, 0.15,$ and 0.20) nanofibers....	190
4.92 CV curves at various scan rates of $Mn_{1-x}Zn_xCo_2O_4$ nanofibers: (a) $x = 0.00,$ (b) $x = 0.05,$ (c) $x = 0.10,$ (d) $x = 0.15,$ and (e) $x = 0.20$	194
4.93 Galvanostatic charge-discharge curves at various current densities of $Mn_{1-x}Zn_xCo_2O_4$ nanofibers: (a) $x = 0.00,$ (b) $x = 0.05,$ (c) $x = 0.10,$ (d) $x = 0.15,$ and (e) $x = 0.20$	196
4.94 Comparison of the specific capacitance at a function of a current density of $Mn_{1-x}Zn_xCo_2O_4$ ($x = 0.00, 0.05, 0.10, 0.15,$ and 0.20) nanofibers.....	197
4.95 Capacity retention (%) of $Mn_{1-x}Zn_xCo_2O_4$ ($x = 0.00, 0.05, 0.10, 0.15,$ and 0.20) nanofibers and after 1000 cycles at a current density of $2 A/g$	197
4.96 The Nyquist plots of the of $Mn_{1-x}Zn_xCo_2O_4$ ($x = 0.00, 0.05, 0.10, 0.15,$ and 0.20) NFs electrodes at various calcination temperature.....	199

LIST OF FIGURES (Continued)

Figure	Page
4.97	The specific surface area as a function of calcination temperature of MnCo ₂ O ₄ nanoparticles and MnCo ₂ O ₄ nanofibers.....200
4.98	The specific capacitance at current density of 1 A/g as a function of calcination temperature of MnCo ₂ O ₄ nanoparticles and MnCo ₂ O ₄ nanofibers.....200
4.99	Capacity retention after 1000 cycles at current density of 2 A/g as a function of calcination temperature of MnCo ₂ O ₄ nanoparticles and MnCo ₂ O ₄ nanofibers.....201
4.100	The specific surface area as a doping content.....203
4.101	The specific capacitance at current density of 1 A/g as a doping content.....203
4.102	Capacity retention after 1000 cycles at current density of 2 A/g as a doping content.....204

LIST OF ABBREVIATIONS

BET	Brunauer-Emmett-Teller method
BJH	Barrett-Joyner-Halenda method
CV	Cyclic voltammetry
DMF	N, N-dimethylformamide
EDLC	Electrical double layer capacitor
EIS	Electrochemical impedance spectroscopy
FE-SEM	Field emission scanning electron microscopy
GCD	Galvanostatic charge/discharge
IUPAC	International Union of Pure and Applied Chemistry
NMP	N-Methyl-2-pyrrolidone
NPs	Nanoparticles
NFs	Nanofibers
PAN	Polyacrylonitrile
PVDF	Polyvinylidene fluoride
SCs	Supercapacitors
SEM	Scanning electron microscopy
TEM	Transmission electron microscopy
XANES	X-ray absorption near edge structure
XRD	X-ray diffraction

CHAPTER I

INTRODUCTION

1.1 Background and motivation

Nowadays, electrochemical capacitors or supercapacitors (SCs) have advantages i.e. their high power density and energy density, fast charging and discharging, and excellent cycling stability (Kötz and Carlen, 2000). The increasing demand for energy which has resulted in the development of electrode materials for supercapacitors is receiving increasing attention (Mondal *et al.*, 2015). To obtain the requirements of the high energy density, high-power density, and long cycle life, the research trends have been emphasized in the improvement of excellent electrode materials for the next generation of smart electrochemical storage devices. Two types of the supercapacitors are classified according to charge collection mechanism : (i) electric double-layer capacitive materials with a high specific surface area (activated carbon), achieving separation of the charges in a double layer on an electrode, and (ii) pseudocapacitive materials (metal oxides, conductive polymers, etc.), which use the faradaic charge-transfer processes at electrode surfaces (Inagaki *et al.*, 2010; Xu *et al.*, 2010). Especially, the pseudocapacitive materials such as MnO₂ (Nakayama *et al.*, 2007; Wang and Li, 2002), NiO (Wu *et al.*, 2006; Yuan *et al.*, 2009), and Co₃O₄ (Meher and Rao, 2011; Srinivasan and Weidner, 2002), etc., have been inspected as electrode materials with a high capacity performance. Among them, the Co₃O₄ exhibits high conductivity and high specific capacitance. Moreover, the expense

and toxicity of Co_3O_4 are limited to practical use. Recently, the mixed transition metal oxides with spinel structure of AB_2O_4 type such as ZnCo_2O_4 (Karthikeyan *et al.*, 2009; Huang *et al.*, 2015; Wu *et al.*, 2015; Fu *et al.*, 2015), MnCo_2O_4 (Che *et al.*, 2016; Che *et al.*, 2016; Xu *et al.*, 2014), and NiCo_2O_4 (Bai *et al.*, 2016; Gupta *et al.*, 2015; Khalid *et al.*, 2016; Kim *et al.*, 2016; Sun *et al.*, 2016; Waghmode and Torane, 2016; Wang *et al.*, 2015; Xu *et al.*, 2016; Zheng *et al.*, 2016) have attracted as alternative electrode materials for energy storage due to their lower cost, excellent electrochemical performance, and environmentally friendliness. Among these ternary cobaltites, MnCo_2O_4 materials are the most promising as the energy storage materials. Furthermore, the reported specific capacitance value of ZnCo_2O_4 nanoflakes at a current density of 2 A/g is 1220 F/g and this material provides a very long cycle life (94.2% retention after 5000 cycles) (Cheng *et al.*, 2015). NiCo_2O_4 spinel presents higher electrochemical performance than other mixed transition metal oxides due to a good conductive properties of them (Wei *et al.*, 2010). Moreover, S. Tamboli and his research group have obtained $\text{Mn}_{0.4}\text{Ni}_{0.6}\text{Co}_2\text{O}_4$ nanowires with highest specific capacitance 1762 F/g and good cycling stability (89.2% after 2000 cycles), which is very higher than the pure MnCo_2O_4 and NiCo_2O_4 (Tamboli *et al.*, 2017). Therefore, the Ni and Zn doping in MnCo_2O_4 could much enhance the electrochemical properties. A several kinds of methods including hydrothermal (Duan *et al.*, 2013; Li *et al.*, 2014; Krishnan *et al.*, 2016), solvothermal (Padmanathan and Selladurai, 2014; Che *et al.*, 2016), sol-gel (Kong *et al.*, 2014), combustion (Tholkappiyan *et al.*, 2015), and electrodeposition (Sahoo *et al.*, 2015; Xu *et al.*, 2014) have been employed to synthesize the MnCo_2O_4 materials. Moreover, the electrospinning technique was used to fabricate MnCo_2O_4 nanofibers (NFs), which can provide the high surface area

leading to the fast-diffusion of the electrolyte ions and fast charge transfer (Pettong *et al.*, 2016). A simple polymer solution method, which has many benefits such as low-temperature synthesis and creation of homogeneity and purity in products, and very fine powders with high specific surface, has never been used to prepare MnCo_2O_4 materials. Also, the electrospinning technique and a simple polymer solution method are the best choices for the synthesis of the electrode materials.

The purposes of this research are the development of electrode materials for high performance supercapacitors. The pure MnCo_2O_4 and $\text{Mn}_{1-x}\text{M}_x\text{Co}_2\text{O}_4$ (M = Ni and Zn) nanoparticles were prepared by a facile a simple polymer solution method while the pure MnCo_2O_4 and $\text{Mn}_{1-x}\text{M}_x\text{Co}_2\text{O}_4$ (M = Ni and Zn) nanofibers were fabricated by electrospinning technique. XRD, TEM, SAED, FESEM, XANES, XPS, and BET were used to characterize the MnCo_2O_4 nanostructures. The effect of calcination temperatures and Ni and Zn ions substitution in MnCo_2O_4 nanostructures on the electrochemical properties of the MnCo_2O_4 nanostructures were investigated. The electrochemical performance was examined by cyclic voltammetry (CV), galvanostatic charge-discharge (GCD), and electrochemical impedance spectroscopy (EIS).

1.2 Research objective

1.2.1 To synthesize the pure MnCo_2O_4 and $\text{Mn}_{1-x}\text{M}_x\text{Co}_2\text{O}_4$ (M = Ni and Zn) nanoparticles by a simple polymer solution method and to fabricate the pure MnCo_2O_4 and $\text{Mn}_{1-x}\text{M}_x\text{Co}_2\text{O}_4$ (M = Ni and Zn) nanofibers by electrospinning technique.

1.2.2 To characterize the structure and morphology of the MnCo_2O_4 -based nanoparticles and nanofibers.

1.2.3 To study the effect of calcination temperatures on the electrochemical properties of the pure MnCo_2O_4 nanoparticles and nanofibers.

1.2.4 To study the effect of the substituted Ni and Zn ions concentration on the electrochemical properties of $\text{Mn}_{1-x}\text{M}_x\text{Co}_2\text{O}_4$ ($\text{M} = \text{Ni}$ and Zn) nanoparticles and nanofibers.

1.2.5 To study the effect of nanostructures on electrochemical properties of MnCo_2O_4 -based nanoparticles and nanofibers.

1.3 Scope and limitations

1.3.1 This study focuses on the synthesis of $\text{Mn}_{1-x}\text{M}_x\text{Co}_2\text{O}_4$ ($\text{M} = \text{Ni}$ and Zn) nanoparticles by a simple polymer solution method and fabrication of $\text{Mn}_{1-x}\text{M}_x\text{Co}_2\text{O}_4$ ($\text{M} = \text{Ni}$ and Zn) nanofibers by electrospinning technique with $x = 0.00, 0.05, 0.10, 0.15,$ and 0.20 .

1.3.2 The electrochemical properties of the substituted Ni and Zn ions $\text{Mn}_{1-x}\text{M}_x\text{Co}_2\text{O}_4$ nanostructures are compared with those of the pure MnCo_2O_4 nanostructures.

1.3.3 The electrochemical performances were investigated by cyclic voltammetry (CV), galvanostatic charge-discharge (GCD), and electrochemical impedance spectroscopy (EIS).

1.4 Location of research

1.4.1 Advanced Materials Physics Laboratory, School of Physics, Institute of Science, Suranaree University of Technology, Nakhon Ratchasima, Thailand.

1.4.2 The Center for Scientific and Technological Equipment, Suranaree University of Technology, Nakhon Ratchasima, Thailand.

1.4.3 Synchrotron Light Research Institute (Public Organization), Nakhon Ratchasima, Thailand.

1.5 Expected results

1.5.1 Able to synthesize of MnCo_2O_4 -based nanostructures and fabricate of the MnCo_2O_4 -based electrode for supercapacitors.

1.5.2 Experience in the basic and advanced characterization of materials.

1.5.3 Good knowledge of the electrochemical performance of MnCo_2O_4 -based nanostructures.

1.5.4 Publications in International ISI journals.

1.6 Outline of thesis

The thesis is divided into five main chapters. The first chapter includes of the background and motivation, research objectives, scope and limitations, location of research, expected results, and outline of the thesis. Second, Chapter II (literature reviews) presents the information of MnCo_2O_4 , synthesis method, and electrochemical properties of MnCo_2O_4 -based electrodes. Moreover, the principle of the electrochemical capacitor is explained in this chapter. In Chapter III displays the preparation of the MnCo_2O_4 -based nanoparticles by a simple polymer solution method and the fabrication of the MnCo_2O_4 -based nanofibers by an electrospinning technique. Furthermore, the characterization techniques are shown in this section. Chapter IV exposes the basic characterization results and electrochemical performance of

MnCo₂O₄-based electrodes. Base on the results obtained in this research, a discussion of the finding is minutely clarified in this section. Finally, the conclusions and suggestions of this thesis are given in Chapter V.



CHAPTER II

LITERATURE REVIEWS

2.1 Electrochemical capacitors

The earliest electrochemical capacitors or supercapacitors were invented by Howard Becker of General Electric (GE) in 1957 that an electric double-layer capacitor (EDLC) consists of the porous carbon electrodes and sulfuric electrolyte (Becker, 1957). The first practical supercapacitor based on carbon was developed by Boos in 1970 (Boos, 1970). In the 1990s, the supercapacitor was Invented and published by the United States Department of Energy (DOE). Since then, the development of the supercapacitor has focused on electrode materials, suitable electrolytes, composites, and hybridizations to improve performance and reduce costs (Yu *et al.*, 2017). Supercapacitors have many advantages because they can complement the disadvantages of other energy storage devices. Figure 2. shows a Ragone plot that represents the energy density and power density of conventional capacitors, supercapacitors, batteries, and fuel cells. It is obvious that the supercapacitors are efficient in achieving a greater power density than batteries and fuel cells and higher energy density than capacitors. Furthermore, the chemical phase changes during the charging/discharging processes in supercapacitors are a rare occurrence when compare to batteries. This is due to the supercapacitors have a longer cyclic stability than batteries (Yu *et al.*, 2012). The energy storage principles of supercapacitors were divided into two principles;

1. Double-layer capacitance is electrostatic storage that the separation of charge occurs in a Helmholtz.

2. Pseudocapacitance is electrochemical storage that faradaic redox reactions with charge-transfer occur during the charging/discharging processes.

Nowadays, the supercapacitors were classified according to energy storage mechanisms; electrochemical double-layer capacitors (EDLCs), pseudocapacitors, and hybrid-capacitors.

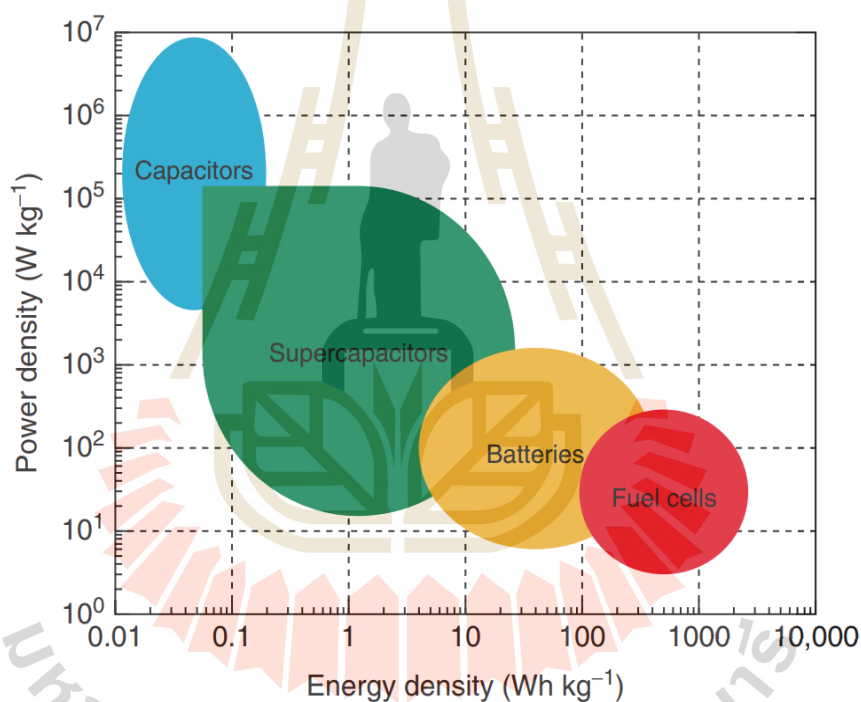


Figure 2. Ragone plot represents an energy density and power density of energy storage devices (Kim *et al.*, 2015).

2.1.1 Electrochemical double-layer capacitors (EDLCs)

The electrochemical capacitor has the 2-electrodes, separator, and electrolyte. The electrolyte consisting of positive and negative ions was prepared by dissolving in ID water. The energy storage principle of EDLCs is similar to

conventional capacitors. However, the conventional capacitors have storage charges in the dielectric layer while the storage charges of EDLCs occur in the interfaces between the electrolyte and surface of electrodes (as presented in Figure 2.1). To induce the different polarities in electrodes, the voltage is applied to both electrodes of an EDLCs. This has resulted in the translocation of the positive and negative ions to the micropores of the negative and positive electrodes, respectively. Normally, the commercial EDLCs have been using the activated carbon as an electrode material because it can provide the values of specific capacitance in the range of 100-120 F/g in the organic electrolyte (Simon and Gogotsi, 2008).

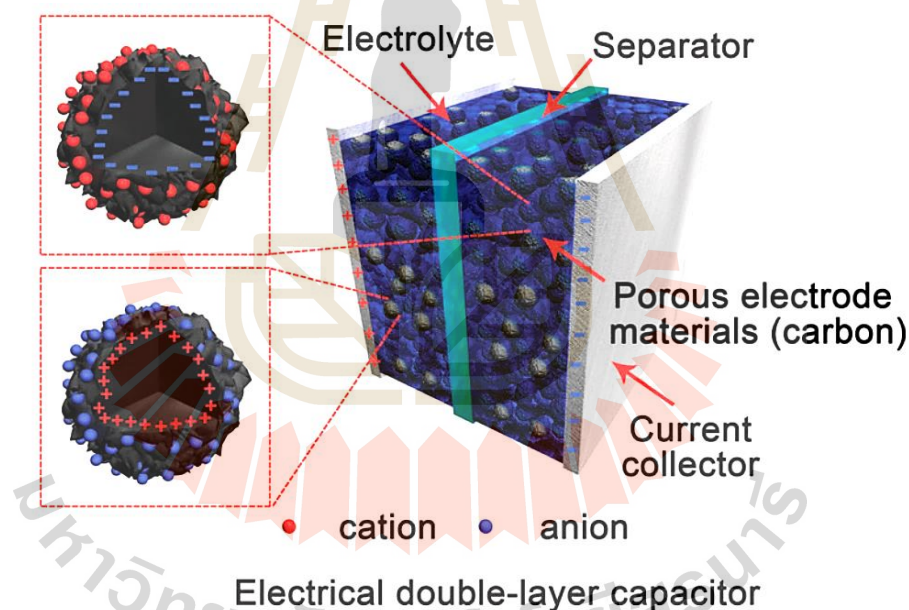


Figure 2.1 A schematic of charged electrochemical double-layer capacitor (Zhong *et al.*, 2015).

2.1.2 Pseudocapacitors

The electrode materials of pseudocapacitors have been fabricated by composite the conductive polymers or metal oxides with the carbon material which is the performance enhancement of supercapacitors. Hence, the charge storage of EDLCs

at the interface between the electrolyte and surface of electrodes is not simply a physical mechanism, and the faradaic redox reactions with charge-transfer occur during the charging/discharging processes, as demonstrated in Figure 2.2.

Ruthenium oxide is one typical material used as electrodes for pseudocapacitors. In a proton-rich electrolyte environment, the ruthenium oxide has multiple redox phases (i.e., $\text{Ru}^{+4/+3}$ and $\text{Ru}^{+3/+2}$), indicating more electron transfers leading to the higher charge storage (Zhang and Zhao, 2009). In the same way, the synthesized RuO_2 nanotubes present the specific capacitance of 1300 F/g in the H_2SO_4 electrolyte (Hu *et al.*, 2006). In addition, the transition metal oxide of Co_3O_4 , NiO , MnO_2 , and conductive polymers are investigated widely as electrode materials as shown in Table 2.1. However, RuO_2 is expensive, toxic, and scarce in nature while Co_3O_4 , NiO , MnO_2 have low electrical conductivity which is limits for practical application in supercapacitors. Hence, the research and development of supercapacitors have focused on the resources of electrode materials with a non-toxic and inexpensive.

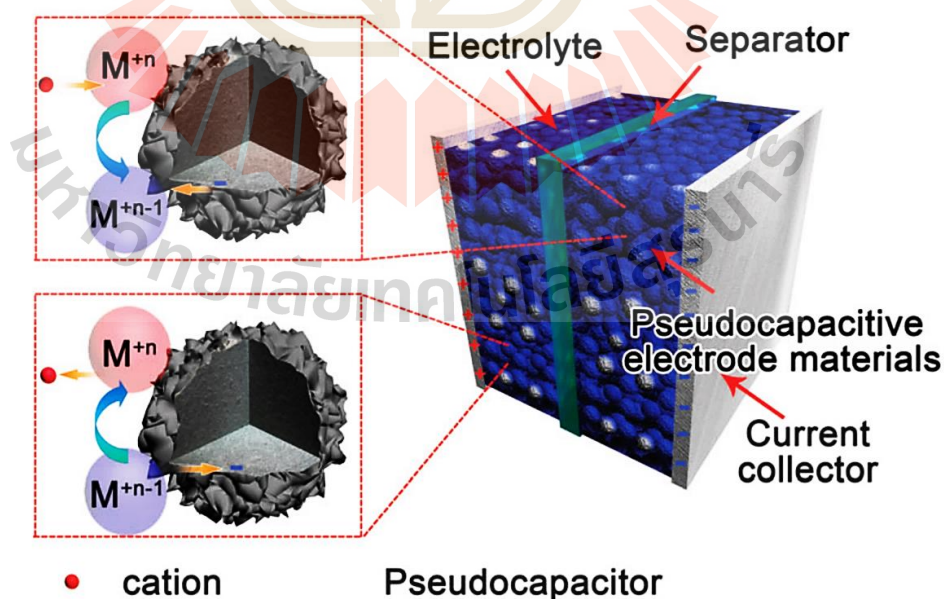


Figure 2.2 A schematic of charged pseudocapacitors (Zhong *et al.*, 2015).

Table 2.1 Summary of the metal oxide electrodes.

Electrode materials	Electrolytes	Specific capacitance (F/g)	References
RuO ₂ ·H ₂ O	0.5 M H ₂ SO ₄	650	(Kim and Kim, 2006)
RuO _x ·H ₂ O	0.1 M NaOH	1580	(Hu and Chen, 2004)
MnO ₂	0.5 M K ₂ SO ₄	261	(Yang <i>et al.</i> , 2007)
MnO ₂	0.1 M H ₂ SO ₄	678	(Pang <i>et al.</i> , 2000)
MnO ₂ /AC	0.65 M K ₂ SO ₄	29	(Brousse <i>et al.</i> , 2004)
NiO	1 M KOH	138	(Zhao <i>et al.</i> , 2007)
NiO	1 M KOH	278	(Nam <i>et al.</i> , 2002)
Co ₃ O ₄	6 M KOH	746	(Gao <i>et al.</i> , 2010)
Polypyrrole	1 M H ₂ SO ₄	400	(Zhang <i>et al.</i> , 2010)
Polyaniline	NaClO ₄ and HClO ₄	609	(Zhou <i>et al.</i> , 2005)

2.1.3 Hybrid-capacitors

Hybrid-capacitors is one of energy storages devices that consist of an EDLC electrode or pseudocapacitive electrode and the battery-type electrode. To enhance the performance of hybrid-capacitors, the charge storage mechanisms of them combine both electrostatic and faradaic process. The new battery-type hybrid such as LIC (Figure 2.3) and carbon/PbO₂ have been developed (Zhong *et al.*, 2015). The reviewed hybrid-capacitors in this thesis comprise:

1. One EDLC electrode and the other pseudocapacitive or battery-type electrode were used to design the asymmetric supercapacitors (Wu *et al.*, 2010).

2. The electrodes were fabricated from EDLC electrode materials and pseudocapacitive electrode materials (Wu *et al.*, 2010).

3. The asymmetric supercapacitors comprises of one pseudocapacitive electrode and the other battery-type electrode (Wu *et al.*, 2010).

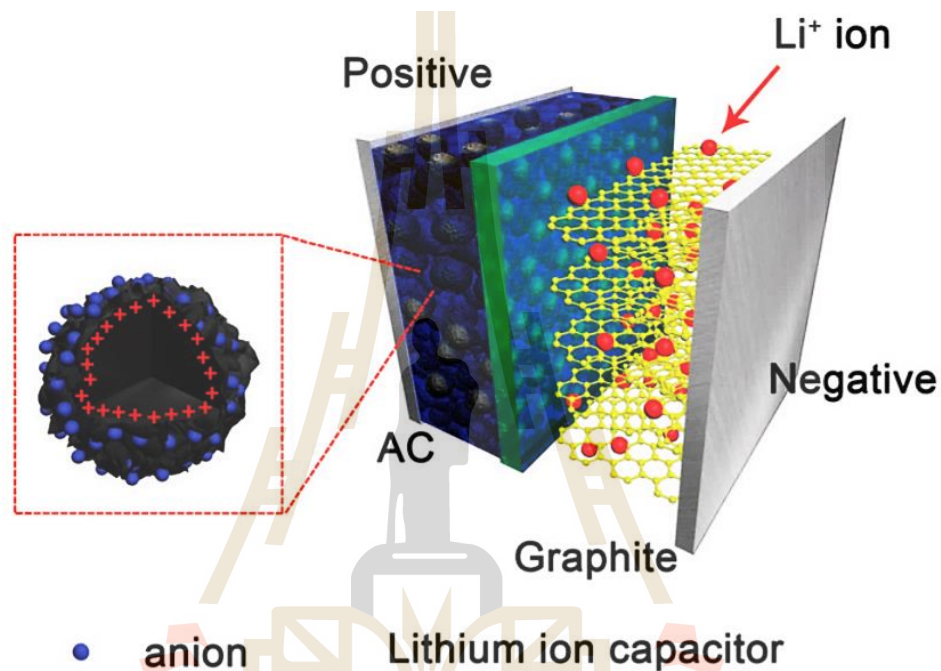


Figure 2.3 Schematic of an a hybrid-capacitor (Zhong *et al.*, 2015).

2.2 Manganese cobalt spinel oxides

Most AB_2O_4 cubic spinel oxides are mixed valent metal oxides of Cobalt (II, III) oxide, where A and B indicate the divalent and trivalent cations, respectively. These complex oxides have spinel structure with a space group $Fd\bar{3}m$ (Zhai *et al.*, 2015). This close packing includes 32 octahedral interstice sites and 64 tetrahedral interstice sites with O^{2-} ions (Figure 2.4). The trivalent metal ion exists in the octahedral sites while Co ions dominate both octahedral and tetrahedral sites (Zhu *et al.*, 2014). Cobalt-based

spinel oxides have versatile applications owing to their interesting functional properties such as electrode materials (Bai *et al.*, 2016; Che *et al.*, 2016; Dong *et al.*, 2017; Fu *et al.*, 2015; Huang *et al.*, 2015), catalysts (Cao *et al.*, 2016; Kim *et al.*, 2015; Kim *et al.*, 2015; Liu *et al.*, 2013), and magnetic materials (Borges *et al.*, 2006; Habjanič *et al.*, 2014; Joy and Date, 2000; Marco *et al.*, 2001; Meena *et al.*, 2015; Nguyen *et al.*, 2015).

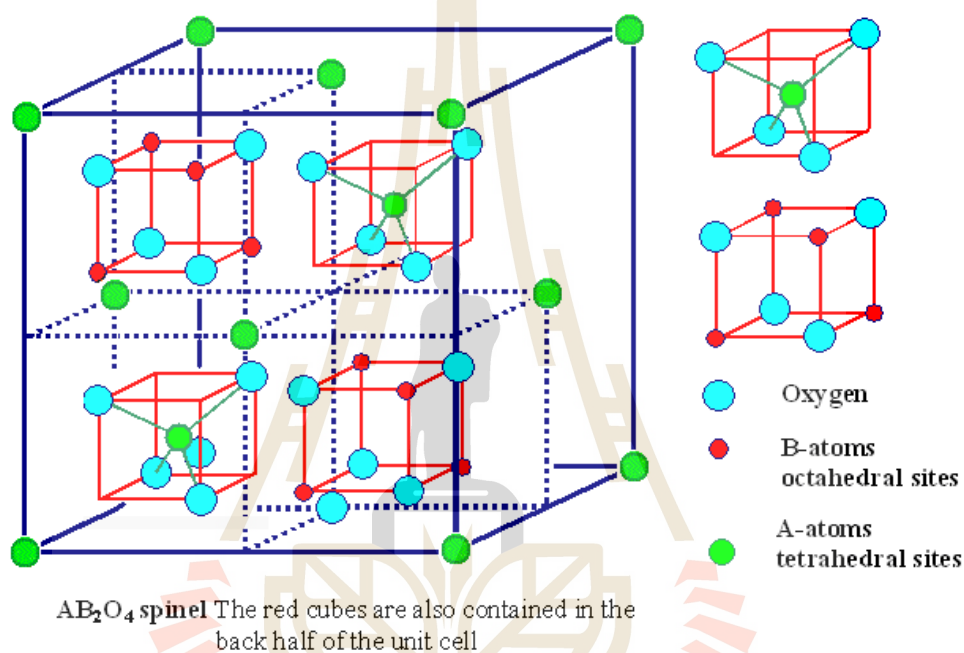


Figure 2.4 Crystal Structure of AB₂O₄ cubic spinel (Issa *et al.*, 2013).

2.3 Electrochemical properties of MnCo₂O₄

Recently, the cobalt-based spinel oxides such as CuCo₂O₄, ZnCo₂O₄, NiCo₂O₄, and MnCo₂O₄ have been investigated in term of electrode materials for supercapacitors. The CuCo₂O₄ nanowires, which are prepared by nanocasting using a silica SBA-15 template provide good specific capacitance of 1210 F/g at current densities of 2 A/g (Pendashteh *et al.*, 2015). At current densities of 2 A/g, the spinel CuCo₂O₄ nanobelts exhibit maximum specific capacitance of 809 F/g (Vijayakumar *et al.*, 2015). Further,

the $\text{CuCo}_2\text{O}_4/\text{CuO}$ nanocomposites were conducted at scan rate of 2 mV/s in 1 M KOH electrolyte which provide the specific capacitance of 781 F/g. These material were design to asymmetric supercapacitor (ASC) with activated carbon (AC) as negative electrode, which exhibit the specific capacitance of 141 F/g (Shanmugavani and Selvan, 2016). Huang *et al.* obtain the rodlike ZnCo_2O_4 porous nanostructure (Huang *et al.*, 2015), which exhibit the specific capacitance (at 1 A/g) of 604.52 F/g. The obtained ZnCo_2O_4 microspheres exhibit remarkable electrochemical performances, which show excellent capacitance retention of 97.1% After 1500 cycles at 10 A/g and a specific capacitance of 689.4 F/g at 1 A/g (Fu *et al.*, 2015). The spinel NiCo_2O_4 nanoparticles that provide specific capacitance of 1400 F/g and 1254 F/g (Wei *et al.*, 2010; Zhu *et al.*, 2014) were prepared by a facile sol-gel method. As presented in Table 2.2, among these ternary cobaltites, Manganese cobalt oxides (MnCo_2O_4) previously demonstrate some remarkable electrochemical properties. In addition, the MnCo_2O_4 have a theoretical specific capacitance of $\text{MnCo}_2\text{O}_4 \sim 3620$ F/g. This value is quite high when compared to other electrode materials. For example, nanocage MnCo_2O_4 shows a high performance supercapacitor, that possess a high specific capacitance of 1763 F/g and 95% capacitance retention at 1 A/g (after 4500 cycles) (Dong *et al.*, 2017). In the 2014, Xu *et al.* reported that the MnCo_2O_4 nanowires show the desirable performance and great specific capacitance of 1342 F/g at 1 A/g and 988 F/g at 20 A/g (Xu *et al.*, 2014). To improve the performance supercapacitor, Ni substituted into MnCo_2O_4 structure has obtained that the $\text{Mn}_{0.4}\text{Ni}_{0.6}\text{Co}_2\text{O}_4$ spinel shows an excellent specific capacitance of 1762 F/g (Tamboli *et al.*, 2017) Accordingly, the excellent capacitive performance and long-time cyclic stability suggest that the MnCo_2O_4 is the best choice for electrode materials of supercapacitors.

Table 2.2 Comparison of the MnCo₂O₄-based performance for supercapacitor.

Material	Synthesis method	Specific capacitance (F/g)	References
1D MnCo ₂ O ₄ nanowire	Hydrothermal	349.8 (1 A/g)	(Li <i>et al.</i> , 2014)
MnCo ₂ O ₄ nanowire	Thermal decomposition	1342 (1 A/g)	(Xu <i>et al.</i> , 2014)
MnCo ₂ O ₄ nanoparticles	Hydrothermal	671 (5 mV/s)	(Tholkappiyan <i>et al.</i> , 2015)
Flower-like MnCo ₂ O ₄	Solvothermal	539 (1 A/g)	(Che <i>et al.</i> , 2016)
Mesoporous MnCo ₂ O ₄	Solvothermal	346 (1 A/g)	(Padmanathan and Selladurai, 2014)
MnCo ₂ O ₄ nanosheet	Electrodeposition	290 (1 mV/s)	(Sahoo <i>et al.</i> , 2015)
MnCo ₂ O ₄ nanosheet	Electrodeposition	400(1 A/g)	(Nguyen <i>et al.</i> , 2015)
MnCo ₂ O ₄ nanoparticles	Sol-gel	405 (1 mA/cm)	(Kong <i>et al.</i> , 2014)
1D MnCo ₂ O ₄ nanoneedles	Hydrothermal	1535 (1 A/g)	(Hui <i>et al.</i> , 2016)
Mn _{0.4} Ni _{0.6} Co ₂ O ₄ nanowire	Hydrothermal	1762 (1 A/g)	(Tamboli <i>et al.</i> , 2017)
MnO ₂ / MnCo ₂ O ₄ composites	Solution combustion processes	497 (0.5 A/g)	(Zhang <i>et al.</i> , 2016)
MnCo ₂ O ₄ @RGO	Hydrothermal	334 (1 A/g)	(Yuan <i>et al.</i> , 2014)

CHAPTER III

RESEARCH METHODOLOGY

This chapter explains the experimental procedure, consisting three parts. First, the materials and apparatus are given. Second, the materials fabrication is explained. Finally, the method of materials characterization is also given.

3.1 Materials and apparatus

3.1.1 Materials

- Cobalt (II) Nitrate Hexahydrate ($\text{Co}(\text{NO}_3)_2 \cdot 6\text{H}_2\text{O}$) $M_w = 291.03$ g/mol, 99.95%, Kanto.
- Manganese (II) Nitrate. hydrate ($\text{Mn}(\text{NO}_3)_2 \cdot x\text{H}_2\text{O}$) $M_w = 178.95$ g/mol, 99.99% , Aldrich.
- Nickel (II) Nitrate Hexahydrate ($\text{Ni}(\text{NO}_3)_2 \cdot 6\text{H}_2\text{O}$) $M_w = 290.79$ g/mol, 99.95%, Kanto.
- Zinc Nitrate. hydrate ($\text{Zn}(\text{NO}_3)_2 \cdot x\text{H}_2\text{O}$) $M_w = 297.49$ g/mol, 99.99% , Aldrich.
- Polyacrylonitrile, M_w 150,000, Aldrich.
- *N,N*-dimethylformamide anhydrous ($\text{C}_3\text{H}_7\text{NO}$), 99.8%, SIAL.
- Polyvinylidene fluoride (PVDF), M_w 180,000, Aldrich.
- Potassium hydroxide (KOH).

3.1.2 Apparatus

- Electrospinning system
- Plastic syringe 10 ml.
- Stainless needle No. 23
- Aluminum foil
- Beaker
- Hot Plate & Magnetic stirrer (IKA, C-MAC HS7)
- Electrochemical station (AUTOLAB-PGSTAT302N, Netherlands)
- Nickel foam, 99.99%, MTI, USA
- Ag/AgCl reference electrode, Basic, ME-2079, USA
- Platinum wire 0.5 in diameter, PT541009, ADVENT, England
- Tweezer
- Ultrasonicate
- Hydraulic presser
- Copper grid

3.2 Materials fabrication

3.2.1 Precursor preparation

The MnCo_2O_4 -based nanostructures which consist of the MnCo_2O_4 , Ni-doped MnCo_2O_4 , and Zn-doped MnCo_2O_4 were prepared by a simple polymer solution and electrospinning method. The polyacrylonitrile (PAN), *N,N*-dimethylformamide (DMF), and metal (Mn, Co, Ni, and Zn) nitrates were used as the precursor materials. The polymer solutions were prepared by dissolving PAN in DMF, whereas metal solutions were obtained by using mixed of the metal nitrates in DMF, which used the

PAN 10 g for metal nitrates 2 g. Both solutions were mixed by using the magnetic stirrer at room temperature for 3 h, and then the mixture was sonicated for 45 min. After that, mixed precursor solution was used to synthesize MnCo_2O_4 -based nanoparticles and fabricate MnCo_2O_4 -based nanofibers. The details about the chemical compositions of the precursor solution for MnCo_2O_4 -based nanoparticles and MnCo_2O_4 -based nanofibers are summarized in Table 3.1-3.3.

3.2.2 Synthesis of MnCo_2O_4 -based nanoparticles

The precursor solution was subsequently stirred overnight at 60 °C, until a gel was formed. The gel was dried at 70 °C in the oven and the dried gel was ground to a fine powder. Finally, the MnCo_2O_4 nanoparticles were obtained by calcination the precursors in the air for 2 h at 500, 600, 700, and 800 °C while the $\text{Mn}_{1-x}\text{Ni}_x\text{Co}_2\text{O}_4$ and $\text{Mn}_{1-x}\text{Zn}_x\text{Co}_2\text{O}_4$ ($x = 0.0, 0.05, 0.1, 0.15, \text{ and } 0.20$) nanoparticles were produced by calcination the precursors at 600 °C in the air for 2. The schematic diagram for the synthesis of MnCo_2O_4 -based nanoparticles is presented in Figure 3.2.

3.2.3 Fabrication of MnCo_2O_4 -based nanofibers

The precursor solution was used to fabricates electrospun nanofibers by using the electrospinning system. The electrospun nanofibers were obtained by applying the voltage about 10-11 kV with a feeding rate of 0.6 ml/h as shown in Figure 3.1. The distance between the syringe nozzle and collector was fixed at 15 cm. After that the as-spun was dried at 70 °C for 48 h. Finally, the electrospun nanofibers were calcined at 700 °C for 3 h in air. The diagram for the fabrication of MnCo_2O_4 -based nanofibers is presented in Figure 3.3.

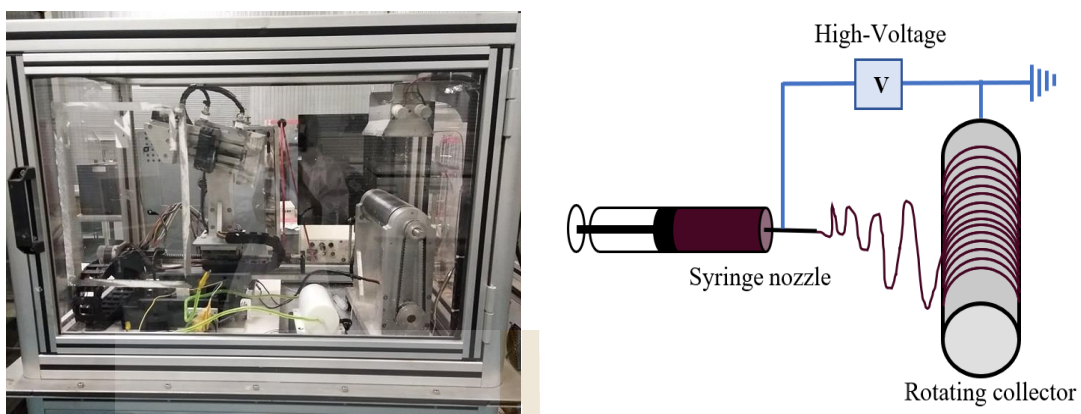


Figure 3.1 Diagram showing the electrospinning system.

Table 3.1 List of starting raw materials for preparation of the precursor solution of MnCo_2O_4 nanostructures.

Material	Polymer source		Metal source		
	PAN (g)	DMF (ml)	$\text{Co}(\text{NO}_3)_2$ (g)	$\text{Mn}(\text{NO}_3)_2$ (g)	DMF (ml)
MnCo_2O_4 nanoparticles	10	80	1.530	0.470	20
MnCo_2O_4 nanofibers	6	50	0.918	0.282	10

Table 3.2 List of starting raw materials for preparation of the precursor solution of $Mn_{1-x}Ni_xCo_2O_4$ nanostructures.

Material	Samples	Polymer source		Metal source			
		PAN (g)	DMF (ml)	Co(NO ₃) ₂ (g)	Mn(NO ₃) ₂ (g)	Ni(NO ₃) ₂ (g)	DMF (ml)
$Mn_{1-x}Ni_xCo_2O_4$ nanoparticles	0.00	10	80	1.530	0.470	-	20
	0.05	10	80	1.519	0.444	0.038	20
	0.10	10	80	1.508	0.417	0.075	20
	0.15	10	80	1.497	0.391	0.112	20
	0.20	10	80	1.486	0.365	0.148	20
$Mn_{1-x}Ni_xCo_2O_4$ Nanofibers	0.00	6	50	0.918	0.282	-	10
	0.05	6	50	0.911	0.266	0.023	10
	0.10	6	50	0.905	0.250	0.045	10
	0.15	6	50	0.898	0.235	0.067	10
	0.20	6	50	0.892	0.219	0.089	10

Table 3.3 List of starting raw materials for preparation of the precursor solution of $Mn_{1-x}Zn_xCo_2O_4$ nanostructures.

Material	Samples	Polymer source		Metal source			
		PAN (g)	DMF (ml)	Co(NO ₃) ₂ (g)	Mn(NO ₃) ₂ (g)	Zn(NO ₃) ₂ (g)	DMF (ml)
$Mn_{1-x}Zn_xCo_2O_4$	0.00	10	80	1.530	0.470	-	20
nanoparticles	0.05	10	80	1.518	0.443	0.039	20
	0.10	10	80	1.506	0.417	0.077	20
	0.15	10	80	1.495	0.391	0.115	20
	0.20	10	80	1.483	0.365	0.152	20
	$Mn_{1-x}Zn_xCo_2O_4$	0.00	6	50	0.918	0.282	-
Nanofibers	0.05	6	50	0.911	0.266	0.023	10
	0.10	6	50	0.904	0.250	0.046	10
	0.15	6	50	0.897	0.234	0.069	10
	0.20	6	50	0.890	0.219	0.091	10

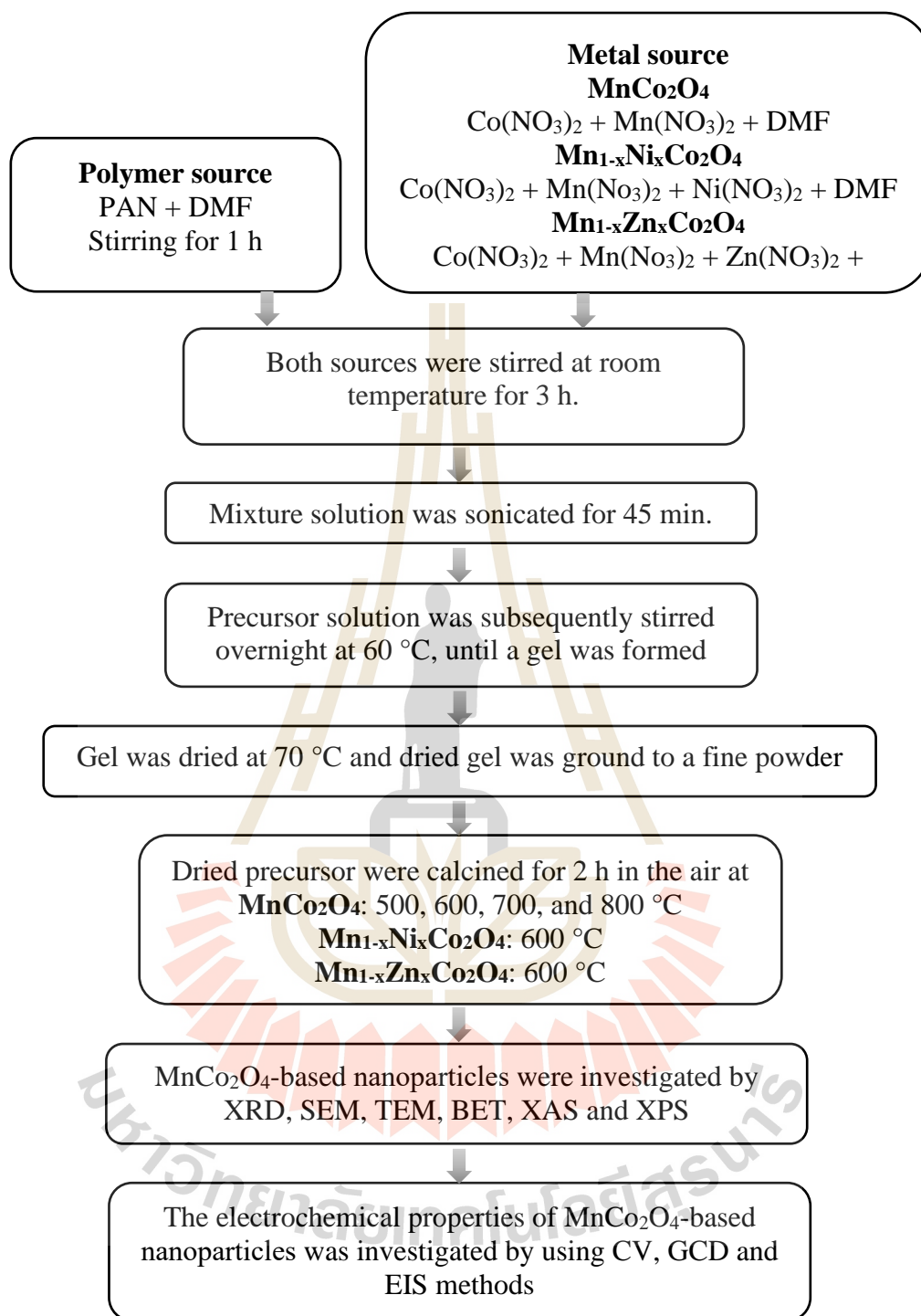


Figure 3.2 A schematic of the preparation and characterization of MnCo₂O₄-based nanoparticles.

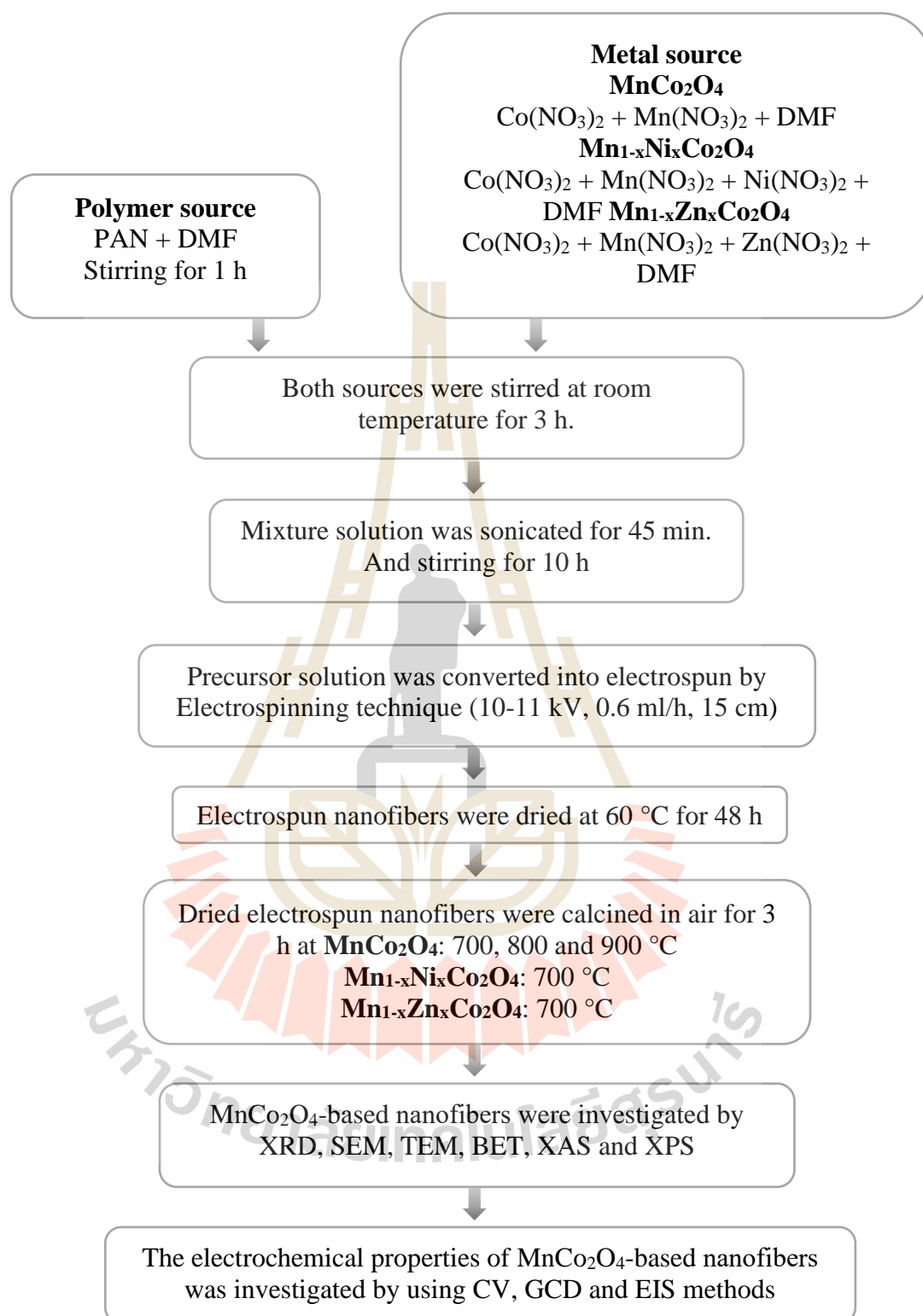


Figure 3.3 A schematic of the preparation and characterization of MnCo₂O₄-based nanofibers.

3.3 Material characterization

3.3.1 X-Ray diffraction (XRD)

The X-ray diffraction (XRD) is the principal technique used for phase identification of a crystalline material and determine the unit-cell dimensions. X-ray diffraction depends on the crystalline sample and the constructive interference of X-rays are produced from X-ray tubes. Then it is filtered to provide monochromatic X-rays and directed directly to the sample. The interaction between the incident radiation and the sample leading to the constructive interference. The geometrical interpretation of the XRD phenomenon (constructive interferences) has been given by W.L. Bragg (Bragg, 1929). Figure 3.4 presents the geometrical of diffraction and the determination of Bragg's law.

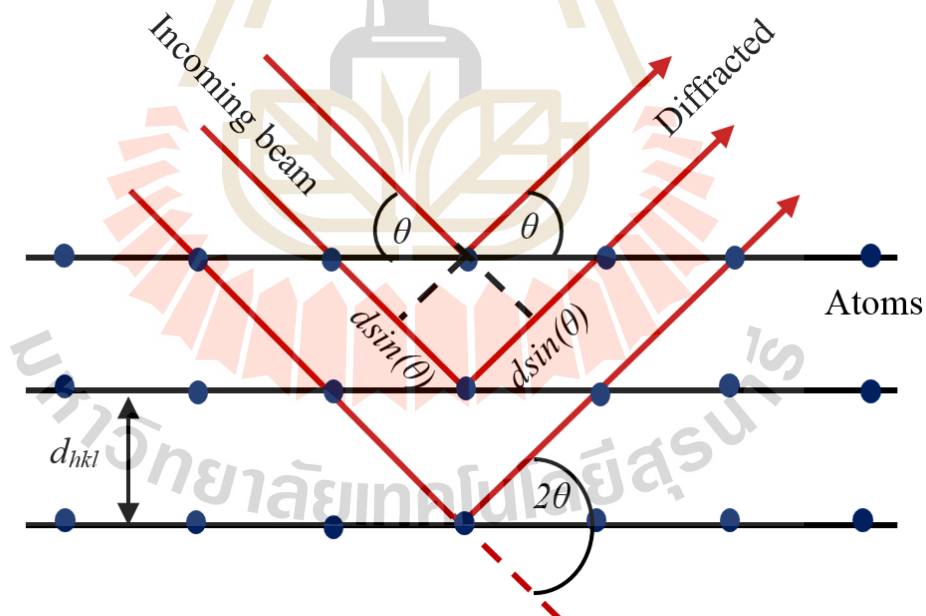


Figure 3.4 Diagram showing geometrical condition for diffraction from lattice planes
Bragg's law is given in equation (3.1).

$$n\lambda = 2d_{hkl} \sin(\theta) \quad (3.1)$$

where n is the order of diffraction, λ is the wavelength of the incident beam, d_{hkl} is the lattice spacing, and θ is the angle of the diffracted beam in degree. According to the diffraction pattern, the average crystallite sizes were determined by using Scherrer's equation as follows (Patterson, 1939).

$$D = \frac{0.9\lambda}{\beta \cos(\theta)} \quad (3.2)$$

where λ is the incident wavelength of Cu K α radiation, θ angle of the Bragg diffraction, and β is the full width at half maximum (FWHM) of the respective peaks in radians. The lattice parameter " a " of cubic structure can be estimated from the XRD data as follows:

$$\frac{1}{d_{hkl}^2} = \frac{h^2 + k^2 + l^2}{a^2} \quad (3.3)$$

where d_{hkl} is the interplanar spacing and hkl are the Miller indices.

In this work, the structure of MnCo₂O₄-based nanostructures was examined on a D2 Advance Bruker with Cu K α and $\lambda = 0.15406$ nm. The samples were placed on a silicon glass. The step size of 0.02 and step time of 0.4 were used to records the XRD patterns in the 2θ of 10° to 80°. The crystalline material was identified by comparison of the XRD pattern with the registered patterns of the Joint Committee for Powder Diffraction Standards (JCPDS).

3.3.2 Scanning electron microscopy

Scanning electron microscopy (SEM) is a power technique for observing the morphology of materials. This technique uses a focused electron beam to obtain information about the chemical composition and external morphology of a sample. The principles of SEM are as follows. The electron gun is heated to produce

the electrons. These electrons are propelled towards as the sample. Since the measurement sample must be conductivity to prevent charging, the coating sample with conducting material such as gold is necessary. When the electrons crash the conductive sample, the primary electrons penetrate through the sample with a depth that is based on the energy level of those electrons. The inelastic interactions between the primary electrons and the sample lead to occurring the secondary electrons, while the backscattered electrons result from elastic interactions. The secondary electron detector and backscattered detector are used for measuring these reflected electrons. The sample image is shown on the computer screen after signal processing (Figure 3.5).

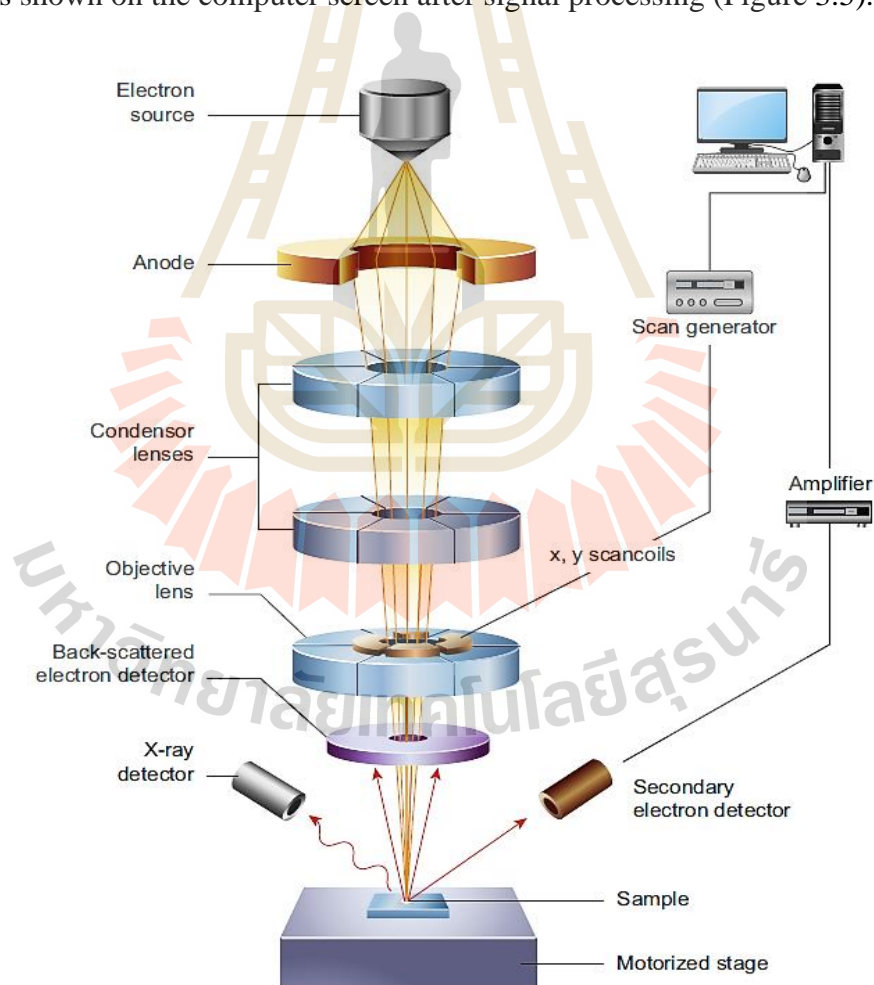


Figure 3.5 Illustration of the core components of a SEM microscope (Inkson, 2016).

In this work, the samples were placed onto stubs by using the carbon tape to attach the samples to the stubs and coated with gold in a vacuum for 10 min. Field-emission scanning electronic microscopy (FESEM; JEOL, JEM. 7800X) was used to investigate the morphology of MnCo_2O_4 -based nanostructures.

3.3.3 Transmission electron microscopy

Transmission electron microscopy (TEM) is employed for observing the crystallization, morphology and particle size distribution. The scanning electron microscope contains an electron emission source, electromagnetic lenses, and electron detector. The electrons are produced by heating electron gun. The electromagnetic lenses are employed for acceleration and focusing the electron beam toward the very thin sample. Then, the transmitted electrons are measured by a parallel detector, and the sample image is shown on the computer screen while the X-rays analysis gives information about the chemical composition (Figure 3.6). In the selected area electron diffraction technique, the diffraction pattern which shows in the focal plane is formed by an objective lens. The first image of the diffraction pattern is magnified by lenses and is shown on the screen of the TEM. The electron diffraction pattern is obtained by select the small sample area.

In this work, the MnCo_2O_4 -based nanostructures were dispersed in alcohol. After that, the dispersed solution was dripped onto the copper grid following by dried in air. The morphology, particle size distribution, and selected-area electron diffraction (SAED) patterns of MnCo_2O_4 -based nanostructures were investigated by using the transmission electron microscopy (TEM; Zeiss, West Germany).

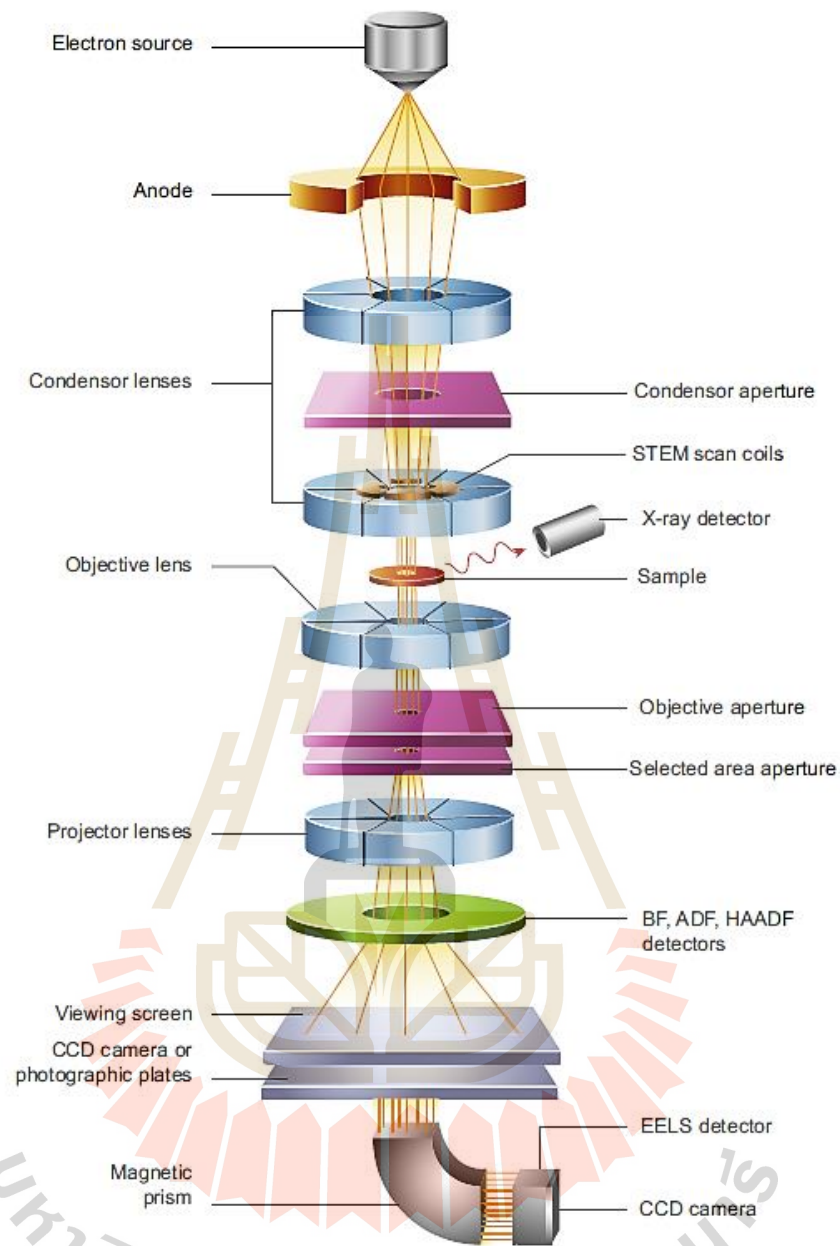


Figure 3.6 Schematic of the core components of a TEM microscope (Inkson, 2016).

3.3.4 Brunauer-Emmett-Teller (BET) and Barrett-Joyner-Halenda (BJH)

The specific surface area of the MnCo_2O_4 -based nanostructures is obtained from the BET analysis by measuring the adsorption of multiple layers of nitrogen relative to the relative pressure.

The phenomenon multi-layer adsorption can be explained by the following equation:

$$\frac{1}{w[(P_0/P)-1]} = \frac{P}{P_0} \left(\frac{C-1}{W_m C} \right) + \frac{1}{W_m C} \quad (3.4)$$

where w is the gas adsorbed volume (ml) at standard temperature and pressure ($T = 273.15$ K and $P = 1.013 \times 10^5$ Pa). W_m is the gas adsorbed volume (ml) at STP to creates a monolayer on the surface of the sample. P_0 is saturated pressure of adsorbate gas (Pa). P is partial vapour pressure of adsorbate gas in equilibrium with the surface at 77.4 K. C is BET constant. At the relative pressures (P_0/P), N_2 is adsorbed in the form of single molecules. The physical adsorption of gas molecules provides the specific surface areas of the materials. The total surface area (S_{total}) and the specific surface area (S_{BET}) are estimated by the following equations:

$$S_{total} = \frac{W_m N A_{cs}}{M} \quad (3.5)$$

$$S_{BET} = \frac{S_{total}}{m} \quad (3.6)$$

where A_{cs} is adsorbate cross section area (16.2 Å for nitrogen), M is the molecular weight of the adsorbate, N is the Avogadro number (6.023×10^{23}), and m is the sample mass.

In addition, the adsorption/desorption techniques are used to evaluate the pore area and total pore volume using BJH analysis. At relative pressures ($P_0/P=0.99$), the total pore volume (V_{total}) of materials can be estimated from the amount of vapor adsorbed by the following equation:

$$V_{total} = \frac{P_a V_{ads} V_m}{RT} \quad (3.7)$$

Where V_{ads} is the gas adsorbed volume, V_m is the liquid adsorbate volume, P_a is

the ambient pressure, R is gas constant (8.314 J/mol.K), and T is ambient temperature. The total pore volume can be used to estimate the average pore size which is evaluated by assuming the porous shape as cylindrical geometry (type A hysteresis). The average pore radius (r_p) can be given by the following equation:

$$r_p = \frac{2V_{total}}{S_{BET}} \quad (3.8)$$

The six types of IUPAC standard adsorption isotherms are shown in Figure 3.7. The materials with pore diameter < 2 nm are microporous materials that have a small external surface area (Type I). Type II is non-porous materials. Type III is typical feature of a non-porous materials or a macropores materials (pore diameter >50 nm). The hysteresis loop feature is referred to the mesopores materials (pore diameter 2-50 nm) and the macropores materials (type IV). Type V isotherm is referred to the mesoporous materials and macropores materials that have the rather weak adsorbate/adsorbent interaction. Finally, type VI is typical isotherm of non-porous solid with homogeneous surface.

In this work, the specific surface area and pore character of the samples were obtained from the N₂ adsorption-desorption at a liquid nitrogen temperature (77 K) on automatic specific surface area/pore size distribution analyser (BET, BEL SORP MINI II, JAPAN). The MnCo₂O₄-based nanostructures were degassed at 120 °C for 10 h at 10⁻⁵ Pa before measurement to ensure that the composite samples were clean and free of moisture. The mean pore diameter, total pore volume, and specific surface area were evaluated by BET method. BJH method was used to estimate pore area, pore volume, and pore size distribution.

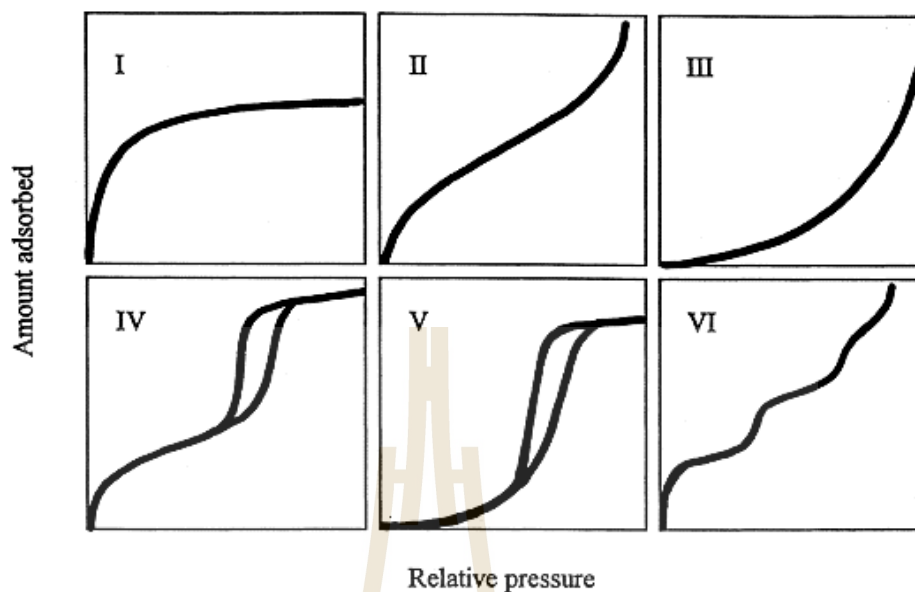


Figure 3.7 Categories of gas adsorption loops (IUPAC) (Donohue and Aranovich, 1998).

3.3.5 X-ray absorption spectroscopy (XAS)

X-ray absorption spectroscopy (XAS) is a high-efficiency technique for determining the chemical and structural information at the local environment of the absorber. The XAS spectrum consists of X-ray absorption near edge structure (XANES) and extended X-ray absorption fine structure (EXAFS). The XANES spectrum often gives information on the coordination geometry (e.g., octahedral, tetrahedral coordination) and oxidation state of the absorbing atom. On the other hand, the EXAFS provides information about coordination number and the distances to nearest neighbor of the absorbing atom. XANES or EXAFS measurement can be carried out in transmission or fluorescent modes. The samples for transmission mode must be have a uniform composition and thickness. In the transmission measurements, an X-ray beam striking the sample at 90° and traverses the sample. Then, the intensity of transmitted X-ray beam will be attenuated. X-ray absorption was obtained by

measuring a transmitted X-ray beam, then converts the transmittance spectra to absorption spectra. The intensity ratio of the incident x-ray beam and the transmitted x-ray beam is directly proportional to the exponential of the absorption coefficient multiplied by the sample thickness. X-ray Absorption is described by equation (3.9).

$$\mu(E)x = -\ln\left(\frac{I}{I_0}\right) \quad (3.9)$$

where I_0 is the intensity of incident X-ray beam, x is the sample thickness, $\mu(E)$ is absorption coefficient and I is the intensity of transmitted X-ray beam. In a fluorescence experiment, the photon hits the sample and it is absorbed by the core electron. After that, the core electron ejects from its core-shell leading to the occurrence of a core hole that is in highly excited state. Then, the phenomenon of an X-ray fluorescence or Auger electron emission occurs to relax the core hole state. In term of higher-energy excitation, the primary relaxation process is X-ray fluorescence. The $\mu(E)$ is calculated using the equation (3.10):

$$\mu(E) = C\left(\frac{F}{I_0}\right) \quad (3.10)$$

where C is approximately constant, F is the intensity of the fluorescence X-rays, and I_0 is the intensity of incident X-ray beam.

In this work, the oxidation states of Co, Mn, Ni and Zn were obtained by measured the Co and Mn *K*-edge XANES spectra using the transmission mode while Ni and Zn *K*-edge XANES spectra were collected in the fluorescence mode. XANES measurement was conducted in the electron energy of 1.2 GeV and a beam current of 80-150 mA at the SUT-NANOTEC-SLRI XAS (BL5.2), the Synchrotron Light Research Institute (SLRI), Thailand.

The ATHENA software is employed for normalization and analysis the XANES data.

3.3.6 X-ray photoelectron spectroscopy (XPS)

X-ray photoelectron spectroscopy (XPS) is a surface analytical technique that is employed to identify the elemental composition and electronic state of the elements on the surface (2 to 5 nm) of the sample. The principle of XPS is as follows. The short X-ray is projected in the sample surface. The core electron of an atom on the surface absorbs the energy of the incident photon. Consequently, the interaction of the atoms on the surface of the samples and incident photons provides the emitted electrons with the kinetic energy of E_k (photoelectron). The kinetic energy (E_k) of the emitted electrons is described in equation (3.11).

$$E_k = h\nu - E_b - \phi \quad (3.11)$$

where $h\nu$ is the energy of the photon (Al $K\alpha$, 1.4866 keV), ϕ , is the work function of spectrometer (4-5 eV), and E_b is the binding energy. Since the value of ϕ can be eliminated, then the value of E_b can be given by:

$$E_b = h\nu - E_k \quad (3.12)$$

The emitted electrons with their kinetic energy (E_k) were investigated by the electron energy analyser. The result of measurement is an XPS spectra, which presents the intensity of detected signal on the binding energy as presented in Figure 3.8. The binding energy was devised to comparisons of chemical states of the elements of the sample. Due to the surface charging, the binding energy can be expressed by (3.13), which is resulted in the shifting of XPS spectrum to higher values of the binding energy.

$$E_b = h\nu - E_k - E_{ch} \quad (3.13)$$

E_{ch} can be obtained by calibrating the instrument to spectral feature. In this case, the

C 1s with C-C peak at 284.8 eV was used as a reference for calibration.

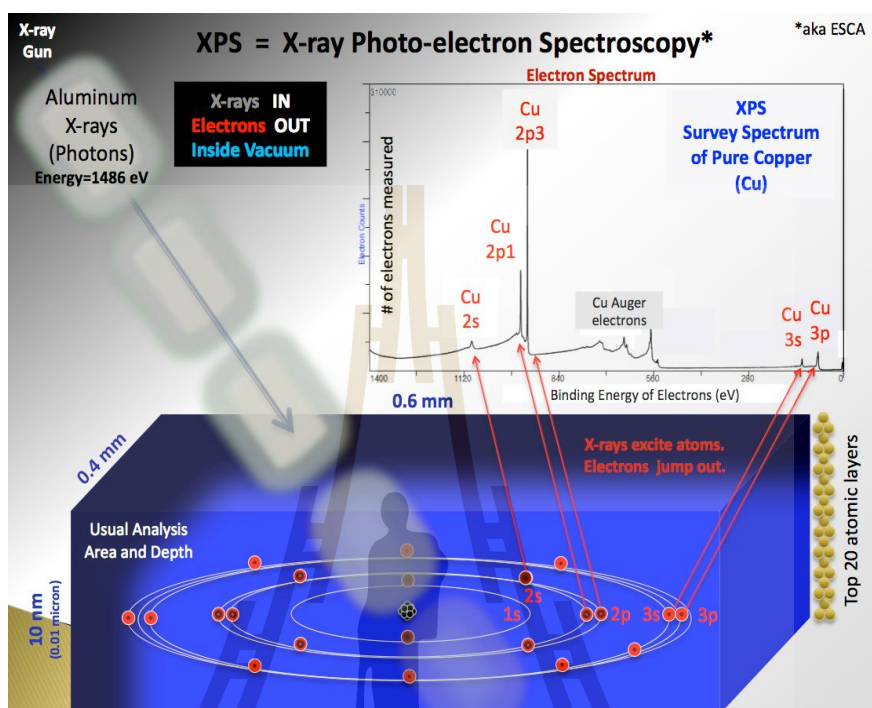


Figure 3.8 Rough schematic of XPS physics - "Photoelectric Effect. (Image from Wikimedia commons, public domain).

3.4 Electrochemical measurements

Capacitance (F/g) and energy/power density (Wh/kg and W/kg), tested at a specific current density (A/g), are generally used to evaluate the electrochemical performance of an electrode material or a supercapacitor device. Several typical electrochemical measurements have been well used to evaluation of supercapacitors such as cyclic voltammetry, galvanostatic charge/discharge, and electrochemical impedance spectroscopy. Therefore, we only briefly summarize these electrochemical measurements and clarify the evaluation process using these measurements.

3.4.1 Electrode preparation

The working electrodes were prepared by mixing 10 wt% acetylene black, 10 wt% polyvinylidene fluoride (PVDF), and 80 wt% MnCo_2O_4 -based nanostructures as the conducting agent, binder, and the active material, respectively. The mixture was dispersed in N-methyl-2-pyrrolidone (NMP) solvent, and the slurry were dropped on a nickel foam plate (surface, 1.2×2 cm). To remove the NMP solvent, the as formed electrodes were dried at 60°C for 12 h in the oven. After the drying process, these electrodes were compressed with a pressure of 10 MPa for 5 min. The formed electrodes have the mass of the active electrode material of about 1-2 mg.

3.4.2 Electrochemical cell setup

The electrochemical measurements were performed in a three-electrode system including a platinum counter electrode, an Ag/AgCl reference electrode, and a working electrode as shown in Figure 3.9. In this study, the measurement was performed using a Modulab (Solartron Analytical) electrochemical workstation as shown in Figure 3.10. The cyclic voltammetry, galvanostatic current charge/discharge, and EIS were used to evaluate the electrochemical properties of the MnCo_2O_4 -based nanostructures electrodes in 6M KOH electrolyte at room temperature.

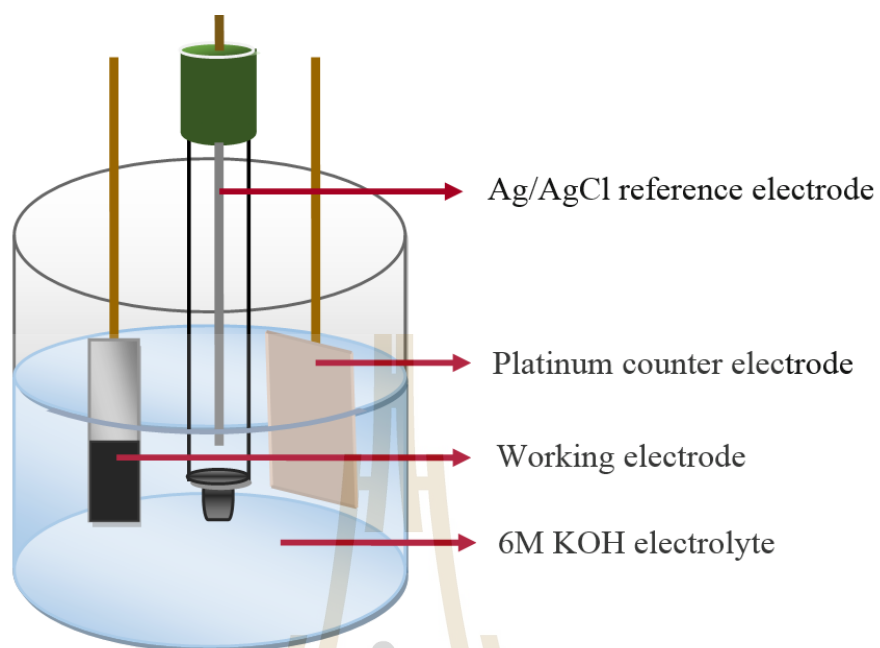


Figure 3.9 Three-electrode electrochemical cell setup consist of Reference electrode (Ag/AgCl), counter electrode (Platinum wire), and working electrode.



Figure 3.10 Electrochemical measurements set up contains with the three-electrode system, computer, and potentiostat/galvanostat.

3.4.3 Cyclic voltammetry

Cyclic voltammetry is widely used to characterize electrode materials. The potential applied to the electrode is scanned between two voltage limits with linear scan rate and the current is measured. The voltage scan reverses direction on reaching the voltage limit to complete cycle. The current at the electrode is plotted vs applied voltage which results in cyclic voltammogram (CV). The CV curve of an ideal EDLC electrode is rectangular. For the pseudocapacitors, a voltammogram deviates from rectangular CV shape, as shown in Figure 3.11. The peaks in the CV curve that occurs from the redox reaction arising at the surface of the electrodes demonstrate the pseudocapacitance. The capacitance of an ideal supercapacitor can be calculated using equation (3.15):

$$\frac{dq}{dt} = C \left(\frac{dV}{dt} \right) \quad (3.14)$$

$$C = \frac{I}{\nu} \quad (3.15)$$

Where dq/dt is the current (I) and dV/dt is the scan rate (ν).

In the experimental, the specific capacitance can be calculated according to equations (3.16) or (3.17):

$$C_{cv} = \frac{1}{m\nu\Delta V} \int I(V)dV \quad (3.16)$$

$$C_{cv} = \frac{1}{m\Delta V} \int I(t)dt \quad (3.17)$$

where term $\int I(V)dV$ and $\int I(t)dt$ refers to the area surround the CV curve and discharge curve, m is the mass of the active material, ν is the scan rate and ΔV is the voltage window.

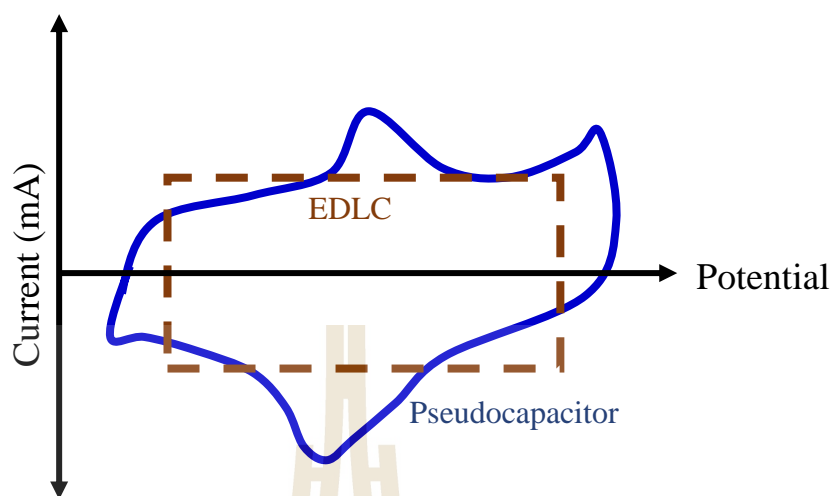


Figure 3.11 Cyclic Voltammograms showing rectangular features for an EDLC system, and oxidation peaks for a redox active pseudocapacitor.

In this study, the potential window in the range of -1.0 to 0.4 V was used for MnCo₂O₄-based nanoparticles and MnCo₂O₄-based nanofibers electrodes. The potential window has chosen a range that is not over -1.0 to 0.4 V to avoid occurring of oxygen and hydrogen evolution, which may cause damage to the electrode. The potential range in this work is consistent with several studies, which have reported both positive and negative (Che *et al.*, 2016; Che *et al.*, 2016; Nguyen *et al.*, 2015; Hui *et al.*, 2016; Li *et al.*, 2014; Tamboli *et al.*, 2017).

3.4.4 Galvanostatic charge/discharge testing (GCD)

A Galvanostatic charge/discharge (GDD) test is the most efficient measurement for the evaluation of capacitance and cycle life of the supercapacitor. In GCD the charging and discharging are performed by using controlling of the current and voltage vs. time, unlike CV where the controlled voltage is used for charging/discharging. The charge and discharge curves are linear and symmetrical at various current for an ideal capacitor. The capacitance is estimated from the discharge

curve using the basis of equation (3.18).

$$C = \frac{I\Delta t}{\Delta V} \quad (3.18)$$

The specific capacitance with mass m of electrode materials can be calculated by:

$$C_{cv} = \frac{I\Delta t}{m\Delta V} \quad (3.19)$$

where I is the discharge current (A), m is the mass of active materials (g), ΔV is the potential during the discharge process (V), and Δt is the discharge time (s).

In this work, the GCD curves were tested to investigate the capacitance performances of the electrodes at different current densities of 1, 2, 3, 5, 7, 10, 15, and 20 A/g.

3.4.5 Electrochemical impedance spectroscopy (EIS)

Electrochemical impedance spectroscopy (EIS) is a frequency domain technique to characterize batteries and supercapacitors. In this technique, the system is performed using a small voltage amplitude of 5 or 10 mV, applied in the frequency range 0.01 Hz to 100 kHz. The ratio of corresponding sinusoidal current and voltage signal provides the complex impedance with a particular frequency. In a capacitor, the current lags the voltage (less angle than voltage) by an angle (ϕ). The ϕ is 90° for ideal capacitor when the applied voltage is

$$V(\omega) = V_0 e^{j\omega t} \quad (3.20)$$

The current will be

$$I(\omega) = I_0 e^{j(\omega t + \phi)} \quad (3.21)$$

where the V_0 and I_0 are the maximum amplitude of voltage and current signal. The electrochemical impedance can be estimated by following equation:

$$Z = \frac{V(\omega)}{I(\omega)} = \frac{V_0}{I_0} e^{-j\phi} \quad (3.22)$$

The complex impedance is then defined as:

$$|Z| = Z' + (Z'') \quad (3.23)$$

where Z' and Z'' are the real and imaginary parts of the impedance, respectively. The modulus ($|Z|$) and the phase angle (ϕ) are defined as

$$|Z| = \sqrt{(Z')^2 + (Z'')^2} \quad (3.24)$$

$$\phi = \tan^{-1} \left(\frac{Z''}{Z'} \right) \quad (3.25)$$

The EIS measurement can provide the frequency (f), real and imaginary parts of the impedance. Then, the capacitance can be calculated using equation (3.26).

$$C = \frac{1}{2\pi f |Z|} \quad (3.26)$$

Two types of plots are derived from the EIS data for analysis of supercapacitor: the Nyquist plot and Bode plot. The Nyquist plot is the plot of the opposite imaginary part impedance ($-Z''$) versus the real part impedance (Z') while the logarithm of the impedance (Z) or phase angle (ϕ) versus the logarithm of the frequency is the Bode plot. In an ideal EDLC, the Nyquist plot will be a vertical line containing only the EDLC as presented in Figure 3.12(a). Figure 3.12(b), the Nyquist plot consists of the three regions. The intercept at the real part axis (Z') at high frequency presents an Ohmic resistance (R_s) that is the sum of the current collector and bulk electrolyte resistances. The charge transfer resistance (R_{ct}) corresponds to a diameter of the semi-circle at high-frequency region. The linear part over low frequencies refers to the Warburg resistance (R_w) which is employed to explain the diffusion of ions into the surface of the electrode.

In this work, the EIS was performed at the frequency range of 0.1 Hz-10 kHz with 10 mV (vs. SCE).

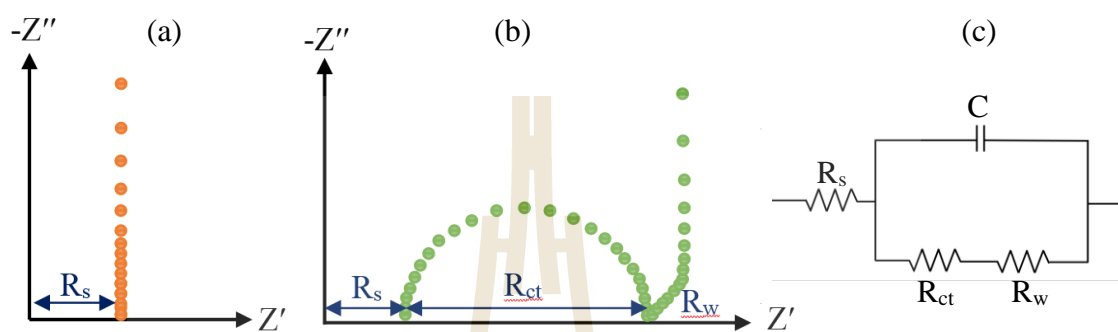


Figure 3.12 Nyquist plot of EDLC a) Ideal, b) Ordinary, and c) Basic equivalent circuit of EDLC.

CHAPTER IV

RESULTS AND DISCUSSION

This chapter presents the experimental results and discussion of prepared samples. It is divided into six major sections: MnCo_2O_4 nanoparticles, $\text{Mn}_{1-x}\text{Ni}_x\text{Co}_2\text{O}_4$ nanoparticles, $\text{Mn}_{1-x}\text{Zn}_x\text{Co}_2\text{O}_4$ nanoparticles, MnCo_2O_4 nanofibers, $\text{Mn}_{1-x}\text{Ni}_x\text{Co}_2\text{O}_4$ nanofibers, and $\text{Mn}_{1-x}\text{Zn}_x\text{Co}_2\text{O}_4$ nanofibers. Each section consists of characterization, and electrochemical study. For each section of study, the phase composition and crystal structure of the prepared samples can be examined by using X-ray diffraction (XRD) results. The transmission electron microscopy (TEM) and field-emission scanning electron microscopy (FE-SEM) were used to investigate the morphologies of the prepared samples. The valence state of the prepared samples was investigated by using the X-ray absorption near edge structure (XANES). The mean pore diameter, total pore volume, and specific surface area were evaluated by BET method, and BJH method was used to estimate pore area, pore volume, and pore size distribution. The electrochemical properties of prepared samples were carried out by cyclic voltammetry (CV), galvanostatic charge-discharge, and electrochemical impedance spectroscopy (EIS) method. The effect of calcination at various temperatures on the electrochemical properties were only studied for the MnCo_2O_4 nanoparticles and MnCo_2O_4 nanofibers. The effects of doping concentrations on electrochemical properties of different electrode materials (Ni-doped MnCo_2O_4 NPs, Zn-doped MnCo_2O_4 NPs, Ni-doped MnCo_2O_4 NFs, and Zn-doped MnCo_2O_4 NFs) is discussed.

4.1 MnCo₂O₄ nanoparticles

4.1.1 Structural and morphology characterization

4.1.1.1 X-ray diffraction (XRD) analysis of the MnCo₂O₄ nanoparticles

The XRD results of the precursor and calcined samples are shown in Figure 4.1. The XRD peaks of the samples calcined at 500, 600, 700, and 800 °C can be indexed to the MnCo₂O₄ phase with cubic structure (JCPDS No. 23-1237) which indicates that the material is crystallized MnCo₂O₄. However, the impurities phase of MnO₂ with cubic structure can also be seen in the sample calcined at 500 °C. It was observed that the increase of calcination temperatures resulted in with higher crystallinity of the samples, and consequently giving them different electrochemical performances.

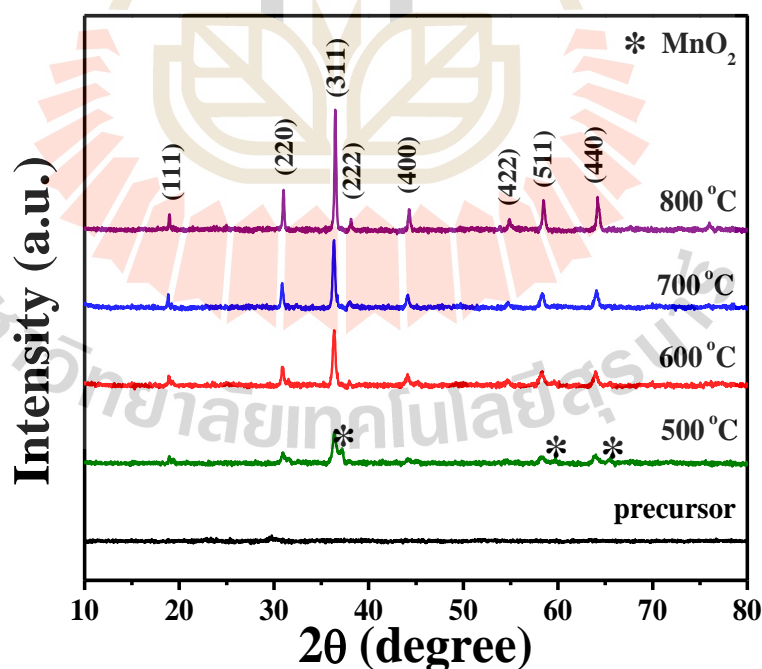


Figure 4.1 XRD patterns of precursor and MnCo₂O₄ nanoparticles calcined for 2 h in atmosphere at different calcined temperatures.

The crystallite sizes of MnCo_2O_4 were estimated by Scherrer's equation as the following equation (3.2). The calculations were carried out on the same set of (311) planes because they had the strongest line for all MnCo_2O_4 samples. The crystallite size of MnCo_2O_4 was found to range from 26 to 43 nm, as summarized in Table 4.1. The variations of the crystallite size at the calcination temperature were nonlinear. The crystallite size tends to increase at higher calcination temperature, except the samples calcined at 500 °C, which is higher than the crystallite size at 600 °C. This may be due to the present and overlapping of the diffraction peak of the MnO_2 secondary phase in the 500 °C sample. The d -spacing values of the MnCo_2O_4 phase for the crystalline planes (311) can be determined using Bragg's law as equation (3.1). The results show that the d -spacing values are 2.470, 2.471, 2.472, and 2.463 Å at calcination temperatures of 500, 600, 700, and 800 °C, respectively. It is evident that the d -spacing values are lower than the standard value ($d_s = 2.480$ Å) of a cubic MnCo_2O_4 (JCPDS No. 23-127). The crystal structure of MnCo_2O_4 cubic with lattice parameter " a " can be estimated from the XRD data as follows equation (3.3). The hkl are the Miller indices, which is obtained from the XRD peak (311) position. The results show that the lattice constants were 8.183, 8.186, 8.190, and 8.161 Å at calcination temperatures of 500, 600, 700, and 800 °C, respectively. Clearly, the values of the lattice parameters are very close to 8.269 Å of the hierarchical porous MnCo_2O_4 (Li *et al.*, 2015).

Table 4.1 Summary of crystallite sizes (D) from XRD, d -spacing (d), and lattice constant (a) of MnCo_2O_4 nanoparticles at different calcined temperatures.

MnCo ₂ O ₄ samples	Crystallite sizes	d -spacing	Lattice constant
	D (nm)	d (Å)	a (nm)
Precursor	-	-	-
500 °C	26.5	2.470	8.192
600 °C	22.3	2.471	8.196
700 °C	27.7	2.472	8.199
800 °C	43.4	2.463	8.169

4.1.1.2 The Morphology of the MnCo_2O_4 nanoparticles by FESEM and TEM

The morphology and structure of the MnCo_2O_4 nanoparticles were studied using FESEM and TEM, as shown in Figure 4.2 and Figure 4.3. The FESEM images reveal that the size of MnCo_2O_4 nanoparticles also tends to increase with an increase in the calcination temperature. The TEM bright field images show that the size distribution of the MnCo_2O_4 nanoparticles is about 40-65, 60-220, 60-230, and 65-240 nm for the samples calcined at 500, 600, 700, and 800 °C, respectively. The crystallite sizes acquired from the XRD pattern are smaller than the particle sizes obtained from the TEM results. The corresponding SAED patterns reveal the polycrystalline characteristic of the MnCo_2O_4 nanoparticles, which is according to the results of the X-ray diffraction analysis.

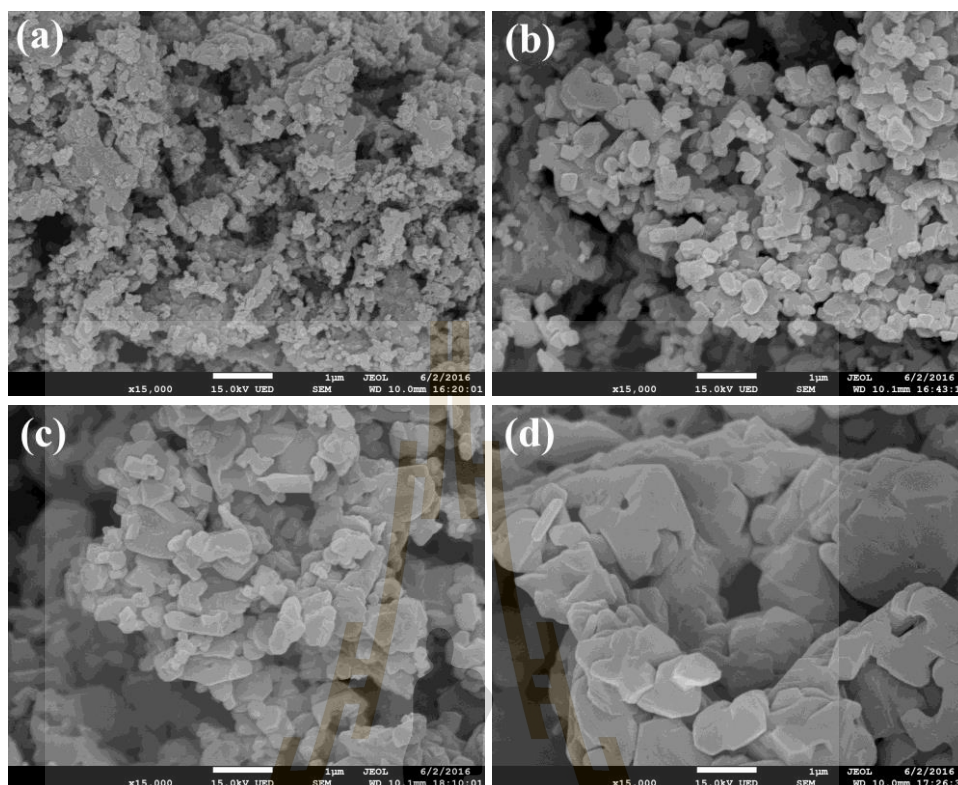


Figure 4.2 FESEM images of MnCo₂O₄ nanoparticles calcined for 2 h in atmosphere at (a) 500 °C, (b) 600 °C, (c) 700 °C, and (d) 800 °C.

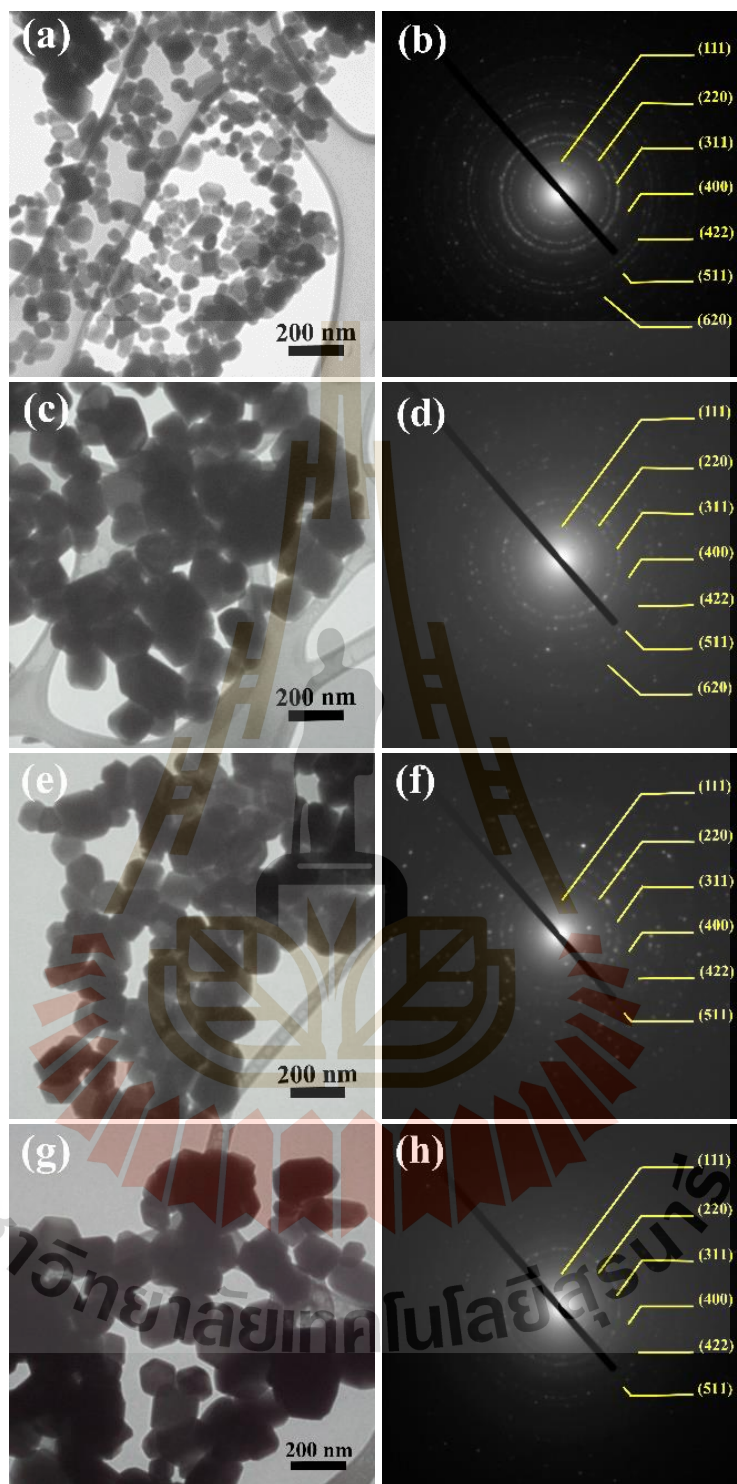


Figure 4.3 TEM images with corresponding SAED of MnCo₂O₄ nanoparticles calcined for 2 h in atmosphere at (a,b) 500 °C, (c,d) 600 °C, (e,f) 700 °C, and (g,h) 800 °C.

4.1.1.3 X-ray absorption spectroscopy study of the MnCo₂O₄ nanoparticles

The XANES measurements were conducted to examine the valence states of Co and Mn in the prepared nanoparticles. The normalized Co K-edge XANES spectra recorded from MnCo₂O₄ nanoparticles and reference samples of Co foil (Co⁰⁺), CoO (Co²⁺), and Co₃O₄ (Co^{2+,3+}) are presented in Figure 4.4. Basically, the shift of K-edge energy was investigated of the valence states of the elements in the compound. When the K-edge energy shifts to higher energies, the oxidation states of the elements increase. The edge position of Co K-edge XANES spectra for all the MnCo₂O₄ samples are between CoO (Co²⁺) and Co₃O₄ (Co^{2+,3+}) reference samples as shown in the Figure 4.4(a). The results imply that Co ions in all of the MnCo₂O₄ samples were mixed oxidation state of Co²⁺ and Co³⁺, as confirmed by the first derivative plot (Figure 4.4(b)) and the edge energy (Table 2). Similarly, Mn K-edge XANES spectra for all MnCo₂O₄ samples are positioned between Mn₂O₃ (Mn³⁺) and MnO₂ (Mn⁴⁺) reference samples, as shown in Figure 4.5(a). These findings indicate that the oxidation states of Mn ion exist both of Mn³⁺ and Mn⁴⁺ in all the MnCo₂O₄ samples. The first derivative plot and edge energy can be used to confirm the mix oxidation state of Mn ion, as shown in Figure 4.5(b) and Table 4.2, respectively.

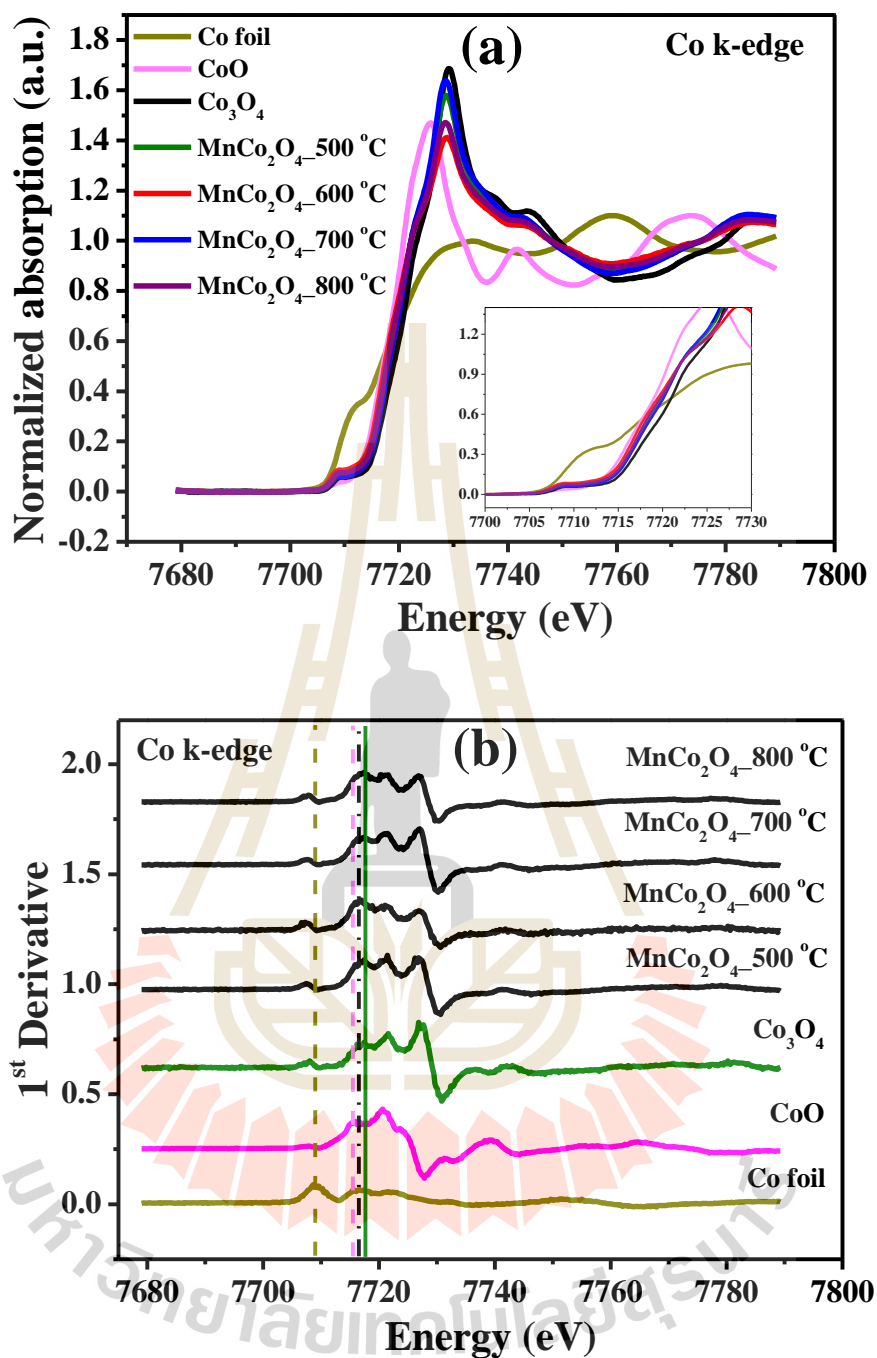


Figure 4.4 Normalized XANES spectra and their corresponding first-derivative at Co K-edge of MnCo_2O_4 nanoparticles.

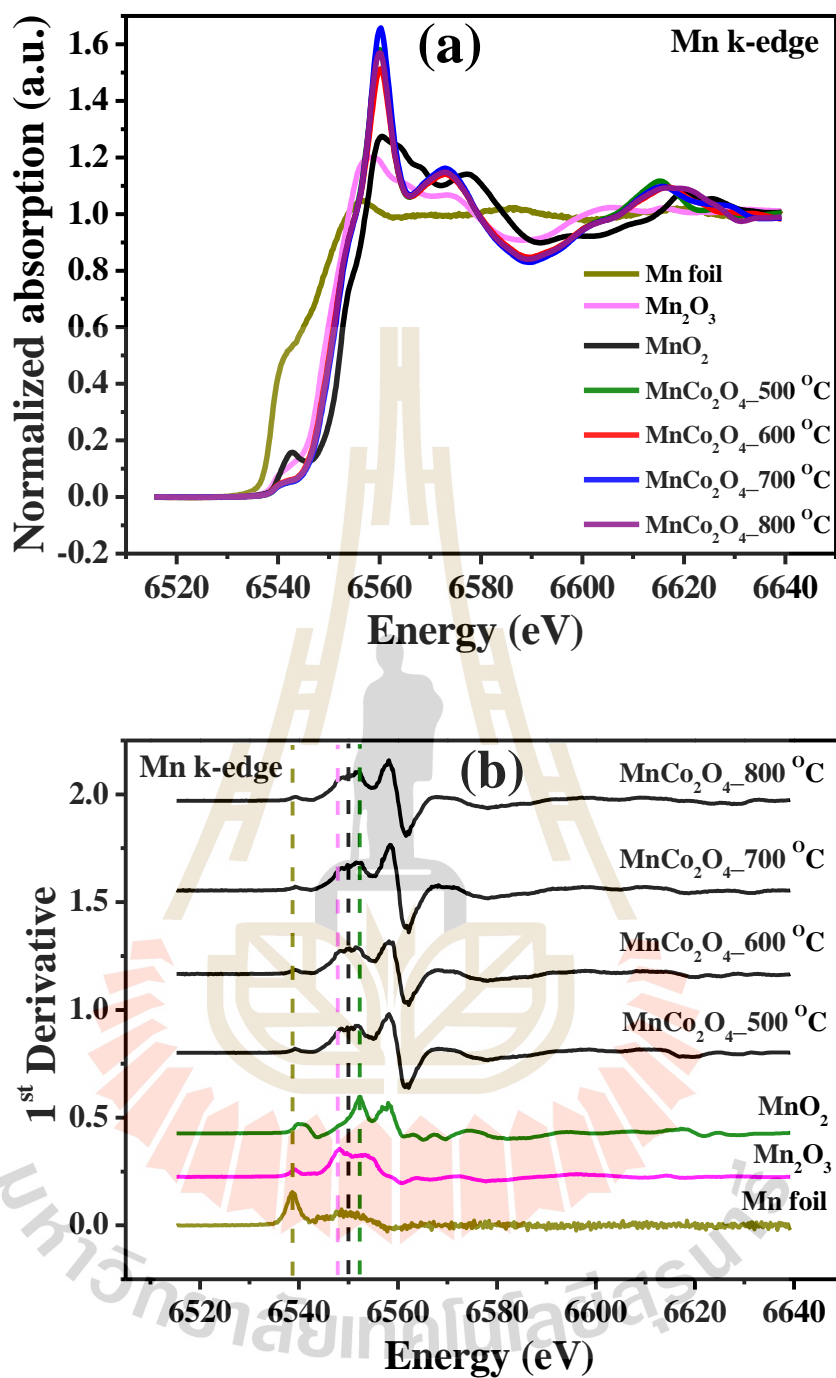


Figure 4.5 Normalized XANES spectra and their corresponding first-derivative at Mn K-edge of $MnCo_2O_4$ nanoparticles.

Table 4.2 Edge energy and oxidation state of the standard samples and MnCo₂O₄ nanoparticles.

Samples	Edge element	Absorption Edge (eV)	Oxidation state
CoO	Co	7716.30	2
Co ₃ O ₄	Co	7721.32	+2, +3
Mn ₂ O ₃	Mn	6548.82	3
MnO ₂	Mn	6552.22	4
MnCo ₂ O ₄ _500 °C	Co	7716.90	+2, +3
	Mn	6550.16	+3, +4
MnCo ₂ O ₄ _600 °C	Co	7716.95	+2, +3
	Mn	6550.20	+3, +4
MnCo ₂ O ₄ _700 °C	Co	7717.10	+2, +3
	Mn	6550.26	+3, +4
MnCo ₂ O ₄ _800 °C	Co	7717.20	+2, +3
	Mn	6550.34	+3, +4

4.1.1.4 X-ray photoelectron spectroscopy (XPS) study of the MnCo₂O₄ nanoparticles

The composition of the elemental and the oxidation state of MnCo₂O₄ nanoparticles were examined by XPS measurement. The binding energies associated with Co 2p, Mn 2p, and O 1s were presented in Figure 4.6. For a high-resolution Co 2p spectrum, two main peaks at ~779.5 eV and ~795.0 eV were observed in all the MnCo₂O₄ samples that conform to the core level of Co 2p_{3/2} and Co 2p_{1/2} with the separation of ~15.5 eV (Figure 4.6). In general, the energy gap between the Co 2p main

peaks and satellite peaks was used to identify the oxidation state of Co ion. The energy gap in the range of ~3.5 to 6.5 and ~9 to 10 eV is a feature of the Co^{2+} and Co^{3+} cations, respectively, as reported in the literature (Che *et al.*, 2016; Li *et al.*, 2015; Wang *et al.*, 2015; Qiu *et al.*, 2015; Naveen and Selladurai, 2015). In this study, the Co 2p spectrum of all the MnCo_2O_4 samples was best fitted with two spin-orbit doublets and four shake-up satellite peaks (denoted as sat.) by using a Gaussian fitting method. These can be employed to confirm the coexistence of the Co^{2+} and Co^{3+} cations in the MnCo_2O_4 products obtained. For the Mn 2p XPS spectrum, the electronic configuration of Mn atoms in $2p_{3/2}$ and $2p_{1/2}$ states were observed at the binding energy of ~642.0 and ~653.7 eV, respectively with spin-orbit splitting of ~11.7 eV (Figure 4.7). After fitting, the Mn 2p spectrum could be fitted into four sub-peaks, suggesting that all the MnCo_2O_4 samples present consist of two Mn ions. The two main peaks of binding energy at ~642.0 (Mn $2p_{3/2}$) and ~653.5 eV (Mn $2p_{1/2}$) is referred to Mn^{3+} and the other two peaks were observed at binding energy of ~644.6 (Mn $2p_{3/2}$) and ~655.8 eV (Mn $2p_{1/2}$) indicate that the Mn^{4+} has existed in all the MnCo_2O_4 samples (Naveen and Selladurai, 2015; Li *et al.*, 2016; Zhu and Gao, 2009; Papavasiliou *et al.*, 2007). As shown in Figure 4.8, the O1s spectrum can be fitted into three peaks. The large peak at a binding energy of ~529.7 eV refers to the lattice oxygen in the spinel structure (denoted as I), and the other two peaks (II and III) correspond to the oxygen atom of OH^- ions, and the oxygen atom of the adsorbed water molecules, respectively (Che *et al.*, 2016; Che *et al.*, 2016; Tholkappiyan *et al.*, 2015; Wang *et al.*, 2015; Qiu *et al.*, 2015). Consequently, the XPS results confirm that all the MnCo_2O_4 samples have mixing of Co^{2+} and Co^{3+} and Mn^{3+} and Mn^{4+} in all samples corresponding to the XANES analysis. The coexistence of the Co^{2+} and Co^{3+} and Mn^{3+} and Mn^{4+} may provide the electrochemical activity that led to

improvement in the electrochemical properties.

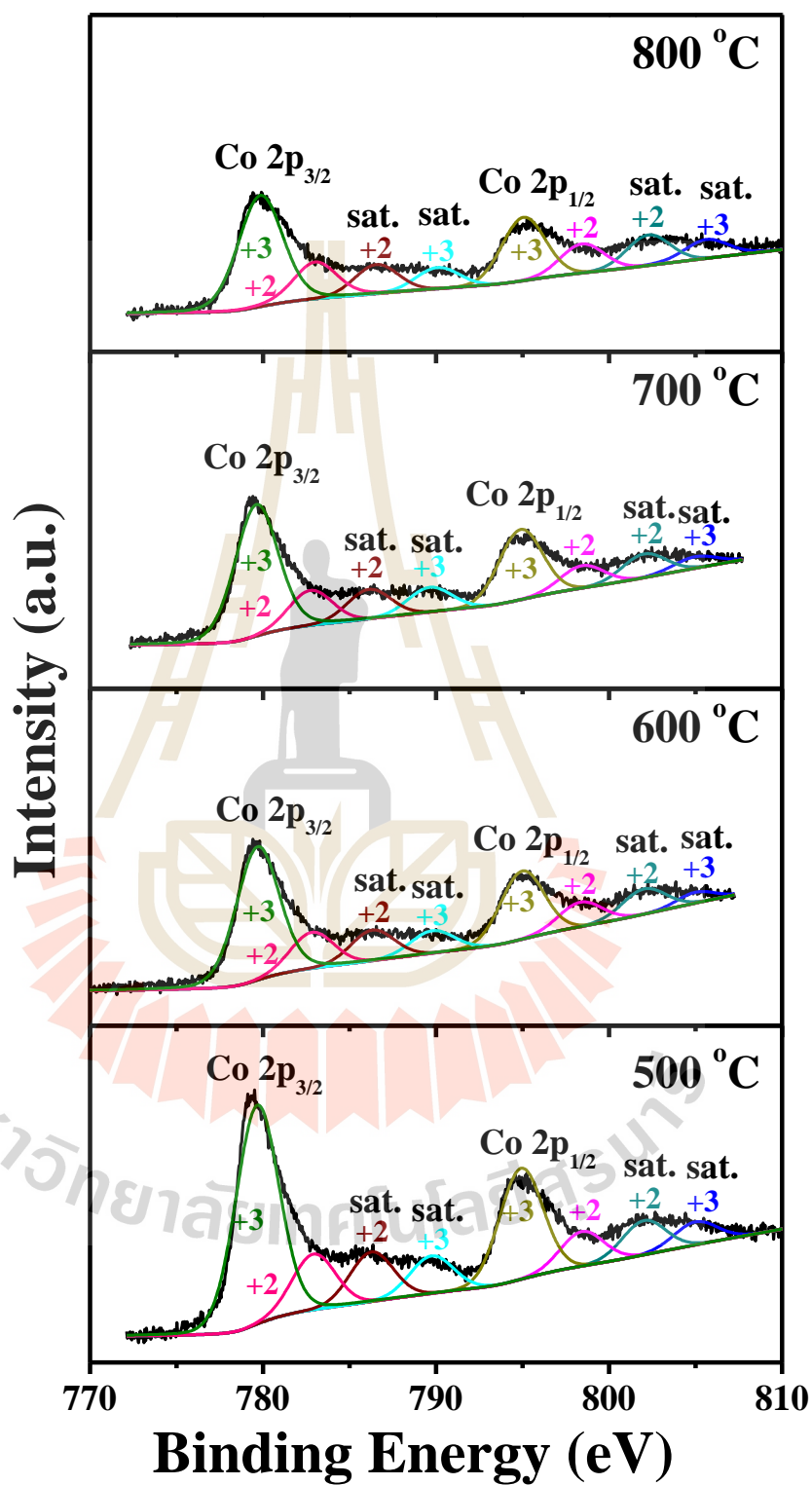


Figure 4.6 XPS spectra at Co 2p of the MnCo₂O₄ nanoparticles.

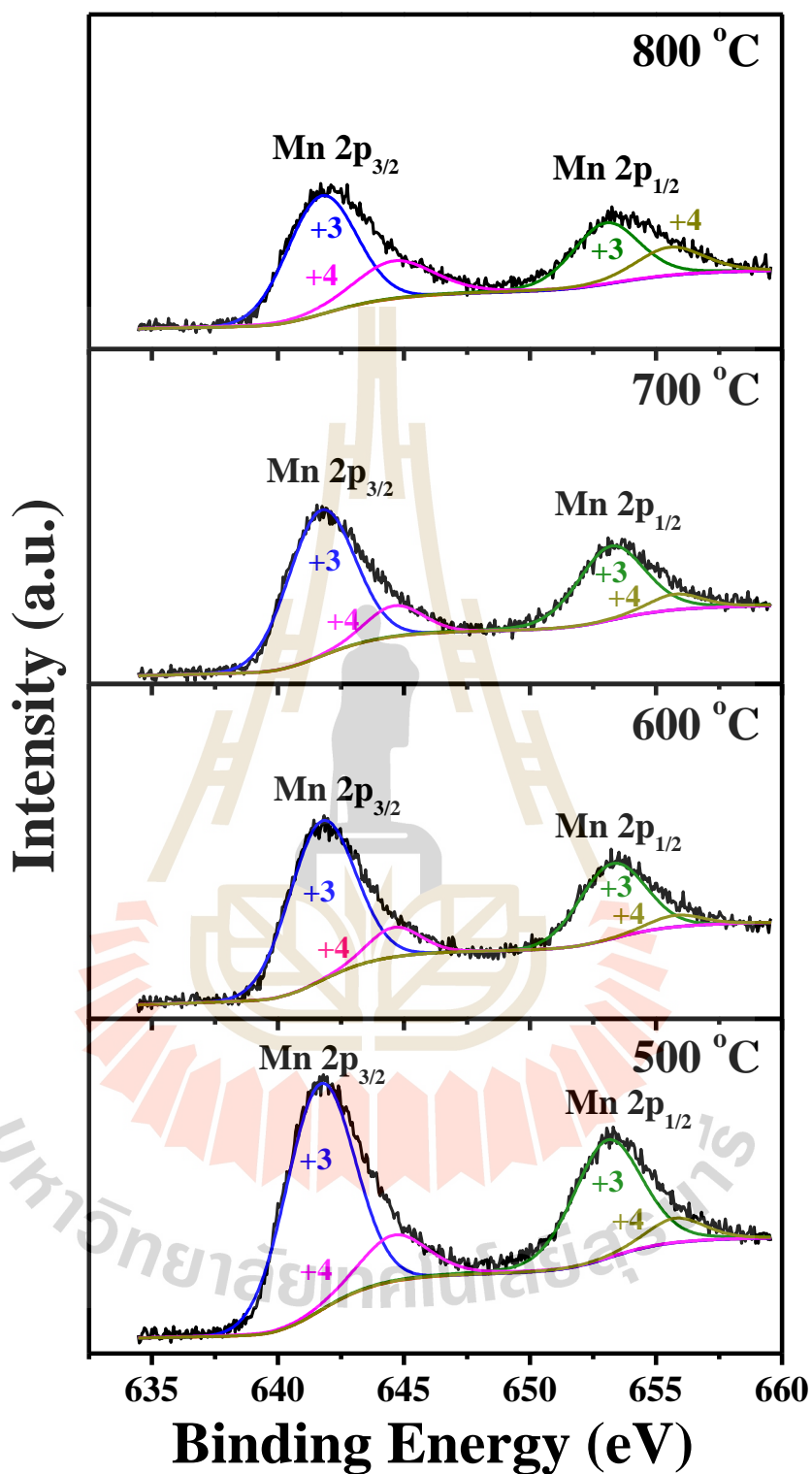


Figure 4.7 XPS spectra at Mn 2p of the MnCo₂O₄ nanoparticles.

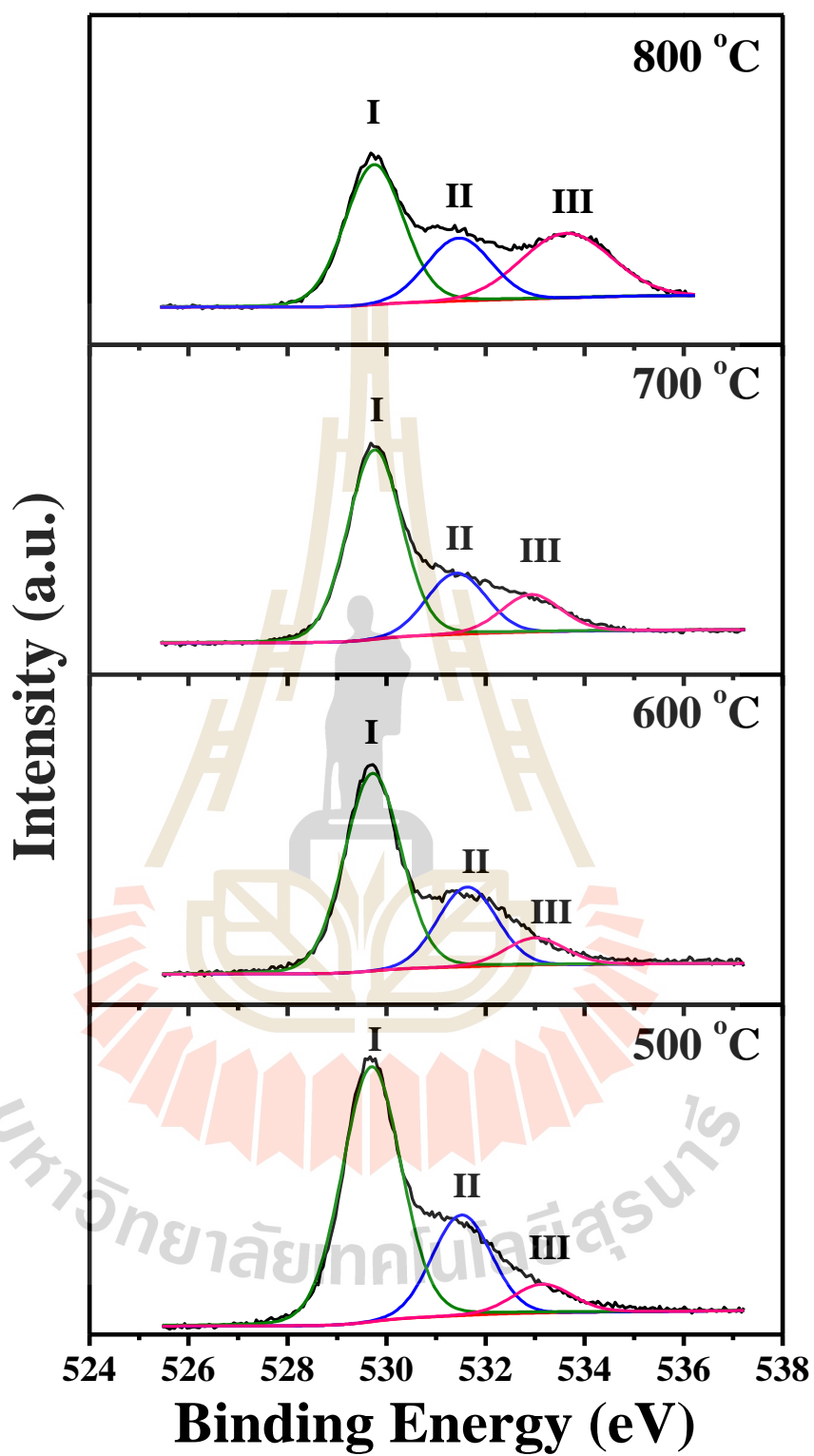


Figure 4.8 XPS spectra at O 1s of the MnCo₂O₄ nanoparticles.

4.1.1.5 Characterization of surface area and pore size distribution of the MnCo₂O₄ nanoparticles by BET method and BJH method

To study the specific surface areas and pore character in MnCo₂O₄ nanoparticles, the adsorption/desorption of N₂ was measured at the temperature of 77 K. Figure 4.9(a-d) shows the adsorption/desorption isotherms of N₂ and pore size distributions (inset) of all the calcined samples. The results reveal that the N₂ adsorption/desorption isotherms of all the MnCo₂O₄ samples display a hysteresis loop appearing in the range of 0 to 1, which presents the typical feature of a mesoporous structure. The BET specific surface areas were determined to be 25.56, 71.92, 33.88, and 27.26 m²/g for the samples calcined at 500, 600, 700, and 800 °C, respectively. The mean pore diameters of the MnCo₂O₄ nanoparticles are 5.54, 4.39, 7.98 and 8.08 nm for the samples calcined at 500, 600, 700, and 800 °C, respectively. The pore size distributions of all the calcined samples (Figure 4.9(a-d), inset) reveal that all the calcined samples exhibit a pore size distribution in the range of about 2.42 to 10 nm. According to IUPAC notation, porous materials are divided into three types by their size, namely, microporous materials (average pore diameters: $d < 2$), mesoporous materials (average pore diameters: $2 < d < 50$) and macroporous materials (average pore diameters: $d > 50$). Also, that the obtained MnCo₂O₄ products are mesoporous materials. Moreover, the total volume of the pores was calculated as 0.035, 0.079, 0.067, and 0.051 cm³/g for the samples calcined at 500, 600, 700, and 800 °C, respectively. The BET specific surface areas, mean pore diameters, and pore volumes are summarized in Table 4.3. Generally, a high specific surface area can bring about a high specific capacitance because large active sites can provide multiple redox reactions, demonstrating good electrochemical capacitance (Naveen and Selladurai,

2015). Therefore, the MnCo_2O_4 nanoparticles calcined at different calcination temperature with the differences in BET results of specific surface area, mean pore diameter, and pore volume exhibited different electrochemical performances, which will be discussed in the electrochemical properties section.

Table 4.3 Structural parameters of spinel MnCo_2O_4 .

Samples	BET specific surface area (m^2/g)	Total pore volume (cm^3/g)	Mean pore diameter (nm)
500 °C	25.56	0.035	5.54
600 °C	71.92	0.079	4.39
700 °C	33.88	0.067	7.98
800 °C	27.26	0.051	8.08

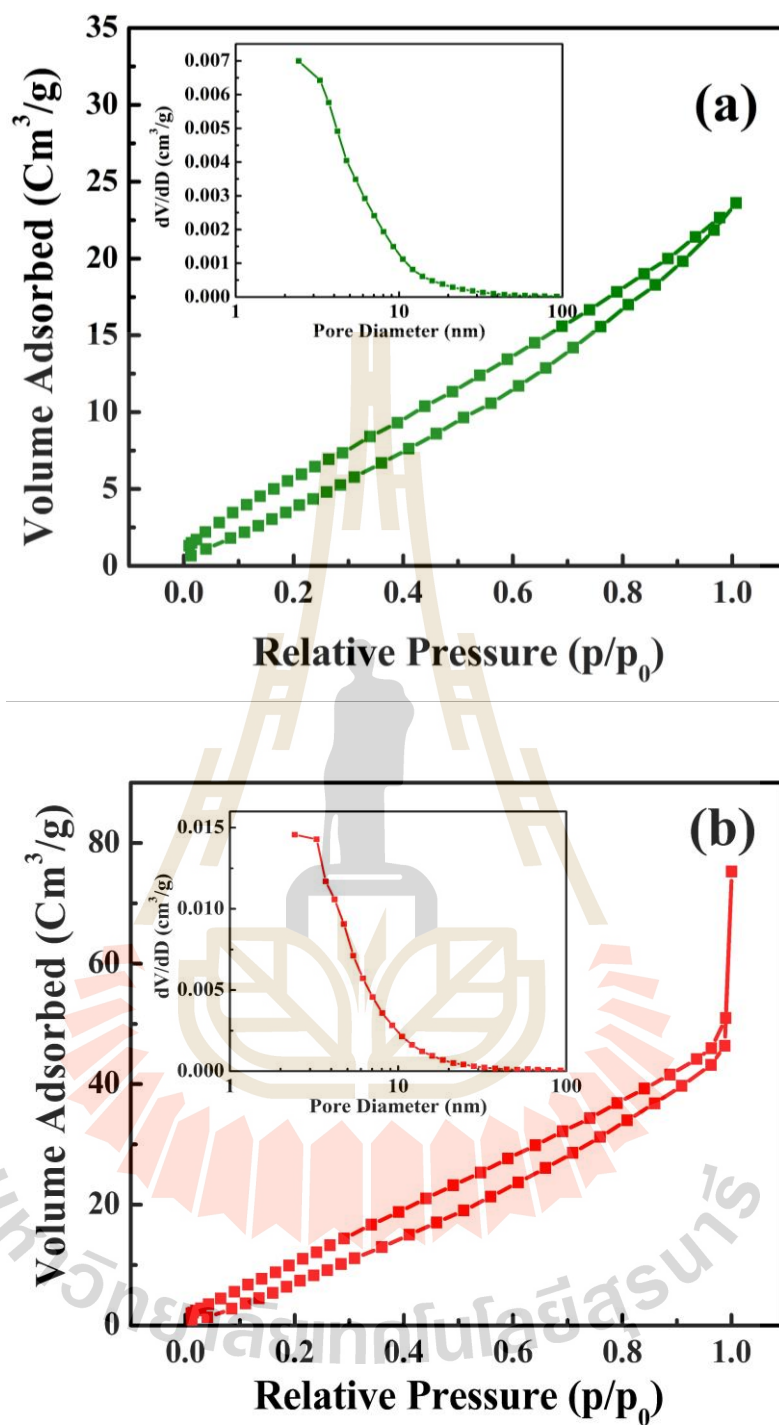


Figure 4.9 Nitrogen adsorption/desorption isotherms and pore size distribution (inset) of MnCo₂O₄ nanoparticles calcined at (a) 500 °C, (b) 600 °C, (c) 700 °C, and (d) 800 °C.

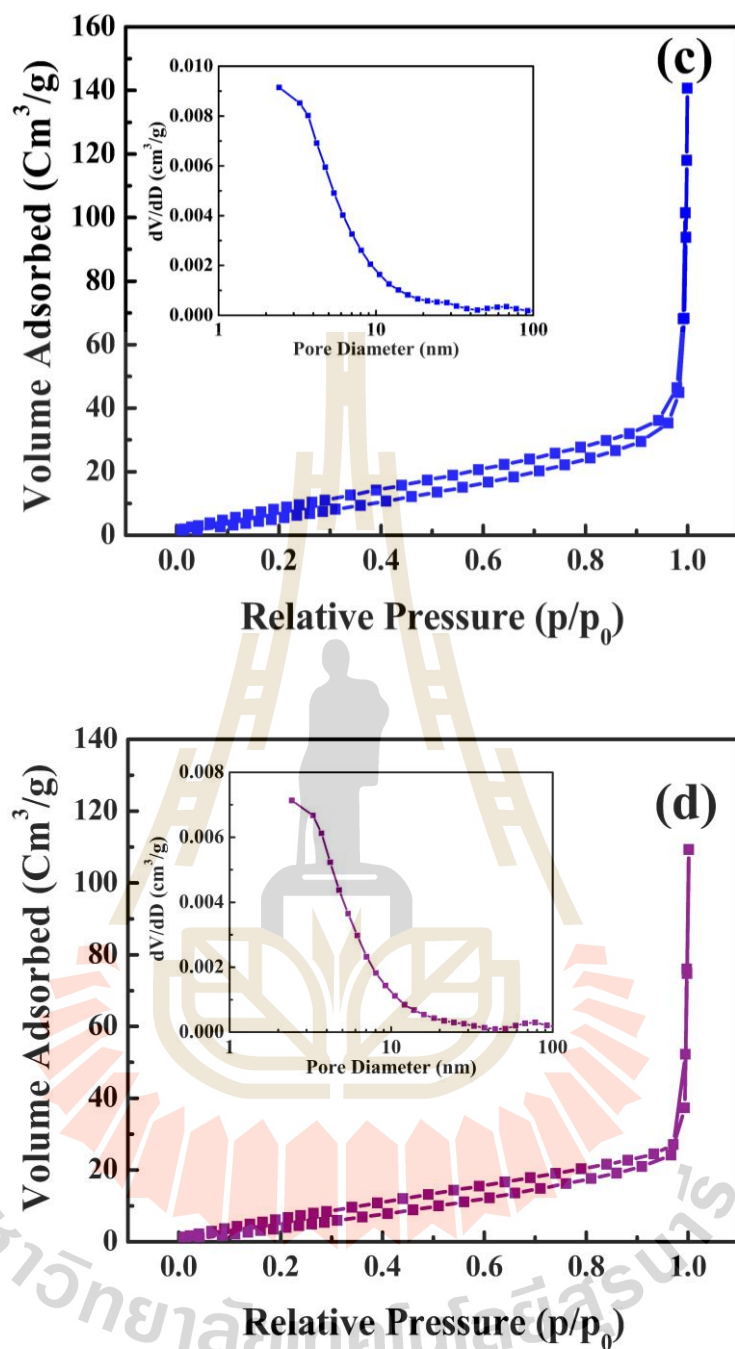
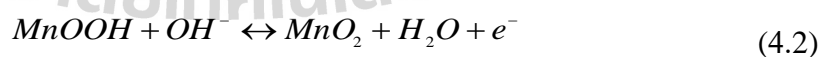


Figure 4.9 (Continued) Nitrogen adsorption/desorption isotherms and pore size distribution (inset) of MnCo₂O₄ nanoparticles calcined at (a) 500 °C, (b) 600 °C, (c) 700 °C, and (d) 800 °C.

4.1.2 Electrochemical properties

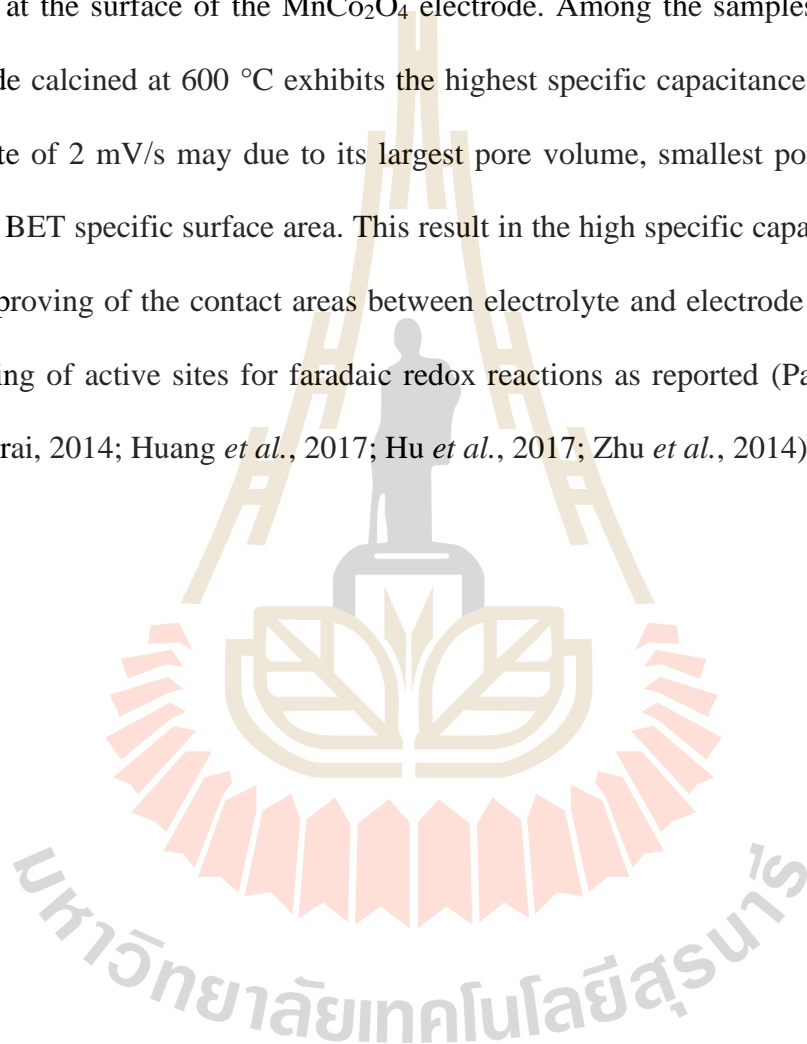
4.1.2.1 Cyclic voltammetry measurement

The studies of electrochemical properties of the MnCo_2O_4 nanoparticles, cyclic voltammetry and galvanostatic charge/discharge techniques were also investigated. The CV curves of the MnCo_2O_4 electrodes, which were examined within potential window from -1.0 and 0.4 V with various scan rates in the range 2 to 60 mV/s in 6M KOH electrolyte at room temperature are shown in Figure 4.1(a-d). The results indicate that the redox peaks at the potentials of about -0.2 and -0.5 were found in the CV curves for all the MnCo_2O_4 samples, which present the typical feature of pseudocapacitive electrode material. In the charge/discharge process, the faradaic charge transfer is accompanied by a very fast of reversible faradaic redox and intercalation of protons at the surface of the MnCo_2O_4 electrodes. The Co and Mn oxidation states were able to transfer from $\text{Co}^{2+}/\text{Co}^{3+}$ and $\text{Mn}^{3+}/\text{Mn}^{4+}$ as previously reported (Krishnan *et al.*, 2016; Padmanathan and Selladurai, 2014; Kong *et al.*, 2014; Sahoo *et al.*, 2015; Hao *et al.*, 2015). The equation (4.1) and equation (4.2) were used to explain the reversible redox reactions (Bai *et al.*, 2016; Li *et al.*, 2014; Hao *et al.*, 2015);



The shifting position of the anodic and cathodic peaks with an increasing scan rate were found in all the MnCo_2O_4 electrodes, suggesting good electrochemical reversibility and high-rate performance (Peng *et al.*, 2015). The formula equation (3.17) is employed for evaluating the specific capacitance of the MnCo_2O_4 electrodes (Padmanathan and Selladurai, 2014). The calculated specific capacitance as a function

of scan rate of all electrodes was plotted in Figure 4.11. The specific capacitance of all the MnCo_2O_4 samples was found to decrease with increase of the scan rate from 5 to 60 mV/s. This phenomenon is also present in pseudocapacitive electrode material because of the time was constrained at high scan rate leading to the ion diffusion is limited at the surface of the MnCo_2O_4 electrode. Among the samples, the MnCo_2O_4 electrode calcined at 600 °C exhibits the highest specific capacitance of 282 F/g at a scan rate of 2 mV/s may due to its largest pore volume, smallest pore diameter and highest BET specific surface area. This result in the high specific capacitance because this improving of the contact areas between electrolyte and electrode bring about the increasing of active sites for faradaic redox reactions as reported (Padmanathan and Selladurai, 2014; Huang *et al.*, 2017; Hu *et al.*, 2017; Zhu *et al.*, 2014).



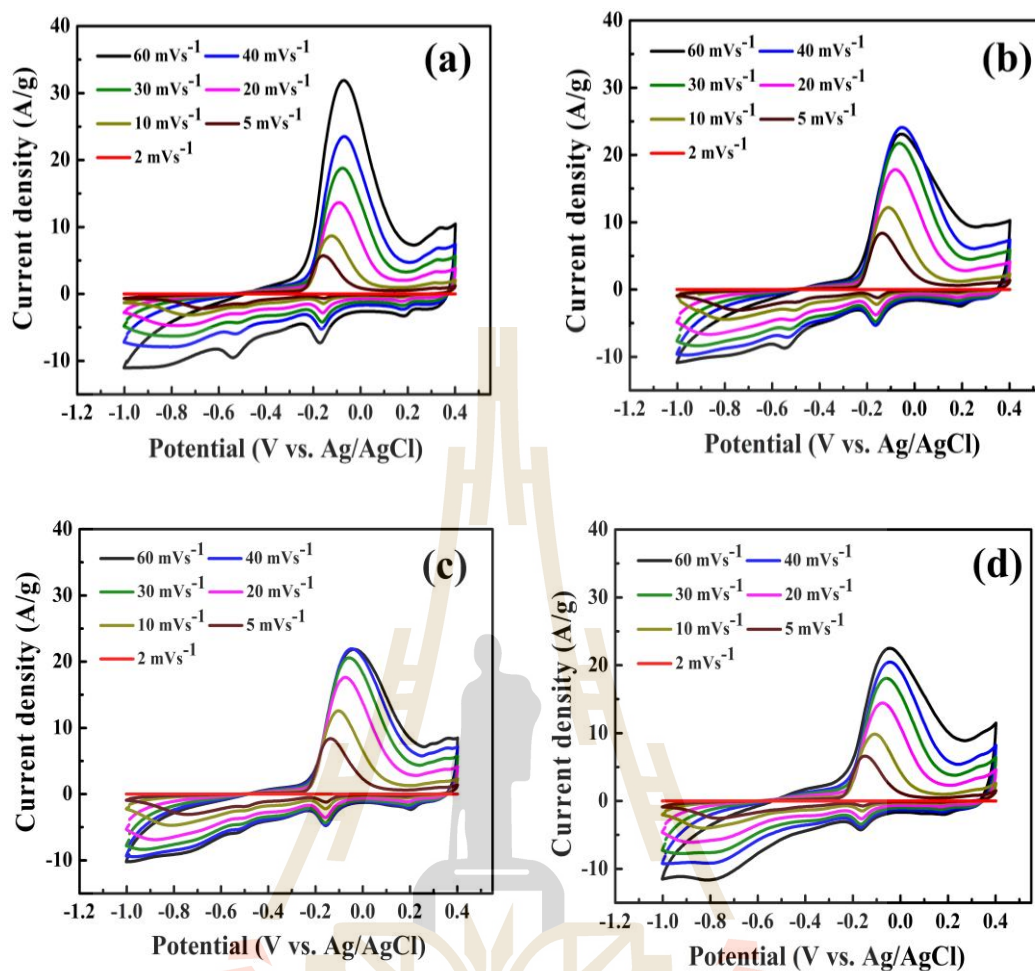


Figure 4.10 CV curves at various scan rates of MnCo₂O₄ nanoparticles calcined at (a) 500 °C, (b) 600 °C, (c) 700 °C, and (d) 800 °C.

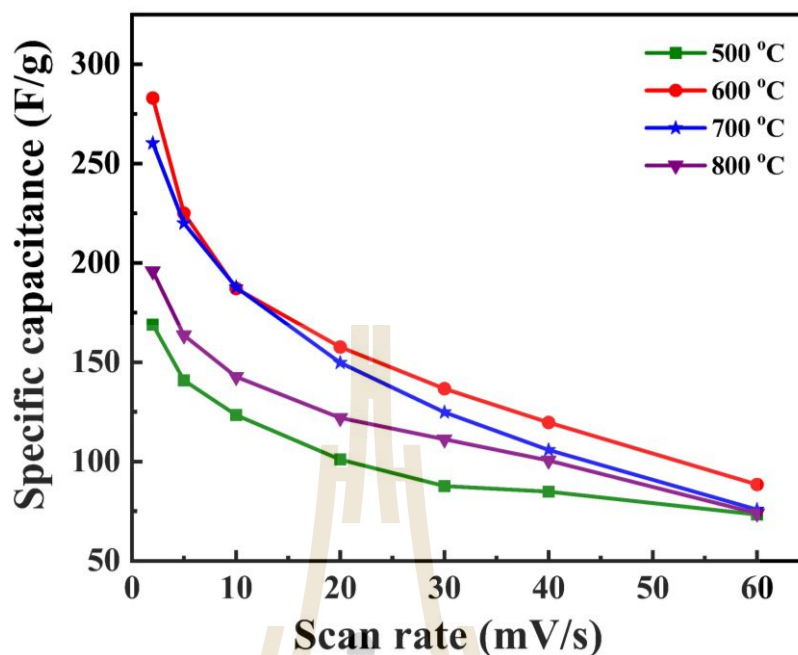


Figure 4.11 Comparison of the specific capacitance at various calcination temperature of MnCo_2O_4 nanoparticles as a function of scan rate.

4.1.2.2 Galvanostatic charge-discharge measurements

The galvanostatic charge/discharge curves of all the MnCo_2O_4 electrodes at a function of the current densities with range from 1 to 20 A/g are shown in Figure 4.12(a-d). The nonlinear galvanostatic charge/discharge curves correspond to the redox peaks which were observed from the CV curves can be interpreted as a pseudocapacitance behavior of the MnCo_2O_4 electrodes. In the galvanostatic charge/discharge testing, the discharge curve and the equation (3.19) were used to estimate the specific capacitance values of the MnCo_2O_4 electrodes (Padmanathan and Selladurai, 2014). Using the above equation, the specific capacitance of all the samples decreases with increases of the current density as shown in Figure 4.13. This may be owing to the increase of the polarization and the internal resistance of the MnCo_2O_4 electrodes. For low current densities of 1 A/g, the samples calcined at 500, 600, 700,

and 800 °C demonstrate the specific capacitance of 121, 208, 154 and 150 F/g, respectively. This is consistent with the specific capacitance found from the CV measurements as well. The samples calcined at 500 °C with lowest specific surface area and pore volume exhibits the lowest the specific capacitance. As for the samples without a secondary phase which were calcined at 600, 700, and 800 °C, the specific capacitance decreases with increases in the calcination temperature. This may due to the increasing of crystal size, which leads to the lower BET specific surface area and smaller of active sites for the faradaic redox reactions. Interestingly, the 600 °C electrode with highest surface area exhibits improved electrochemical properties such as the highest the specific capacitance and capacity retention, which is the result of the improving of the structure of the electrode material.

Additionally, the cycling stability of the MnCo_2O_4 electrodes was investigated by measuring the continuous charge-discharge for 1000 cycles at the current density of 2 A/g with the potential window in the range of -1.0 to 0.4 V in 6M KOH solution. Figure 4.14 displays the Capacity retention (%) of all the MnCo_2O_4 electrodes at different calcination temperatures. The increase of the capacitance retention was found in the range of 10 to 30 cycles. This indicates that the MnCo_2O_4 electrodes have a complete activation (Liu *et al.*, 2013). After 1000 cycles of charge-discharge, the MnCo_2O_4 electrodes calcined at 500, 600, 700, and 800 °C exhibit a capacitance retention of 55%, 73%, 66%, and 65%, respectively. These results suggest that the MnCo_2O_4 electrode was calcined at 600 °C which reveals a higher specific capacitance and a better capability rate. However, the capacitance value decreases with increasing in the cycling number owing to the electrochemical stability of the MnCo_2O_4 electrode material.

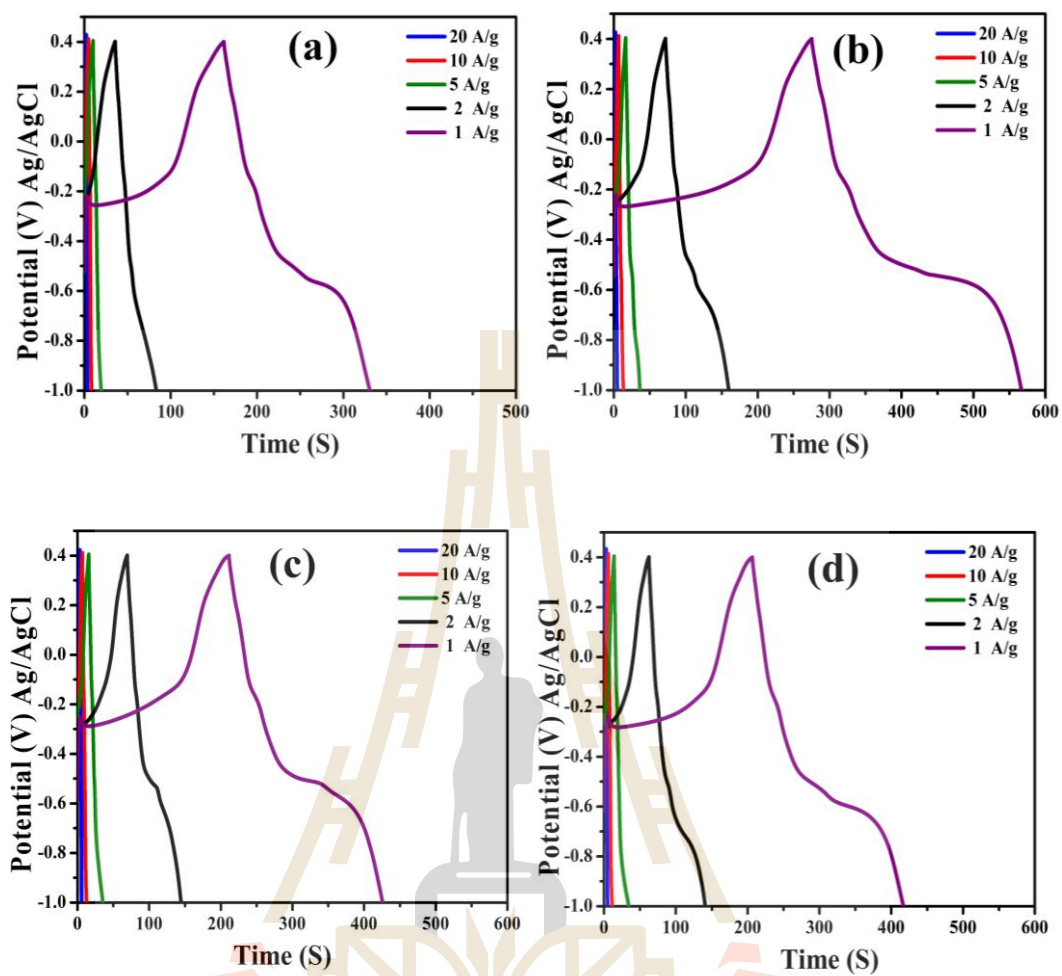


Figure 4.12 Galvanostatic charge-discharge curves at various current densities of MnCo_2O_4 nanoparticles calcined at (a) 500 °C, (b) 600 °C, (c) 700 °C, and (d) 800 °C.

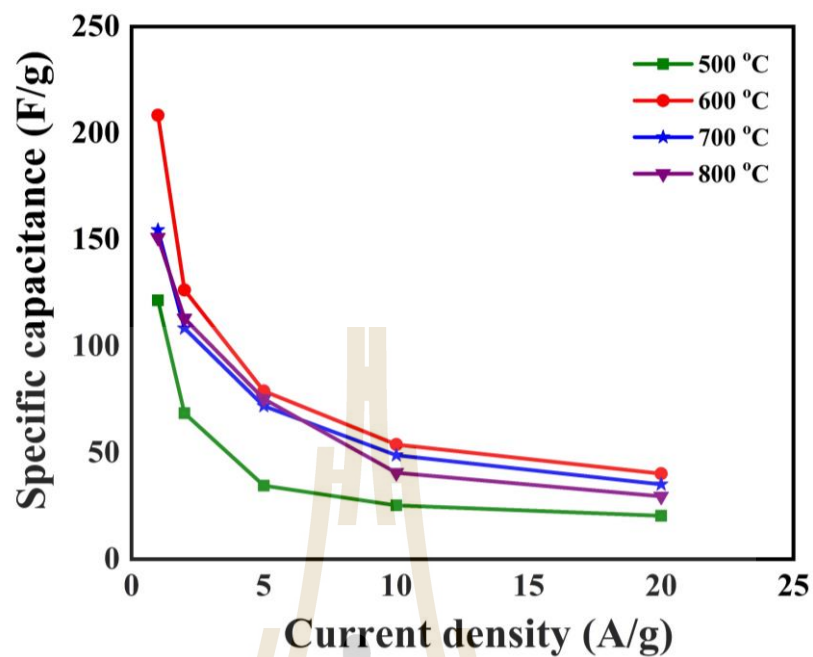


Figure 4.13 Comparison of the specific capacitance at various calcination temperature of MnCo_2O_4 nanoparticles as a current density.

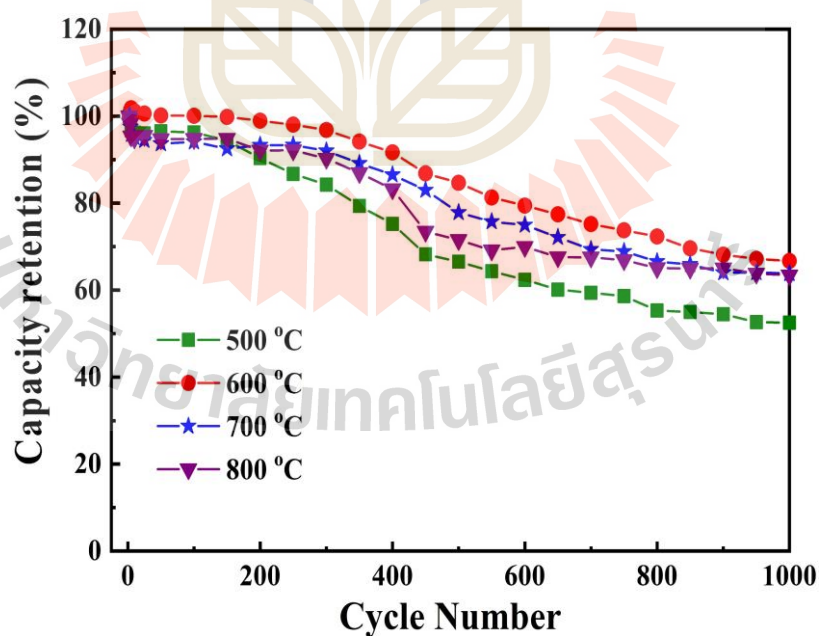


Figure 4.14 Capacity retention (%) at various calcination temperature of MnCo_2O_4 electrodes after 1000 cycles at a current density of 2 A/g.

4.1.2.3 Electrochemical impedance spectroscopy (EIS)

In order to understand about mechanism of energy storage of MnCo_2O_4 , electrochemical impedance spectroscopy (EIS) experiments were carried out from the frequency range of 0.1 Hz - 100 kHz with 10 mV (vs. SCE). An incomplete semicircle was observed in the high-frequency region of EIS curves of all MnCo_2O_4 electrodes which is characteristics of the resistance at the oxide–electrolyte interface as shown in Figure 4.15. The equivalent series resistance (R_{ESR}) or solution resistance (R_s) is obtained from the intercept on the real axis at high frequency. The values of R_s are 1.07, 0.38, 0.42, and 0.38 Ω for the samples calcined at 500, 600, 700, and 800 $^\circ\text{C}$, respectively. Besides, the diameter of the semicircle corresponds to the charge transfer resistance (R_{ct}). The R_{ct} values for the samples calcined at 500, 600, 700, and 800 $^\circ\text{C}$ were 0.23, 0.11, 0.09, and 0.10 Ω , respectively. Clearly, the lowest and highest value of the R_s and R_{ct} can provide highest and lowest specific capacitance value for 600 $^\circ\text{C}$ and 500 $^\circ\text{C}$, respectively. However, the R_s and R_{ct} of 700 $^\circ\text{C}$ and 800 $^\circ\text{C}$ electrode is slightly different. The low frequency area, the slope of the straight line for samples calcined at 600 $^\circ\text{C}$ is significantly higher than that of the other electrodes, indicating a lower diffusion resistance (Warburg impedance) of the electrolyte ions in host material. A comparison of the electrochemical properties for the supercapacitors of the MnCo_2O_4 nanostructures prepared using the different methods is presented in Table 4.4. The MnCo_2O_4 electrode material in this work exhibits a lower specific capacitance value than that of MnCo_2O_4 nanowire (Li *et al.*, 2014), MnCo_2O_4 nanoparticles (Tholkappiyan *et al.*, 2015), Flower-like MnCo_2O_4 (Che *et al.*, 2016), and Mesoporous MnCo_2O_4 (Padmanathan and Selladurai, 2014). However, the MnCo_2O_4 nanoparticles prepared by a simple polymer solution method with a calcination temperature of

600 °C have high specific capacitance value, close to those of MnCo₂O₄ nanostructures in other research (Kong *et al.*, 2014; Li *et al.*, 2014; Sahoo *et al.*, 2015). Thus, the MnCo₂O₄ nanoparticle electrodes in this work have a potential as the next-generation supercapacitor for energy storage applications.

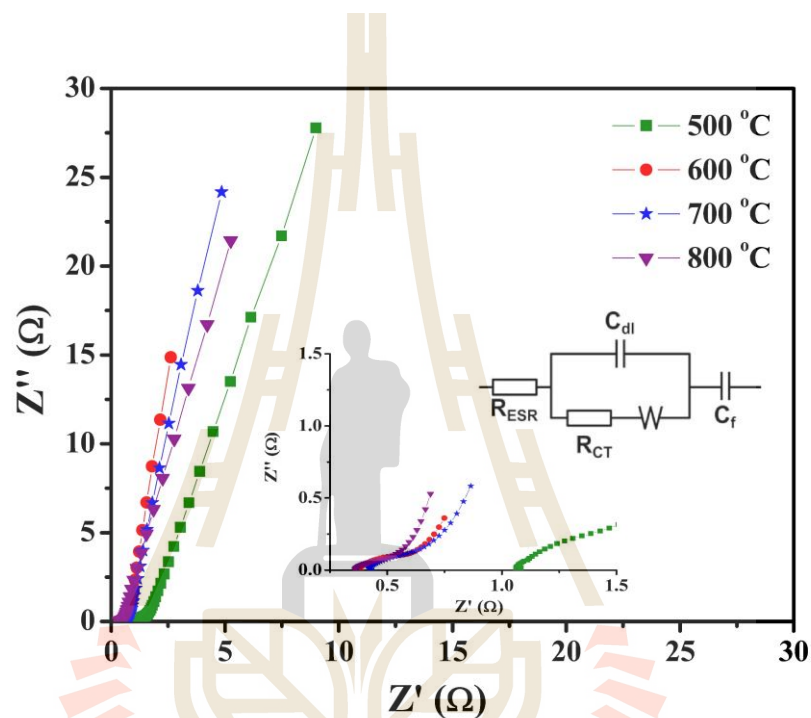


Figure 4.15 The EIS curves of the MnCo₂O₄ at various calcination.

Table 4.4 Comparison of supercapacitor performance of the MnCo₂O₄-based electrode materials.

Material	Synthesis method	Specific capacitance (F/g)	Reference
Flower-like MnCo ₂ O ₄	Solvothermal	539 (at 1 A/g)	(Che <i>et al.</i> , 2016)
1D MnCo ₂ O ₄ nanowire	Hydrothermal	349.8 (at 1 A/g)	(Li <i>et al.</i> , 2014)
Mesoporous MnCo ₂ O ₄	Solvothermal	346 (at 1 A/g)	(Padmanathan and Selladurai, 2014)
MnCo ₂ O ₄ nanoparticles	Sol-gel	405 (at 1 mA/cm ²)	(Kong <i>et al.</i> , 2014)
MnCo ₂ O ₄ nanoparticles	Hydrothermal	671 (at 5 mV/s)	(Tholkappiyan <i>et al.</i> , 2015)
MnCo ₂ O _{4.5} Urchin-like microspheres	Hydrothermal	151.2 (at 5 mV/s)	(Li <i>et al.</i> , 2014)
MnCo ₂ O ₄ nanosheet	Electrodeposition	290 (at 1 mV/s)	(Sahoo <i>et al.</i> , 2015)
MnCo ₂ O ₄ _500 °C nanoparticles	polymer-solution	169 (at 2 mV/s)	This work
MnCo ₂ O ₄ _600 °C nanoparticles	polymer-solution	282 (at 2 mV/s)	This work
MnCo ₂ O ₄ _700 °C nanoparticles	polymer-solution	260 (at 2 mV/s)	This work
MnCo ₂ O ₄ _800 °C nanoparticles	polymer-solution	195 (at 2 mV/s)	This work

4.2 Ni-doped MnCo_2O_4 nanoparticles

4.2.1 Structural and morphology characterization

4.2.1.1 X-ray diffraction (XRD) analysis of the Ni-doped MnCo_2O_4 nanoparticles

Figure 4.16(a) displays the XRD results of the $\text{Mn}_{1-x}\text{Ni}_x\text{Co}_2\text{O}_4$ ($x = 0.00, 0.05, 0.10, 0.15,$ and 0.20). The diffraction patterns with intensity correspond to the plane (111), (220), (311), (222), (400), (422), (511), and (440). which indicates that all the samples have MnCo_2O_4 spinel structure (JCPDS No. 23-1237). No other impurity peaks were detected, indicating that all samples are single phase. The XRD peaks are shifted to higher angles with the increasing of Ni content related to the successful substitution of Ni ions in the Mn ions (as presented in Figure 4.16(b)).

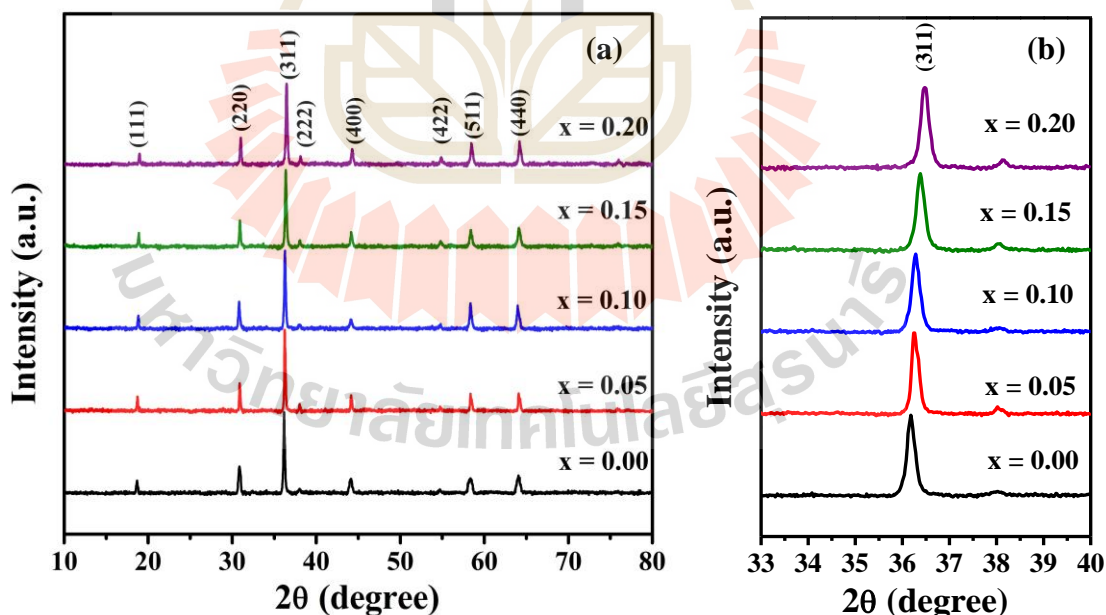


Figure 4.16 (a) XRD patterns of $\text{Mn}_{1-x}\text{Ni}_x\text{Co}_2\text{O}_4$ ($x = 0.00, 0.05, 0.10, 0.15,$ and 0.20) nanoparticles and (b) relative shift in (311) peak of MnCo_2O_4 with respect to Ni-doping.

Normally, the broad diffraction peaks suggest a very small crystallite size. Using the Scherrer's equation to estimate the crystallite sizes which are 22.3, 22.0, 21.5, 20.9, and 19.8 nm for Ni doping concentration $x = 0.00, 0.05, 0.10, 0.15,$ and $0.20,$ respectively. It is evident that the crystallite size decreases with increasing Ni concentration. The d -spacing values and the lattice constant, which is obtained from the XRD peak (311) position are summarized in Table 4.5. It is evident that the decreasing of the d -spacing and Lattice constant with increasing Ni concentration, which might be due to the Ni^{2+} (0.69 \AA) ion with small ionic radius substituted in the Mn^{3+} (0.72 \AA) site.

Table 4.5 Summary of crystallite sizes (D) from XRD, d -spacing (d), and lattice constant (a) of $\text{Mn}_{1-x}\text{Ni}_x\text{Co}_2\text{O}_4$ ($x = 0.00, 0.05, 0.10, 0.15,$ and 0.20) nanoparticles.

samples	Crystallite sizes	d -spacing	Lattice constant
	D (nm)	d (\AA)	a (nm)
$x = 0.00$	22.3	2.471	8.196
$x = 0.05$	22.0	2.466	8.177
$x = 0.10$	21.5	2.465	8.175
$x = 0.15$	20.9	2.463	8.169
$x = 2.00$	19.8	2.461	8.162

4.2.1.2 The Morphology of the Ni-doped MnCo_2O_4 nanoparticles by FESEM and TEM

The morphologies and structures of the Ni-doped MnCo_2O_4 nanoparticles were further investigated by FESEM and TEM. Figure 4.17(a-e) presents

the FESEM images of the Ni-doped MnCo_2O_4 nanoparticles with different doping concentrations, which demonstrates the particle size tended to decrease with increasing Ni doping concentration. After Ni doping, the sample $x = 0.20$ presents uniform nanoparticles (Figure 4.17(e)). Figure 4.18(a-e) show the TEM bright field images and particle size distribution reveal that the average particle sizes are 103, 84, 81, 73, and 64 nm for the samples with Ni content $x = 0.00, 0.05, 0.10, 0.15,$ and $0.20,$ respectively. It can be seen that the average particle size decreases with increasing the Ni doping concentration. The nanoparticle is massively accumulation in the sample $x = 0.20$. The observed smaller particle size leads to a higher BET surface area. Furthermore, the distribution of the particles can affect BET surface area, which is discussed in the sections 4.2.1.5. The corresponding SAED patterns present spotty and ring, suggesting the polycrystalline feature of the MnCo_2O_4 nanoparticles, in good agreement with the XRD analysis.



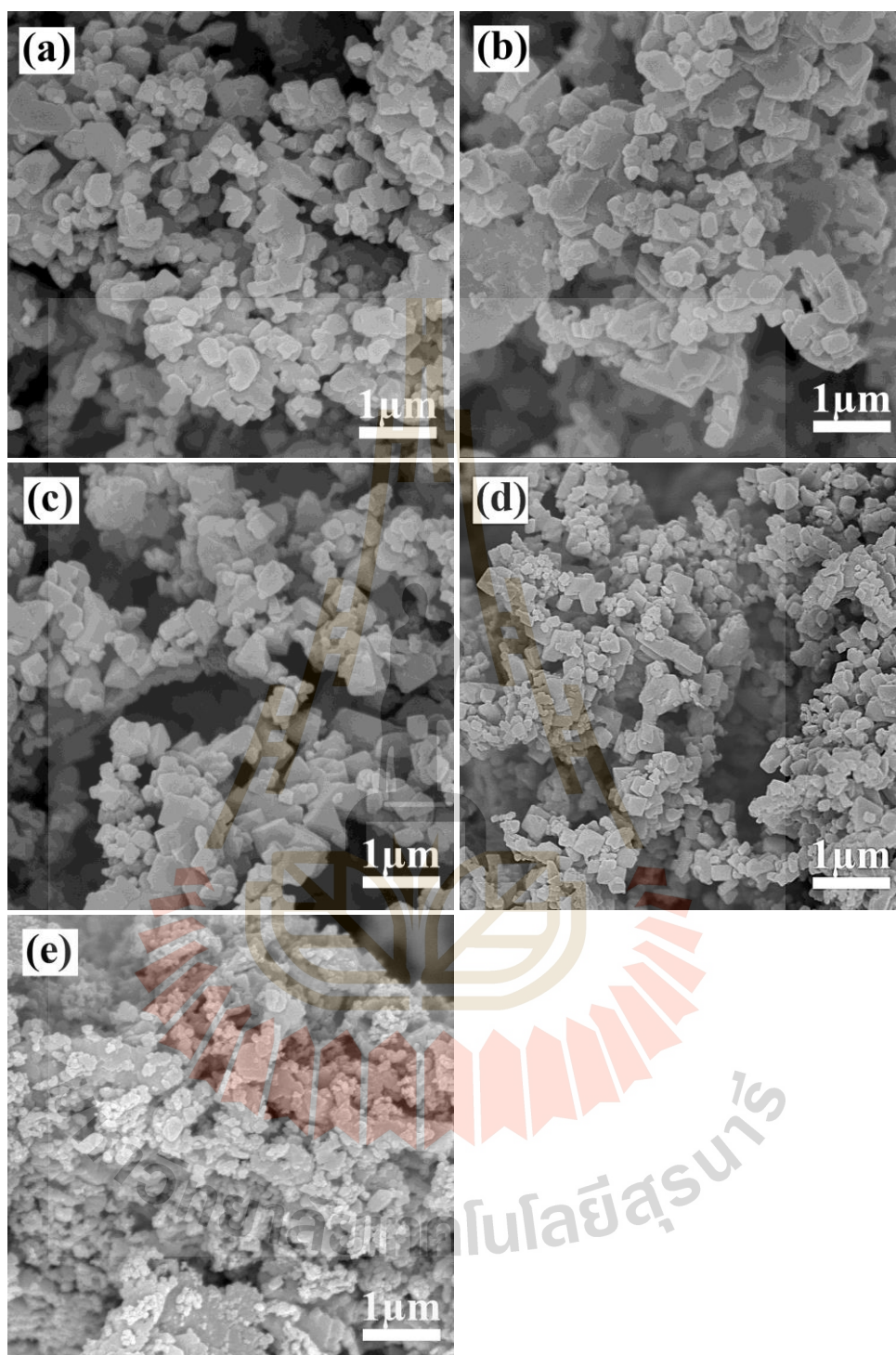


Figure 4.17 FESEM images of $\text{Mn}_{1-x}\text{Ni}_x\text{Co}_2\text{O}_4$ nanoparticles: (a) $x = 0.00$, (b) $x = 0.05$, (c) $x = 0.10$, (d) $x = 0.15$, and (e) $x = 0.20$.

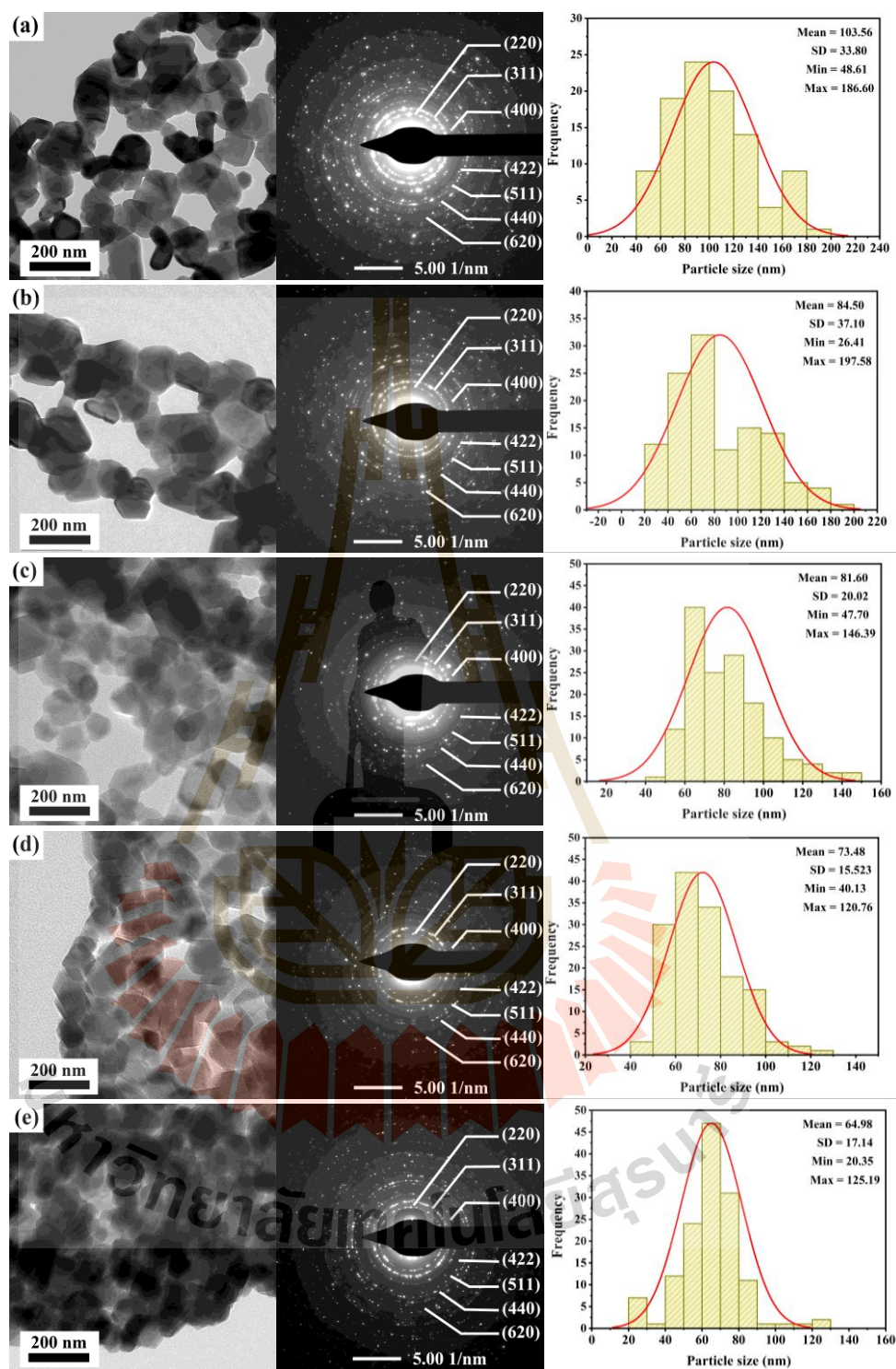


Figure 4.18 TEM images with corresponding SAED of $\text{Mn}_{1-x}\text{Ni}_x\text{Co}_2\text{O}_4$ nanoparticles and particle size distribution: (a) $x = 0.00$, (b) $x = 0.05$, (c) $x = 0.10$, (d) $x = 0.15$, and (e) $x = 0.20$.

4.2.1.3 X-ray absorption spectroscopy study of the Ni-doped MnCo₂O₄ nanoparticles

To study the valence states of Co, Mn, and Ni in the Ni-doped MnCo₂O₄ nanoparticles, the XANES technic was used. For this analysis, we have used XANES spectra of eight standard samples, viz, Co foil (Co⁰⁺), CoO (Co²⁺), Co₃O₄ (Co^{2+,3+}), Mn foil (Mn⁰⁺), Mn₂O₃ (Mn³⁺), MnO₂ (Mn⁴⁺), Ni foil (Ni⁰⁺), and NiO (Ni²⁺), along with Mn_{1-x}Ni_xCo₂O₄ (x = 0.00, 0.05, 0.10, 0.15, and 0.20) samples. Generally, the shift of the edge position can be employed to evaluate the valence states of Co, Mn, and Ni. The XANES spectra at Co K-edge of the Ni-doped MnCo₂O₄ samples shows an edge position between CoO (Co²⁺) and Co₃O₄ (Co^{2+,3+}) standard sample (as shown in the inset of Figure 4.19(a)). This suggests an existence of a coupling of Co valence states in all samples (Co²⁺/Co³⁺), which can be affirmed by the first derivative plot (Figure 4.19(b)) and the edge energy (Table 4.6). At Mn K-edge, the XANES spectra of all the samples lay between Mn₂O₃ (Mn³⁺) and MnO₂ (Mn⁴⁺) standard samples (Figure 4.20) that Mn ions in all the samples were mixed oxidation state of Mn³⁺ and Mn⁴⁺. These results were confirmed by their edge energy (Table 4.6). XANES spectra at Ni K-edge for all samples are very close to NiO (Ni²⁺) standard samples which indicate that Ni ion for all samples have oxidation state of Ni²⁺, as shown in Figure 4.21(a).

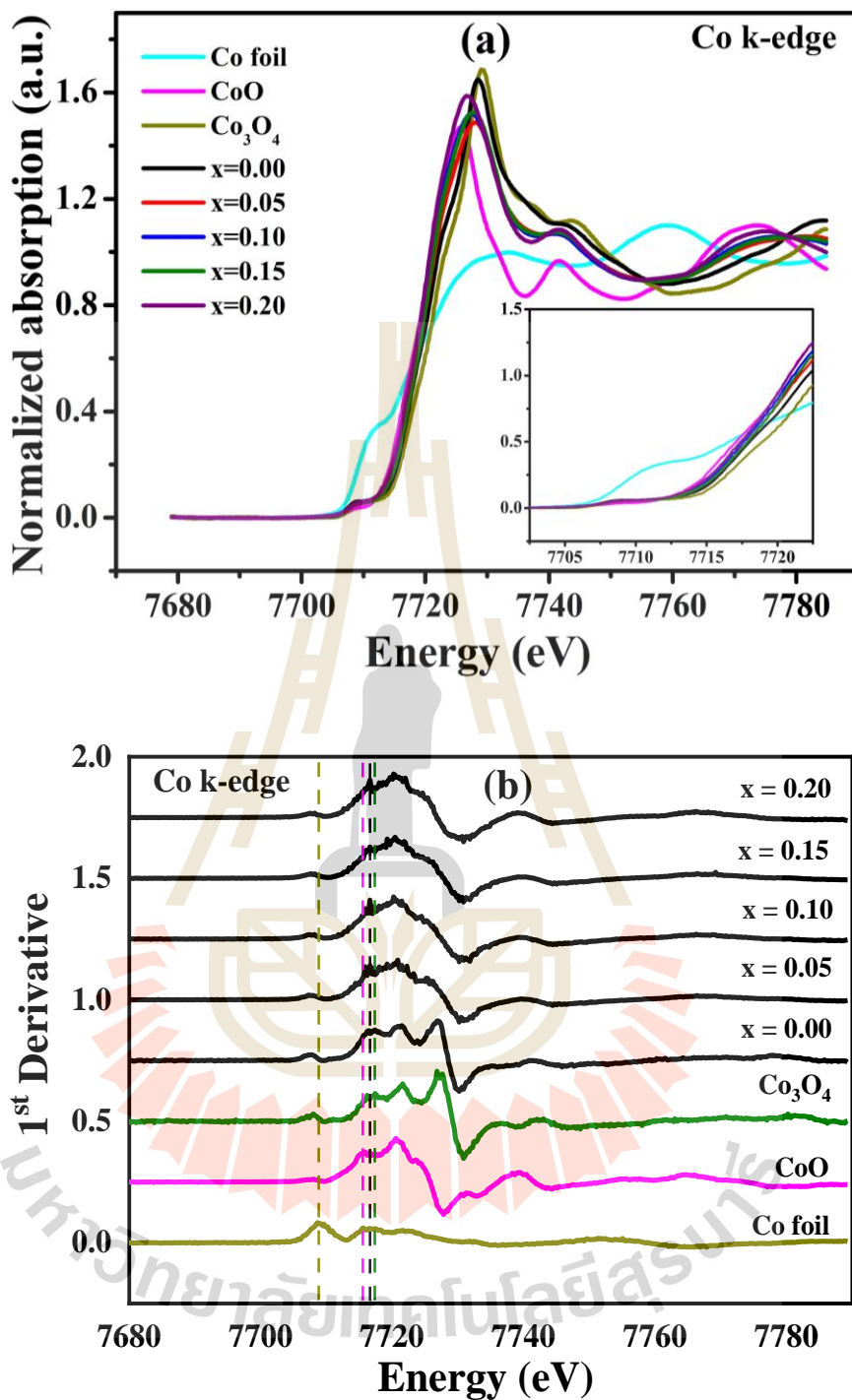


Figure 4.19 (a) Normalized XANES spectra (*Inset* of a present edge shift of samples) and (b) their Corresponding first-derivative of the Ni-doped MnCo_2O_4 nanoparticles at Co K-edge.

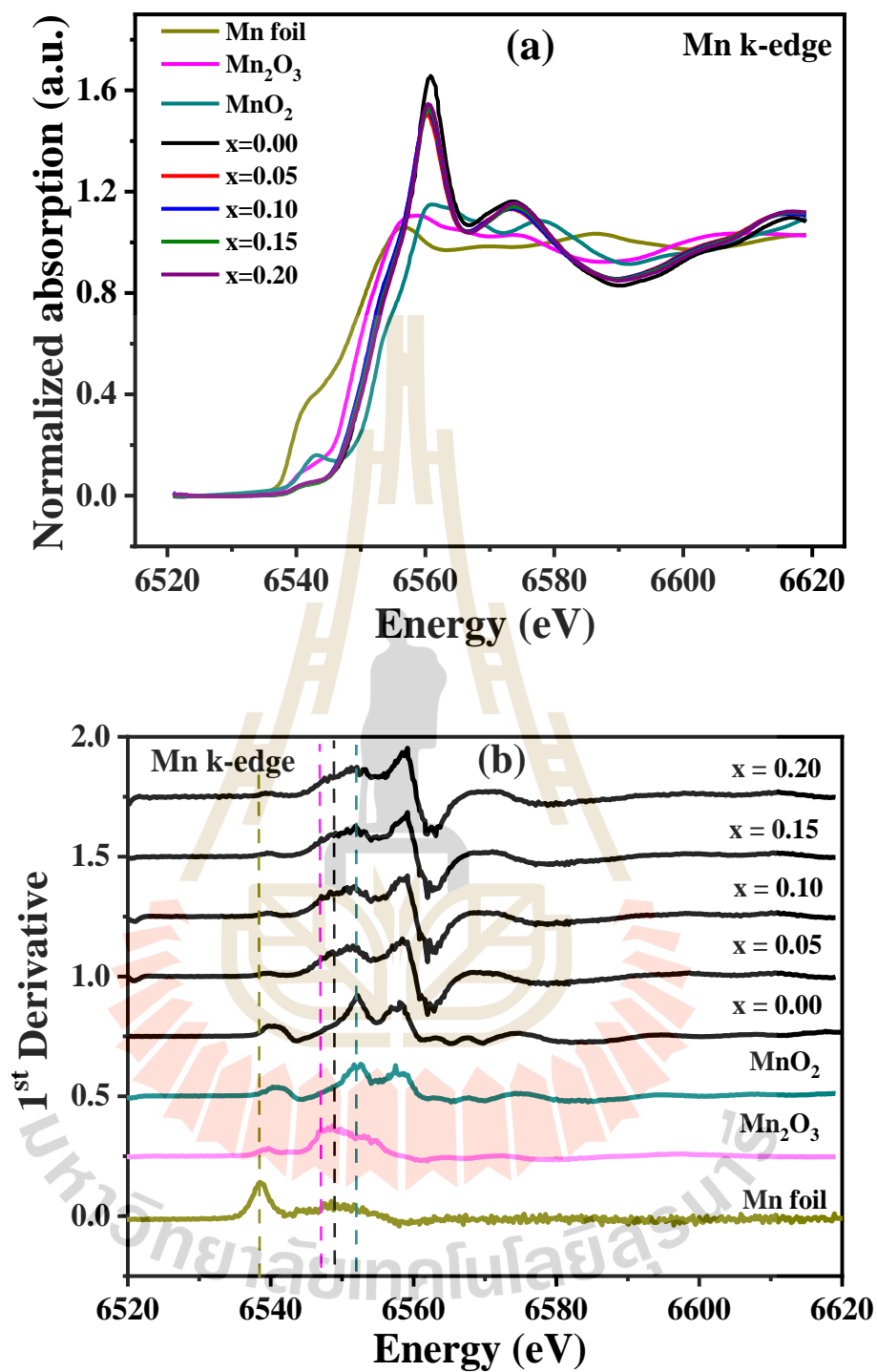


Figure 4.20 (a) Normalized XANES spectra and (b) their Corresponding first-derivative of the Ni-doped MnCo_2O_4 nanoparticles at Mn K-edge.

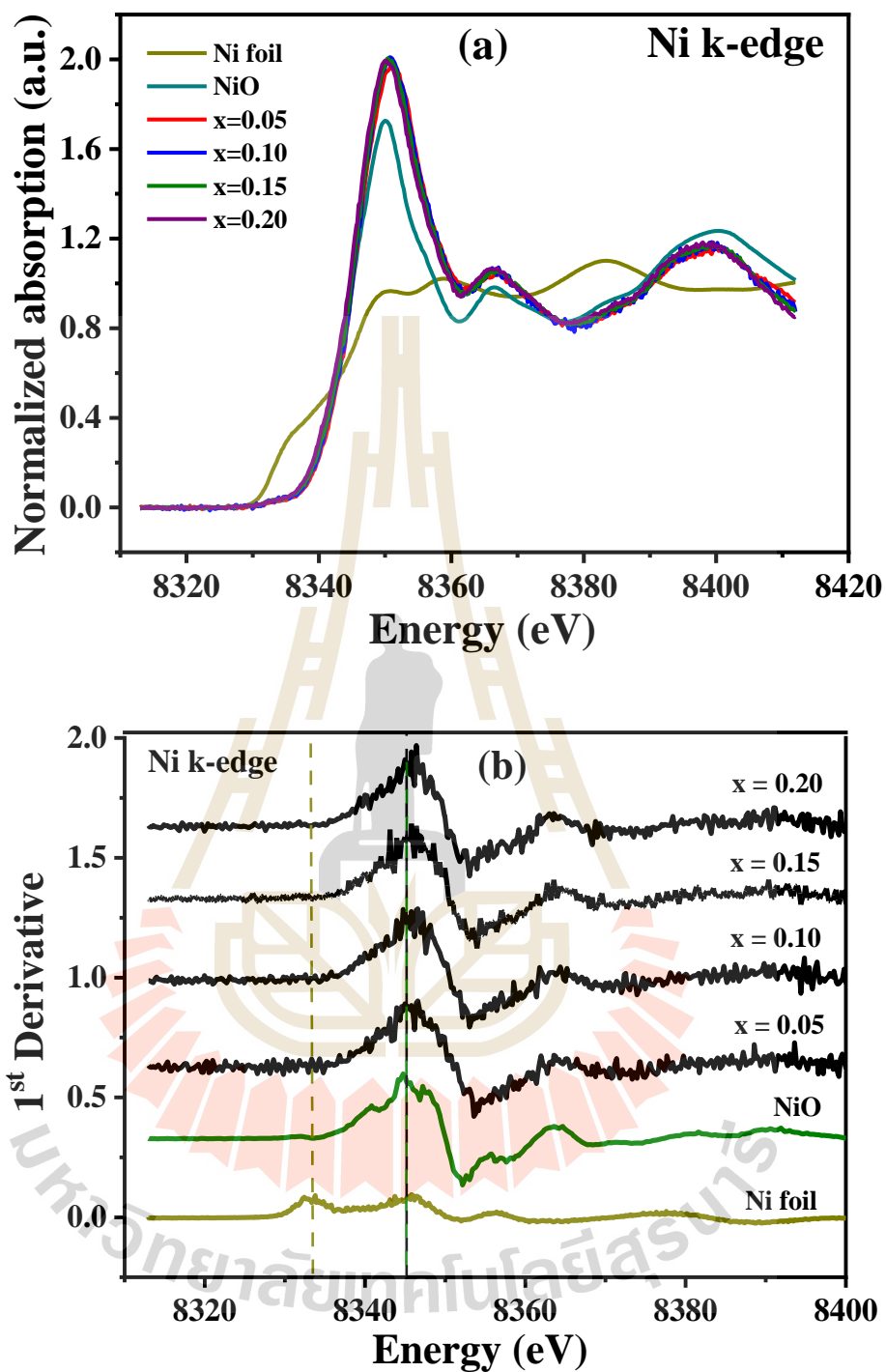


Figure 4.21 (a) Normalized XANES spectra and (b) their Corresponding first-derivative of the Ni-doped MnCo₂O₄ nanoparticles at Ni K-edge.

Table 4.6 Edge energy and Oxidation state of the standard samples and Ni-doped MnCo_2O_4 nanoparticles.

Samples	Edge element	Absorption Edge (eV)	Oxidation state
CoO	Co	7716.30	+2
Co ₃ O ₄	Co	7721.45	+2, +3
Mn ₂ O ₃	Mn	6546.60	+3
MnO ₂	Mn	6551.57	+4
NiO	Ni	8345.00	+2
x = 0.00	Co	7717.15	+2, +3
	Mn	6550.13	+3, +4
x = 0.05	Co	7719.80	+2, +3
	Mn	6550.58	+3, +4
	Ni	8345.44	+2
x = 0.10	Co	7719.63	+2, +3
	Mn	6550.67	+3, +4
	Ni	8345.44	+2
x = 0.15	Co	7720.08	+2, +3
	Mn	6550.70	+3, +4
	Ni	8345.44	+2
x = 0.20	Co	7719.99	+2, +3
	Mn	6550.81	+3, +4
	Ni	8345.44	+2

4.2.1.4 X-ray photoelectron spectroscopy (XPS) study of the Ni-doped MnCo₂O₄ nanoparticles

The surface valence state and composition of the elemental of the Ni-doped MnCo₂O₄ nanoparticles were conducted by using XPS analysis. As shown in Figure 4.22, two major peaks with binding energy of ~ 780 and ~ 795 eV corresponding to the energy levels of Co 2p_{3/2} and Co 2p_{1/2}, respectively were observed in Co 2p XPS spectra. By the Gaussian fitting method, the Co 2p spectra of the Ni-doped MnCo₂O₄ samples can be fitted into two spin-orbit doublets and four shake-up satellite peaks (denoted as sat.). The energy gap between the Co 2p main peaks and their satellite peaks in the range of 3.5-5 and 9.4-10 eV is the presence of Co²⁺ and Co³⁺ cations, respectively as reported in the previous works (Li *et al.*, 2015; Wang *et al.*, 2015; Naveen and Selladurai, 2015). Mn 2p XPS spectrum can be divided into the 2 major spin-orbit doublets of Mn 2p_{1/2} at 653 eV and Mn 2p_{3/2} at 641 eV, as shown in Figure 4.23. After fitting, the spectrums were best fitted into four peaks at the binding energy about at ~ 653.5, ~ 655.5, ~ 641.8, and ~ 644.7 eV that are related to Mn³⁺ (2p_{1/2}), Mn⁴⁺ (2p_{1/2}), Mn³⁺ (2p_{3/2}), and Mn⁴⁺ (2p_{3/2}) species, respectively (Chen *et al.*, 2018; Wang *et al.*, 2018; Chen *et al.*, 2017). As presented in Figure 4.24, Ni 2p XPS spectra show the main peak at binding energy of ~ 856 eV (Ni 2p_{3/2}), indicating that Ni²⁺ is existing in all the Ni-doped MnCo₂O₄ samples (Chen *et al.*, 2017). The high-resolution spectra for the O 1s (Figure 4.25) present the three peaks at 530.2, 531.8, and 533.2 eV. The large peak at 530.2 eV is assigned to the metal-oxygen bonds while the other peaks are oxygen in OH⁻ groups and the oxygen atom of the adsorbed water molecules.

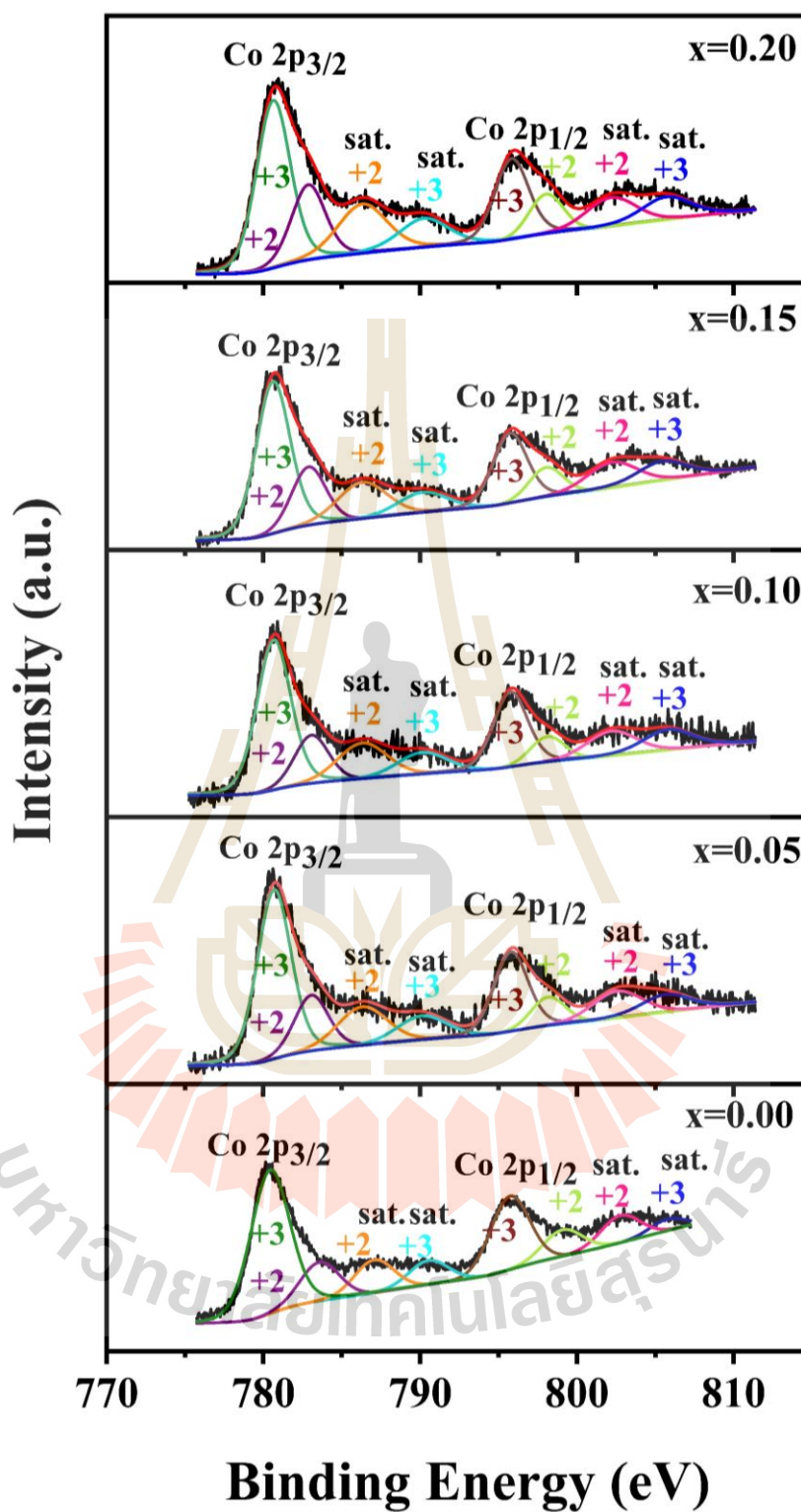


Figure 4.22 XPS spectra at Co 2p of the $\text{Mn}_{1-x}\text{Ni}_x\text{Co}_2\text{O}_4$ ($x = 0.00, 0.05, 0.10, 0.15,$ and 0.20) nanoparticles.

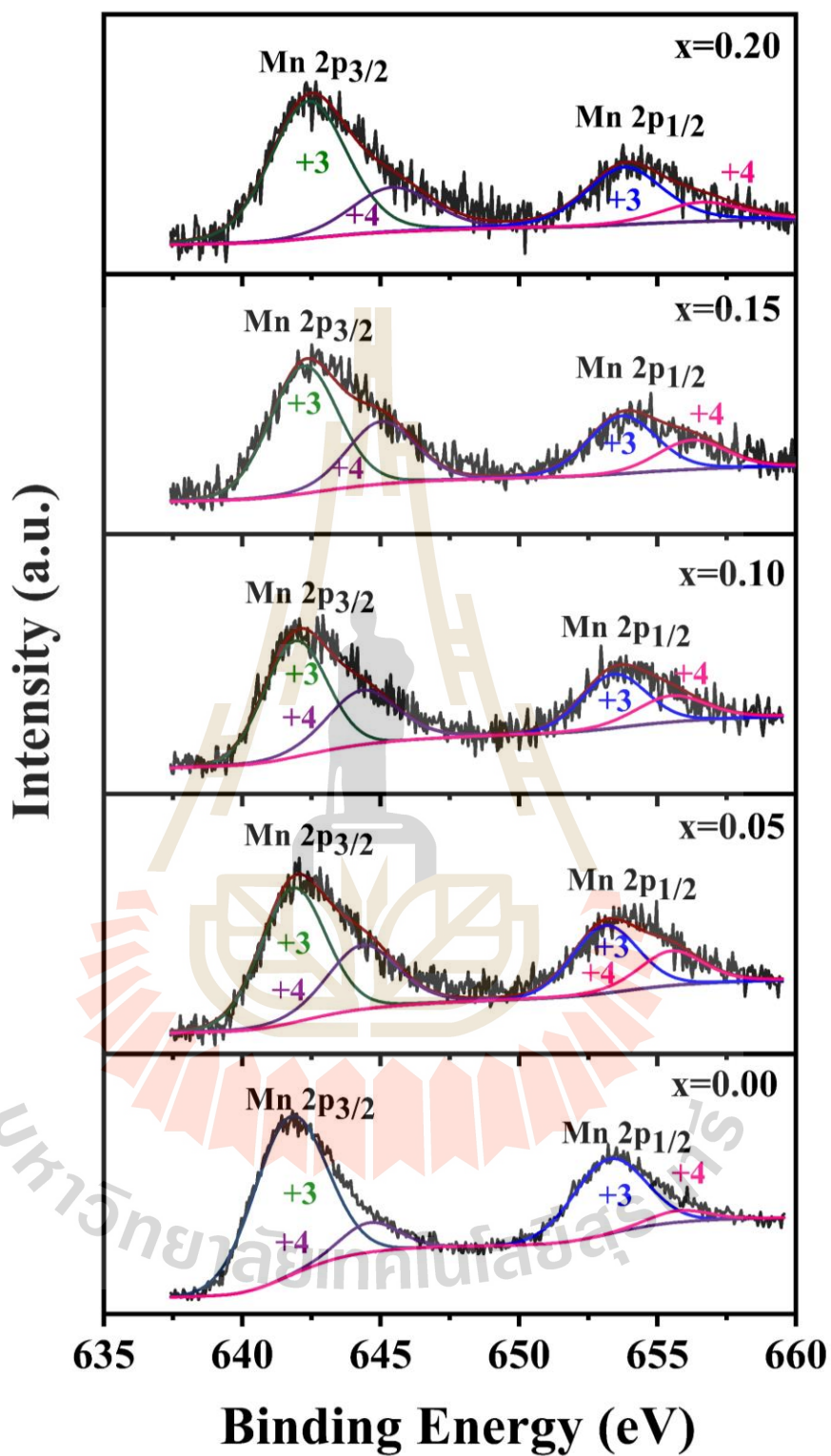


Figure 4.23 XPS spectra at Mn 2p of the Ni-doped MnCo₂O₄ nanoparticles.

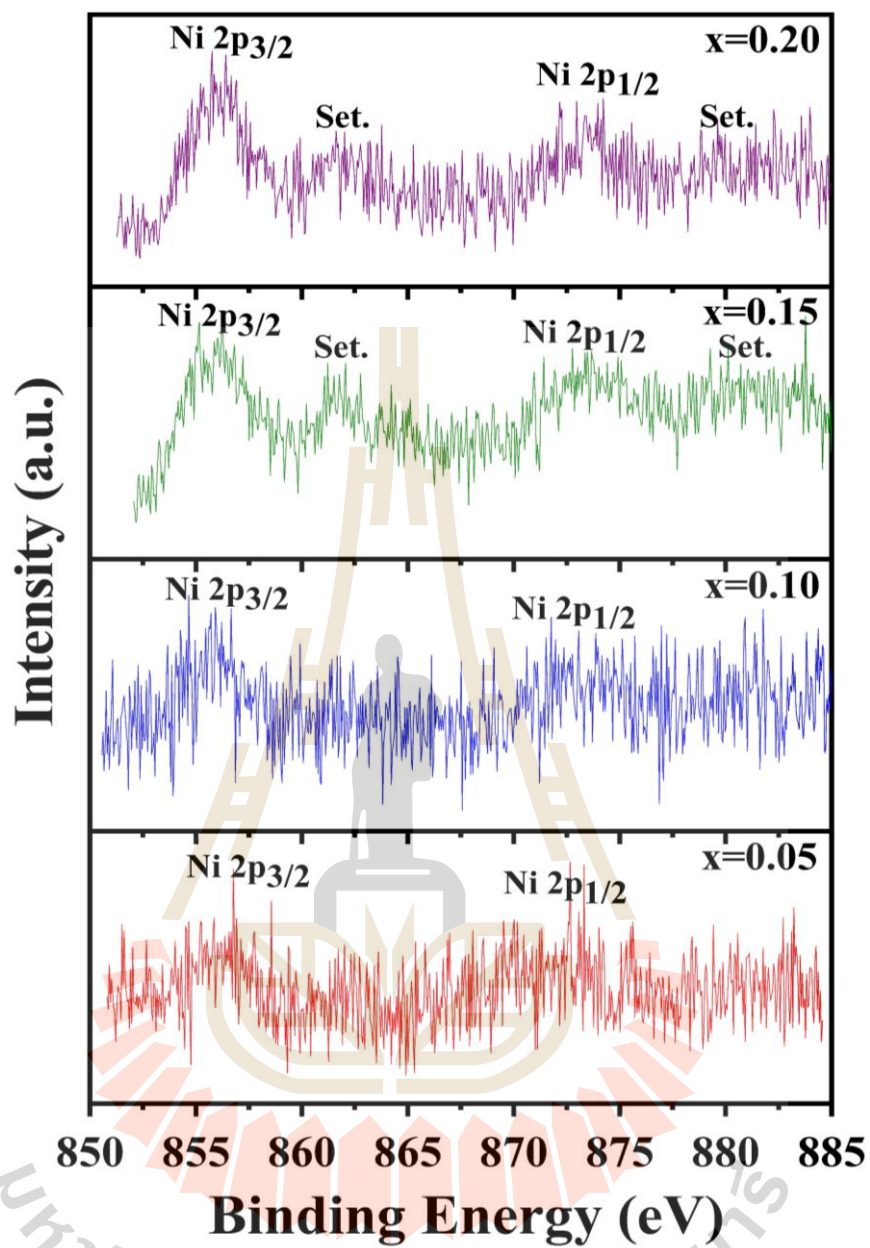


Figure 4.24 XPS spectra at Ni 2p of the Ni-doped MnCo₂O₄ nanoparticles.

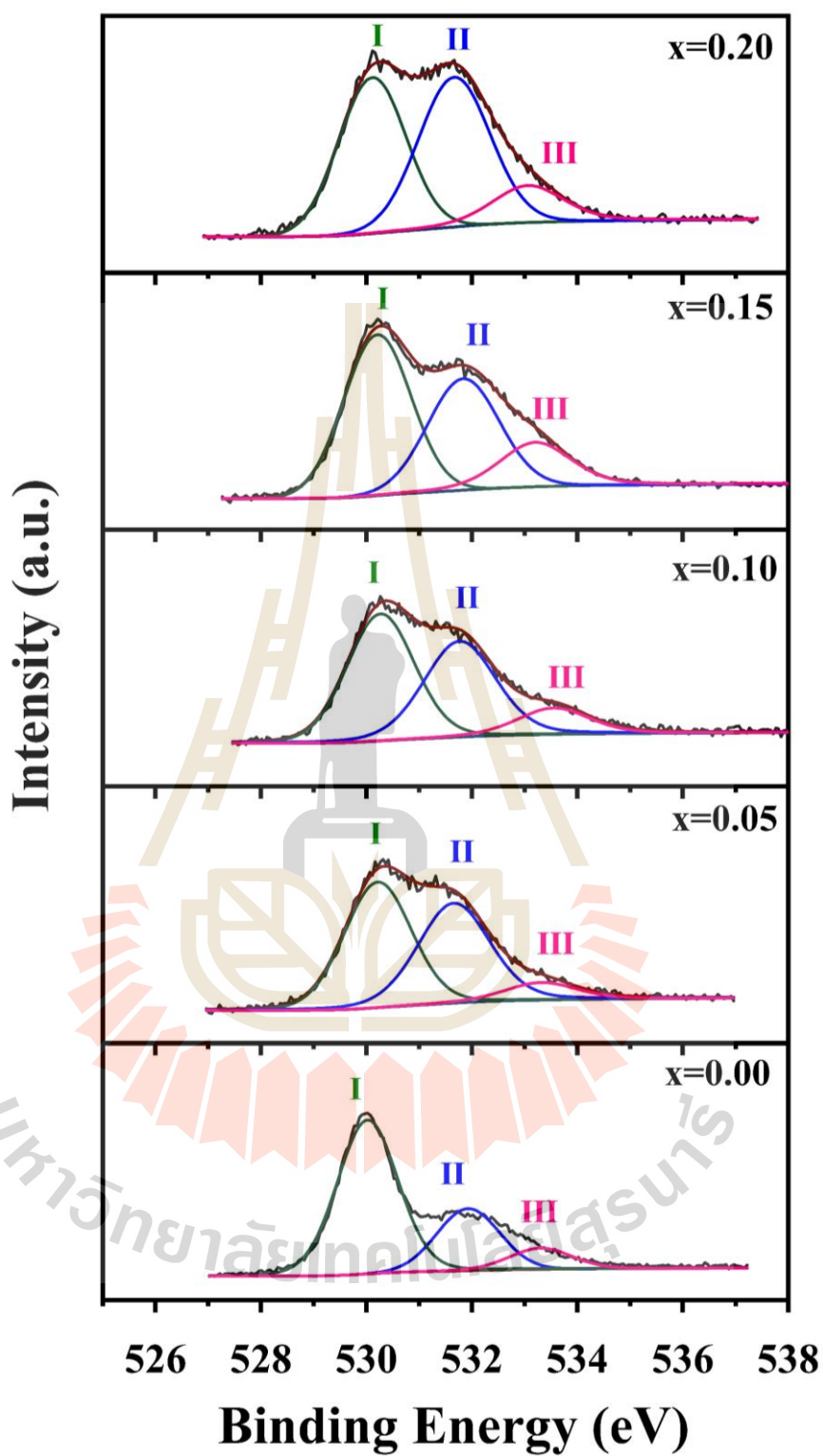


Figure 4.25 XPS spectra at O1s of the Ni-doped MnCo₂O₄ nanoparticles.

Table 4.7 XPS data of the Ni-doped MnCo₂O₄ nanoparticles.

Samples	Binding energy position (eV)									
	Co 2p _{3/2}		Co 2p _{1/2}		Mn 2p _{3/2}		Mn 2p _{1/2}		Ni 2p _{3/2}	Ni 2p _{1/2}
	Co ²⁺	Co ³⁺	Co ²⁺	Co ³⁺	Mn ³⁺	Mn ⁴⁺	Mn ³⁺	Mn ⁴⁺	Ni ²⁺	Ni ²⁺
x = 0.00	782.83	779.69	798.34	794.98	641.73	644.60	653.26	655.77		
x = 0.05	783.07	780.69	798.17	795.80	641.83	644.34	653.11	655.50	856.10	873.50
x = 0.10	783.07	780.67	798.12	795.77	641.91	644.34	653.41	655.50	856.13	873.52
x = 0.15	782.89	780.63	798.04	795.74	642.23	645.02	653.72	656.25	856.13	873.52
x = 0.12	782.87	780.64	798.04	795.84	642.40	645.42	653.81	656.62	856.14	873.59

มหาวิทยาลัยเทคโนโลยีสุรนารี

4.2.1.5 Characterization of surface area and pore size distribution of the Ni-doped MnCo₂O₄ nanoparticles by BET method and BJH method

The specific surface area and the pore structure of the prepared Ni-doped MnCo₂O₄ nanoparticles were determined by using BET measurements. The N₂ adsorption-desorption isotherms and corresponding pore size distributions of the Mn_{1-x}Ni_xCo₂O₄ nanoparticles are shown in Figure 4.26(a-e). The isotherms of all the samples exhibit a small hysteresis loop appearing in the range of 0 to 1, which presents the typical feature of a mesoporous structure. The BET specific surface area values are 71.92, 83.07, 85.61, 90.78, and 73.21 m²/g for Mn_{1-x}Ni_xCo₂O₄ nanoparticles with x = 0.00, 0.05, 0.10, 0.15, and 0.20, respectively. The BET specific surface area values tend to increase with increasing Ni content of x = 0.00 to x = 0.15 owing to the decreasing of the particle size. In contrast, the sample with Ni content of x = 0.20 with smallest the particle size has smallest the BET specific surface area, which may be due to the thick accumulation of nanoparticles. The average pore diameters of the materials are 4.39, 4.09, 3.90, 3.25, and 4.23 nm for the samples with x = 0.00, 0.05, 0.10, 0.15, and 0.20, respectively. The pore size distribution was evaluated by BJH method from the desorption part of the isotherms as shown in the insets of Figure 4.26(a-e). The pore size distribution in the range of 2-10 nm also indicates a typical feature of mesoporous materials. The BET specific surface areas, average pore diameter, and pore volume are summarized in Table 4.8. Generally, a large surface area of as-synthesized material leading to more active sites for providing multiple redox reactions can result in the higher the specific capacitance and demonstrating good electrochemical capacitance (Naveen and Selladurai, 2015; Cao *et al.*, 2016). According to the results of the pore volume, pore size distribution, and BET specific surface area. It has reason to guess

that the Ni-doped MnCo_2O_4 nanoparticles prepared with different Ni doping concentration will display different electrochemical performances.

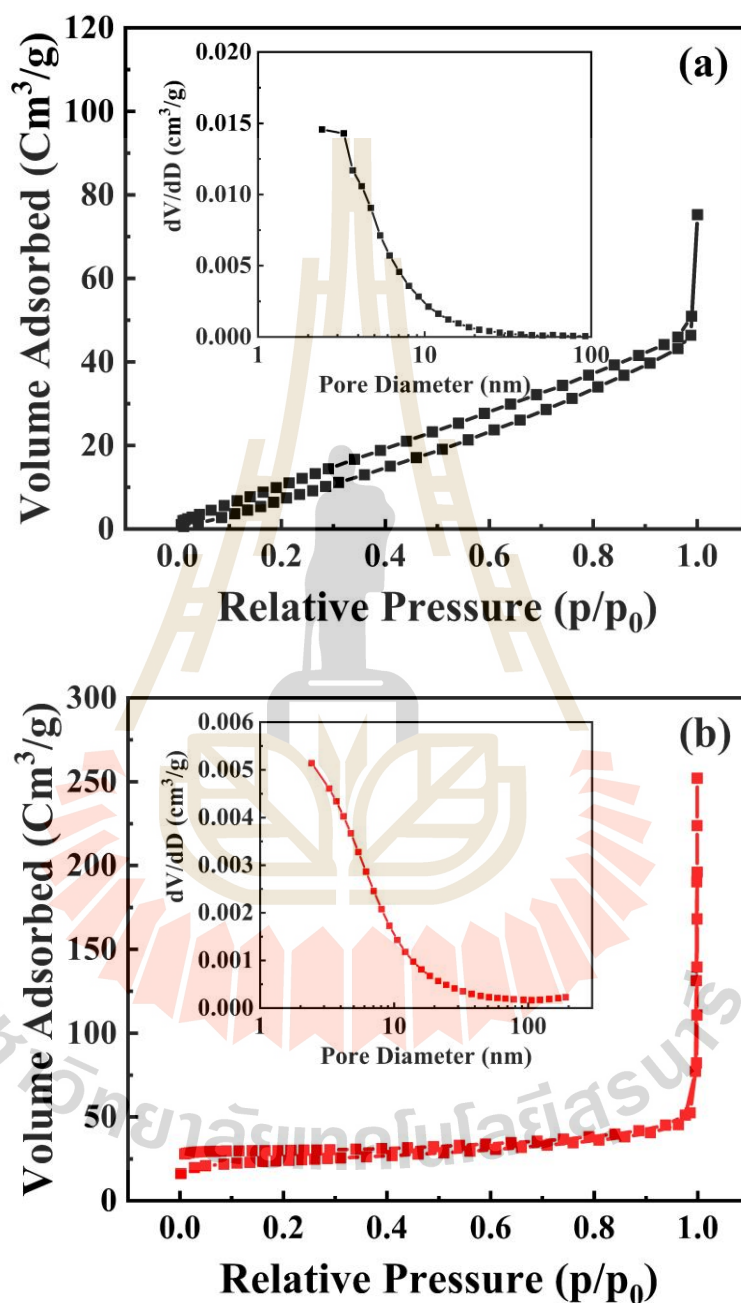


Figure 4.26 Nitrogen adsorption/desorption isotherms and pore size distribution (inset) of $\text{Mn}_{1-x}\text{Ni}_x\text{Co}_2\text{O}_4$ nanoparticles: (a) $x = 0.00$, (b) $x = 0.05$, (c) $x = 0.10$, (d) $x = 0.15$, and (e) $x = 0.20$.

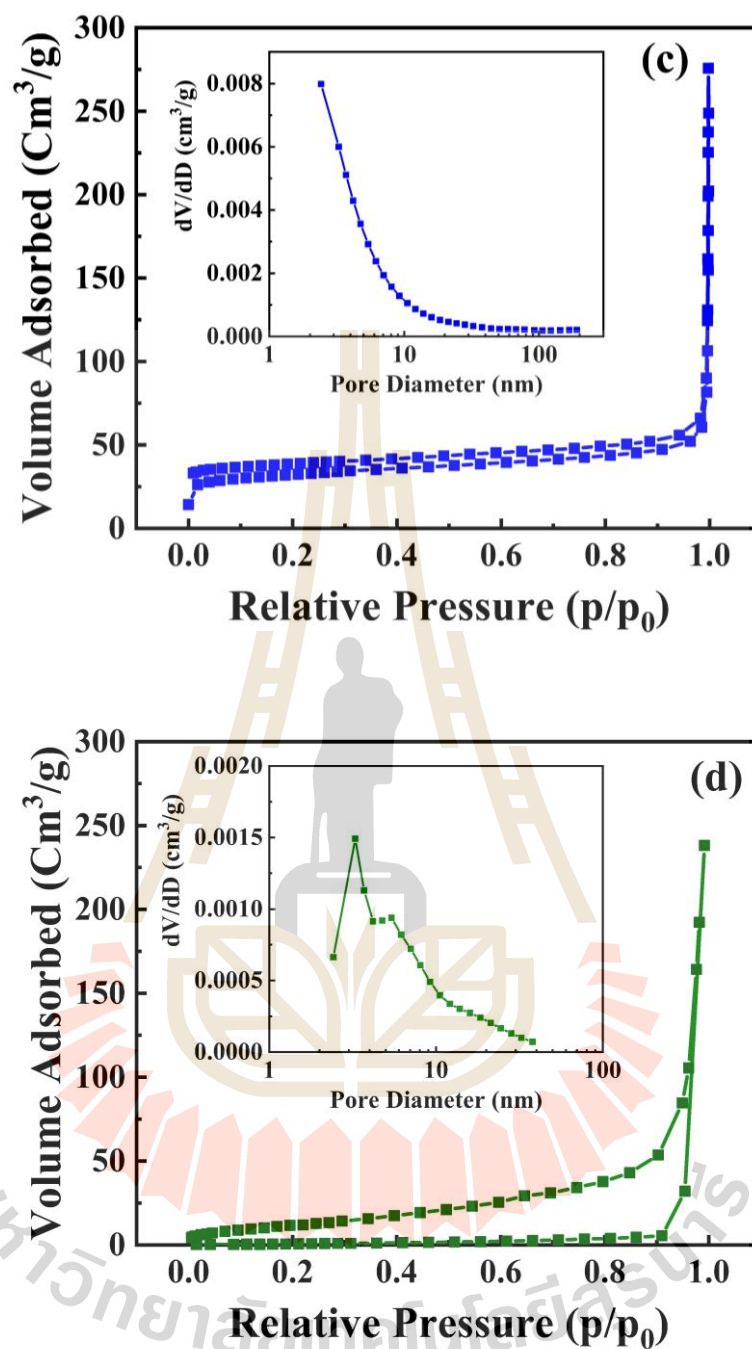


Figure 4.26 (Continued) Nitrogen adsorption/desorption isotherms and pore size distribution (inset) of $\text{Mn}_{1-x}\text{Ni}_x\text{Co}_2\text{O}_4$ nanoparticles: (a) $x = 0.00$, (b) $x = 0.05$, (c) $x = 0.10$, (d) $x = 0.15$, and (e) $x = 0.20$.

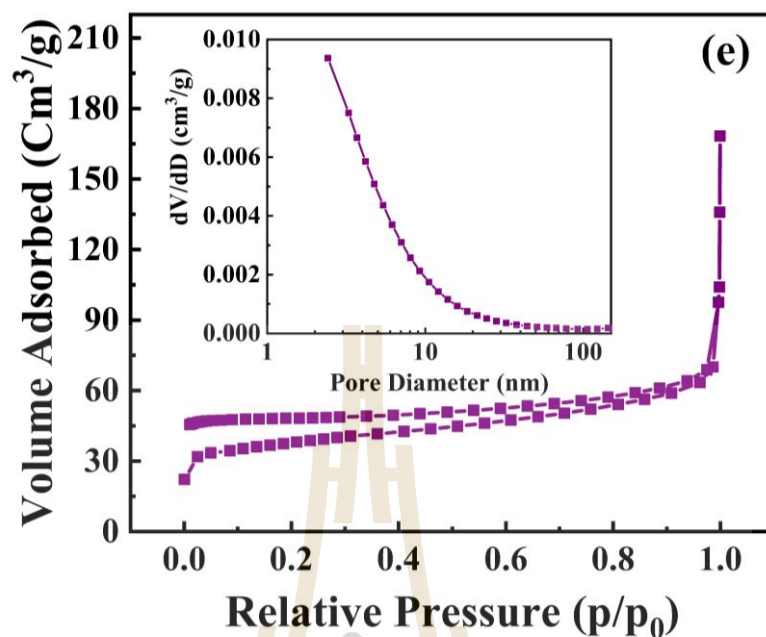


Figure 4.26 (Continued) Nitrogen adsorption/desorption isotherms and pore size distribution (inset) of Mn_{1-x}Ni_xCo₂O₄ nanoparticles: (a) x = 0.00, (b) x = 0.05, (c) x = 0.10, (d) x = 0.15, and (e) x = 0.20.

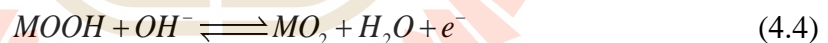
Table 4.8 Physical properties of spinel Mn_{1-x}Ni_xCo₂O₄ (x = 0.00, 0.05, 0.10, 0.15, and 0.20) nanoparticles.

Samples	BET specific surface area (m ² /g)	Total pore volume (cm ³ /g)	Mean pore diameter (nm)
x = 0.00	71.92	0.079	4.39
x = 0.05	83.07	0.080	3.85
x = 0.10	85.61	0.082	3.83
x = 0.15	90.78	0.085	3.74
x = 0.20	73.21	0.080	4.37

4.2.2 Electrochemical properties

4.2.2.1 Cyclic voltammetry measurement

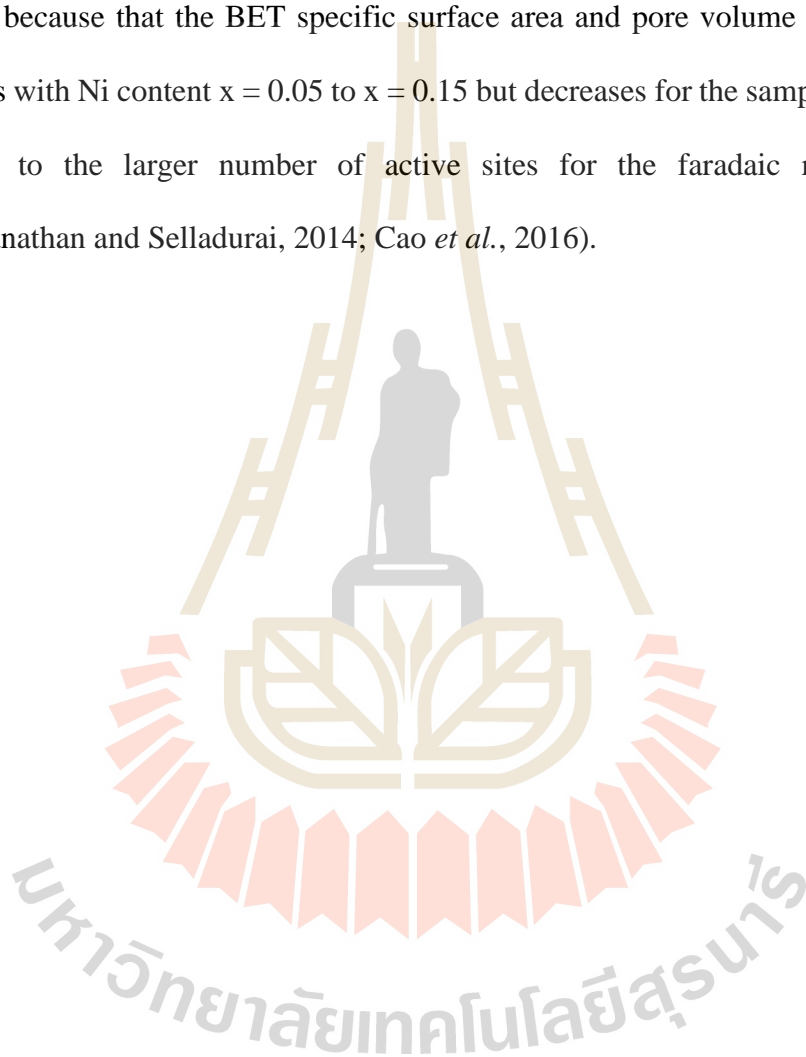
Cyclic voltammetry techniques have been performed to evaluate the electrochemical characteristics and quantify the specific capacitance of $Mn_{1-x}Ni_xCo_2O_4$ electrode. Figure 4.27(a-e) present the CV curves of $Mn_{1-x}Ni_xCo_2O_4$ nanoparticles, which were examined between -1.0 and 0.4 V with various scan rates ranging from 2 to 500 mV/s in 6M KOH electrolyte at room temperature. The redox peaks appear in the CV curves for all samples, which indicates that a typical pseudocapacitive characteristic comes from the faradaic redox reactions of Co^{2+}/Co^{3+} , Mn^{3+}/Mn^{4+} , and Ni^{2+} as reported (Kong *et al.*, 2014; Padmanathan and Selladurai, 2014; Sahoo *et al.*, 2015; Krishnan *et al.*, 2016; Hao *et al.*, 2015; Tamboli *et al.*, 2017). The redox reactions in the a KOH electrolyte are described by equation (4.3) and equation (4.4) (Li *et al.*, 2014; Bai *et al.*, 2016; Hao *et al.*, 2015; Tamboli *et al.*, 2017).



where M is indicative of Co or Ni and Mn.

The increasing of a scan rate results in the shifting of the position of anodic and cathodic peaks which suggests good electrochemical reversibility and excellent high-rate performance (Peng *et al.*, 2015). The calculated specific capacitance vs scan rate for $Mn_{1-x}Ni_xCo_2O_4$ samples is presented in Figure 4.27(f). The specific capacitance of all the samples decreases with the increase of scan rate from 2 to 500 mV/s that ion diffusion is limited at the surface of the electrode at a higher scan rate thereby dominating the electric double-layer capacitors (EDLC) over pseudocapacitive

characteristics. For low scan rate of 2 mV/s, the maximum specific capacitances of 201, 256, 288, 330, and 211 F/g are obtained for the $\text{Mn}_{1-x}\text{Ni}_x\text{Co}_2\text{O}_4$ nanoparticles with $x = 0.00, 0.05, 0.10, 0.15,$ and 0.20 , respectively. The specific capacitance value increases in the samples with Ni content $x = 0.05$ to $x = 0.15$, and then decreases with $x = 0.20$. This is because that the BET specific surface area and pore volume increases in the samples with Ni content $x = 0.05$ to $x = 0.15$ but decreases for the sample $x = 0.20$, and leading to the larger number of active sites for the faradaic redox reactions (Padmanathan and Selladurai, 2014; Cao *et al.*, 2016).



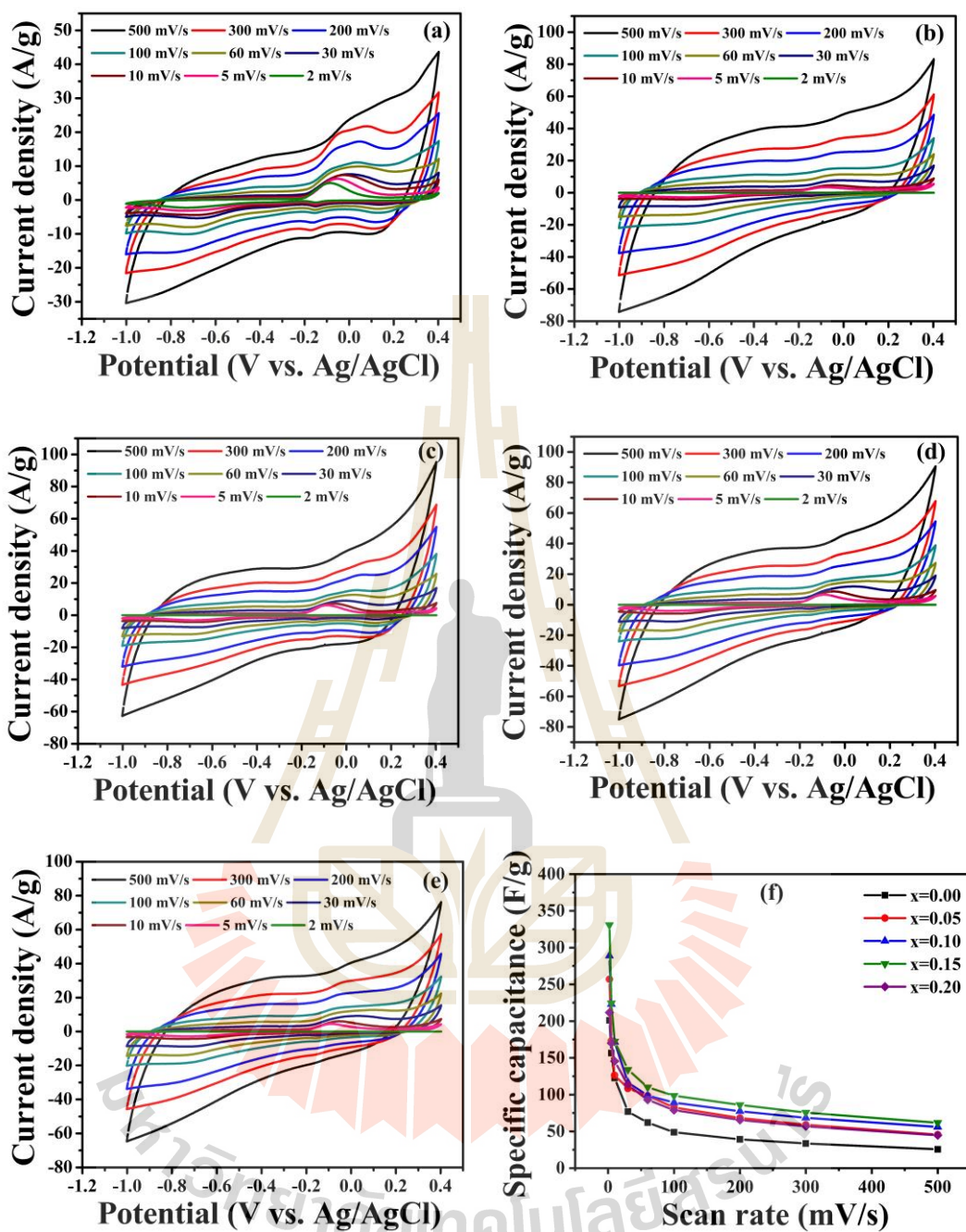


Figure 4.27 CV curves at various scan rates of $\text{Mn}_{1-x}\text{Ni}_x\text{Co}_2\text{O}_4$ nanoparticles: (a) $x = 0.00$, (b) $x = 0.05$, (c) $x = 0.10$, (d) $x = 0.15$, and (e) $x = 0.20$. (f) specific capacitance as a function of scan rates.

4.2.2.2 Galvanostatic charge-discharge measurements

The GCD curves of the $\text{Mn}_{1-x}\text{Ni}_x\text{Co}_2\text{O}_4$ electrodes was conducted at current densities range of 1 to 20 A/g as shown in Figure 4.28(a-e). The nonlinear charge-discharge curves match well with peaks observed from the CV curves which can confirm the pseudocapacitance behavior of the $\text{Mn}_{1-x}\text{Ni}_x\text{Co}_2\text{O}_4$ electrodes. The specific capacitance of the $\text{Mn}_{1-x}\text{Ni}_x\text{Co}_2\text{O}_4$ electrodes was estimated from the discharge curve by using the equation (3.17) (Padmanathan and Selladurai, 2014). Using the above equation, the specific capacitance of all the samples decreases with increases of the current density as shown in Figure 4.28(f). This may due to the increase of the polarization and internal resistance of the electrode. The $\text{Mn}_{1-x}\text{Ni}_x\text{Co}_2\text{O}_4$ electrode with $x = 0.15$ exhibits the highest specific capacitance of 378 F/g at the current density of 1 A/g, which is consistent with the specific capacitance from CV measurement as well. Due to higher BET specific surface area and larger pore volume, the contact areas between the electrolyte and electrode are increased resulting in more active sites for faradaic redox reactions. Additionally, the cycling stability of the $\text{Mn}_{1-x}\text{Ni}_x\text{Co}_2\text{O}_4$ electrodes was investigated by the continuous 1000 cycles charge-discharge measurements at the current density of 2 A/g in the potential range of -1.0 to 0.4 V in 6M KOH solution. Figure 4.29 shows the capacity retention (%) of the $\text{Mn}_{1-x}\text{Ni}_x\text{Co}_2\text{O}_4$ electrodes with $x = 0.00, 0.05, 0.10, 0.15,$ and 0.20 after 1000 cycles. It can be seen that the Ni-doped MnCo_2O_4 electrodes with $x = 0.00, 0.05, 0.10, 0.15,$ and 0.20 exhibit the capacitance retention of 73%, 75%, 76%, 84% and 74%, respectively after 1000 cycles of charge-discharge. This result suggests that the $\text{Mn}_{0.85}\text{Ni}_{0.15}\text{Co}_2\text{O}_4$ electrode presents higher capacitance and better rate capability. However, with a continuous increase in

the cycling number, the capacitance decreases gradually due to the electrochemical stability of the active material.

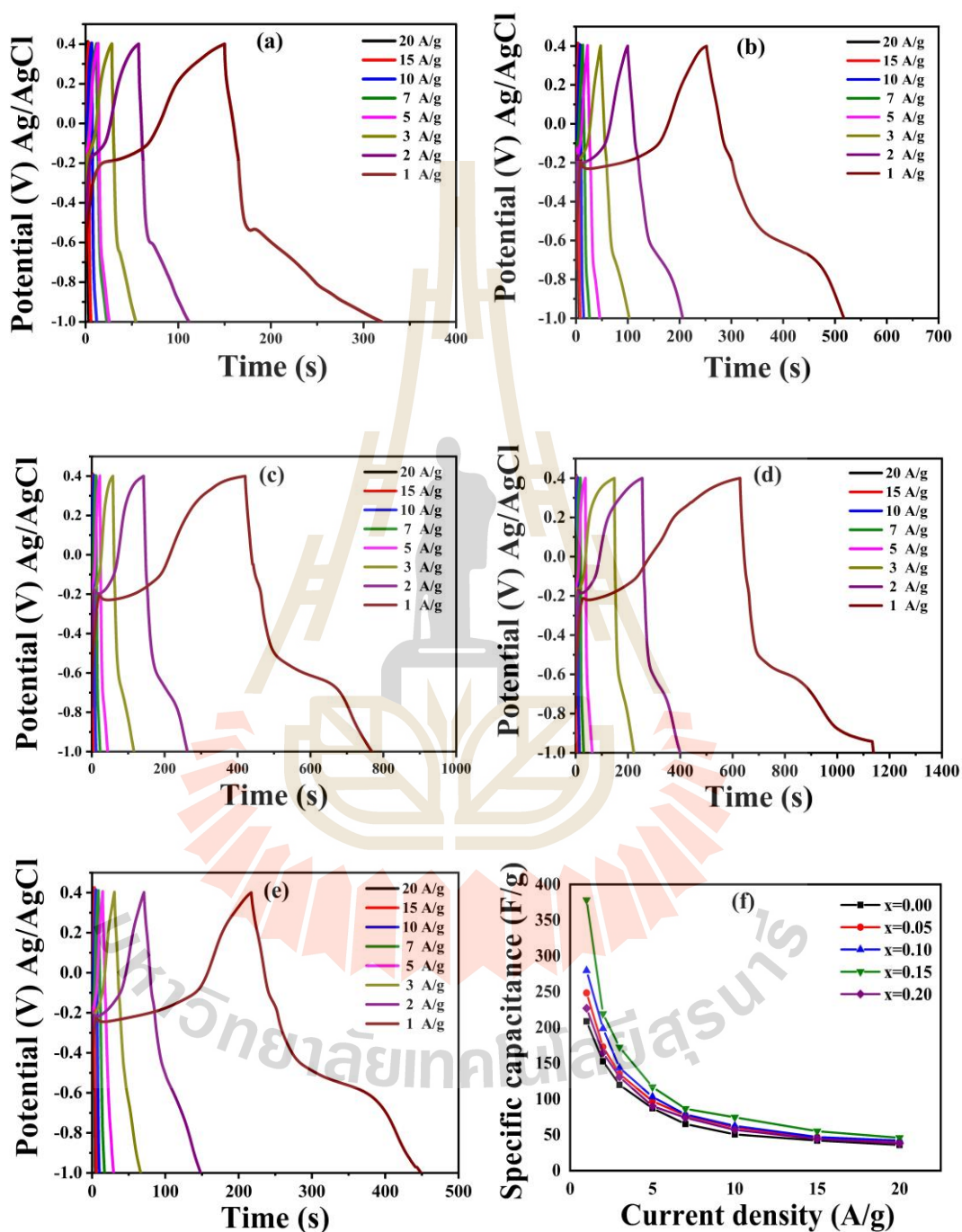


Figure 4.28 Galvanostatic charge-discharge curves at various current densities of $\text{Mn}_{1-x}\text{Ni}_x\text{Co}_2\text{O}_4$ nanoparticles: (a) $x = 0.00$, (b) $x = 0.05$, (c) $x = 0.10$, (d) $x = 0.15$, and (e) $x = 0.20$. (f) specific capacitance as a function of current density.

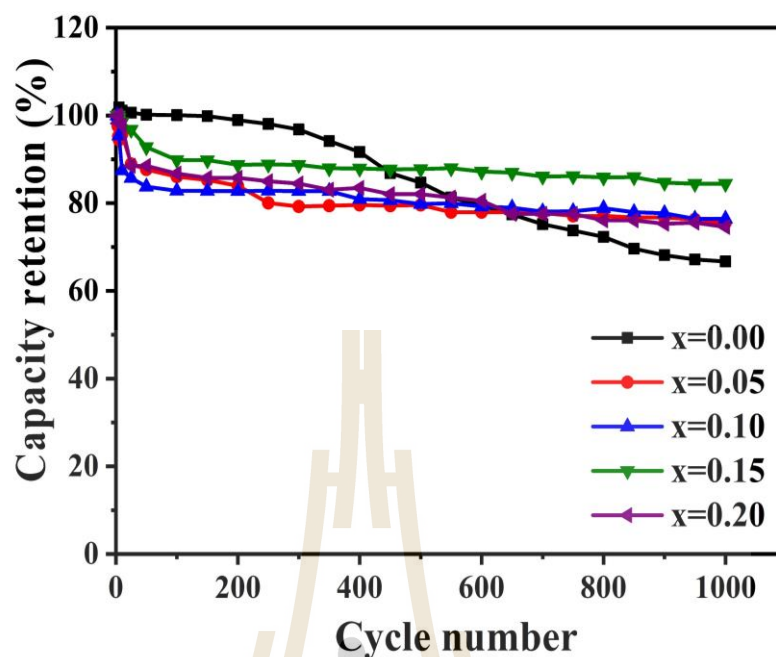


Figure 4.29 Capacity retention (%) of $\text{Mn}_{1-x}\text{Ni}_x\text{Co}_2\text{O}_4$ ($x = 0.00, 0.05, 0.10, 0.15,$ and 0.20) electrodes after 1000 cycles at a current density of 2 A/g.

4.2.2.3 Electrochemical impedance spectroscopy (EIS)

The Nyquist plots of $\text{Mn}_{1-x}\text{Ni}_x\text{Co}_2\text{O}_4$ ($x = 0.00, 0.05, 0.10, 0.15,$ and 0.20) electrodes carried out at frequency range from 0.1 Hz - 100 kHz with 10 mV (vs. SCE) was presented in Figure 4.30. The internal resistance (R_s) of the samples can be estimated from the intercept of the Nyquist plots on the real axis at high frequency (Li *et al.*, 2015; Kong *et al.*, 2014; Padmanathan and Selladurai, 2014). The internal resistance (R_s) values of the Ni-doped MnCo_2O_4 with $x = 0.00, 0.05, 0.10, 0.15,$ and 0.20 are 0.37, 0.36, 0.27, 0.22, and 0.38 Ω , respectively. Moreover, the slope of the line in the low frequency region gives the measure of Warburg impedance or diffusion resistance. The higher slope is observed in the sample $\text{Mn}_{0.85}\text{Ni}_{0.15}\text{Co}_2\text{O}_4$ leading to the easier for ions diffusion in solution and the adsorption of ions into the electrode surface indicating the better capacitive performance and the lower Warburg resistance

(electrolyte diffusion impedance). The faradaic charge transfer at the electrode/electrolyte interface associate with a small semicircle at high-frequency region (Padmanathan and Selladurai, 2014). The charge transfer resistance (R_{ct}) during the faradaic redox reaction process dependence with the electronic conductivity and surface area of the electrode material. The semicircle diameter at the high-frequency region of the Nyquist plot is employed to evaluate the R_{ct} . All of the samples have very low charge transfer resistance which confirms the high electrical conductivity of the electrode. The Ni-doped $MnCo_2O_4$ nanoparticles exhibit a good electrode performance owing to the highly mesoporous structure of the material with large surface area of the material, which results in. These results are in good agreement with the previously discussed CV and GCD methods.

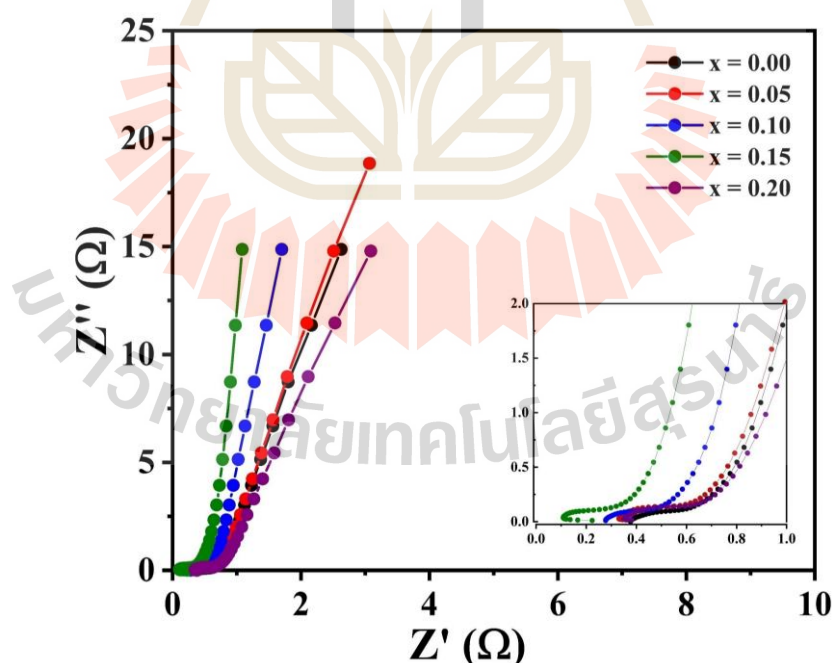


Figure 4.30 The Nyquist plot of $Mn_{1-x}Ni_xCo_2O_4$ ($x = 0.00, 0.05, 0.10, 0.15,$ and 0.20) electrodes.

4.3 Zn-doped MnCo₂O₄ nanoparticles

4.3.1 Structural and morphology characterization

4.3.1.1 X-ray diffraction (XRD) analysis of the Zn-doped MnCo₂O₄ nanoparticles

XRD patterns in Figure 4.31 show the polycrystallinity and phase information of cubic structure of the MnCo₂O₄ (JCPDS No. 23-127). Sharp peaks are obtained for (111), (220), (311) (222), (400), (422), (511), and (440) planes. All the peaks match well to the reported cubic spinel structure with space group Fd3m (227). No impurity phase was detected in all of the Zn-doped MnCo₂O₄ nanoparticles samples. The enhanced view of the major peak (311) at $2\theta \sim 36$ is presented in Figure 4.31(b), which is slightly shifted toward the lower angle upon Zn doping indicating that the lattice parameters of the unit cell are relatively expanded. The crystallite sizes of $x = 0.00, 0.05, 0.10, 0.15,$ and 0.20 are 22.3, 37.1, 42.8, 46.2 and 48.9 nm, respectively, according to the calculation of Scherrer equation. The lattice parameters of Mn_{1-x}Zn_xCo₂O₄ nanoparticles are 8.196, 8.237, 8.255, 8.259 and 8.268 Å for the $x = 0.00, x = 0.00, 0.05, 0.10, 0.15,$ and $0.20,$ respectively. The expansion of lattice parameters can be associated with the substitution of Zn²⁺ (0.74 Å) with a larger ionic radius in Mn³⁺ (0.72 Å) and Mn⁴⁺ (0.53 Å). The d -spacing values and the lattice constant, obtained from the XRD peak (311) position are summarized in Table 4.9.

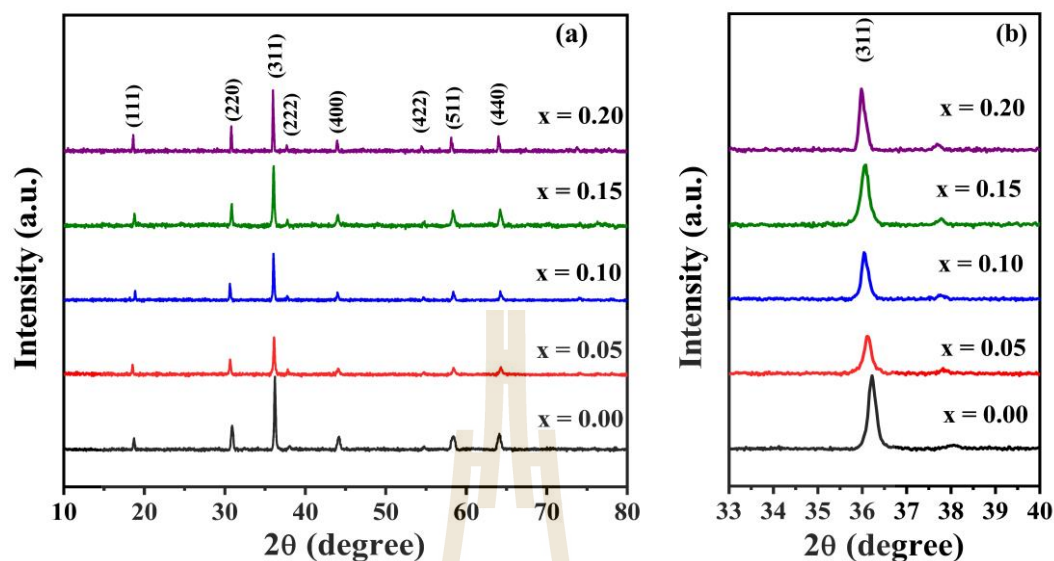


Figure 4.31 (a) XRD patterns of $\text{Mn}_{1-x}\text{Zn}_x\text{Co}_2\text{O}_4$ ($x = 0.00, 0.05, 0.10, 0.15,$ and 0.20) nanoparticles and (b) relative shift in (311) peak of MnCo_2O_4 with respect to Zn-doping.

Table 4.9 Summary of crystallite sizes (D) from XRD, d -spacing (d), and lattice constant (a) of $\text{Mn}_{1-x}\text{Zn}_x\text{Co}_2\text{O}_4$ ($x = 0.00, 0.05, 0.10, 0.15,$ and 0.20) nanoparticles.

samples	Crystallite sizes — d -spacing		Lattice constant
	D (nm)	d (Å)	
$x = 0.00$	22.3	2.471	8.196
$x = 0.05$	37.1	2.484	8.237
$x = 0.10$	42.8	2.489	8.255
$x = 0.15$	46.2	2.490	8.259
$x = 2.00$	48.9	2.493	8.268

4.3.1.2 The Morphology of the Zn-doped MnCo_2O_4 nanoparticles by FESEM and TEM

The SEM images of Zn-doped MnCo_2O_4 nanoparticles are shown in Figure 4.32. The severe agglomeration particles were observed in all the samples, resulting in that all the samples have large nano-sized particles (less than 800 nm). TEM images with corresponding selected-area electron diffraction (SAED) patterns and particle size distribution of Zn-doped MnCo_2O_4 nanoparticles are shown in Figure 4.32. The TEM image clearly elucidates the nanoparticles, which the average particles size of $\text{Mn}_{1-x}\text{Zn}_x\text{Co}_2\text{O}_4$ nanoparticles are about 103, 92, 83, 63, and 62 nm for the $x = 0.00, 0.05, 0.10, 0.15,$ and 0.20 , respectively. The Zn-doped MnCo_2O_4 nanoparticles are uniformly dispersed in the samples with Zn content of $x = 0.00, 0.05, 0.10,$ and 0.15 while the sample with $x = 0.20$ have severe agglomeration of particles. The variation of particle size can result in the difference of specific surface area and capacitance values, which will be discussed in electrochemical results. The SAED patterns of all the samples exhibit many diffraction spots on diffraction rings, indicating a polycrystalline property and the feature of the MnCo_2O_4 phase, which is accepted by the XRD results.

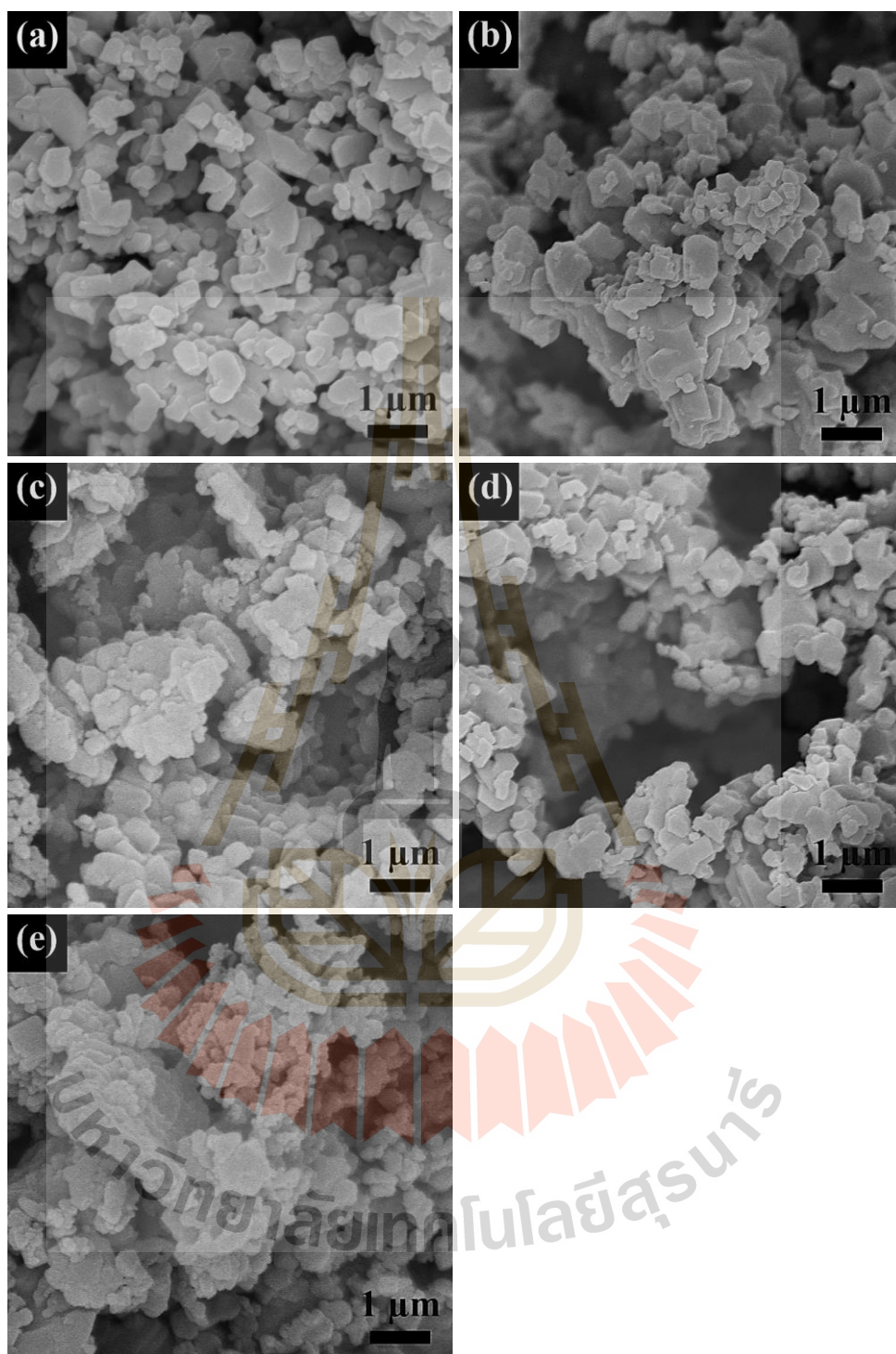


Figure 4.32 FESEM images of $\text{Mn}_{1-x}\text{Zn}_x\text{Co}_2\text{O}_4$ nanoparticles: (a) $x = 0.00$, (b) $x = 0.05$, (c) $x = 0.10$, (d) $x = 0.15$, and (e) $x = 0.20$.

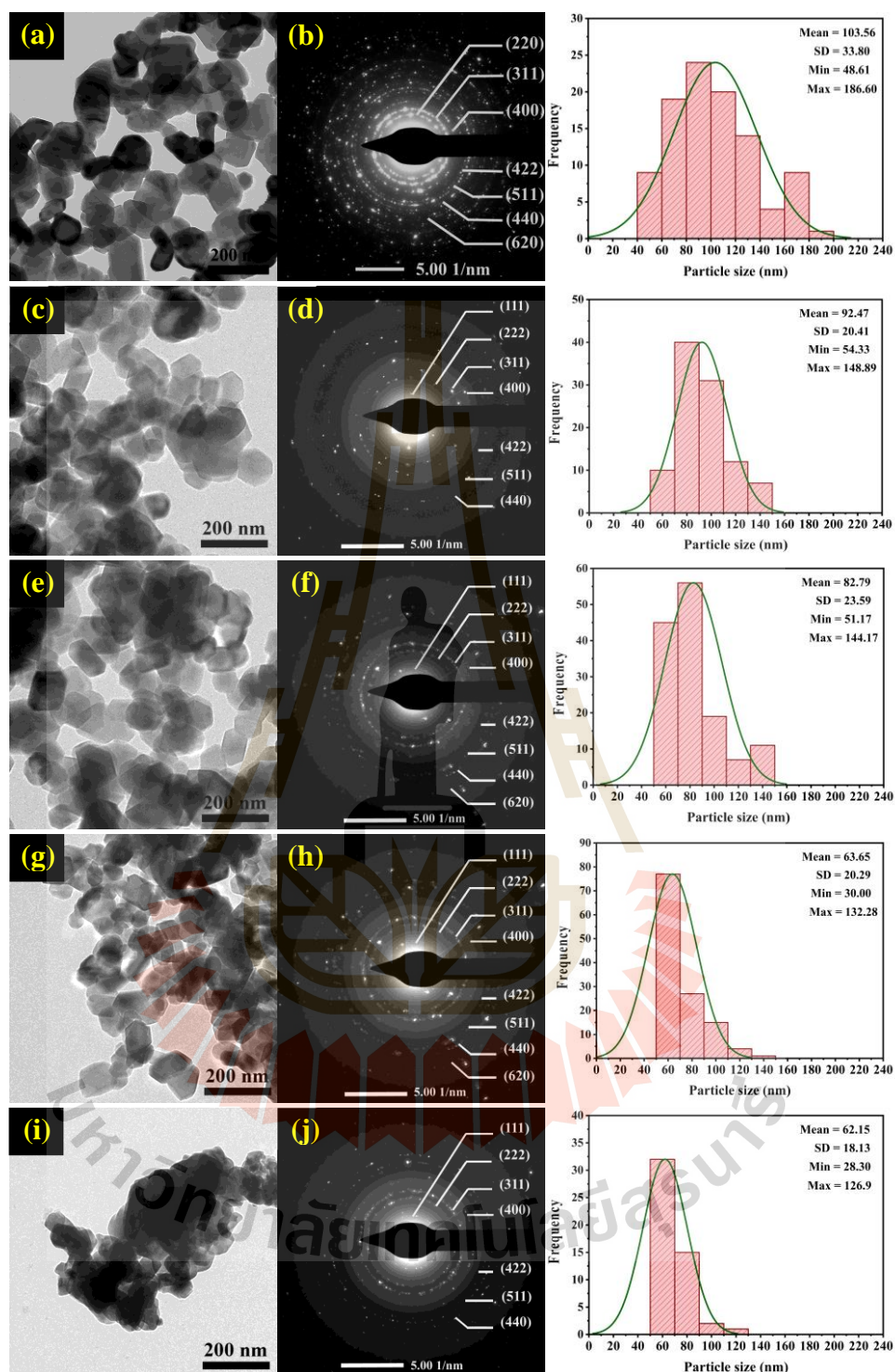


Figure 4.33 TEM images with corresponding SAED of $Mn_{1-x}Zn_xCo_2O_4$ nanoparticles:

(a,b) $x = 0.00$, (c,d) $x = 0.05$, (e,f) $x = 0.10$, (g,h) $x = 0.15$, and (i,j) $x = 0.20$.

4.3.1.3 X-ray absorption spectroscopy study of the Zn-doped MnCo₂O₄ nanoparticles

To confirm the oxidation states of the Mn, Co, and Zn atoms in the Zn-doped MnCo₂O₄ nanoparticles, we also performed X-ray absorption near-edge structure (XANES) analysis. The XANES spectra of Co atoms in the Zn-doped MnCo₂O₄ nanoparticles compared with the Co foil (Co⁰⁺), CoO (Co²⁺) and Co₃O₄ (Co^{2+/3+}) standards displays in Figure 4.34. The Co-edge position of all the samples arise between CoO (Co²⁺) and Co₂O₃ (Co^{2+/3+}) standards reflecting to the combination oxidation state of Co^{2+/3+} (as shown in the inset of Figure 4.34). Figure 4.35 shows the Mn K-edge XANES spectra of Zn-doped MnCo₂O₄ nanoparticles as compared with the Mn foil (Mn⁰⁺), Mn₂O₃ (Mn³⁺), and MnO₂ (Mn⁴⁺) standards. The Mn-edge position of all the samples occur between Mn₂O₃ (Mn³⁺) and MnO₂ (Mn⁴⁺) standards corresponding to the combining oxidations state of Mn^{3+/4+}. The Zn K-edge XANES spectra of Zn-doped MnCo₂O₄ nanoparticles as compared with the Zn foil (Zn⁰⁺) and ZnO (Zn²⁺) standards is illustrated in Figure 4.36. The close resemblance between the Zn K-edge XANES spectrum of Mn_{1-x}Zn_xCo₂O₄ nanoparticles and ZnO standards compound indicates that the zinc ions in all samples have oxidation state of Zn²⁺. Alternatively, the oxidation state of Co, Mn, and Zn can be confirmed by the edge energy as presented in the Table 4.10.

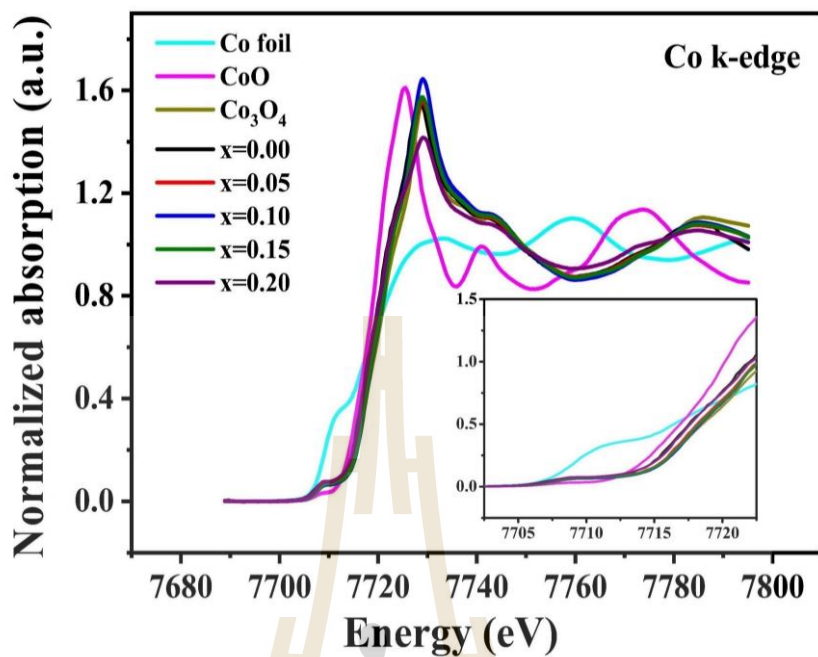


Figure 4.34 Normalized XANES spectra and of $\text{Mn}_{1-x}\text{Zn}_x\text{Co}_2\text{O}_4$ ($x = 0.00, 0.05, 0.10, 0.15,$ and 0.20) nanoparticles at Co K-edge.

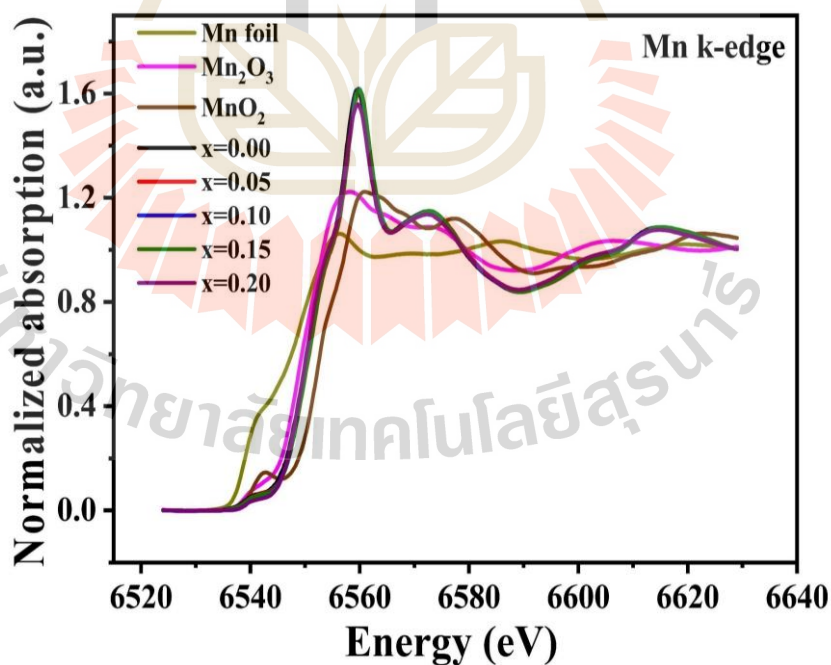


Figure 4.35 Normalized XANES spectra and of $\text{Mn}_{1-x}\text{Zn}_x\text{Co}_2\text{O}_4$ ($x = 0.00, 0.05, 0.10, 0.15,$ and 0.20) nanoparticles at Mn K-edge.

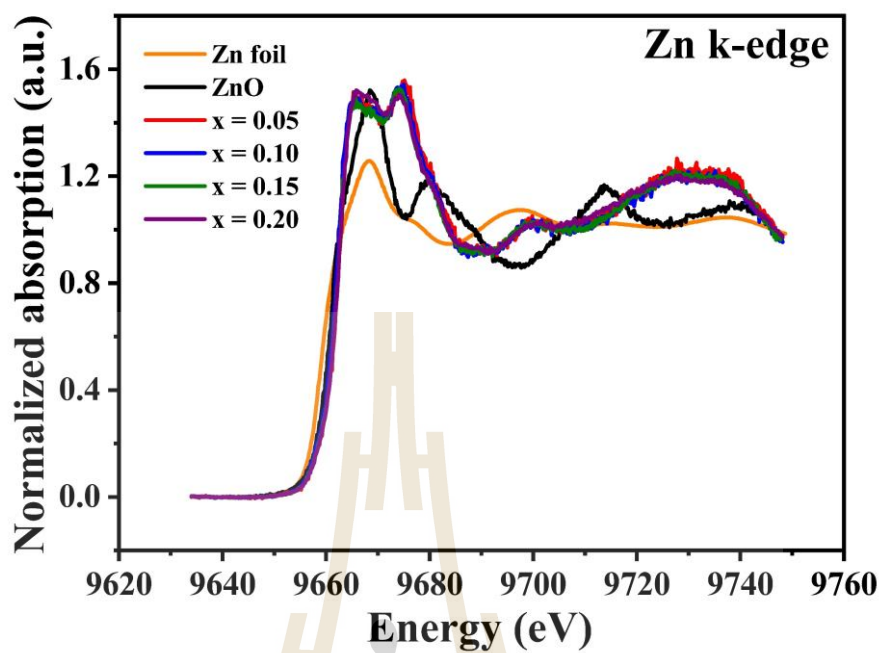


Figure 4.36 Normalized XANES spectra and of $\text{Mn}_{1-x}\text{Zn}_x\text{Co}_2\text{O}_4$ ($x = 0.00, 0.05, 0.10, 0.15,$ and 0.20) nanoparticles at Zn K-edge.

Table 4.10 Edge energy and oxidation state of the standard samples and $Mn_{1-x}Zn_xCo_2O_4$ ($x = 0.00, 0.05, 0.10, 0.15,$ and 0.20) nanoparticles.

Samples	Edge element	Absorption Edge (eV)	Oxidation state
CoO	Co	7716.30	+2
Co ₃ O ₄	Co	7721.45	+2, +3
Mn ₂ O ₃	Mn	6548.61	+3
MnO ₂	Mn	6552.07	+4
ZnO	Zn	9661.03	+2
x = 0.00	Co	7719.37	+2, +3
	Mn	6550.13	+3, +4
x = 0.05	Co	7719.80	+2, +3
	Mn	6549.98	+3, +4
	Zn	9661.16	+2
x = 0.10	Co	7719.37	+2, +3
	Mn	6549.93	+3, +4
	Zn	9661.16	+2
x = 0.15	Co	7719.37	+2, +3
	Mn	6550.07	+3, +4
	Zn	9661.16	+2
x = 0.20	Co	7719.37	+2, +3
	Mn	6549.68	+3, +4
	Zn	9661.16	+2

4.3.1.4 X-ray photoelectron spectroscopy (XPS) study of the Zn-doped MnCo₂O₄ nanoparticles

To investigate the valence state and surface chemical composition of the Co, Mn, Zn and O atoms in the Zn-doped MnCo₂O₄ nanoparticles, X-ray photoelectron spectroscopy (XPS) analysis was performed. Figure 4.37 displays the XPS survey spectrum, which confirm the existence of Zn, Mn, Co and O elements within the Zn-doped MnCo₂O₄ nanoparticles. The Co 2p spectra the Zn-doped MnCo₂O₄ nanoparticles are given in Figure 4.38. By a Gaussian fitting method, the Co 2p spectra of all the samples can be well-fitted with two spin-orbit doublets and 4 shakeup satellites (denoted as “Sat.”), assigned to the presence of Co²⁺/Co³⁺. The binding energies of Co³⁺ are located at ~780 eV and ~795 eV and the peaks at the binding energies of ~782 eV and ~798 eV are ascribed to Co²⁺, according to the literature (Pettong *et al.*, 2016; Wu *et al.*, 2015; Wang *et al.*, 2015) with good agreement with the XAS result. The Mn 2p spectrum of all the samples is represented by the Mn 2p_{3/2} and Mn 2p_{1/2} spin-orbital doublet, which a spin-orbital splitting is ~11.8 eV as shown in Figure 4.39. At the Mn 2p_{3/2} peak, each of the spectra consists of two components with binding energy values of 641.7-642.2 eV and 644.0-644.8 eV corresponding to the characteristic peaks of Mn³⁺ and Mn⁴⁺, respectively, which is well agreeable with the XAS result. The Zn 2p XPS spectra of all the samples exhibit major peaks with binding energy of 1021.4-1022.1 eV (Zn 2p_{3/2}) and 1044.4-1044.9 eV (Zn 2p_{1/2}), indicating that Zn²⁺ is existing in all the Zn-doped MnCo₂O₄ samples as presented in Figure 4.40. Figure 4.41 shows the high-resolution O 1s XPS spectra for Zn-doped MnCo₂O₄ nanoparticles. It reveals that the O 1s spectra of all the samples can be fitted into three components at 530, 532, and 533 eV, which are related to the metal–oxygen bonds, the

oxygen in OH^- groups and the oxygen atom of the adsorbed water molecules, respectively.

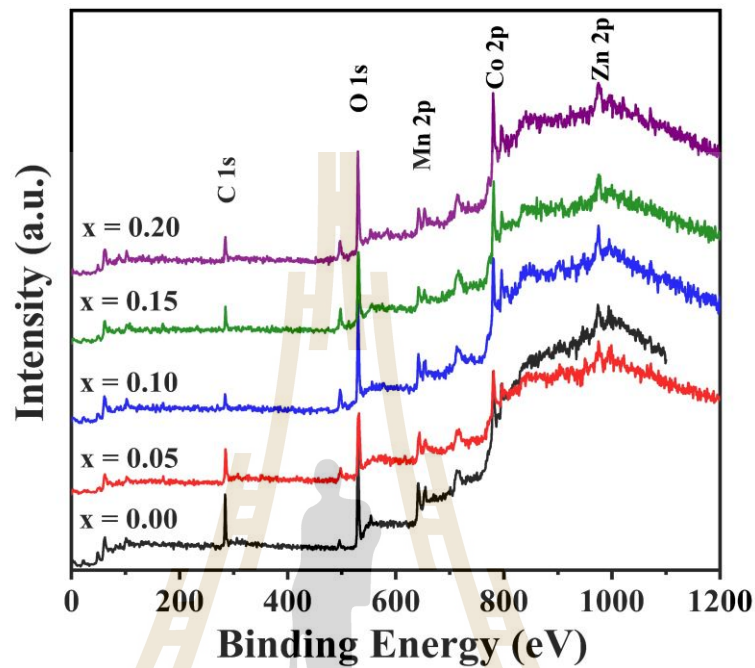


Figure 4.37 XPS survey spectrum of the $\text{Mn}_{1-x}\text{Zn}_x\text{Co}_2\text{O}_4$ ($x = 0.00, 0.05, 0.10, 0.15,$ and 0.20) nanoparticles.



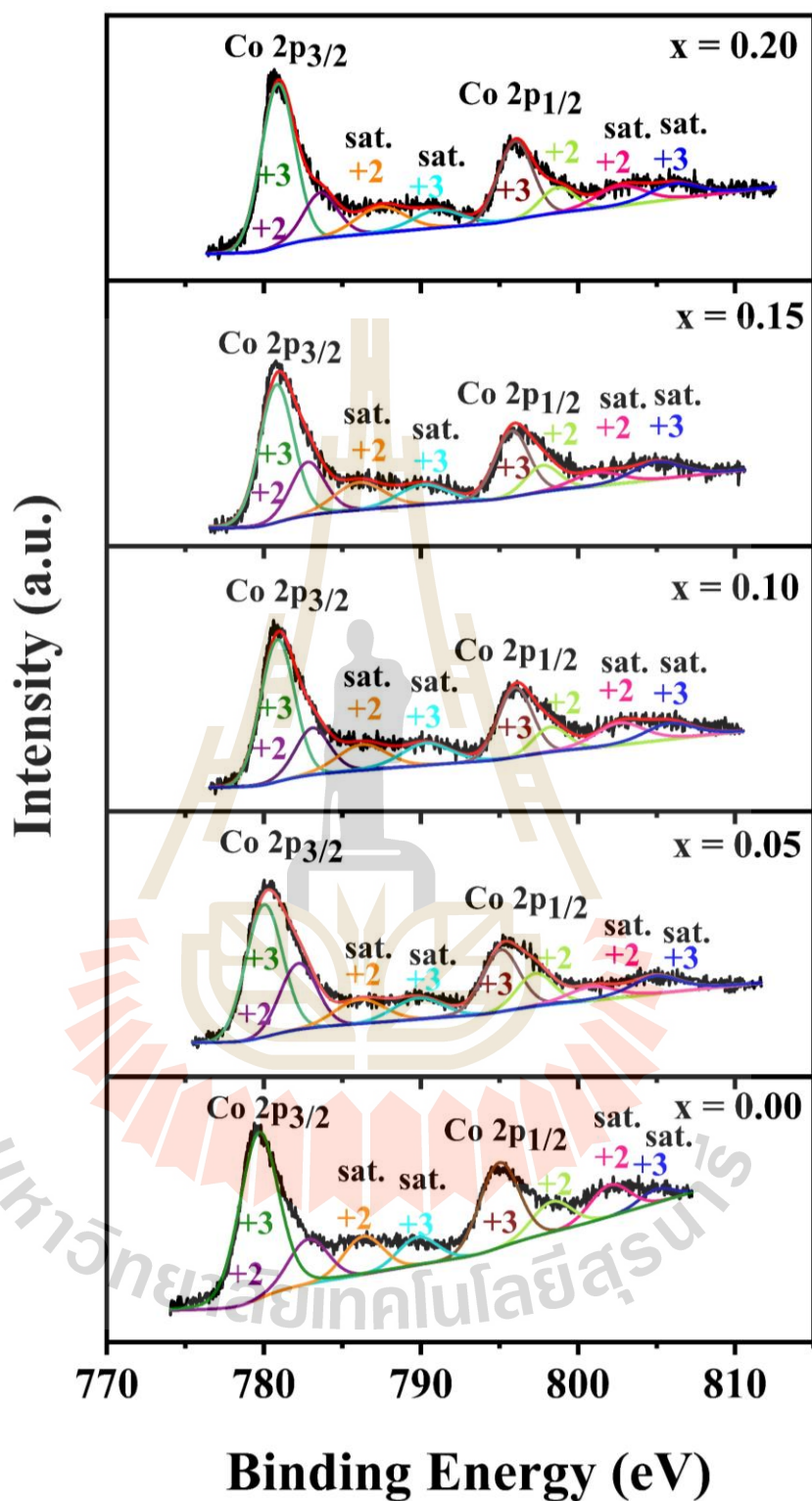


Figure 4.38 XPS spectra at Co 2p of the $\text{Mn}_{1-x}\text{Zn}_x\text{Co}_2\text{O}_4$ ($x = 0.00, 0.05, 0.10, 0.15,$ and 0.20) nanoparticles.

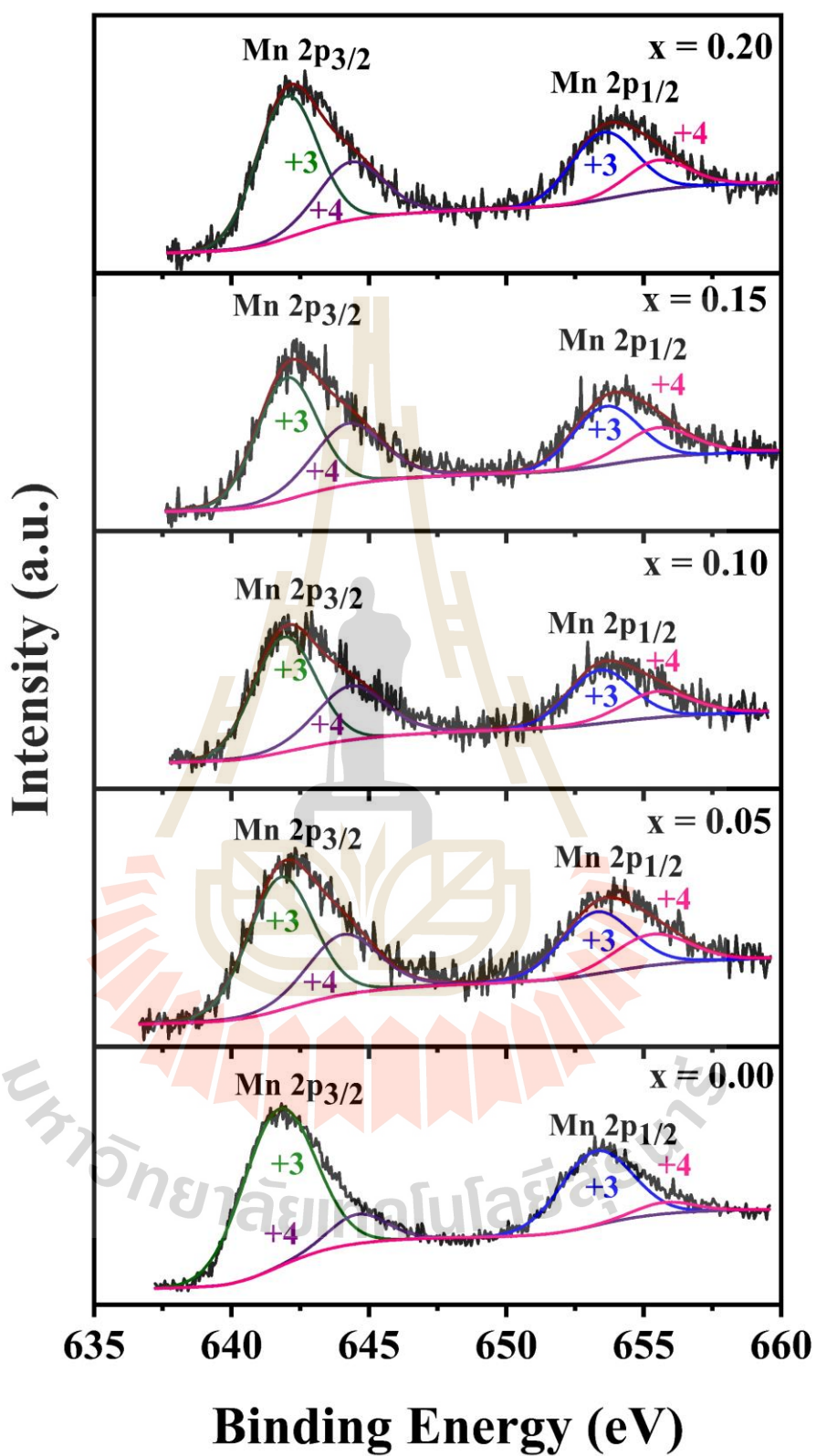


Figure 4.39 XPS spectra at Mn 2p of the $\text{Mn}_{1-x}\text{Zn}_x\text{Co}_2\text{O}_4$ ($x = 0.00, 0.05, 0.10, 0.15,$ and 0.20) nanoparticles.

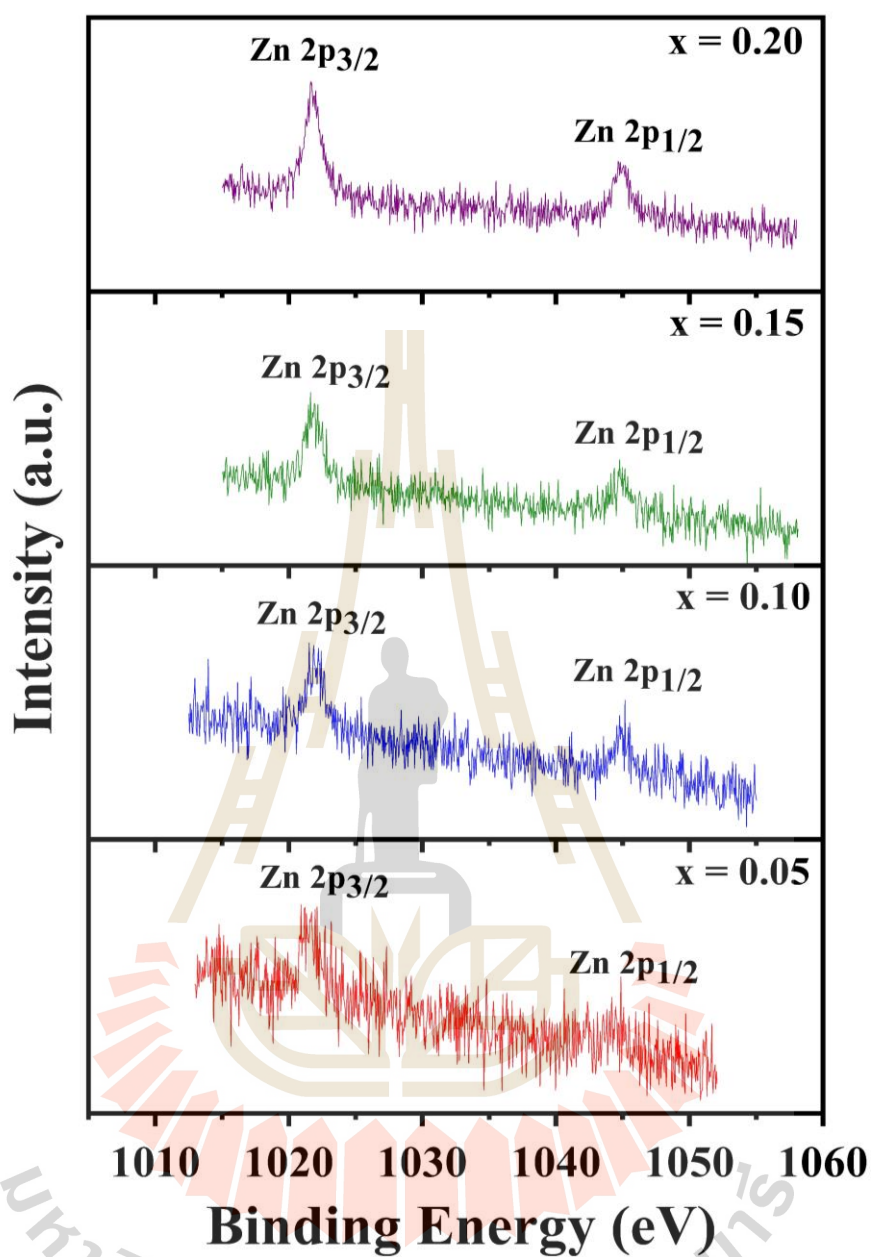


Figure 4.40 XPS spectra at Zn 2p of the $\text{Mn}_{1-x}\text{Zn}_x\text{Co}_2\text{O}_4$ ($x = 0.05, 0.10, 0.15,$ and 0.20) nanoparticles.

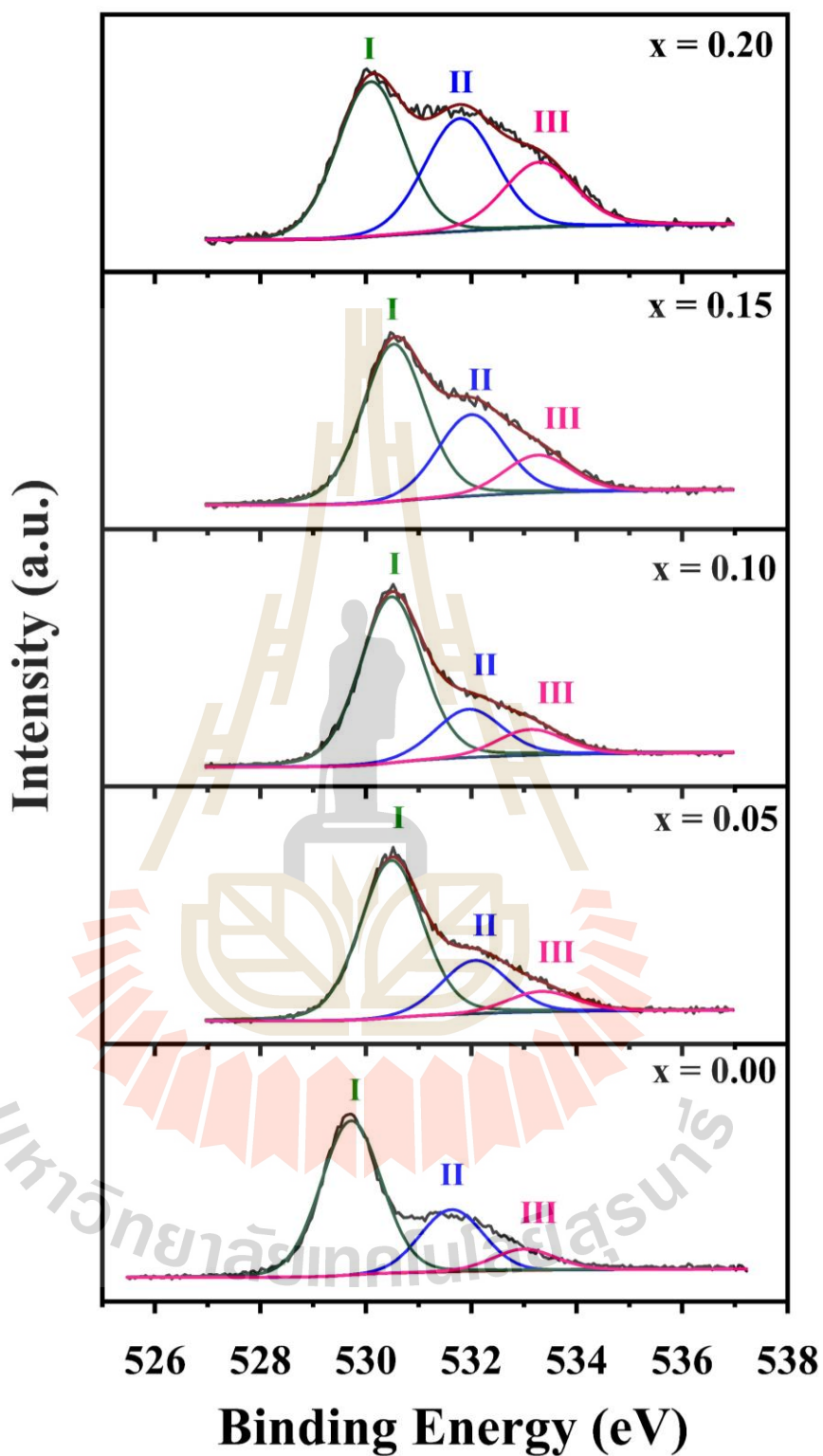


Figure 4.41 XPS spectra at O1s of the $\text{Mn}_{1-x}\text{Zn}_x\text{Co}_2\text{O}_4$ ($x = 0.00, 0.05, 0.10, 0.15,$ and 0.20) nanoparticles.

Table 4.11 XPS data of the $Mn_{1-x}Zn_xCo_2O_4$ ($x = 0.00, 0.05, 0.10, 0.15,$ and 0.20) nanoparticles.

Samples	Binding energy position (eV)									
	Co 2p _{3/2}		Co 2p _{1/2}		Mn 2p _{3/2}		Mn 2p _{1/2}		Zn 2p _{3/2}	Zn 2p _{1/2}
	Co ²⁺	Co ³⁺	Co ²⁺	Co ³⁺	Mn ³⁺	Mn ⁴⁺	Mn ³⁺	Mn ⁴⁺	Zn ²⁺	Zn ²⁺
x = 0.00	782.83	779.69	798.34	794.98	641.73	644.60	653.26	655.77		
x = 0.05	782.83	780.62	798.10	795.72	641.79	644.06	653.27	655.30	1021.49	1044.46
x = 0.10	783.09	780.86	798.24	796.00	642.25	644.89	653.72	656.04	1022.15	1044.97
x = 0.15	782.80	780.80	797.74	795.79	642.01	644.24	653.61	655.50	1021.80	1044.91
x = 0.12	783.61	780.90	798.71	796.0	642.01	644.34	653.53	655.50	1021.78	1044.91

มหาวิทยาลัยเทคโนโลยีสุรนารี

4.3.1.5 Characterization of surface area and pore size distribution of the Zn-doped MnCo₂O₄ nanoparticles by BET method and BJH method

The N₂ adsorption-desorption isotherm of Zn-doped MnCo₂O₄ nanoparticles are depicted in Figure 4.42(a-e). The resulting nitrogen adsorption/desorption isotherms of all the samples exhibits a typical IV isotherm with H3 hysteresis loop, suggesting that there is a mesoporous structure to the sample. The pore size distribution of all the samples are shown in the inset of Figure 4.42(a-e), that the pore size distribution of the Zn-doped MnCo₂O₄ nanoparticles are in the range of 2-40 nm. This result indicates the mesoporous feature of the Zn-doped MnCo₂O₄ nanoparticles. The Brunauer–Emmett–Teller (BET) specific surface area, total pore volume, and Mean pore diameter are summarized in Table 4.12. The increase in BET surface area values with increasing the doping Zn concentration of $x = 0.00$ to $x = 0.15$ was also associated with decreasing particle size. However, the BET surface area values decrease in the samples with Zn content $x = 0.20$ with the smallest particle size, which may be due to severe agglomeration of particles in this sample. The Mn_{1-x}Zn_xCo₂O₄ with $x = 0.15$ shows a relatively high BET surface area of 85.30 m²/g and a total pore volume of 0.214 cm³/g. It is common knowledge that more active sites for the electrolyte-ion insertion/extraction into the electrode material can be given by a large surface area. In addition, the larger pore volume results in that easy diffusion of electrolyte-ion to active material with less resistance (Cai *et al.*, 2014).

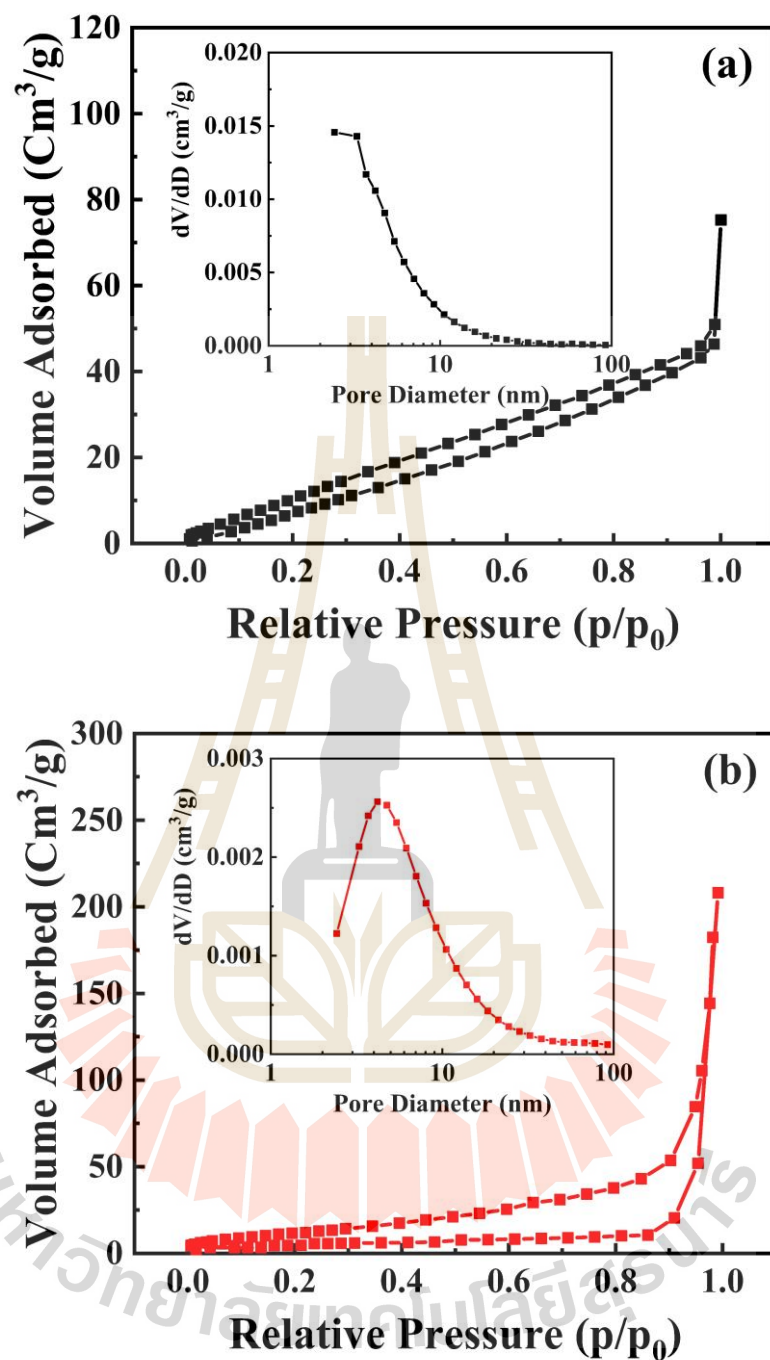


Figure 4.42 Nitrogen adsorption/desorption isotherms and pore size distribution (inset) of $\text{Mn}_{1-x}\text{Zn}_x\text{Co}_2\text{O}_4$ ($x = 0.00, 0.05, 0.10, 0.15,$ and 0.20) nanoparticles.

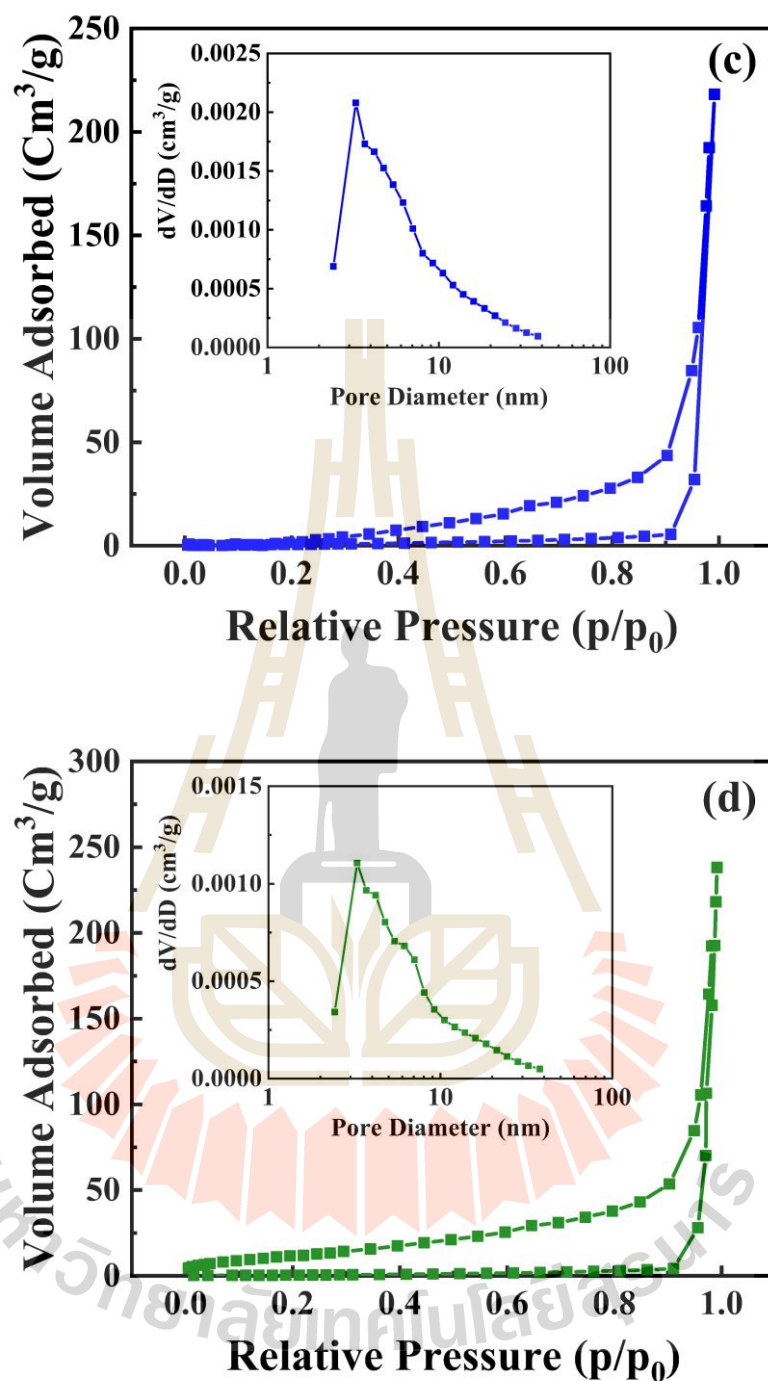


Figure 4.42 (Continued) Nitrogen adsorption/desorption isotherms and pore size distribution (inset) of $\text{Mn}_{1-x}\text{Zn}_x\text{Co}_2\text{O}_4$ ($x = 0.00, 0.05, 0.10, 0.15, \text{ and } 0.20$) nanoparticles.

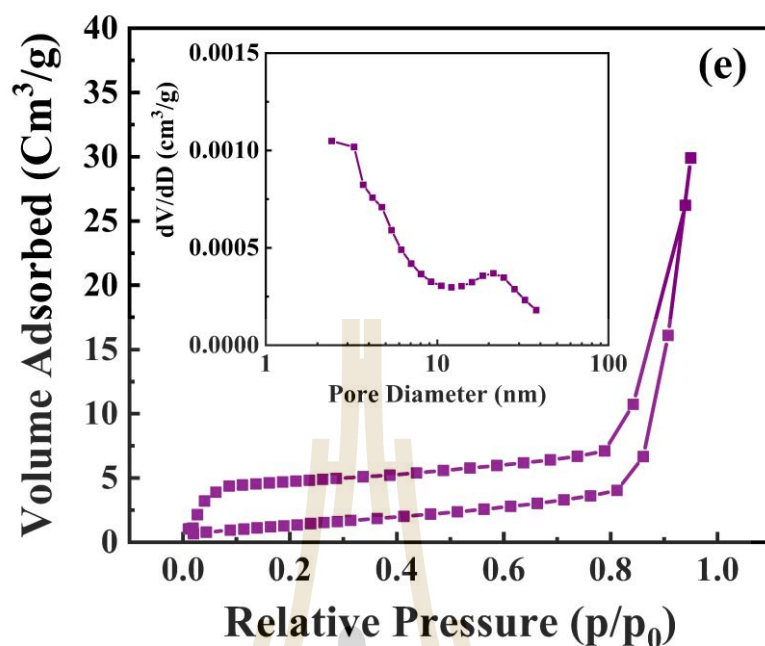


Figure 4.42 (Continued) Nitrogen adsorption/desorption isotherms and pore size distribution (inset) of $\text{Mn}_{1-x}\text{Zn}_x\text{Co}_2\text{O}_4$ ($x = 0.00, 0.05, 0.10, 0.15,$ and 0.20) nanoparticles.

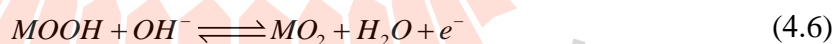
Table 4.12 Physical properties of spinel $\text{Mn}_{1-x}\text{Zn}_x\text{Co}_2\text{O}_4$ ($x = 0.00, 0.05, 0.10, 0.15,$ and 0.20) nanoparticles.

Samples	BET specific surface area (m^2/g)	Total pore volume (cm^3/g)	Mean pore diameter (nm)
$x = 0.00$	71.92	0.079	4.39
$x = 0.05$	73.42	0.080	4.35
$x = 0.10$	76.81	0.083	4.32
$x = 0.15$	85.30	0.085	3.98
$x = 0.20$	72.75	0.079	4.34

4.3.2 Electrochemical properties

4.3.2.1 Cyclic voltammetry measurement

Three-electrode system was used to investigate the electrochemical performance of $Mn_{1-x}Zn_xCo_2O_4$ ($x = 0.00, 0.05, 0.10, 0.15, \text{ and } 0.20$) electrodes. The scan rates at 2, 5, 10, 30, 60, 100, 200, and 300 mV/s and the voltage range from -0.1 V to 0.4 V to measure the cyclic voltammogram (CV) curves of in the 6 M KOH electrolyte, as shown in Figure 4.43(a-e). The redox peaks in the CV curve are related to the faradaic redox reactions, which indicate the feature pseudocapacitive of the as-prepared electrode materials. With the increasing scan rate, the potential of anodic and cathodic peaks shifts toward to the positive and negative potential, respectively, revealing the fast redox reactions for electrochemical energy storage (Wang *et al.*, 2015). According to the literature, the redox reactions in the KOH electrolyte are given by equations 4.5 and 4.6 (Li *et al.*, 2014; Bai *et al.*, 2016; Hao *et al.*, 2015; Tamboli *et al.*, 2017).



where M is indicative of Co or Mn and Zn.

The area of CV curve of the $Mn_{1-x}Zn_xCo_2O_4$ where $x = 0.15$ electrode is largest compared with the other electrodes, suggesting that the calculated specific capacitance value from the CV curves is highest.

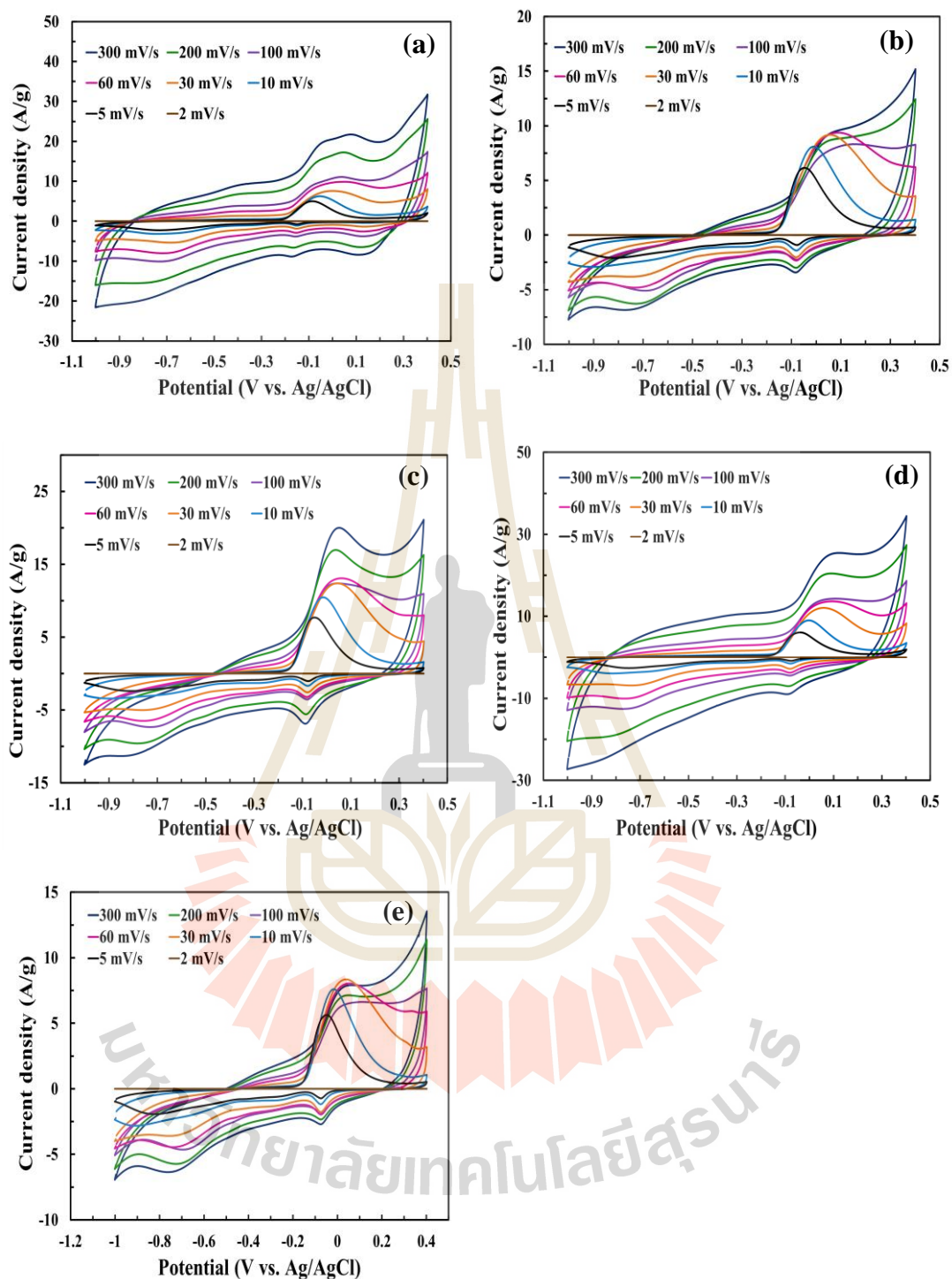


Figure 4.43 CV curves at various scan rates of $\text{Mn}_{1-x}\text{Zn}_x\text{Co}_2\text{O}_4$ nanoparticles: (a) $x = 0.00$, (b) $x = 0.05$, (c) $x = 0.10$, (d) $x = 0.15$, and (e) $x = 0.20$.

4.3.2.2 Galvanostatic charge-discharge measurements

Galvanostatic charge–discharge tests were conducted in 6 M KOH in a voltage range of -1.0–0.4 V with current densities ranging from 1 to 20 A/g, to investigate the electrochemical performances of $\text{Mn}_{1-x}\text{Zn}_x\text{Co}_2\text{O}_4$ ($x = 0.00, 0.05, 0.10, 0.15,$ and 0.20) electrodes. As is shown in Figure 4.44(a-e), not a straight line in the charge–discharge curves suggests the typical pseudocapacitive characteristics, which is in good agreement with the CV curves. Additionally, the $\text{Mn}_{1-x}\text{Zn}_x\text{Co}_2\text{O}_4$ with $x = 0.15$ electrode demonstrates longer discharging time than that of other electrodes. It means that the $\text{Mn}_{1-x}\text{Zn}_x\text{Co}_2\text{O}_4$ with $x = 0.15$ electrode exhibits higher specific capacitance values than other electrodes. The specific capacitance was calculated from the discharge curves, as presented in Figure 4.44(f). At the current density 1 A/g, the specific capacitance values are 208, 222, 244, 264, and 218 F/g for the electrodes with Zn content of $x = 0.00, 0.05, 0.10, 0.15,$ and $0.20,$ respectively. The highest specific surface area of $\text{Mn}_{1-x}\text{Zn}_x\text{Co}_2\text{O}$ with $x = 0.15$ can be resulted in the highest specific capacitance because of more active sites for providing multiple redox reactions.

To investigate the cycling stability of the $\text{Mn}_{1-x}\text{Zn}_x\text{Co}_2\text{O}$ ($x = 0.00, 0.05, 0.10, 0.15,$ and 0.20) electrodes, the charge-discharge measurements of 1000 cycles were carried out at the current density of 2 A/g with the voltage range of -1.0-0.4 V as shown in Figure 4.45. The results show that the initial specific capacitance of $\text{Mn}_{0.85}\text{Zn}_{0.15}\text{Co}_2\text{O}$ electrodes was 204 F/g, with a capacity retention ratio of 85% after 1000 cycles, performing better than the electrodes with Zn content $x = 0.00$ (187 F/g ; 73%), $x = 0.05$ (164 F/g ; 78%), $x = 0.10$ (184 F/g ; 81%), and $x = 0.20$ (154 F/g ; 77%).

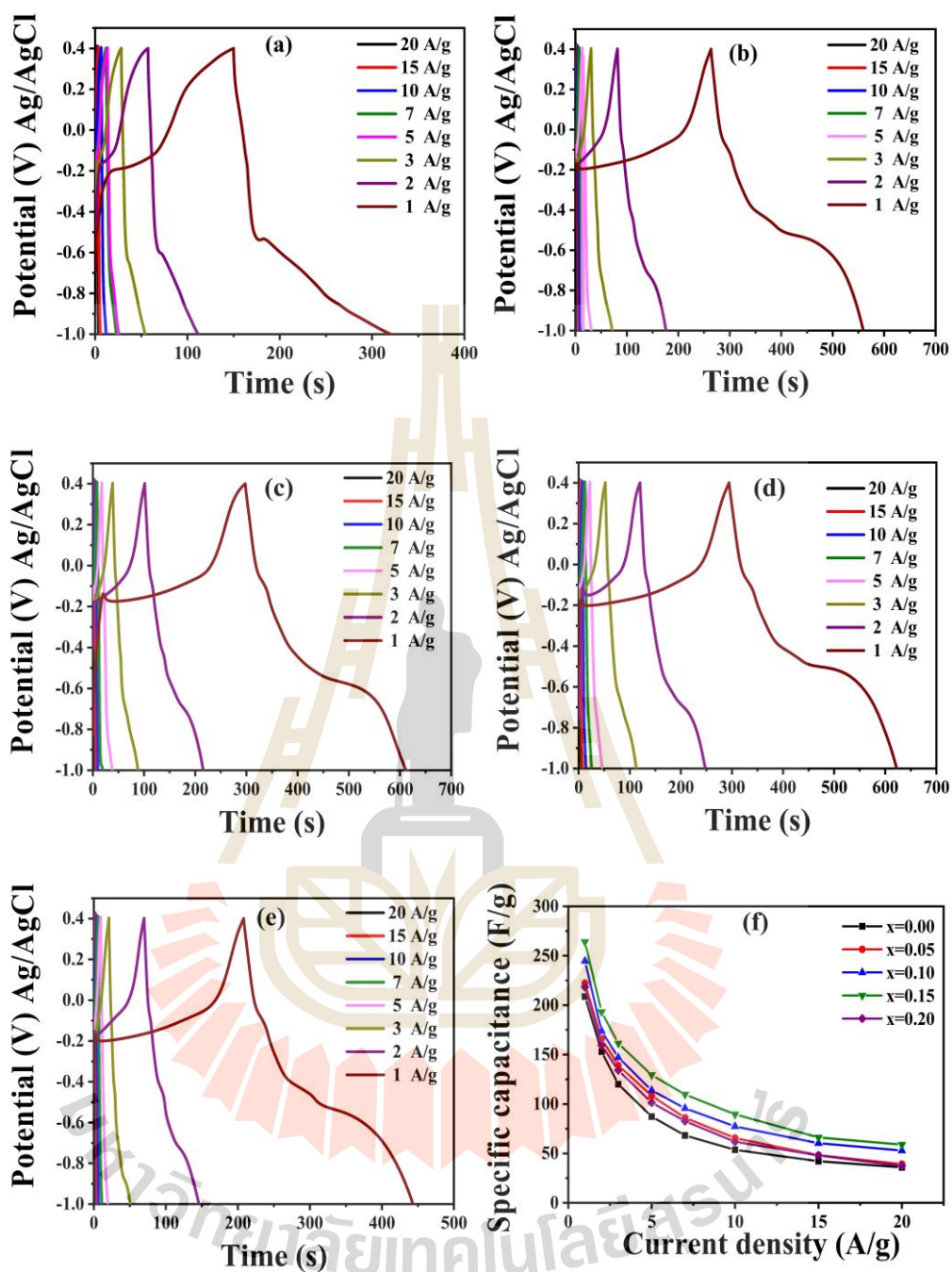


Figure 4.44 Galvanostatic charge-discharge curves at various current densities of $\text{Mn}_{1-x}\text{Zn}_x\text{Co}_2\text{O}_4$ nanoparticles: (a) $x = 0.00$, (b) $x = 0.05$, (c) $x = 0.10$, (d) $x = 0.15$, and (e) $x = 0.20$.

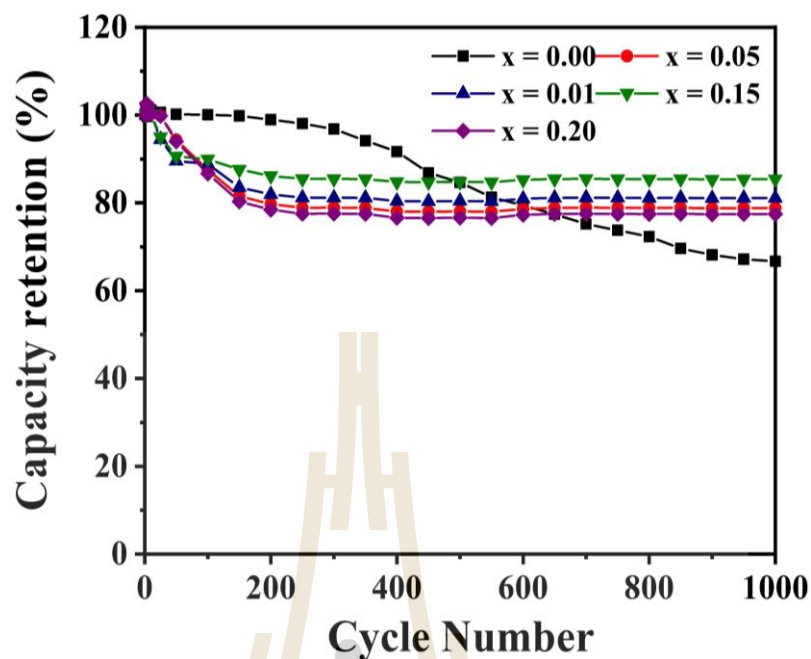


Figure 4.45 Capacity retention (%) of $\text{Mn}_{1-x}\text{Zn}_x\text{Co}_2\text{O}_4$ ($x = 0.00, 0.05, 0.10, 0.15,$ and 0.20) electrodes after 1000 cycles at a current density of 2 A/g .

4.3.2.3 Electrochemical impedance spectroscopy (EIS)

As shown in Figure 4.46, the Nyquist plots of $\text{Mn}_{1-x}\text{Ni}_x\text{Co}_2\text{O}_4$ ($x = 0.00, 0.05, 0.10, 0.15,$ and 0.20) electrodes were measured at frequency range from 0.1 Hz - 100 kHz . The Nyquist plots of Zn-doped MnCo_2O_4 consist of the semicircle at high-frequency and followed by the spike at low-frequency. The intersection on a real axis of the Nyquist plot refers to the solution resistance (R_s) as shown in the inset of Figure 4.46. The Zn-doped MnCo_2O_4 with $x = 0.00, 0.05, 0.10, 0.15,$ and 0.20 have the internal resistance (R_s) values of $0.37, 0.36, 0.31, 0.28,$ and 0.39Ω , respectively. In the low-frequency region, the slope vertical line corresponds to the Warburg impedance that the sample of $\text{Mn}_{0.85}\text{Zn}_{0.15}\text{Co}_2\text{O}_4$ exhibits the lowest Warburg impedance. From this observation, it can be concluded that the $\text{Mn}_{0.85}\text{Zn}_{0.15}\text{Co}_2\text{O}_4$ electrode provides high

electrical conductivity leading to the electrochemical redox process effectively.

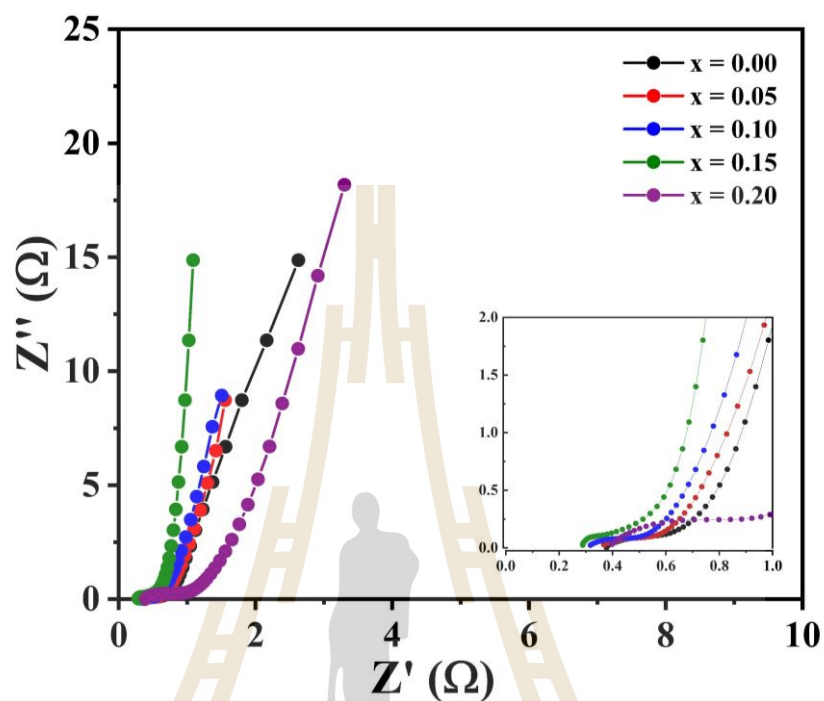


Figure 4.46 The Nyquist plots of the Mn_{1-x}Zn_xCo₂O₄ (x = 0.00, 0.05, 0.10, 0.15, and 0.20) NPs electrodes.

4.4 MnCo₂O₄ nanofibers

4.4.1 Structural and morphology characterization

4.4.1.1 X-ray diffraction (XRD) analysis of the MnCo₂O₄ nanofibers

The phase identification of the fabricated nanofibers was investigated by XRD technique. Figure 4.47 presents the XRD patterns of the fabricated MnCo₂O₄ nanofibers which were fabricated by using the electrospinning technique. It reveals that the XRD peaks patterns of (111), (220), (311), (222), (400), (422), (511), and (440) planes were well matched with Fd3m space group (JCPDS No. 23-1237, $a = b = c = 8.269 \text{ \AA}$) and it can be attributed to the MnCo₂O₄ spinel. No extra/impurity phase was observed in all MnCo₂O₄ nanofibers samples. This confirms the purity of the fabricated nanofibers which is verified by SAED studies. The d -spacing values of the MnCo₂O₄ phase for the crystalline planes (311) can be determined using Bragg's law as equation (3.1). The results show that the d -spacing values are 2.475, 2.461, and 2.460 \AA at calcination temperatures of 700, 800, and 900 $^{\circ}\text{C}$, respectively. It is evident that the d -spacing values are lower than the standard value ($d_s = 2.480 \text{ \AA}$) of a cubic MnCo₂O₄ (JCPDS No. 23-127). Spinel-type crystal structure with a lattice parameter of 8.210, 8.163 and 8.158 \AA for (311) peak is obtained for the MnCo₂O₄ nanofibers calcined at 700, 800, and 900 $^{\circ}\text{C}$. The full width at half maximum (FWHM) of (311) peak was used to calculate the mean crystallite sizes of samples by Scherrer formula. The crystallite sizes of MnCo₂O₄ are 60.0, 52.5, and 42.0 nm after calcination of the samples at 700, 800, and 900 $^{\circ}\text{C}$, respectively, as summarized in Table 4.13.

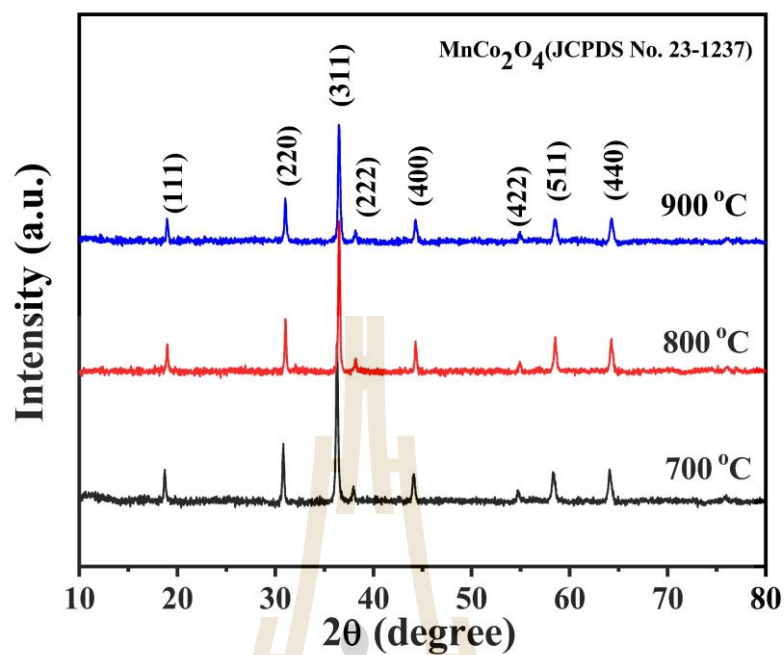


Figure 4.47 XRD patterns of precursor and MnCo_2O_4 nanofibers calcined for 3 h in atmosphere at different calcined temperatures.

Table 4.13 Summary of crystallite sizes (D) from XRD, d -spacing (d), and lattice constant (a) of MnCo_2O_4 nanofibers at different calcined temperatures.

MnCo_2O_4 samples	Crystallite sizes	d -spacing	Lattice constant
	D (nm)	d (Å)	a (nm)
700 °C	60.0	2.475	8.210
800 °C	52.5	2.461	8.163
900 °C	42.0	2.460	8.158

4.4.1.2 The Morphology of the MnCo₂O₄ nanofibers by FESEM and TEM

The morphology and structures of the MnCo₂O₄ nanofibers were examined by FESEM and TEM technique. As Figure 4.48, it is evident that the as-spun fibers with the average diameter of 668 nm had smooth surfaces due to the amorphous nature of the as-electrospun PAN/MnCo₂O₄ fibers. Typical SEM images of MnCo₂O₄ nanofibers calcinated at 700, 800, and 900 °C are shown in Figure 4.48. The PAN was selectively removed by calcinating the as-spun nanofibers at 700, 800, and 900 °C. The average diameters of the nanofibers decreased to 312, 344, and 354 nm for the samples calcinated at 700, 800, and 900 °C, respectively which might be attributed to the losing of PAN from the nanofibers and the crystallization of the MnCo₂O₄ spinel. In addition, the EDS spectra (Figure 4.49) depicted in also indicate the presence of Mn, Co, and O atoms in all samples with the atomic ratio of 2:1 (Co: Mn). Thus, the results reveal that the as-prepared nanofibers were MnCo₂O₄ spinel. The observed peaks in all samples at about 2.1 keV present the element gold (Au) that the gold is the most widely used to coat non-conductive samples for avoiding the charging effect. TEM is employed to further investigate the nanostructures of the MnCo₂O₄ nanofibers. As shown in the TEM image (Figure 4.50). The amorphous feature is observed in the as-electrospun PAN/MnCo₂O₄ fibers, as presented in the Figure 4.50(a-b). The synthesized MnCo₂O₄ nanofibers were composed of MnCo₂O₄ nanoparticles with an average particle size of 28.5, 38.6, and 70.9 nm for the samples calcinated at 700, 800, and 900 °C, respectively and these nanoparticles were loosely connected with each other and stacked along the nanofibers. The SAED patterns of all the samples exhibit many diffraction spots on diffraction rings, indicating a polycrystalline property and the feature of the MnCo₂O₄

phase, which is accepted by the XRD results.

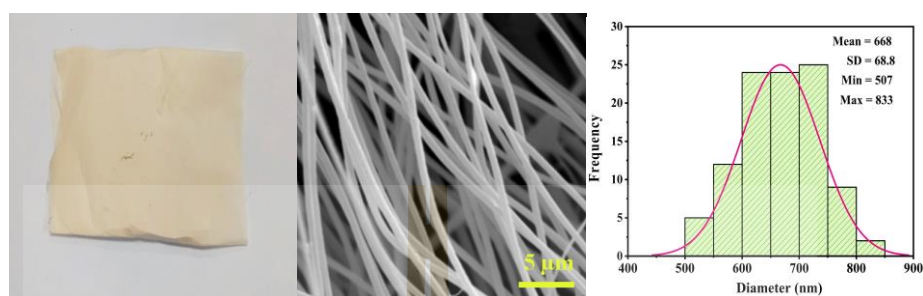


Figure 4.48 The picture and FESEM images of as-electrospun fibers

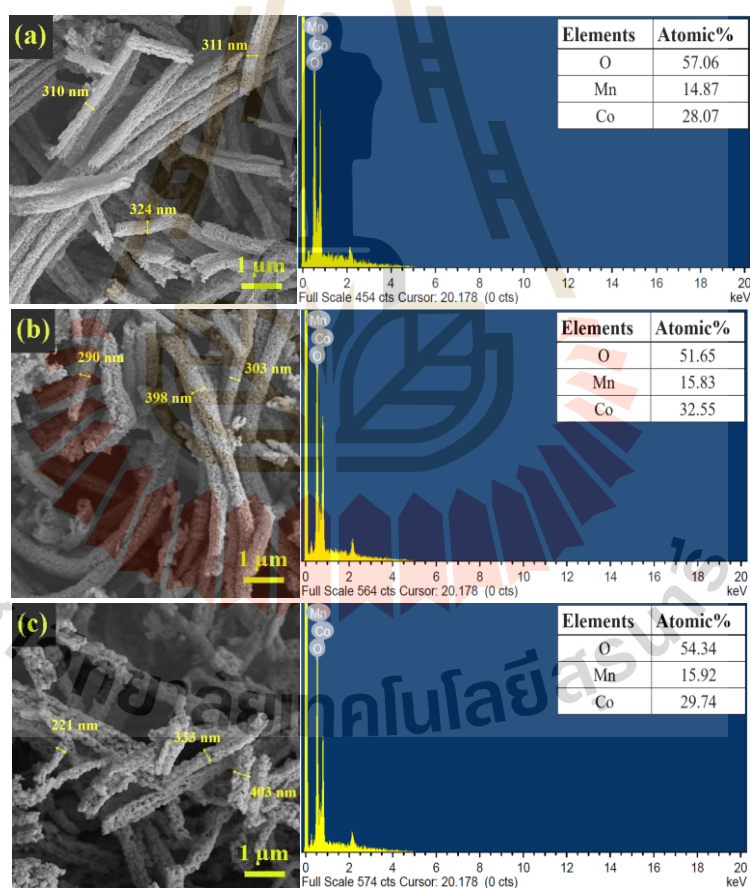


Figure 4.49 FESEM images with EDS spectra of MnCo₂O₄ nanofibers calcined for 3 h in atmosphere at (a) 700 °C, (b) 800 °C, and (c) 900 °C.

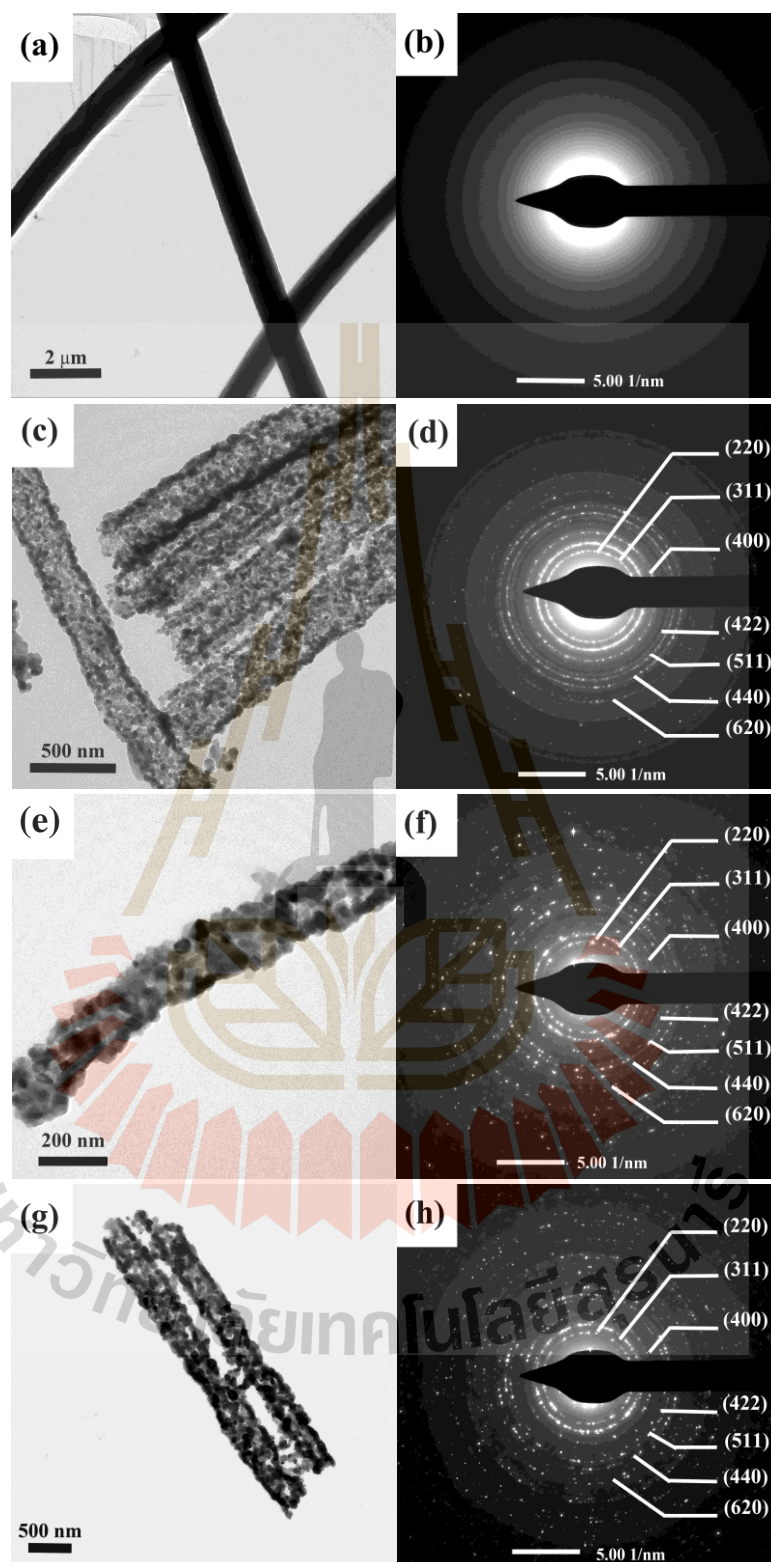


Figure 4.50 TEM images and SAED of MnCo_2O_4 nanofibers calcined for 3 h in atmosphere at (a,b) as-electrospun fibers, (c,d) 700 °C, (e,f) 800 °C and (g,h) 900 °C.

4.4.1.3 X-ray absorption spectroscopy study of the MnCo₂O₄ nanofibers

The valence states of Co and Mn in the prepared nanofibers were examined by X-ray absorption near-edge spectroscopy (XANES). The normalized Co K-edge XANES spectra of MnCo₂O₄ nanofibers as well as the reference samples of Co foil (Co⁰⁺), CoO (Co²⁺), and Co₃O₄ (Co^{2+,3+}) are presented in Figure 4.51. As illustrated in Figure 4.51, the absorption edges of all the samples in Co K-edge XANES spectra are between CoO (Co²⁺) and Co₃O₄ (Co^{2+,3+}) reference samples, demonstrating that Co ions in all of the MnCo₂O₄ samples are mixed the oxidation state of Co^{2+/3+}. Similarly, Mn K-edge XANES spectra for all MnCo₂O₄ samples are positioned between Mn₂O₃ (Mn³⁺) and MnO₂ (Mn⁴⁺) reference samples, as shown in Figure 4.52. These findings indicate that the oxidation states of Mn ion exist both of Mn^{3+/4+} in all the MnCo₂O₄ samples. The edge energy can be used to confirm the mix oxidation state of Co and Mn ion, as shown in Table 4.14. Furthermore, the similar line shapes of Mn K-edge and Co K-edge XANES spectra for the calcined samples indicating the local structure and the electronic structure of Co and Mn ions are not dependent on calcination temperatures.

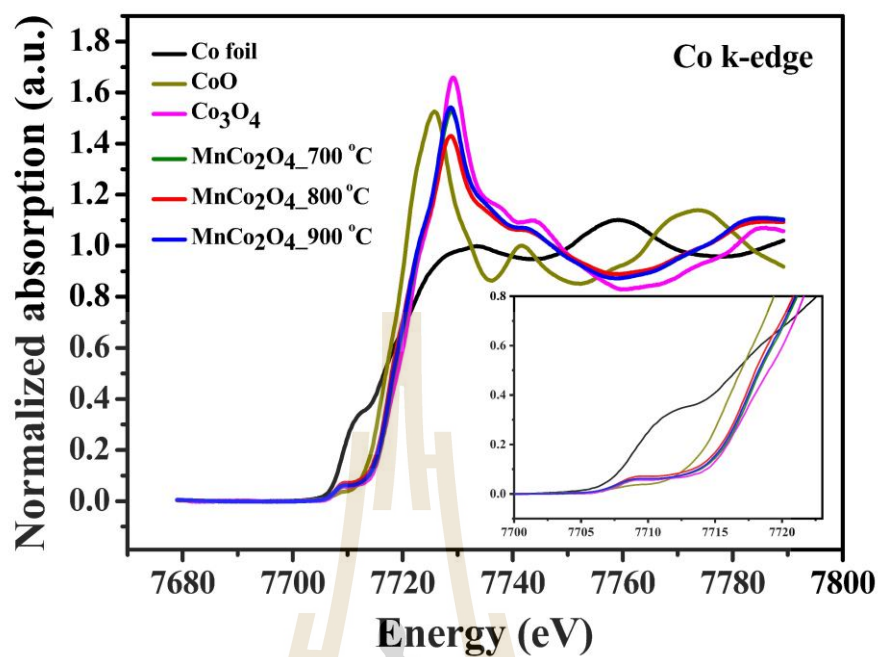


Figure 4.51 Normalized XANES spectra at Co K-edge of MnCo₂O₄ nanofibers.

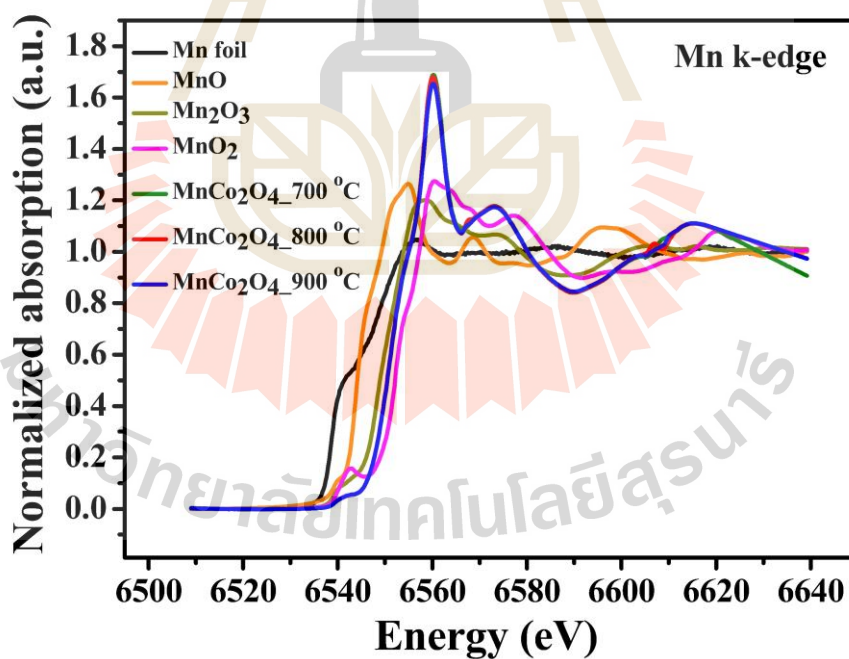


Figure 4.52 Normalized XANES spectra at Mn K-edge of MnCo₂O₄ nanofibers.

Table 4.14 Edge energy and oxidation state of the standard samples and MnCo₂O₄ nanofibers.

Samples	Edge element	Absorption Edge (eV)	Oxidation state
CoO	Co	7716.47	+2
Co ₃ O ₄	Co	7720.09	+2, +3
Mn ₂ O ₃	Mn	6548.82	+3
MnO ₂	Mn	6552.22	+4
MnCo ₂ O ₄ _700 °C	Co	7719.67	+2, +3
	Mn	6550.76	+3, +4
MnCo ₂ O ₄ _800 °C	Co	7719.28	+2, +3
	Mn	6550.83	+3, +4
MnCo ₂ O ₄ _900 °C	Co	7719.53	+2, +3
	Mn	6550.98	+3, +4

4.4.1.4 X-ray photoelectron spectroscopy (XPS) study of the MnCo₂O₄ nanofibers

The composition of the elemental and the oxidation state of MnCo₂O₄ nanofibers were examined using XPS measurement. Figure 4.53 presents the XPS survey spectrum, which confirms the existence of C, Mn, Co and O elements within the MnCo₂O₄ nanofibers. A high-resolution Co 2p spectrum in all the samples consisted of two main peaks at ~780 eV and ~795 eV, which are assigned to the core level of Co 2p_{3/2} and Co 2p_{1/2} with the spin-orbit splitting of ~15 eV (Figure 4.54). After fitted by the Gaussian method, the Co 2p spectrum of all the samples is best fitted with two spin-orbit doublets and four shake-up satellite peaks (denoted as sat.). The two main peaks

at binding energy about $\sim 781/\sim 797$ eV and $\sim 780/\sim 795$ eV can be assigned as Co^{2+} and Co^{3+} cations, respectively corresponding with the reported in the literature (Che *et al.*, 2016; Li *et al.*, 2015; Wang *et al.*, 2015; Qiu *et al.*, 2015; Naveen and Selladurai, 2015). For the Mn 2p XPS spectrum of all the samples, the binding energies separation between Mn $2p_{3/2}$ and Mn $2p_{1/2}$ are ~ 11 eV due to spin-orbit coupling, as shown in Figure 4.55. After fitting, the Mn 2p spectrum is divided in four components that the binding energy of the four components are listed in Table 4.15. The two peaks of binding energy at ~ 642 (Mn $2p_{3/2}$) and ~ 653 eV (Mn $2p_{1/2}$) are associated to Mn^{3+} and the other two peaks at binding energy of ~ 645 (Mn $2p_{3/2}$) and ~ 655 eV (Mn $2p_{1/2}$) is typical of Mn^{4+} indicating that the $\text{Mn}^{3+/4+}$ has existed in all the MnCo_2O_4 samples (Naveen and Selladurai, 2015; Li *et al.*, 2016; Zhu and Gao, 2009; Papavasiliou *et al.*, 2007). The O1s spectrum can be fitted into three components. The large component is found at a binding energy of ~ 530 eV and it is referred to the lattice oxygen in the spinel structure (denoted as I). The component at about 531.5 eV (II) corresponds to the oxygen atom of OH^- ions, and the peak at the highest binding energy value (III) can be ascribed to the oxygen atom of the adsorbed water molecules, respectively (Che *et al.*, 2016; Che *et al.*, 2016; Tholkappiyan *et al.*, 2015; Wang *et al.*, 2015; Qiu *et al.*, 2015; Fantauzzi *et al.*, 2019). As an XPS result, all the samples have mixing of $\text{Co}^{2+}/\text{Co}^{3+}$ and $\text{Mn}^{3+}/\text{Mn}^{4+}$, which are also in good agreement with the XANES analysis. The coexistence of the $\text{Co}^{2+}/\text{Co}^{3+}$ and $\text{Mn}^{3+}/\text{Mn}^{4+}$ may provide the electrochemical activity that led to an improvement in the electrochemical properties.

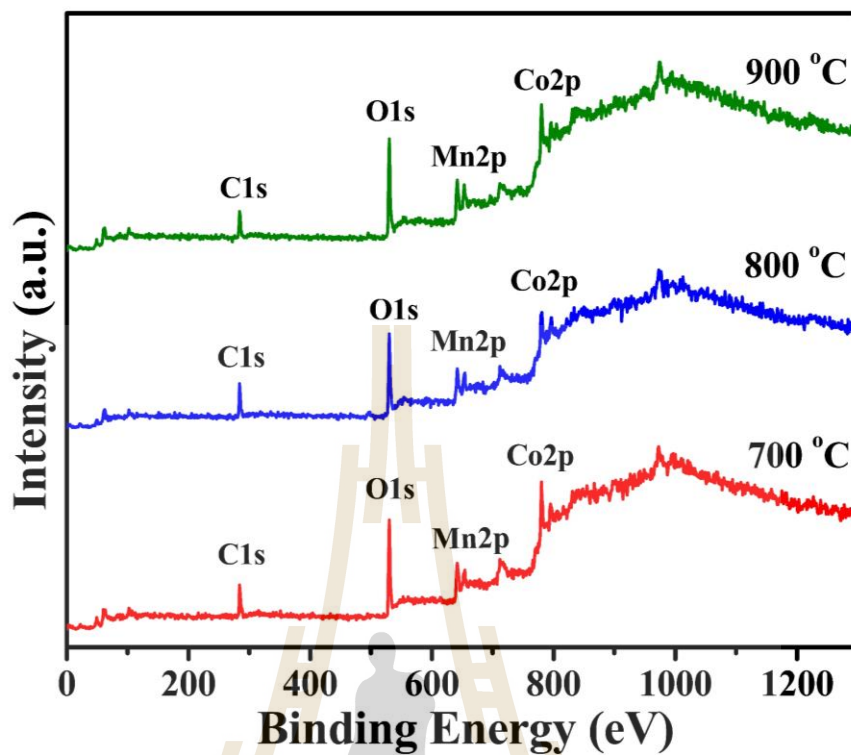


Figure 4.53 XPS survey spectrum of the MnCo₂O₄ nanofibers.

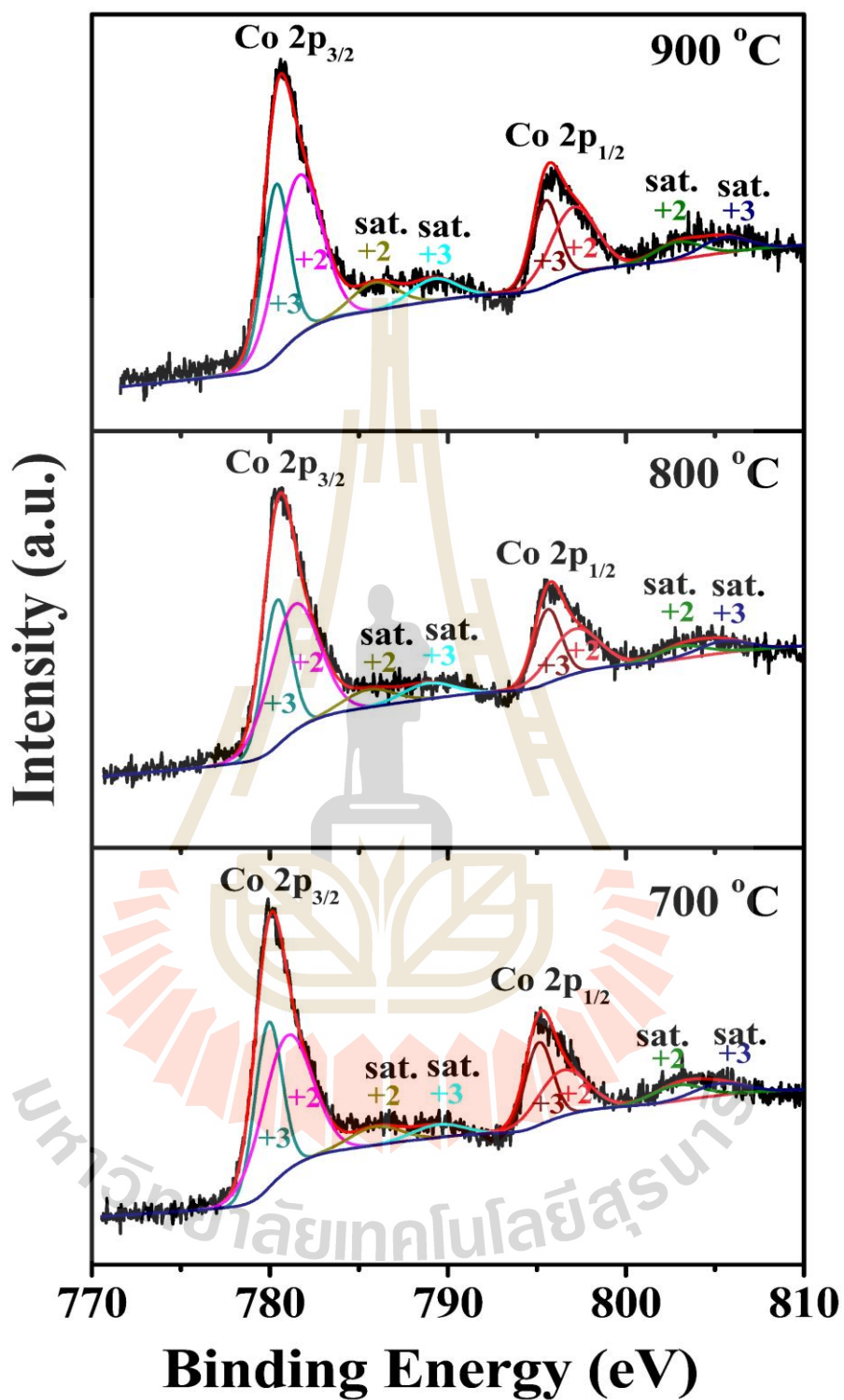


Figure 4.54 XPS spectra at Co 2p of the MnCo₂O₄ nanofibers.

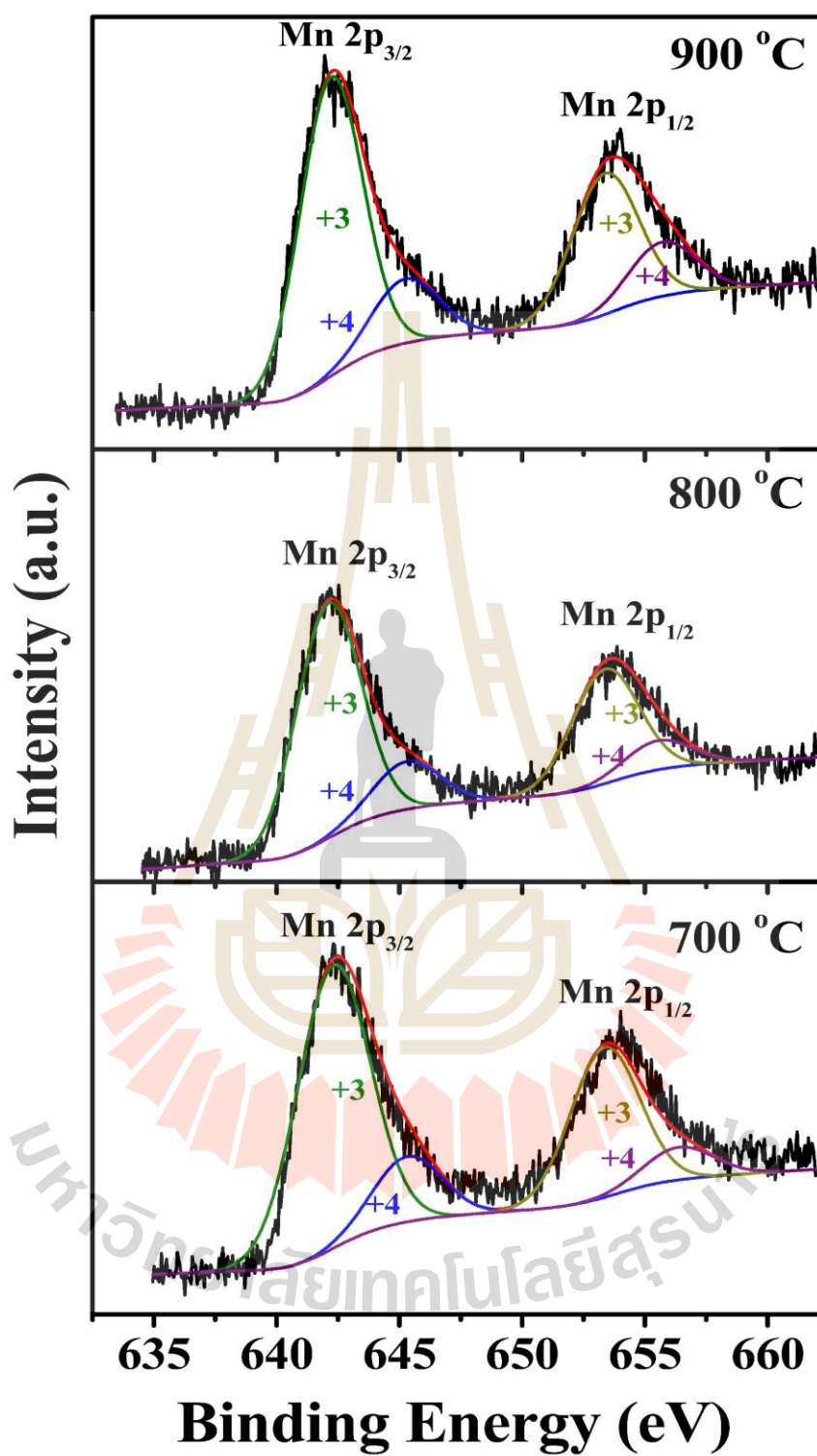


Figure 4.55 XPS spectra at Mn 2p of the MnCo₂O₄ nanofibers.

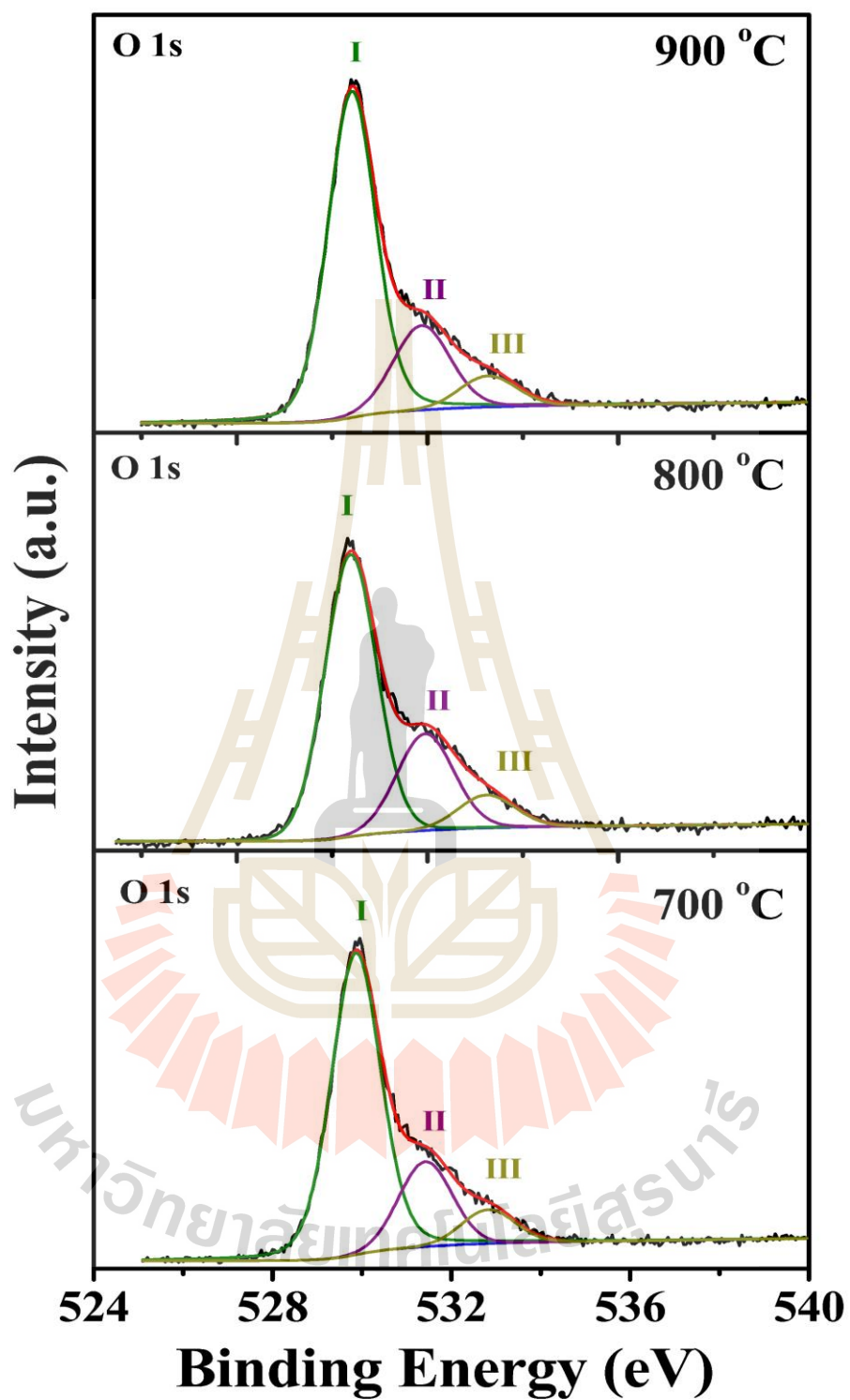
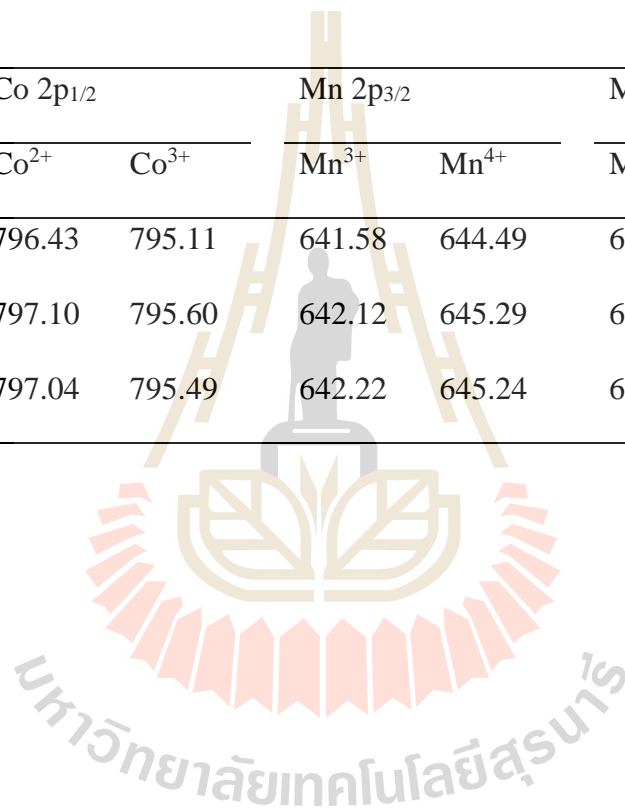


Figure 4.56 XPS spectra at O 1s of the MnCo₂O₄ nanofibers.

Table 4.15 XPS data of the MnCo₂O₄ nanofibers.

Binding energy position (eV)								
Samples	Co 2p _{3/2}		Co 2p _{1/2}		Mn 2p _{3/2}		Mn 2p _{1/2}	
	Co ²⁺	Co ³⁺	Co ²⁺	Co ³⁺	Mn ³⁺	Mn ⁴⁺	Mn ³⁺	Mn ⁴⁺
MnCo ₂ O ₄ _700 °C	780.95	779.91	796.43	795.11	641.58	644.49	652.63	654.82
MnCo ₂ O ₄ _800 °C	781.37	780.40	797.10	795.60	642.12	645.29	653.38	655.52
MnCo ₂ O ₄ _900 °C	781.63	780.35	797.04	795.49	642.22	645.24	653.37	655.71



4.4.1.5 Characterization of surface area and pore size distribution of the MnCo₂O₄ nanofibers by BET and BJH method

The specific surface area values of the MnCo₂O₄ nanofibers were obtained by the measuring of N₂ adsorption/desorption at the temperature of 77 K. Figure 4.57(a-c) displays the N₂ adsorption/desorption isotherms and the insets are BJH pore size distribution curves of all the calcined samples. As the results, all the N₂ adsorption/desorption isotherms show the hysteresis loop, as commonly observed for the typical feature of a mesoporous structure. The BET specific surface areas of the samples calcined at 700, 800, and 900 °C were determined to be 26.56, 23.75, and 11.98 m²/g, respectively. The mean pore diameters of the MnCo₂O₄ nanoparticles are 16.11, 17.51 and 32.72 nm for the samples calcined at 700, 800, and 900 °C, respectively. All the BJH pore size distributions curves Figure 4.57 (a-d), inset) reveal that the samples calcined at 800 and 900 °C exhibit a pore size distribution in the range of about 2.4 to 10 nm while the sample calcined at 700 °C shows a pore size distribution in the range of about 2.4 to 50 nm. As a result, the obtained MnCo₂O₄ nanofibers are mesoporous materials. Moreover, the total pore volume values were calculated as 0.107, 0.104, and 0.098 cm³/g for the samples calcined at 700, 800, and 900 °C, respectively. Mean pore diameter values of the samples calcined at 700, 800, and 900 °C were calculated as 16.11, 17.51, and 32.72 nm, respectively. The total pore volumes, mean pore diameters, and BET specific surface areas are summarized in Table 4.16. It is public knowledge that the larger specific surface area of material can give the more electroactive sites of materials for multiple redox reactions. The sample calcined at 700 °C is well defined smallest diameter of the fabricated MnCo₂O₄ nanofibers with a larger specific surface area, which can encourage the supercapacitor performance (Naveen and Selladurai,

2015; Huang *et al.*, 2018). Therefore, the MnCo_2O_4 nanofibers calcined at different calcination temperature with the differences in BET results of specific surface area, mean pore diameter, and pore volume exhibit different electrochemical performances, which will be discussed in the electrochemical properties section (section 4.4.2).

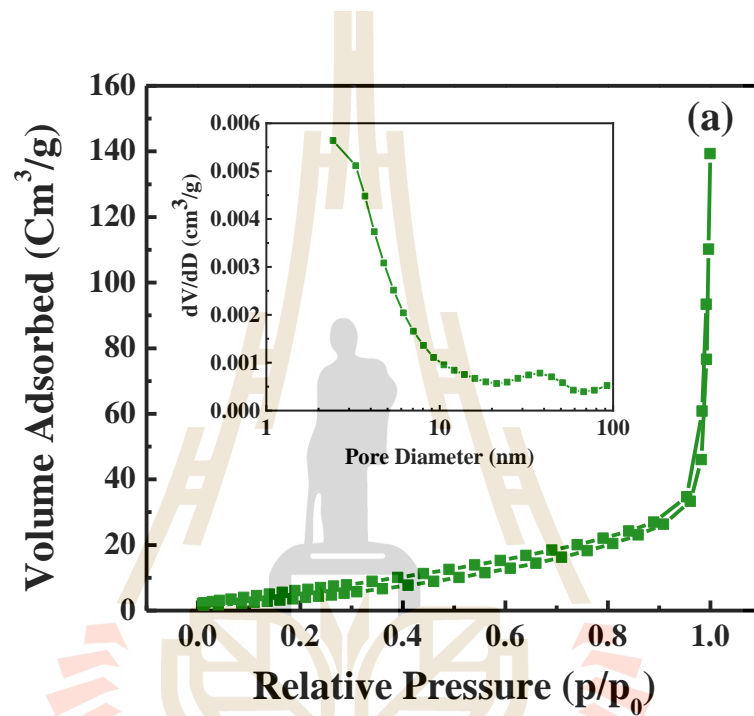


Figure 4.57 Nitrogen adsorption/desorption isotherms and pore size distribution (inset) of MnCo_2O_4 nanofibers calcined at (a) 700 °C, (b) 800 °C, and (c) 900 °C.

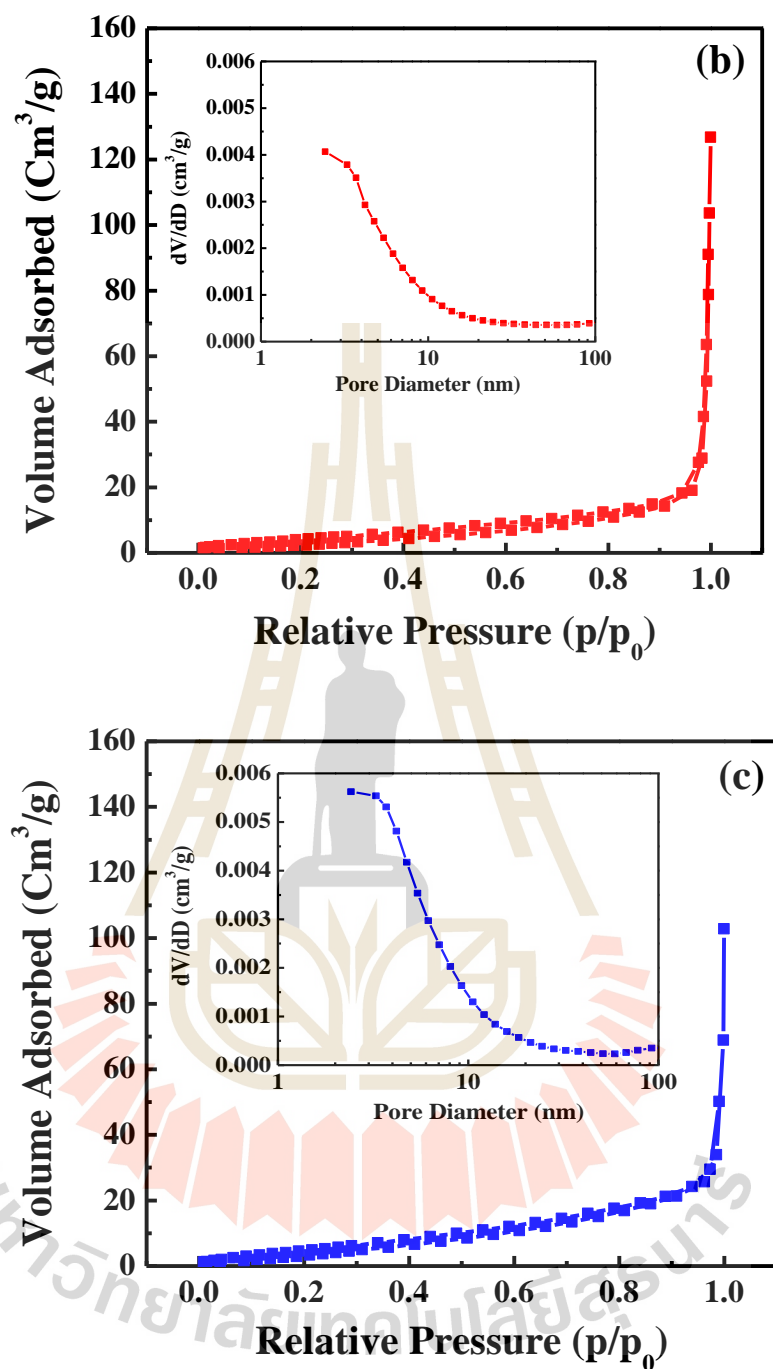


Figure 4.57 (Continued) Nitrogen adsorption/desorption isotherms and pore size distribution (inset) of MnCo₂O₄ nanofibers calcined at (a) 700 °C, (b) 800 °C, and (c) 900 °C.

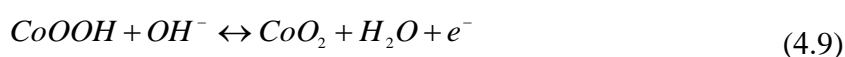
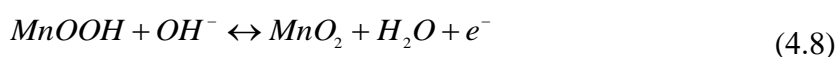
Table 4.16 Structural parameters of spinel MnCo₂O₄

Samples	BET specific surface area (m ² /g)	Total pore volume (cm ³ /g)	Mean pore diameter (nm)
700 °C	26.56	0.107	16.11
800 °C	23.75	0.104	17.51
900 °C	11.98	0.098	32.72

4.4.2 Electrochemical properties

4.4.2.1 Cyclic voltammetry measurement

The electrochemical properties of MnCo₂O₄ nanofibers were conducted in 6M aqueous KOH solution at room temperature using a three-electrode system. The cyclic voltammetry curves of all the MnCo₂O₄ nanofibers electrode at different scan rates ranging of 2 mV/s to 300 mV/s versus Ag/AgCl are presented in Figure 4.58(a-c). Clearly, the redox peaks were observed in these CV curves at about -0.2 and 0.0 V, which might be attributed to the faradaic redox reactions. The reversible redox reactions are described by the following equations (Bai *et al.*, 2016; Li *et al.*, 2014; Hao *et al.*, 2015);



When the scan rate is increased from 2 mV/s to 300 mV/s, the shapes of the CV curves remain the same, while the position of redox peaks has shifted, indicating good electrochemical reversibility. The larger area of the CV curve observed in the MnCo₂O₄

nanofibers electrode calcined at 700 °C indicates that the capacitance calculated from the CV curves is higher.

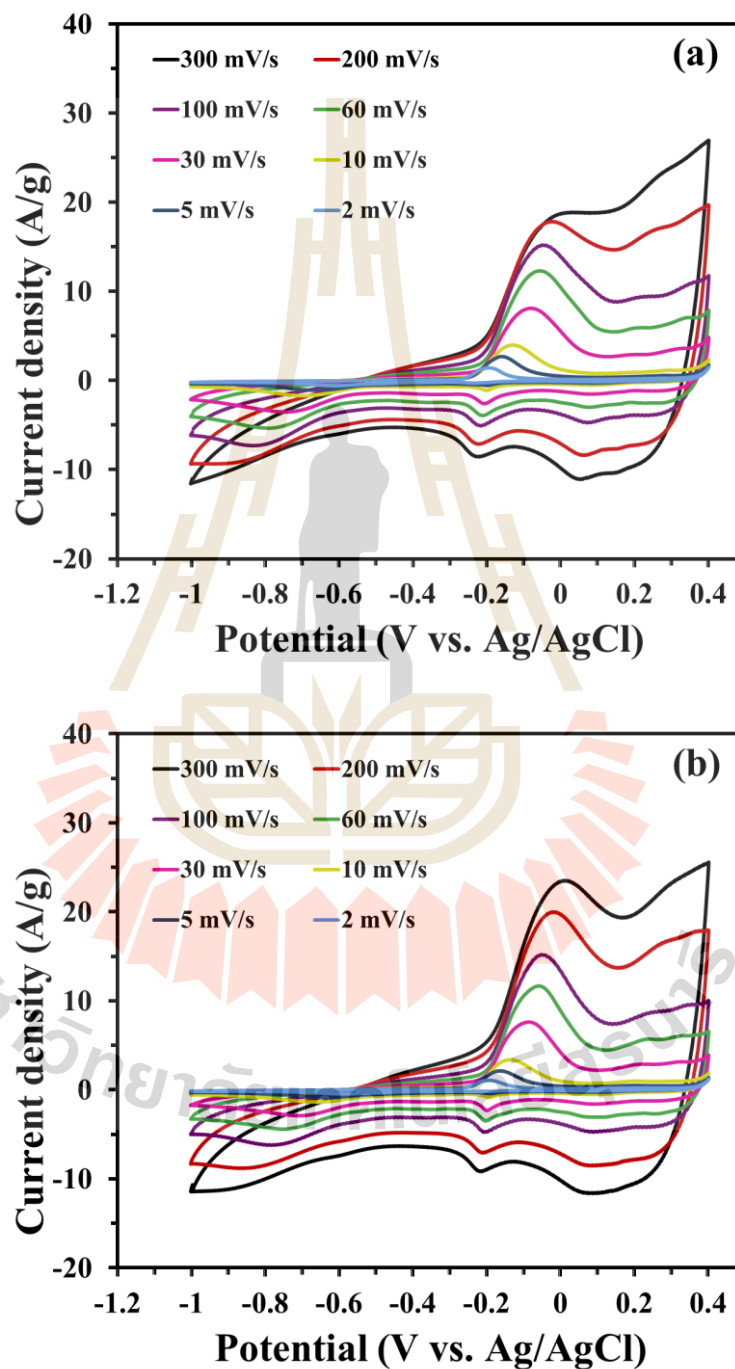


Figure 4.58 CV curves at various scan rates of MnCo₂O₄ nanofibers calcined at (a) 700 °C, (b) 800 °C, and (c) 900 °C.

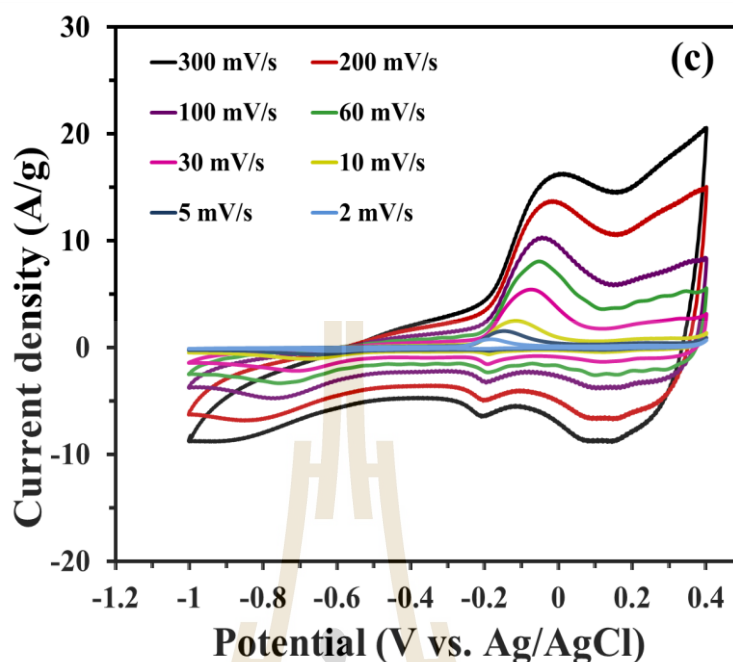


Figure 4.58 (Continued) CV curves at various scan rates of MnCo_2O_4 nanofibers calcined at (a) 700 °C, (b) 800 °C, and (c) 900 °C.

4.5.2.2 Galvanostatic charge-discharge measurements

The galvanostatic charge-discharge curves of the MnCo_2O_4 nanofibers electrodes within the potential range of -1.0-0.4 V at different current densities in 6 M KOH solution are shown in Figure 4.57(a-c). The results show that the nonlinearity of charge-discharge curves indicates the pseudocapacitance behavior owing to the faradaic reactions at the electrode-electrolyte interfaces. Typically, this is different from the electric double layer electrode materials which show linear behavior. Further, MnCo_2O_4 nanofibers electrode calcined at 700 °C shows longer discharge time compared with other electrodes calcined at 800 and 900 °C, this indicates MnCo_2O_4 nanofibers electrode calcined at 700 °C can provides better charge storage performance and higher specific capacitance than other electrodes. The capacitances at current

densities of 1 to 20 A/g calculated from the discharge curves using equation (3.19) are shown in Figure 4.60. It is obvious that the MnCo₂O₄ nanofibers electrode calcined at 700 °C has the highest specific capacitances at all of the current densities among the three electrodes. The MnCo₂O₄ nanofibers electrode calcined at 700 °C shows a highest specific capacitances value 76.3 F/g at the current density of 1 A/g, in good agreement with the CV curves and BET results. The MnCo₂O₄ nanofibers electrode calcined at 700 °C with smallest diameter exhibits the larger BET specific surface lading to more electroactive sites of materials for multiple redox reactions and good electrochemical performance.

To obtain the stability performance of the MnCo₂O₄ nanofibers electrodes as supercapacitors, the charge-discharge curves were conducted for 1000 cycles. This is an important criterion of supercapacitors for energy storage applications. The capacity retention (%) after 1000 cycles at a current density of 2 A/g of MnCo₂O₄ electrodes calcined at 700, 800, and 900 °C shows in Figure 4.61. The capacity retention (%) increase before 100 of cycles, and then decreases slightly. This may be due to the cycling-induced improvement in the wetting of the electrode surface, leading to more electroactive surface areas. Similar phenomena have been reported by other literatures (Huang *et al.*, 2017; Huang *et al.*, 2015; Kim *et al.*, 2016). The MnCo₂O₄ electrodes calcined at 700, 800, and 900 °C display the cycling stability of a capacitance loss of about 76 %, 71 %, and 64 %, respectively after 1000 cycles. In conclusion, the calcination temperature of 700 °C can provide the best morphology of the MnCo₂O₄ nanofibers. it exhibits the highest electrochemical performance. At calcination temperature of 800 and 900 °C, the structure and morphology of MnCo₂O₄ nanofibers change, and the electrochemical properties also decrease.

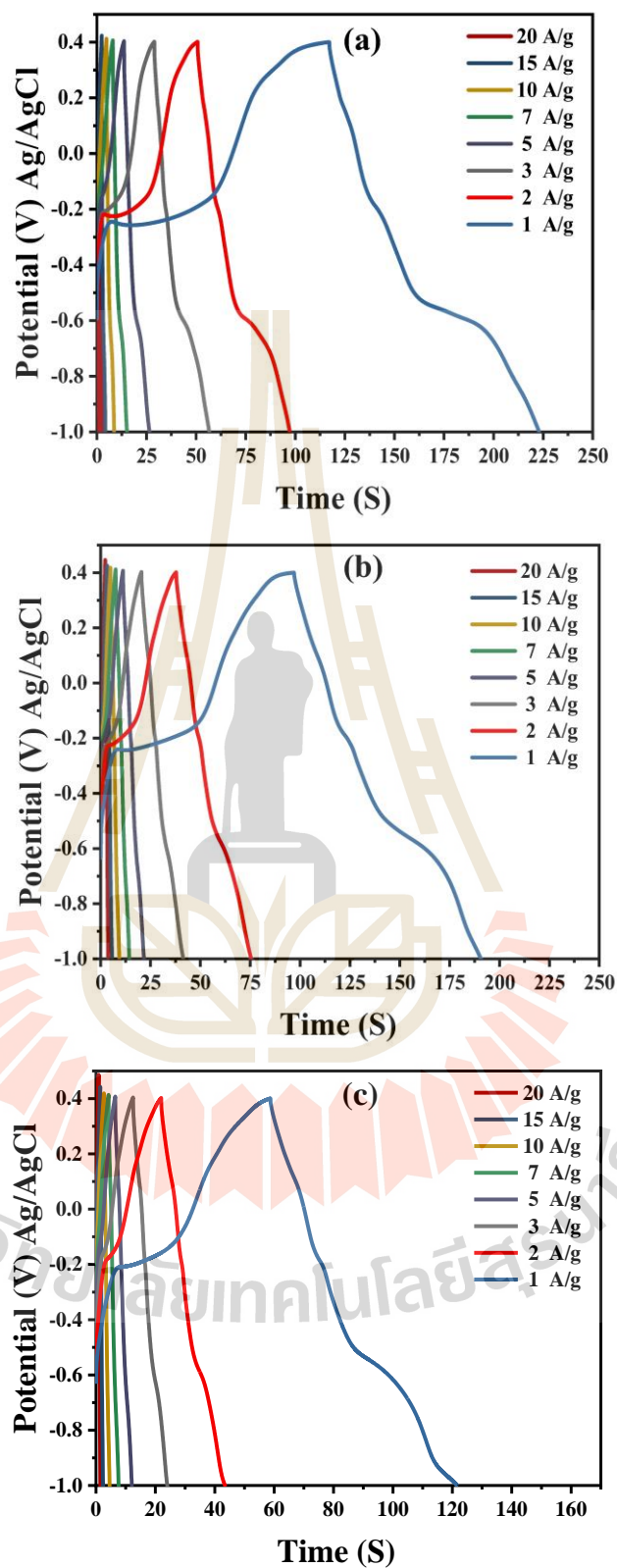


Figure 4.59 Galvanostatic charge-discharge curves at various current densities of MnCo_2O_4 nanofibers calcined at (a) 700 °C, (b) 800 °C, and (c) 900 °C.

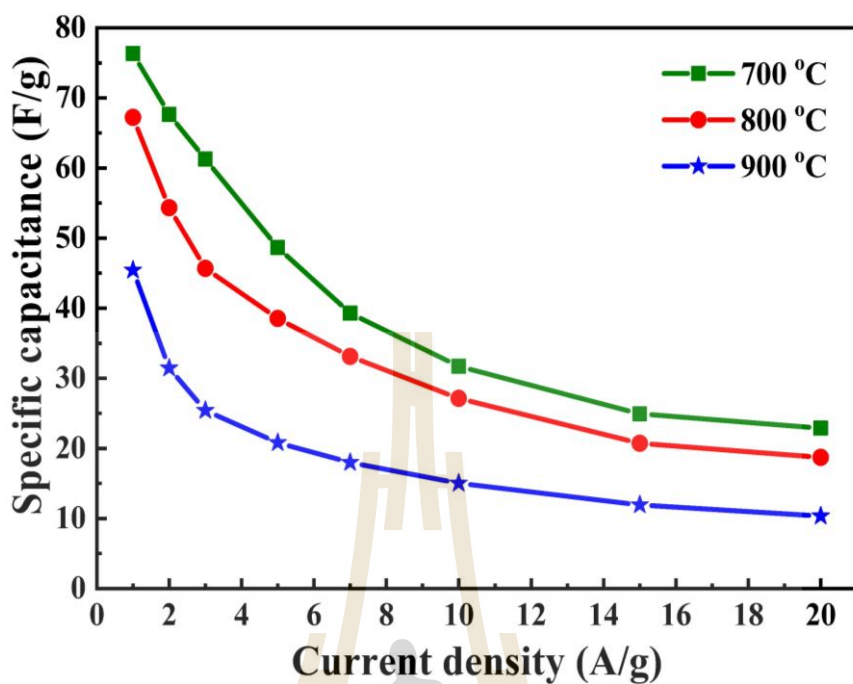


Figure 4.60 Comparison of the specific capacitance as a current density of MnCo_2O_4 nanofibers at various calcination temperature.

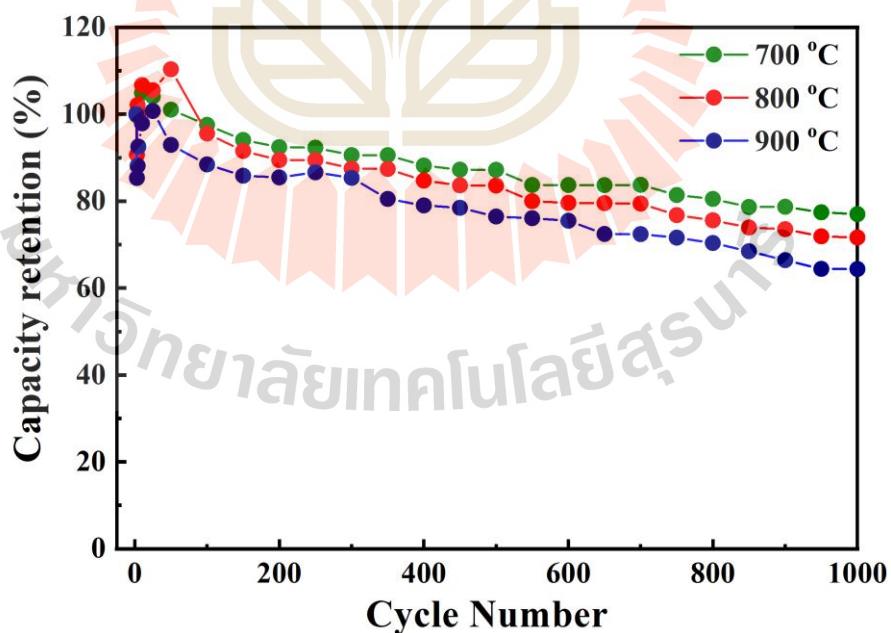


Figure 4.61 Capacity retention (%) at various calcination temperature of MnCo_2O_4 electrodes after 1000 cycles at a current density of 2 A/g.

4.4.2.3 Electrochemical impedance spectroscopy (EIS)

The electrochemical impedance spectrum (EIS) of MnCo_2O_4 nanofibers are shown in Figure 4.62. The intercept at the real part is the total electric series resistance that the MnCo_2O_4 nanofibers calcined at $700\text{ }^\circ\text{C}$ show the smallest intercept with real axis. In addition, the curve of the MnCo_2O_4 nanofibers calcined at $700\text{ }^\circ\text{C}$ exhibits a more vertical slope which demonstrates more facile electrolyte diffusion to the surface of the sample and high reactivity as compared with other samples. The semicircle of the Nyquist curve signifies the Faradic reactions and the corresponding diameter represents the interfacial resistivity. All the electrodes show the small semicircles indicating the high electrical conductivity of the electrode. Thus, MnCo_2O_4 nanofibers calcined at $700\text{ }^\circ\text{C}$ has a high electrochemical performance as compared with other samples.

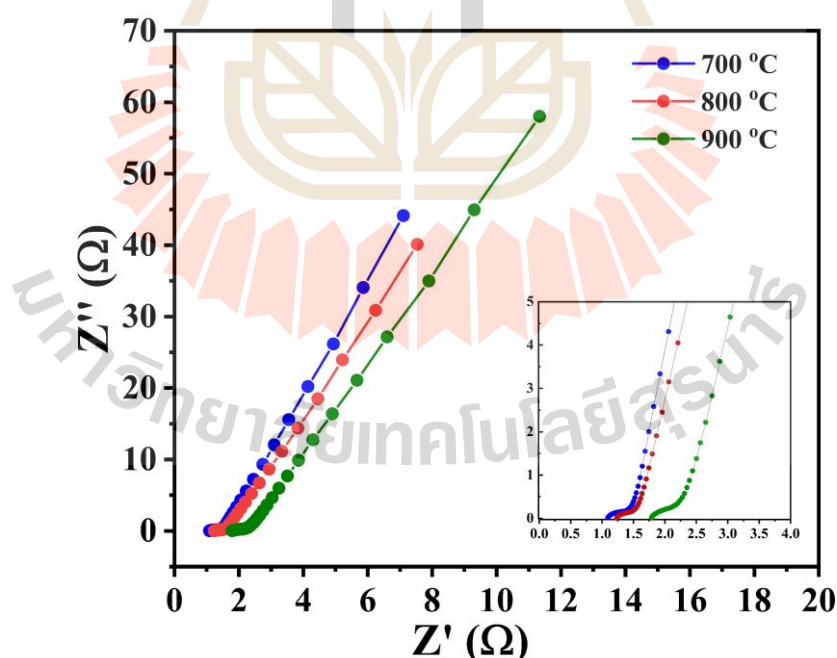


Figure 4.62 The Nyquist plots of the of MnCo_2O_4 NFs electrodes at various calcination temperature.

4.5 Ni-doped MnCo₂O₄ nanofibers

4.5.1 Structural and morphology characterization

4.5.1.1 X-ray diffraction (XRD) analysis of the Ni-doped MnCo₂O₄ nanofibers

The XRD pattern of Ni-doped MnCo₂O₄ nanofibers are presented in Figure 4.67, It can be seen that the diffraction peaks of all the samples can be well-matched to the MnCo₂O₄ cubic structure (JCPDS No. 23-127). Sharp peaks are obtained for (111), (220), (311) (222), (400), (422), (511), and (440) planes, without any impurities. The decrease in the intensity of the diffraction peaks indicates that the Ni-doping affects the crystallinity of the samples. That the Ni-doping has resulted in decreases the crystallinity. The Ni-doped MnCo₂O₄ nanofibers samples observe the position peak shifted to higher 2θ which is attributed to the lattice constants variation. The calculated lattice constants are shown in Table 4.17. It has been observed that the decreasing of the d-spacing and lattice constant with increasing Ni concentration. Variation in the lattice parameters suggests that the Mn³⁺(0.72 Å) ions of the larger ionic radius are replaced by Ni²⁺ (0.69Å) with the smaller ionic radius. The crystallite size of Ni-doped MnCo₂O₄ nanofibers is calculated by Scherrer's equation using the full width at half maximum of high intense peak ((311) plane) as summarized in Table 4.17. The crystallite size values are 60.0, 52.5, 46.7, 43.3, and 42.0 nm for Ni doping concentration with x = 0.00, 0.05, 0.10, 0.15, and 0.20, respectively. It is obvious that the crystallite size decreases with increasing Ni concentration.

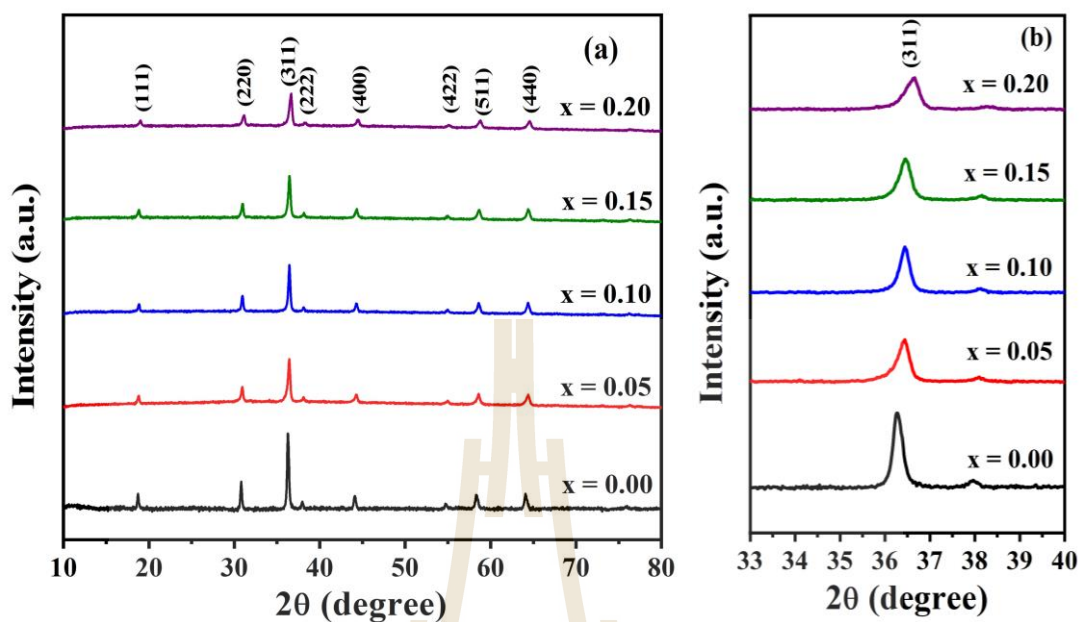


Figure 4.63 (a) XRD patterns of Ni-doped MnCo_2O_4 nanofibers and (b) relative shift in (311) peak of MnCo_2O_4 with respect to Ni-doping.

Table 4.17 Summary of crystallite sizes (D) from XRD, d -spacing (d), and lattice constant (a) of $\text{Mn}_{1-x}\text{Ni}_x\text{Co}_2\text{O}_4$ ($x = 0.00, 0.05, 0.10, 0.15$, and 0.20) nanofibers.

samples	Crystallite sizes	d -spacing	Lattice constant
	D (nm)	d (Å)	a (nm)
$x = 0.00$	60.0	2.475	8.210
$x = 0.05$	52.5	2.463	8.169
$x = 0.10$	46.7	2.462	8.165
$x = 0.15$	43.3	2.460	8.160
$x = 2.00$	42.0	2.449	8.122

4.5.1.2 The Morphology of the Ni-doped MnCo_2O_4 nanofibers by FESEM and TEM

FESEM images of Ni-doped MnCo_2O_4 nanofibers are shown in Figure 4.64 (a-e). It can be seen that these fibers comprise of polygonal-shaped crystallites with the size of 20-30 nm, 20-30 nm, 50-80 nm, 60-90 nm, and 80-100 nm for Ni doping concentration with $x = 0.00, 0.05, 0.10, 0.15,$ and 0.20 , respectively corresponding with each other to form the fibers with the rough surface (Pettong *et al.*, 2016). The average diameters of the nanofibers are 300-400, 250-380, 250-400, 200-400 nm and 200-300 nm for the Ni doping concentration $x = 0.00, 0.05, 0.10, 0.15,$ and 0.20 , respectively. Obviously, the Ni doping slightly changes the particle size. The particle size and surface morphology of the Ni-doped MnCo_2O_4 nanofibers were investigated by TEM technique. Figure 4.65 shows the TEM images at different magnifications with corresponding HRTEM and SAED of Ni-doped MnCo_2O_4 nanofibers, revealing that the fibers consist of polygonal-shaped nanoparticles. The HRTEM images of the nanoparticles reveal the interlayer spacing of about 0.479, 0.477, 0.478, 0.478, and 0.479 nm for the Ni doping concentration $x = 0.00, 0.05, 0.10, 0.15,$ and 0.20 , respectively attributed to the (111) plane of cubic MnCo_2O_4 . The SAED pattern consists of spots and rings, which correspond to (220), (331), (400), (422), (511), (440), and (620) planes of polycrystalline MnCo_2O_4 with cubic structure.

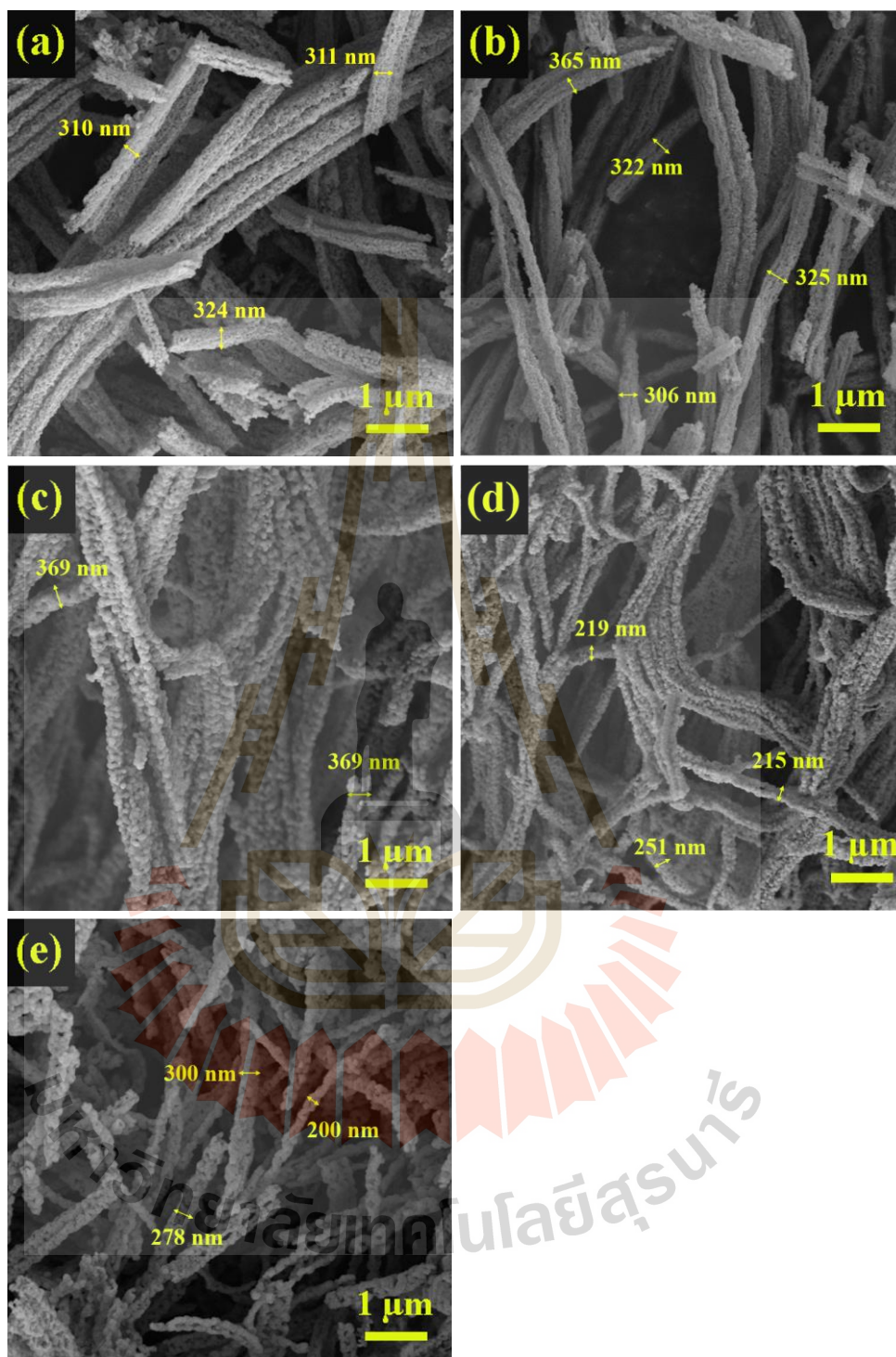


Figure 4.64 FESEM images and EDS spectrums of $\text{Mn}_{1-x}\text{Ni}_x\text{Co}_2\text{O}_4$ nanofibers: (a) $x = 0.00$, (b) $x = 0.05$, (c) $x = 0.10$, (d) $x = 0.15$, and (e) $x = 0.20$.

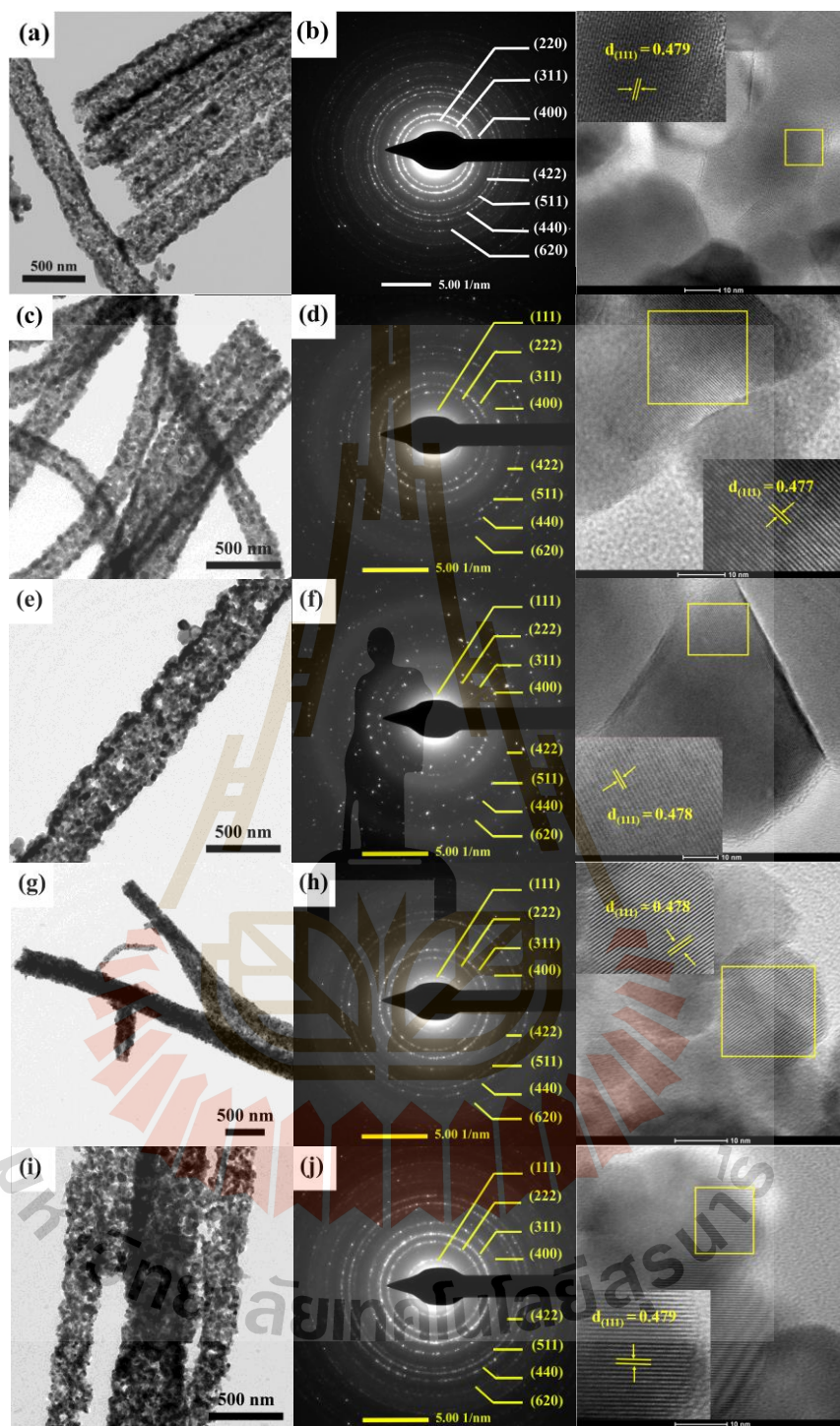


Figure 4.65 TEM images with corresponding HRTEM and SAED of $\text{Mn}_{1-x}\text{Ni}_x\text{Co}_2\text{O}_4$ nanofibers: (a,b) $x = 0.00$, (c,d) $x = 0.05$, (e,f) $x = 0.10$, (g,h) $x = 0.15$, and (i,j) $x = 0.20$.

4.5.1.3 X-ray absorption spectroscopy study of the Ni-doped MnCo₂O₄ nanofibers

The valence states of Ni, Mn, and Co in Mn_{1-x}Ni_xCo₂O₄ nanofibers were determined by XANES. Figure 4.66 presents the edge energies of the Co foil (Co⁰⁺), CoO (Co²⁺), Co₃O₄ (Co^{2+,3+}) and Mn_{1-x}Ni_xCo₂O₄ (x = 0.00, 0.05, 0.10, 0.15, and 0.20) samples for comparison. The edge energies positions of all the samples are very close to the Co₃O₄ (Co^{2+,3+}) standard. This result reveals that the Co ions in all the samples mixed valence state of Co²⁺ and Co³⁺. The Normalized XANE spectra at Mn K-edge of Mn_{1-x}Ni_xCo₂O₄ (x = 0.00, 0.05, 0.10, 0.15, and 0.20) nanofibers comparing with the standard samples of Mn foil (Mn⁰⁺), Mn₂O₃ (Mn³⁺) and MnO₂ (Mn⁴⁺) are presented in Figure 4.67. The results reveal that the spectra of all Ni-doped MnCo₂O₄ nanofibers are the closest to the spectrum of the standard sample MnO₂ (Mn⁴⁺). However, the edge energies positions of all samples are between Mn₂O₃ (Mn³⁺) and MnO₂ (Mn⁴⁺), which suggests that the Mn ions in all samples are in a mixed valence state of Mn³⁺ and Mn⁴⁺. Figure 4.68 shows the normalized XANE spectra at Ni K-edge of Mn_{1-x}Ni_xCo₂O₄ (x = 0.00, 0.05, 0.10, 0.15, and 0.20) nanofibers comparing with the standard samples of Ni foil (Ni⁰⁺), and NiO (Ni²⁺). It can be clearly seen that the edge energies positions of all samples are very close to the NiO (Ni²⁺) standard. These findings indicate that the oxidation states of Ni ion consist of Ni²⁺ in all the samples. The edge energy can be used to confirm the oxidation state of Ni, Co, and Mn ion, as shown in Table 4.18.

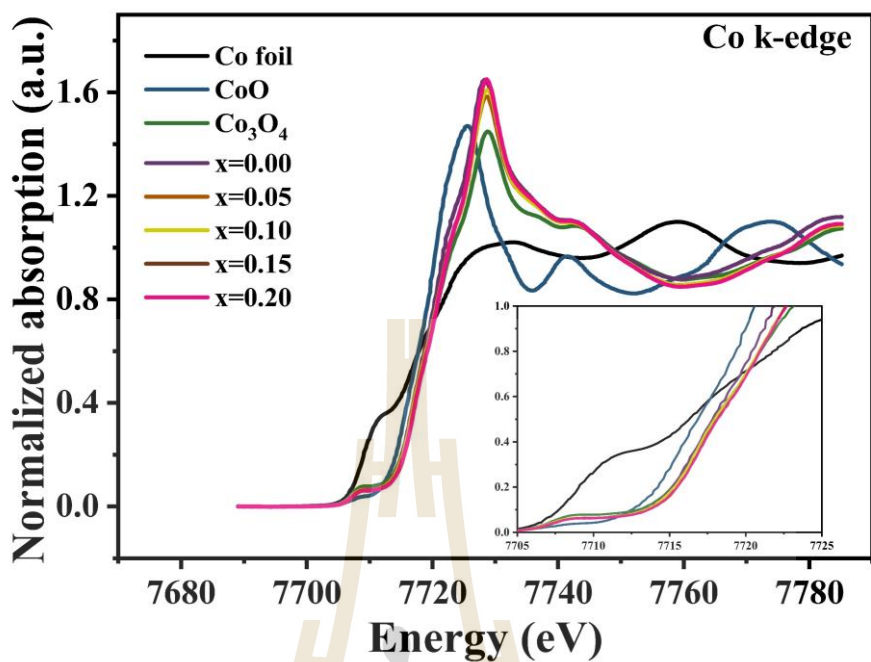


Figure 4.66 Normalized XANES spectra at Co *K*-edge of $\text{Mn}_{1-x}\text{Ni}_x\text{Co}_2\text{O}_4$ ($x = 0.00$, 0.05, 0.10, 0.15, and 0.20) nanofibers.

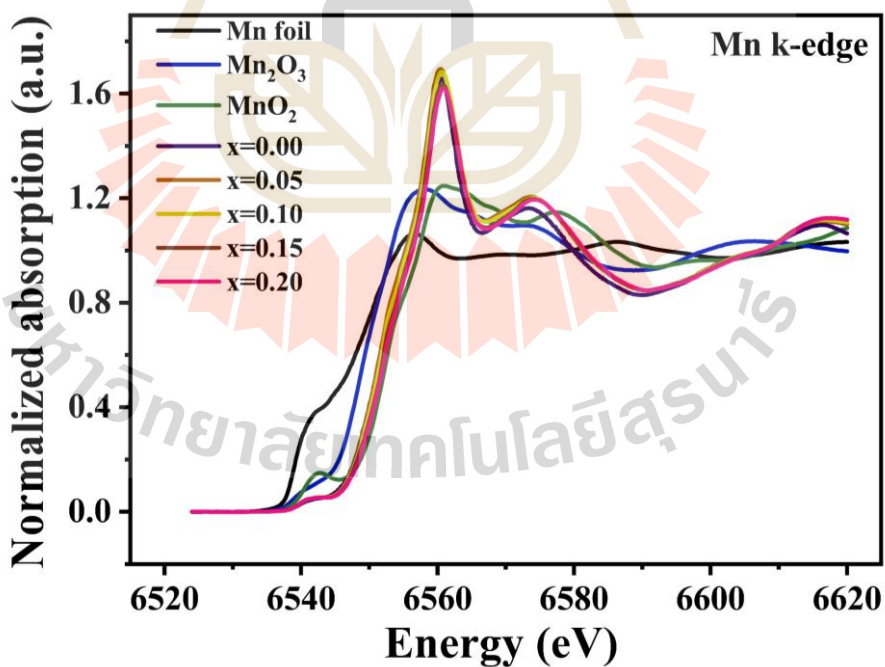


Figure 4.67 Normalized XANES spectra at Mn *K*-edge of $\text{Mn}_{1-x}\text{Ni}_x\text{Co}_2\text{O}_4$ ($x = 0.00$, 0.05, 0.10, 0.15, and 0.20) nanofibers.

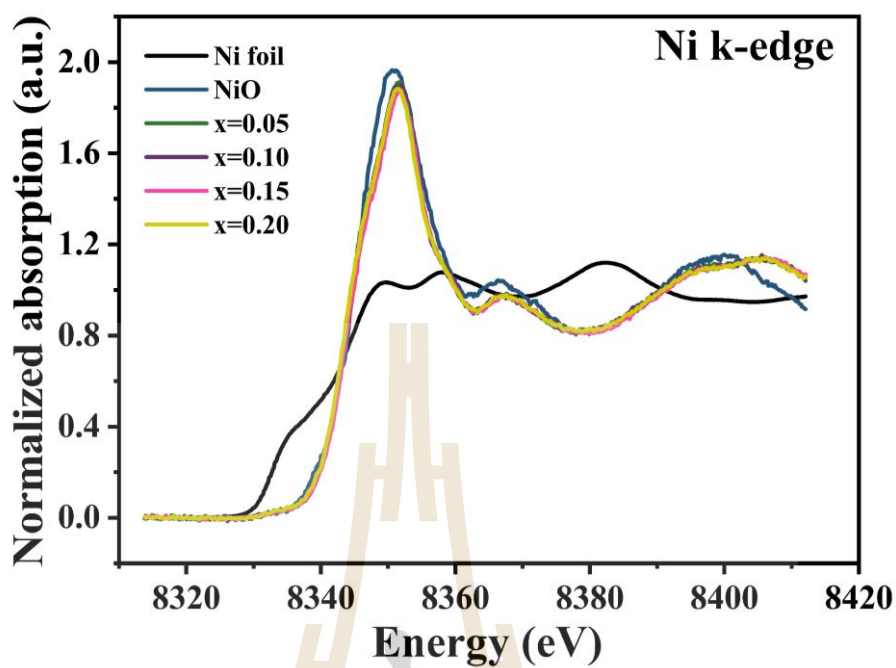


Figure 4.68 Normalized XANES spectra at Ni *K*-edge of $\text{Mn}_{1-x}\text{Ni}_x\text{Co}_2\text{O}_4$ ($x = 0.00, 0.05, 0.10, 0.15,$ and 0.20) nanofibers.

Table 4.18 Edge energy and Oxidation state of the standard samples and $Mn_{1-x}Ni_xCo_2O_4$ ($x = 0.00, 0.05, 0.10, 0.15,$ and 0.20) nanofibers.

Samples	Edge element	Absorption Edge (eV)	Oxidation state
CoO	Co	7716.30	+2
Co ₃ O ₄	Co	7721.45	+2, +3
Mn ₂ O ₃	Mn	6548.72	+3
MnO ₂	Mn	6551.92	+4
NiO	Ni	8343.20	+2
x = 0.00	Co	7719.67	+2, +3
	Mn	6550.76	+3, +4
x = 0.05	Co	7719.35	+2, +3
	Mn	6551.27	+3, +4
	Ni	8343.79	+2
x = 0.10	Co	7719.35	+2, +3
	Mn	6551.27	+3, +4
	Ni	8343.79	+2
x = 0.15	Co	7719.35	+2, +3
	Mn	6551.27	+3, +4
	Ni	8343.79	+2
x = 0.20	Co	7719.35	+2, +3
	Mn	6551.27	+3, +4
	Ni	8343.79	+2

4.5.1.4 X-ray photoelectron spectroscopy (XPS) study of the Ni-doped MnCo₂O₄ nanofibers

The valance states and surface chemical compositions of the Ni-doped MnCo₂O₄ nanofibers were conducted by XPS. As illustrated in Figure 4.69, the survey XPS spectrum of the Mn_{1-x}Ni_xCo₂O₄ (x = 0.00, 0.05, 0.10, 0.15, and 0.20) nanofibers present the peaks of Ni, Mn, Co, O and C, whereas no impurity peak is observed. As presented in Figure 4.70, the Co 2p XPS spectra of all the samples demonstrate two major peaks with binding energy of ~779 (Co 2p_{3/2}) and ~794 eV (Co 2p_{1/2}). After Gaussian fitting, the Co 2p spectra of all the samples can be well-fitted with two spin-orbit doublets and 4 shakeup satellites (denoted as “Sat.”), assigned to the presence of Co²⁺/Co³⁺. The binding energies of Co³⁺ are located at ~780 eV and ~795 eV and the peaks at the binding energies of ~782 eV and ~798 eV are ascribed to Co²⁺, according to the literature (Pettong *et al.*, 2016; Wu *et al.*, 2015; Wang *et al.*, 2015) with good agreement with the XAS result. As shown in Figure 4.71, the Mn 2p XPS spectrum of all the samples exhibits the binding energies separation between Mn 2p_{3/2} and Mn 2p_{1/2} of about ~11 eV due to spin-orbit coupling. After fitting, the Mn 2p spectrum was divided in 4 components that the binding energy of the 4 components are presented in Table 4.19. The two peaks of binding energy at ~642 (Mn 2p_{3/2}) and ~653 eV (Mn 2p_{1/2}) are associated to Mn³⁺ and the other two peaks at binding energy of ~645 (Mn 2p_{3/2}) and ~655 eV (Mn 2p_{1/2}) is typical of Mn⁴⁺ suggesting that the Mn^{3+/4+} has existed in all the MnCo₂O₄ samples (Naveen and Selladurai, 2015; Li *et al.*, 2016; Zhu and Gao, 2009; Papavasiliou *et al.*, 2007). The Ni 2p spectrum (Figure 4.72) of all the sample shows two peaks at 855 and 872 eV, which can be assigned to the Ni 2p_{3/2} and Ni 2p_{1/2} spine orbit peaks in the spinel MnCo₂O₄ phase indicating that Ni²⁺ is existing in all the

Ni-doped MnCo_2O_4 samples (Chen *et al.*, 2017). The O1s spectrum (Figure 4.73) can be fitted into three components. The large component is found at a binding energy of ~ 530 eV and it is typical of metal-oxygen bonds. The component at about 531.5 eV is ascribed to OH^- groups oxygen, and the peak at the highest binding energy value (III) can be ascribed to the oxygen atom of the adsorbed water molecules, respectively (Che *et al.*, 2016; Che *et al.*, 2016; Tholkappiyan *et al.*, 2015; Wang *et al.*, 2015; Qiu *et al.*, 2015; Fantauzzi *et al.*, 2019). The XPS results are also in good agreement with the XANES analysis. The coexistence of the Ni^{2+} , $\text{Co}^{2+}/\text{Co}^{3+}$ and $\text{Mn}^{3+}/\text{Mn}^{4+}$ may provide the electrochemical activity that leads to an improvement in the electrochemical properties.

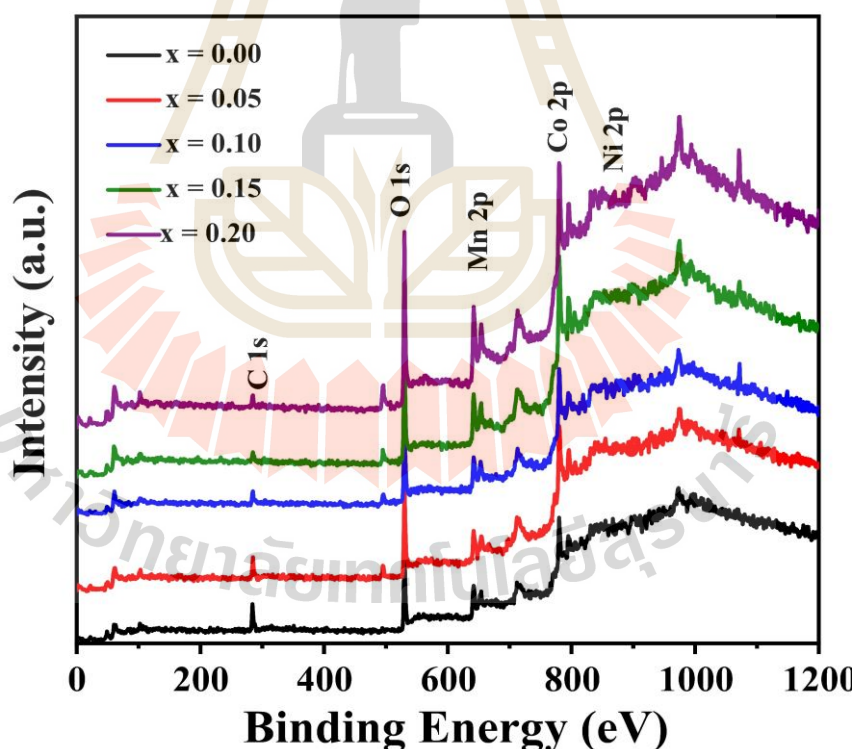


Figure 4.69 XPS survey spectrum of the $\text{Mn}_{1-x}\text{Ni}_x\text{Co}_2\text{O}_4$ ($x = 0.00, 0.05, 0.10, 0.15,$ and 0.20) nanofibers.

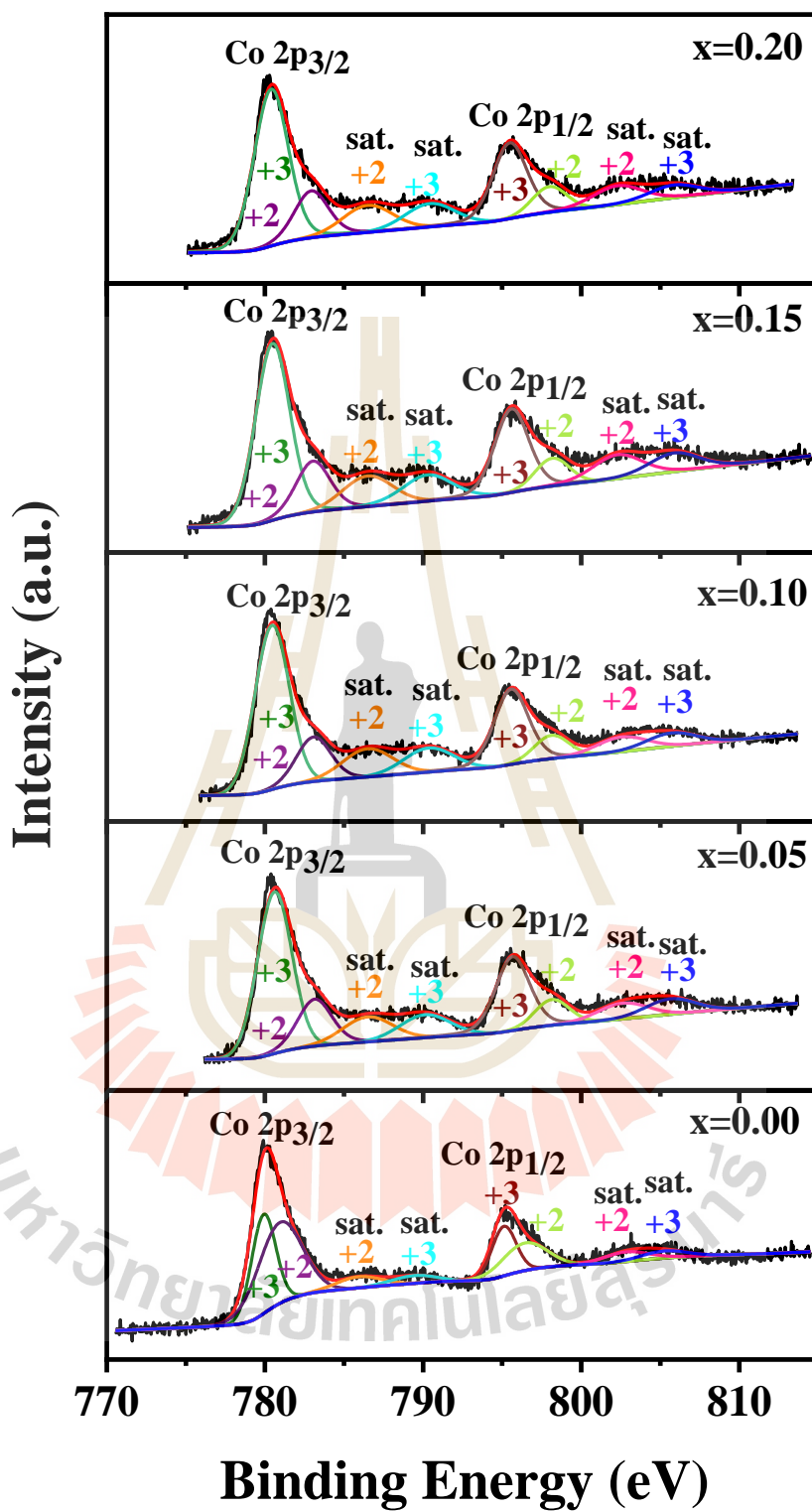


Figure 4.70 XPS spectra at Co 2p of the Mn_{1-x}Ni_xCo₂O₄ (x = 0.00, 0.05, 0.10, 0.15, and 0.20) nanofibers.

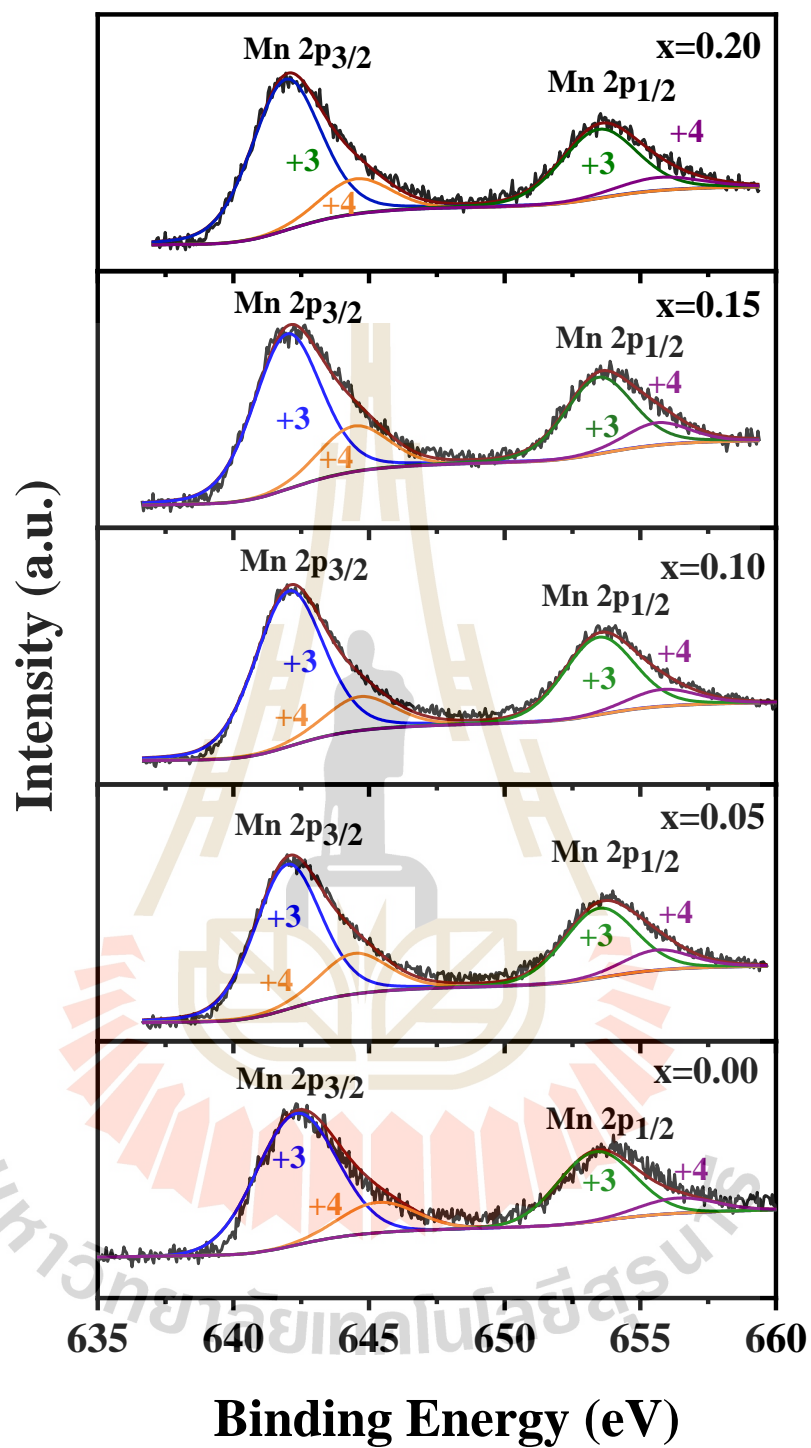


Figure 4.71 XPS spectra at Mn 2p of the $\text{Mn}_{1-x}\text{Ni}_x\text{Co}_2\text{O}_4$ ($x = 0.00, 0.05, 0.10, 0.15,$ and 0.20) nanofibers.

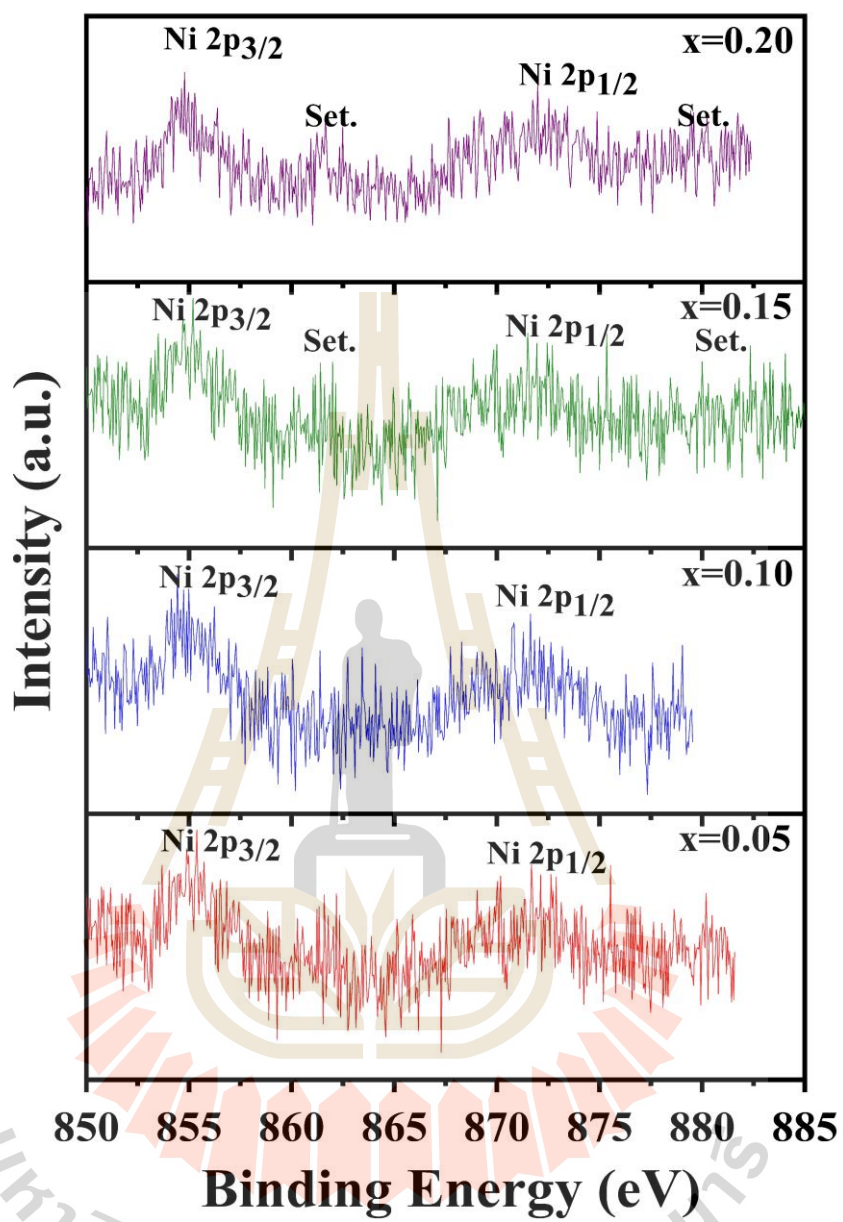


Figure 4.72 XPS spectra at Ni 2p of the Mn_{1-x}Ni_xCo₂O₄ (x = 0.05, 0.10, 0.15, and 0.20) nanofibers.

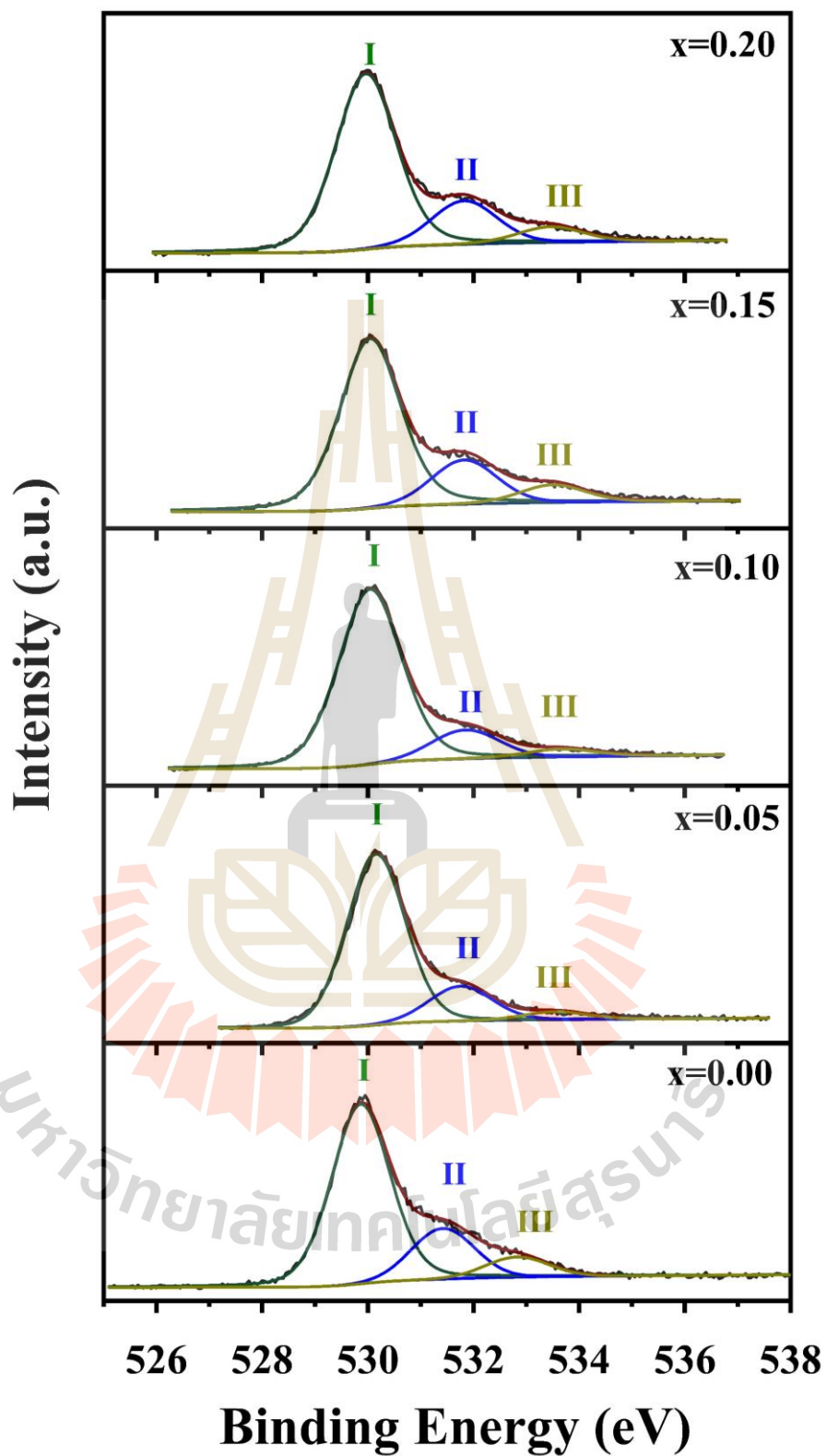
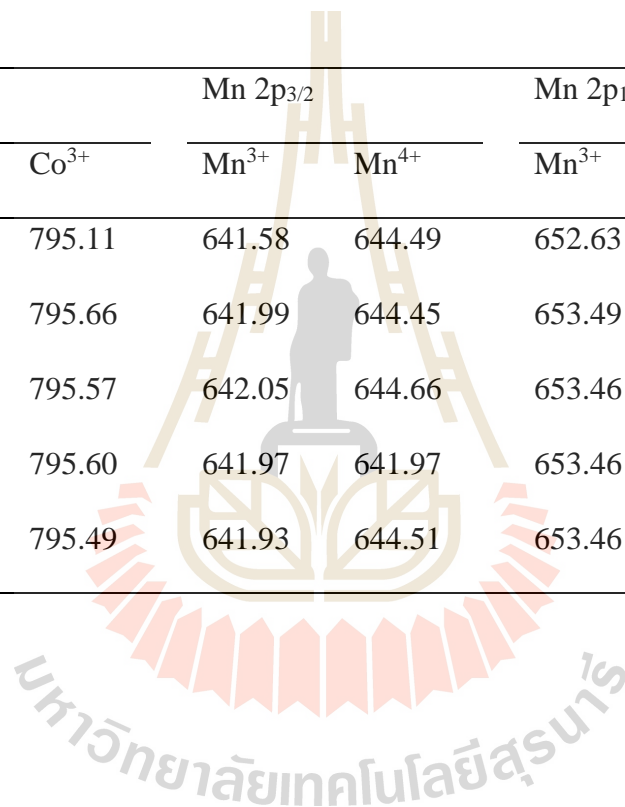


Figure 4.73 XPS spectra at O 1s of the Mn_{1-x}Ni_xCo₂O₄ (x = 0.00, 0.05, 0.10, 0.15, and 0.20) nanofiber.

Table 4.19 XPS data of the $\text{Mn}_{1-x}\text{Ni}_x\text{Co}_2\text{O}_4$ ($x = 0.00, 0.05, 0.10, 0.15,$ and 0.20) nanofibers.

Binding energy position (eV)										
Samples	Co 2p _{3/2}		Co 2p _{1/2}		Mn 2p _{3/2}		Mn 2p _{1/2}		Ni 2p _{3/2}	Ni 2p _{1/2}
	Co ²⁺	Co ³⁺	Co ²⁺	Co ³⁺	Mn ³⁺	Mn ⁴⁺	Mn ³⁺	Mn ⁴⁺	Ni ²⁺	Ni ²⁺
x = 0.00	780.95	779.91	796.43	795.11	641.58	644.49	652.63	654.82		
x = 0.05	783.15	780.61	798.15	795.66	641.99	644.45	653.49	655.61	855.30	872.60
x = 0.10	783.07	780.45	798.11	795.57	642.05	644.66	653.46	655.82	854.89	871.57
x = 0.15	783.04	780.48	798.17	795.60	641.97	641.97	653.46	655.62	854.86	872.40
x = 0.12	782.93	786.50	797.99	795.49	641.93	644.51	653.46	655.69	855.27	872.57



4.5.1.5 Characterization of surface area and pore size distribution of the Ni-doped MnCo_2O_4 nanofibers by BET method and BJH method

Surface area and pore-size distribution analysis of as-fabricated Ni-doped MnCo_2O_4 nanofibers were investigated by using N_2 adsorption/desorption experiments. Figure 4.74 (a-e) present N_2 adsorption/desorption isotherms and pore size distribution (inset) of $\text{Mn}_{1-x}\text{Ni}_x\text{Co}_2\text{O}_4$ ($x = 0.00, 0.05, 0.10, 0.15,$ and 0.20) nanofibers, which are a typical IV isotherm with a hysteresis loop according to the IUPAC classification (Huang *et al.*, 2017). The results suggest that the $\text{Mn}_{1-x}\text{Ni}_x\text{Co}_2\text{O}_4$ ($x = 0.00, 0.05, 0.10, 0.15,$ and 0.20) nanofibers have a mesoporous structure. The pore-size distribution of all samples is in the range of 2-10 nm attributed to a typical feature of a mesoporous structure. The (BET) specific surface area, total pore volume, and Mean pore diameter are summarized in Table 4.20. The BET specific surface area values were calculated to be $26.56 \text{ m}^2/\text{g}$, $61.94 \text{ m}^2/\text{g}$, $76.89 \text{ m}^2/\text{g}$, $89.55 \text{ m}^2/\text{g}$, and $38.8 \text{ m}^2/\text{g}$ for the Ni doping of $x = 0.00, 0.05, 0.10, 0.15,$ and 0.20 , respectively. The sample with Ni doping of $x = 0.15$ exhibits the highest BET specific surface area, which is higher than $58.9 \text{ m}^2/\text{g}$ in the MnCo_2O_4 nanofiber as reported by (Gao *et al.*, 2017). The increase in BET surface area values with increasing the doping Ni concentration of $x = 0.00$ to $x = 0.15$ was also associated with decreasing of the fiber diameter. However, the BET surface area values decrease in the samples with Ni content $x = 0.20$, which may be because the fibers are destroyed severely in this sample. It is common knowledge that more active sites for the electrolyte-ion insertion/extraction into the electrode material can be given by a large surface area. In addition, the larger pore volume results in that easy diffusion of electrolyte-ion to active material with less resistance (Cai *et al.*, 2014).

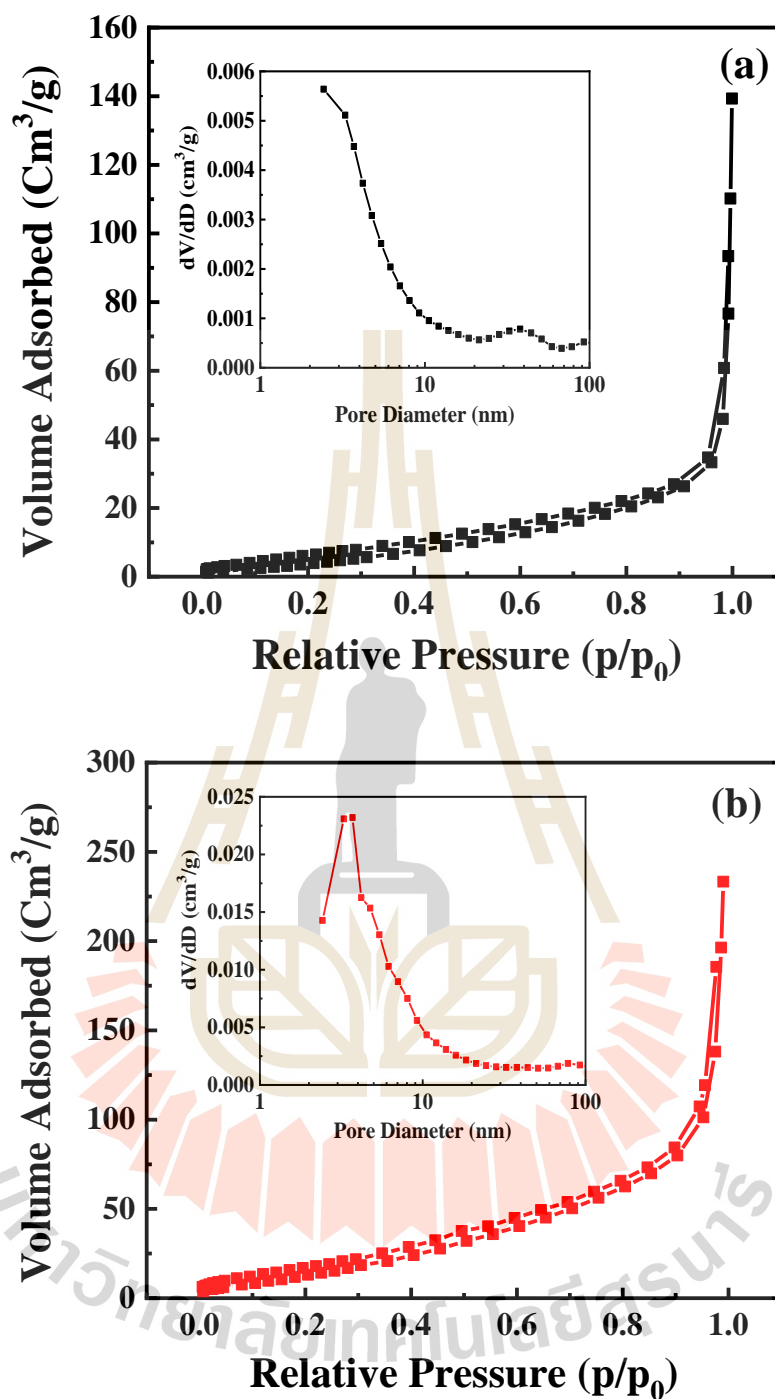


Figure 4.74 Nitrogen adsorption/desorption isotherms and pore size distribution (inset) of $\text{Mn}_{1-x}\text{Ni}_x\text{Co}_2\text{O}_4$ ($x = 0.00, 0.05, 0.10, 0.15,$ and 0.20) nanofibers.

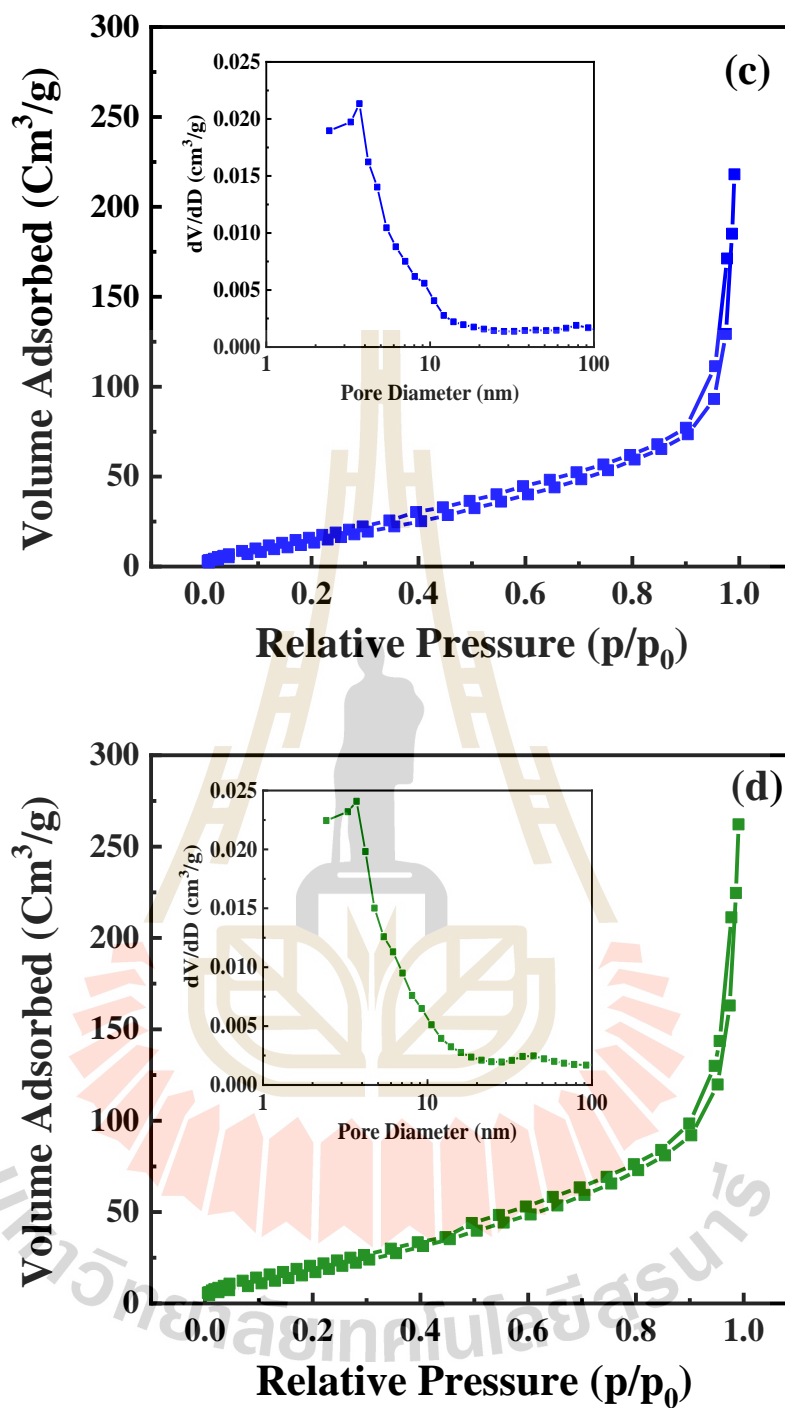


Figure 4.74 (Continued) Nitrogen adsorption/desorption isotherms and pore size distribution (inset) of $\text{Mn}_{1-x}\text{Ni}_x\text{Co}_2\text{O}_4$ ($x = 0.00, 0.05, 0.10, 0.15, \text{ and } 0.20$) nanofibers.

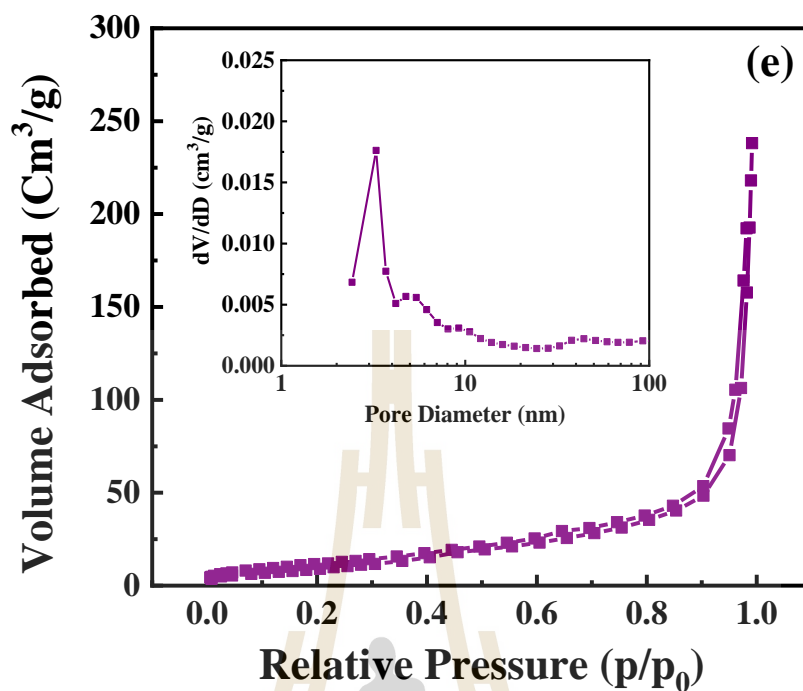


Figure 4.74 (Continued) Nitrogen adsorption/desorption isotherms and pore size distribution (inset) of $\text{Mn}_{1-x}\text{Ni}_x\text{Co}_2\text{O}_4$ ($x = 0.00, 0.05, 0.10, 0.15,$ and 0.20) nanofibers.

Table 4.20 Physical properties of spinel $\text{Mn}_{1-x}\text{Ni}_x\text{Co}_2\text{O}_4$ ($x = 0.00, 0.05, 0.10, 0.15,$ and 0.20) nanofibers.

Samples	BET specific surface area (m^2/g)	Total pore volume (cm^3/g)	Mean pore diameter (nm)
$x = 0.00$	26.56	0.107	16.11
$x = 0.05$	61.94	0.458	29.58
$x = 0.10$	76.89	0.345	18.47
$x = 0.15$	89.55	0.400	17.82
$x = 0.20$	38.80	0.344	35.35

4.5.2 Electrochemical properties

4.5.2.1 Cyclic voltammetry measurement

The electrochemical properties of $Mn_{1-x}Ni_xCo_2O_4$ ($x = 0.00, 0.05, 0.10, 0.15,$ and 0.20) NFs electrodes were carried out in a 6M KOH aqueous solution using three-electrode system. Figure 4.75(a-e) presents the cyclic voltammogram curves of $Mn_{1-x}Ni_xCo_2O_4$ ($x = 0.00, 0.05, 0.10, 0.15,$ and 0.20) NFs electrodes in a potential window in the range of -1.0 and 0.4 V at different scan rates. The three redox peaks are observed in the CV curves of all the samples, suggesting the feature of a faradaic redox reaction. The redox reactions are explained by the following equations (Li *et al.*, 2014; Bai *et al.*, 2016; Hao *et al.*, 2015; Tamboli *et al.*, 2017):



where M is indicative of Co or Ni and Mn.

The specific capacitance is related to the area under the CV curve. According to SEM and TEM analysis, the sample with Ni doping of $x = 0.20$ has the morphology features different from the other samples that the continuity and integrity of the nanofibers are destroyed leading to decreased electrochemical performance. For fabrication $Mn_{1-x}Ni_xCo_2O_4$ nanofibers with optimizing Ni content, the nanofiber structure results in the enlarging of the surface area leading to facilitate the electrons and ions transport and increase active sites or improve the cycling stability.

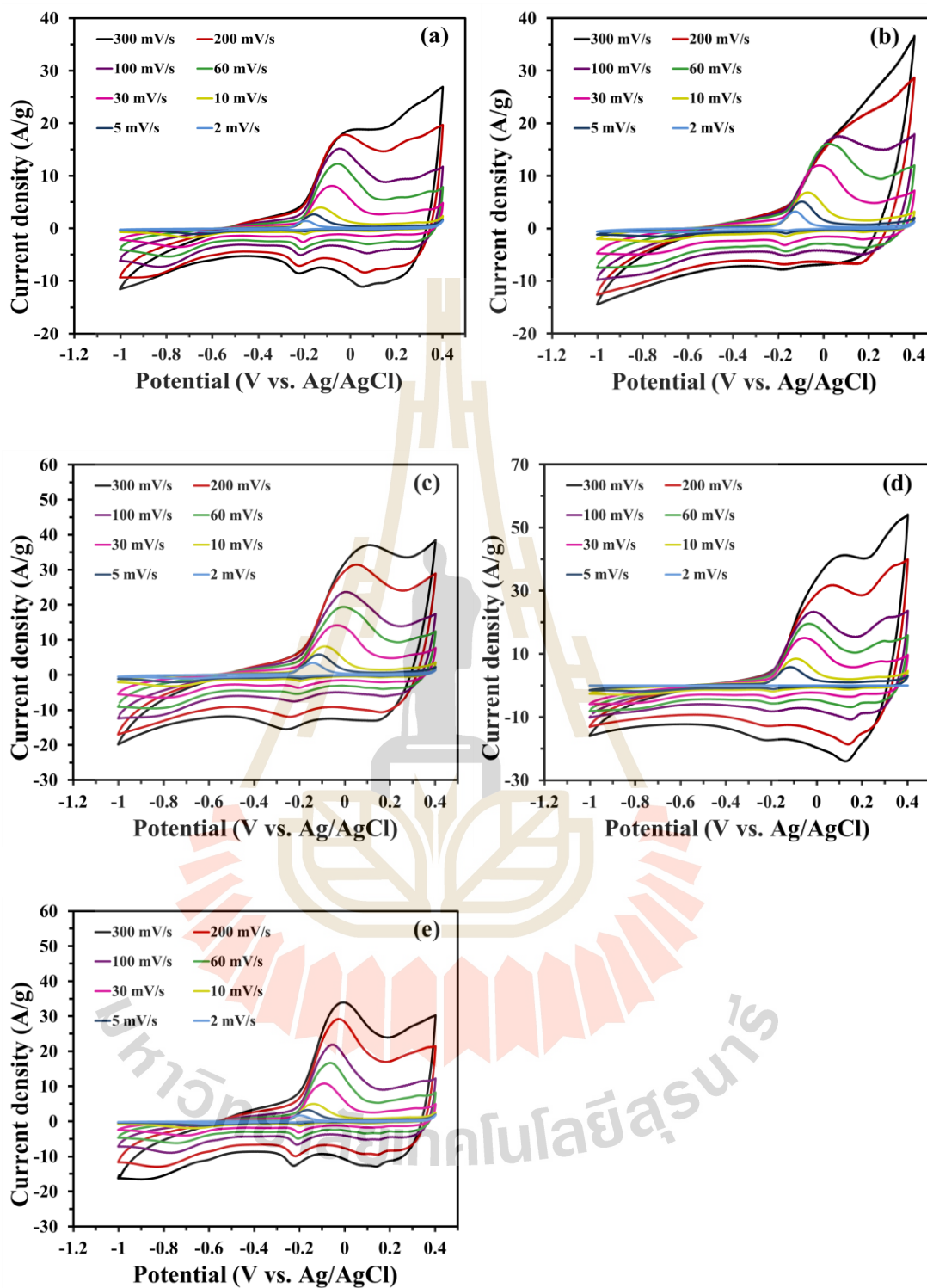


Figure 4.75 CV curves at various scan rates of $\text{Mn}_{1-x}\text{Ni}_x\text{Co}_2\text{O}_4$ nanofibers: (a) $x = 0.00$, (b) $x = 0.05$, (c) $x = 0.10$, (d) $x = 0.15$, and (e) $x = 0.20$.

4.5.2.2 Galvanostatic charge-discharge measurements

GCD measurement is an important technique for investigation the electrode material performance and calculation of the specific capacitance. Figure 4.76(a-e) show the charge-discharge curve of $\text{Mn}_{1-x}\text{Ni}_x\text{Co}_2\text{O}_4$ ($x = 0.00, 0.05, 0.10, 0.15, \text{ and } 0.20$) NFs electrodes with various current density of 1, 2, 3, 5, 7, 10, 15, and 20 A/g. At the same current density, the longest the discharge time suggests the best capacitance performance. It can be seen that the $\text{Mn}_{1-x}\text{Ni}_x\text{Co}_2\text{O}_4$ NFs electrodes with $x = 0.15$ shows the longest charge-discharge time which is consistent with the CV curve analysis. Figure 4.77 shows the calculated specific capacitance at a function of current density. The specific capacitance values at 1 A/g of $\text{Mn}_{1-x}\text{Ni}_x\text{Co}_2\text{O}_4$ NFs electrodes with $x = 0.00, 0.05, 0.10, 0.15, \text{ and } 0.20$ are 76, 128, 190, 208, and 101 F/g, respectively. The specific capacitance decreases with the increase of current density owing to the existence of material resistance resulting in polarization effect under high current (Wang *et al.*, 2018). The BET specific surface area of the Ni-doped MnCo_2O_4 nanofibers with Ni doping of $x = 0.15$ is the highest, and it can improvements in electrochemical performance. With the increase of Ni concentration with $x = 0.20$, the morphology of Ni-doped MnCo_2O_4 nanofibers is destroyed resulting in the decreases of electrochemical properties.

During continuous 1000 cycles, the cyclic performance of the samples was evaluated as shown in Figure 4.78. In the case of the MnCo_2O_4 nanofibers with Ni doping of $x = 0.15$, the capacitance retention was about 84% after 2000 cycles, suggesting a good cycling ability. In conclusion, the effect of Ni substituted in MnCo_2O_4 has really improved the electrochemical properties of electrode materials, but it needs to maintain the integrity and clear interface of the NFs structure.

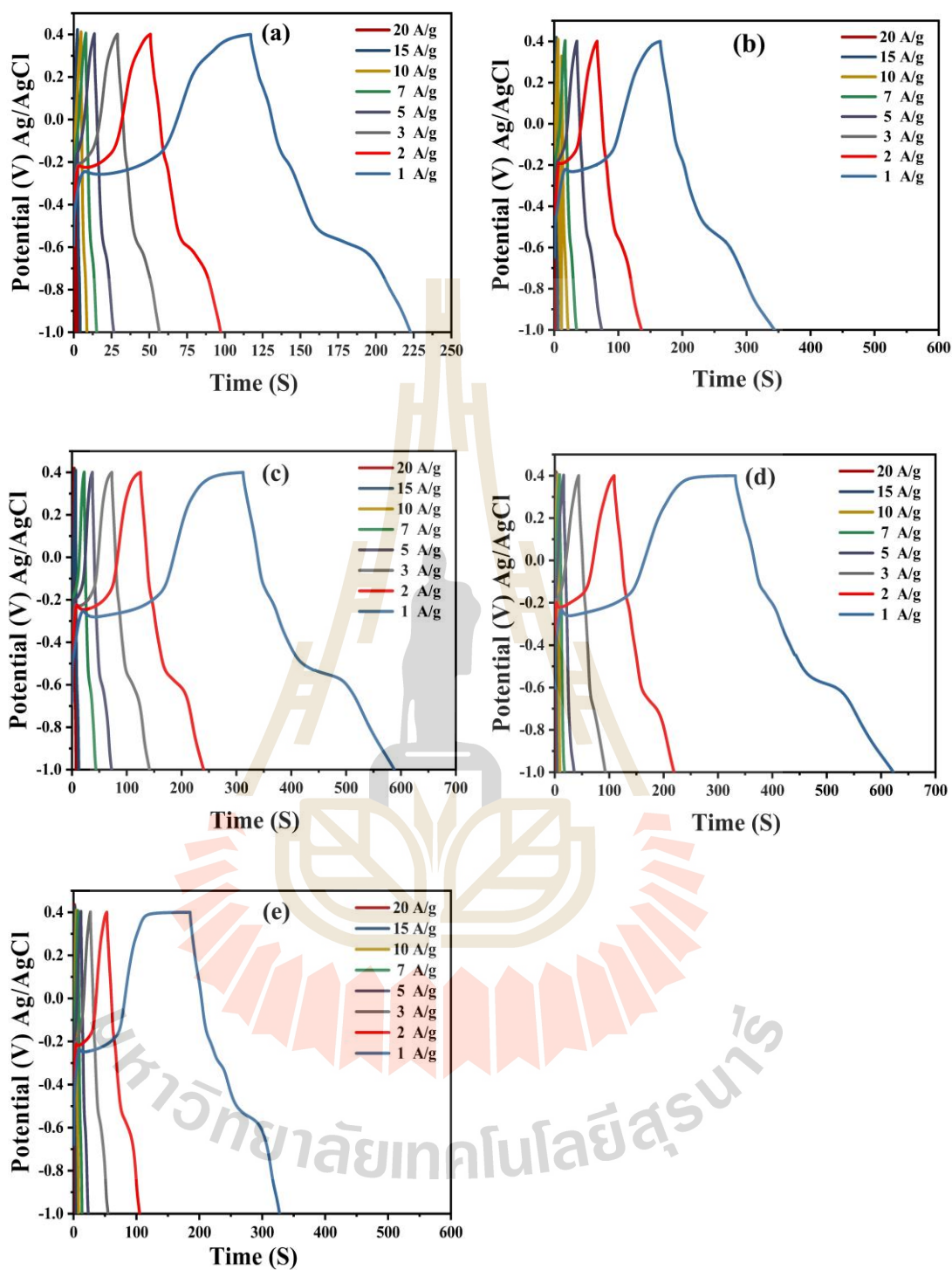


Figure 4.76 Galvanostatic charge-discharge curves at various current densities of $\text{Mn}_{1-x}\text{Ni}_x\text{Co}_2\text{O}_4$ nanofibers: (a) $x = 0.00$, (b) $x = 0.05$, (c) $x = 0.10$, (d) $x = 0.15$, and (e) $x = 0.20$.

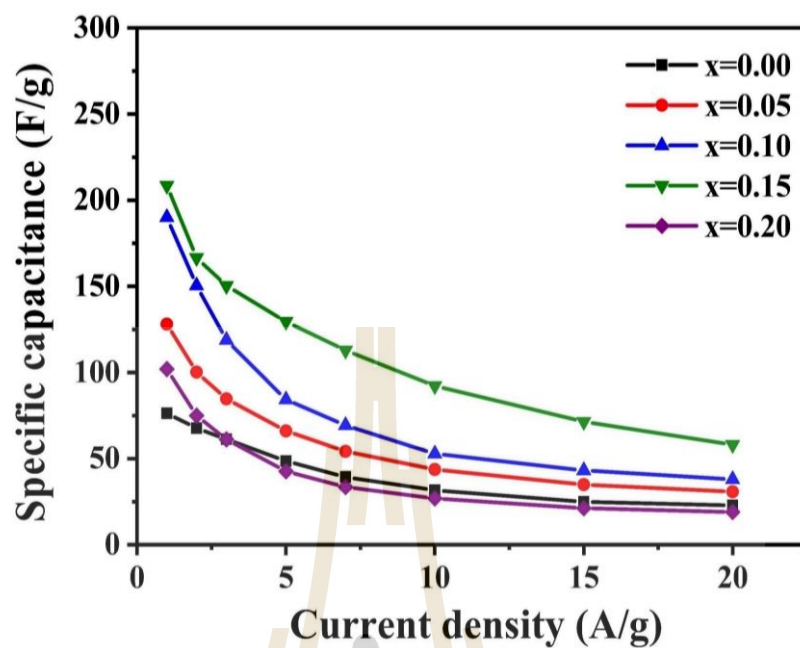


Figure 4.77 Comparison of the specific capacitance at various a current density of $\text{Mn}_{1-x}\text{Ni}_x\text{Co}_2\text{O}_4$ ($x = 0.00, 0.05, 0.10, 0.15,$ and 0.20) nanofibers.

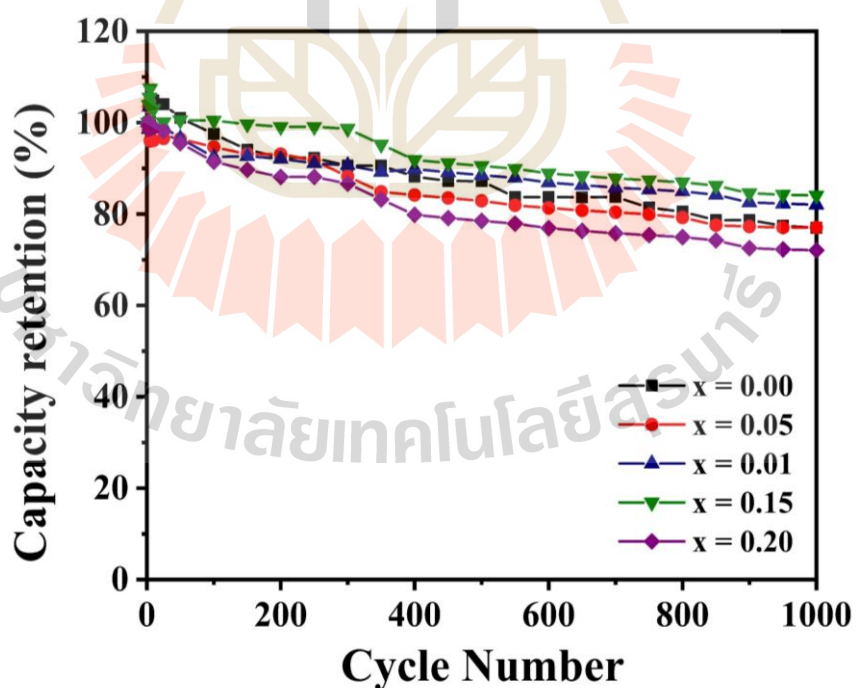


Figure 4.78 Capacity retention (%) of $\text{Mn}_{1-x}\text{Ni}_x\text{Co}_2\text{O}_4$ ($x = 0.00, 0.05, 0.10, 0.15,$ and 0.20) nanofibers and after 1000 cycles at a current density of 2 A/g .

4.5.2.3 Electrochemical impedance spectroscopy (EIS)

Nyquist plots of $\text{Mn}_{1-x}\text{Ni}_x\text{Co}_2\text{O}_4$ ($x = 0.00, 0.05, 0.10, 0.15,$ and 0.20) NFs electrodes are shown in Figure 4.79. The Nyquist plot of $\text{Mn}_{0.85}\text{Ni}_{0.15}\text{Co}_2\text{O}_4$ displays the more vertical the curve as compared with the other electrode, indicating less diffusion resistance than others due to faster ion transportation of the electrolyte inside the porous electrode (Sawangphruk *et al.*, 2013). The equivalent series resistance (R_{ESR}) or solution resistance (R_s) is obtained from the intercept on the real axis at high frequency. All the electrodes show the small semicircles indicating the high electrical conductivity of the electrode. Thus, $\text{Mn}_{0.85}\text{Ni}_{0.15}\text{Co}_2\text{O}_4$ nanofibers has a high electrochemical performance as compared with other samples.

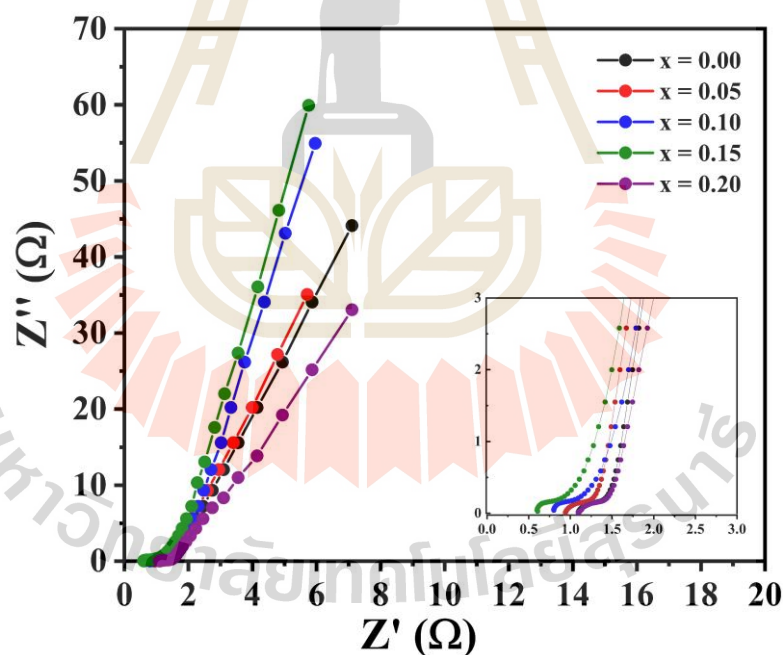


Figure 4.79 The Nyquist plots of the of $\text{Mn}_{1-x}\text{Ni}_x\text{Co}_2\text{O}_4$ ($x = 0.00, 0.05, 0.10, 0.15,$ and 0.20) NFs electrodes at various calcination temperature.

4.6 Zn-doped MnCo_2O_4 nanofibers

4.6.1 Structural and morphology characterization

4.6.1.1 X-ray diffraction (XRD) analysis of the Zn-doped MnCo_2O_4 nanofibers

As shown in Figure 4.80(a), the X-ray diffraction patterns show the presence of pure MnCo_2O_4 phase (JCPDS No. 23-127) without any impurity peaks related to Zn or its suboxides for all the samples. This suggests the good dispersion of Zn^{+2} (0.74 Å) ions on the sites of Mn^{3+} (0.72 Å) ions. Further, the broad crystalline peaks are the result of the nanocrystalline structure of the samples. Interestingly, the shift of diffraction angle (2θ) along the (311) major planes as a function of Zn doping in MnCo_2O_4 nanofibers were observed which can be attributed to the substitution of Zn ions (0.74 Å) in place of Mn ions (0.72 Å) (Figure 4.80(b)). This is due to the tensile stress which results in the shift to a lower angle. The crystallite size was evaluated for (311) peak of all the samples by using Scherrer formula and found to be 60.0, 64.3, 87.0, 108.0, and 118.8 nm for Ni doping concentration $x = 0.00, 0.05, 0.10, 0.15,$ and 0.20, respectively. It is obvious that the crystallite size increases with increasing Zn concentration. The calculated d-spacing values and lattice constant for all samples are shown in Table 4.21. The d-spacing values increases with increasing Zn concentration, which further suggests successful substitution of Zn ions with the larger ionic radius on the sites of the smaller ionic radius of Mn ions in MnCo_2O_4 lattice.

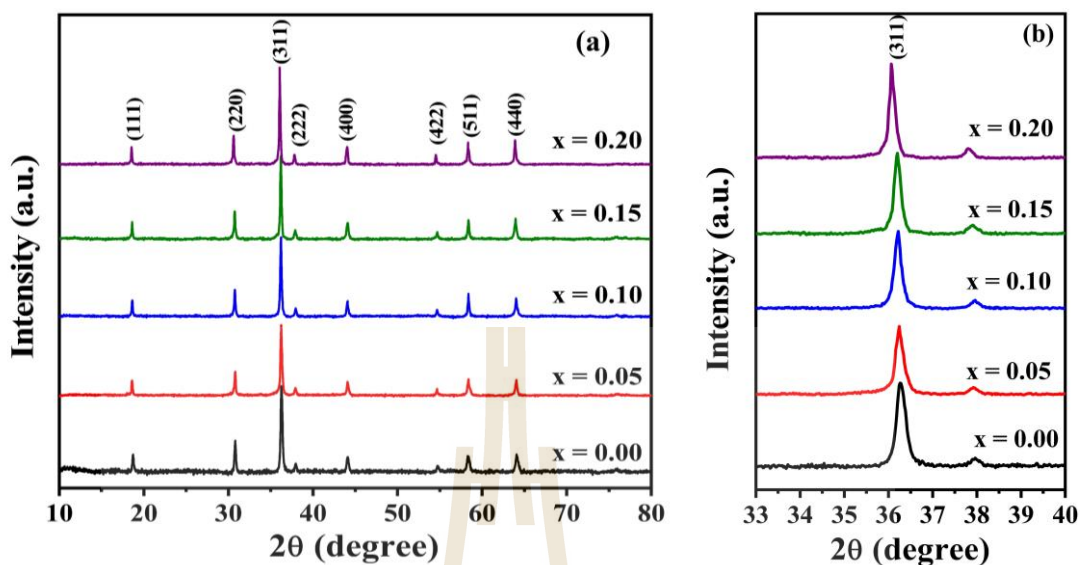


Figure 4.80 (a) XRD patterns of $\text{Mn}_{1-x}\text{Zn}_x\text{Co}_2\text{O}_4$ ($x = 0.00, 0.05, 0.10, 0.15,$ and 0.20) nanofibers and (b) relative shift in (311) peak of MnCo_2O_4 with respect to Zn-doping.

Table 4.21 Summary of crystallite sizes (D) from XRD, d -spacing (d), and lattice constant (a) of $\text{Mn}_{1-x}\text{Zn}_x\text{Co}_2\text{O}_4$ ($x = 0.00, 0.05, 0.10, 0.15,$ and 0.20) nanofibers.

samples	Crystallite sizes	d -spacing	Lattice constant
	D (nm)	d (Å)	a (nm)
$x = 0.00$	60.0	2.475	8.210
$x = 0.05$	64.3	2.476	8.211
$x = 0.10$	87.0	2.480	8.226
$x = 0.15$	108.0	2.481	8.228
$x = 2.00$	118.8	2.490	8.259

4.6.1.2 The Morphology of the Zn-doped MnCo_2O_4 nanofibers by FESEM and TEM

Figure 4.81(a-e) show the FESEM images of the $\text{Mn}_{1-x}\text{Zn}_x\text{Co}_2\text{O}_4$ ($x = 0.00, 0.05, 0.10, 0.15,$ and 0.20) nanofibers. There are small particles obtained everywhere in the main nanofiber and the particle size increase with increasing the Zn content. It can be clearly seen that the nanofiber was destroyed in the samples with $x = 0.15$ and $x = 0.20$. The TEM bright field images with corresponding SAED and particle size distribution are reported in Figure 4.82. As a TEM bright field images, the small particles were observed in nanofibers. The diameters of the nanofibers are about 242-340, 138-200, 137-243, 142-260, and 135-238 nm for the samples with $x = 0.00, 0.05, 0.10, 0.15,$ and 0.20 . The average particle sizes are 29, 42, 67, 68, and 69 nm for the samples with $x = 0.00, 0.05, 0.10, 0.15,$ and 0.20 that the particle sizes tend to increase with increasing the Zn concentration corresponding with the FESEM images. The SAED patterns of all the samples exhibit many diffraction spots on diffraction rings, indicating a polycrystalline property and the feature of the MnCo_2O_4 phase, which is accepted by the XRD results.

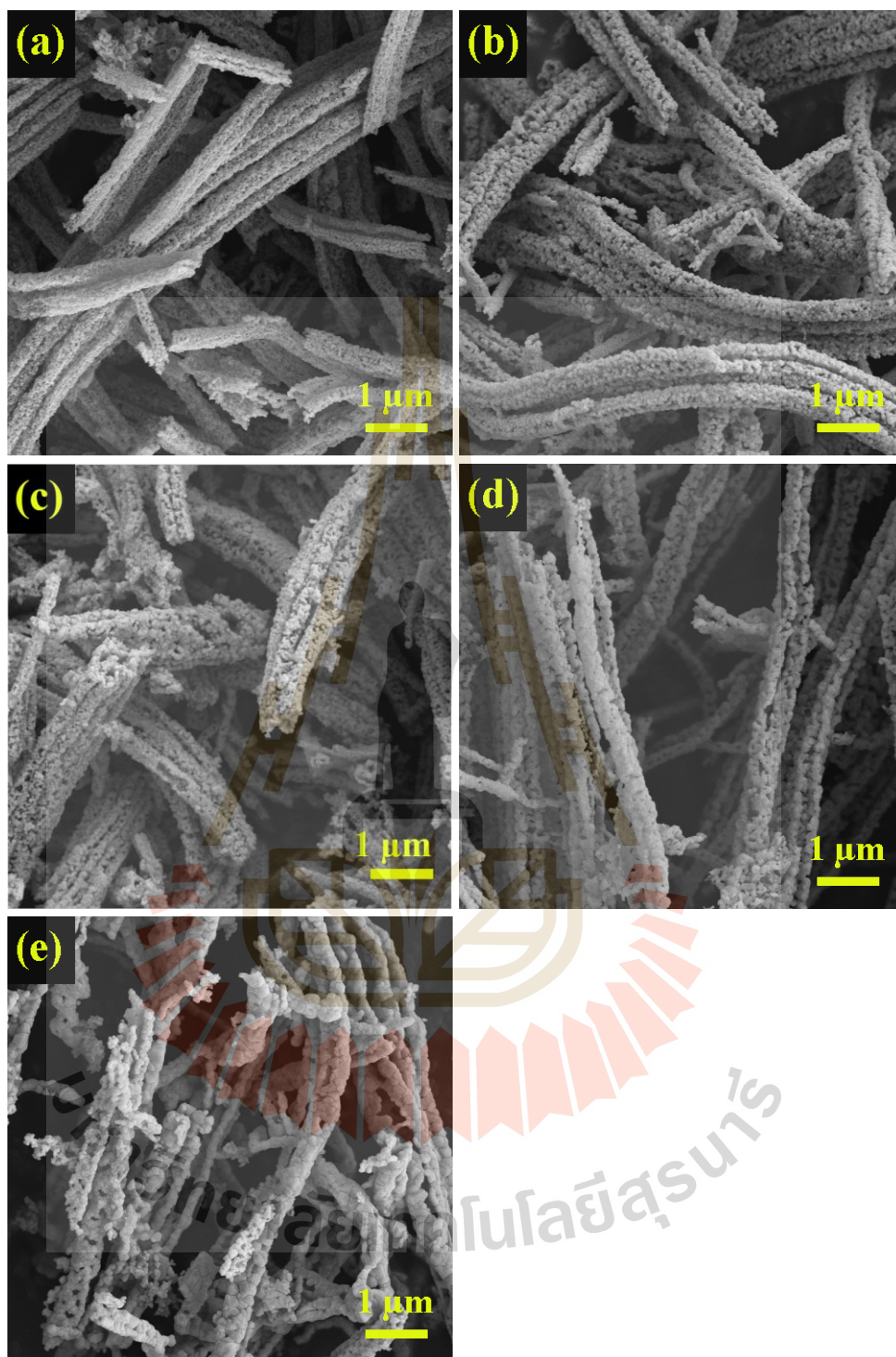


Figure 4.81 FESEM images of $\text{Mn}_{1-x}\text{Zn}_x\text{Co}_2\text{O}_4$ nanofibers: (a) $x = 0.00$, (b) $x = 0.05$, (c) $x = 0.10$, (d) $x = 0.15$, and (e) $x = 0.20$.

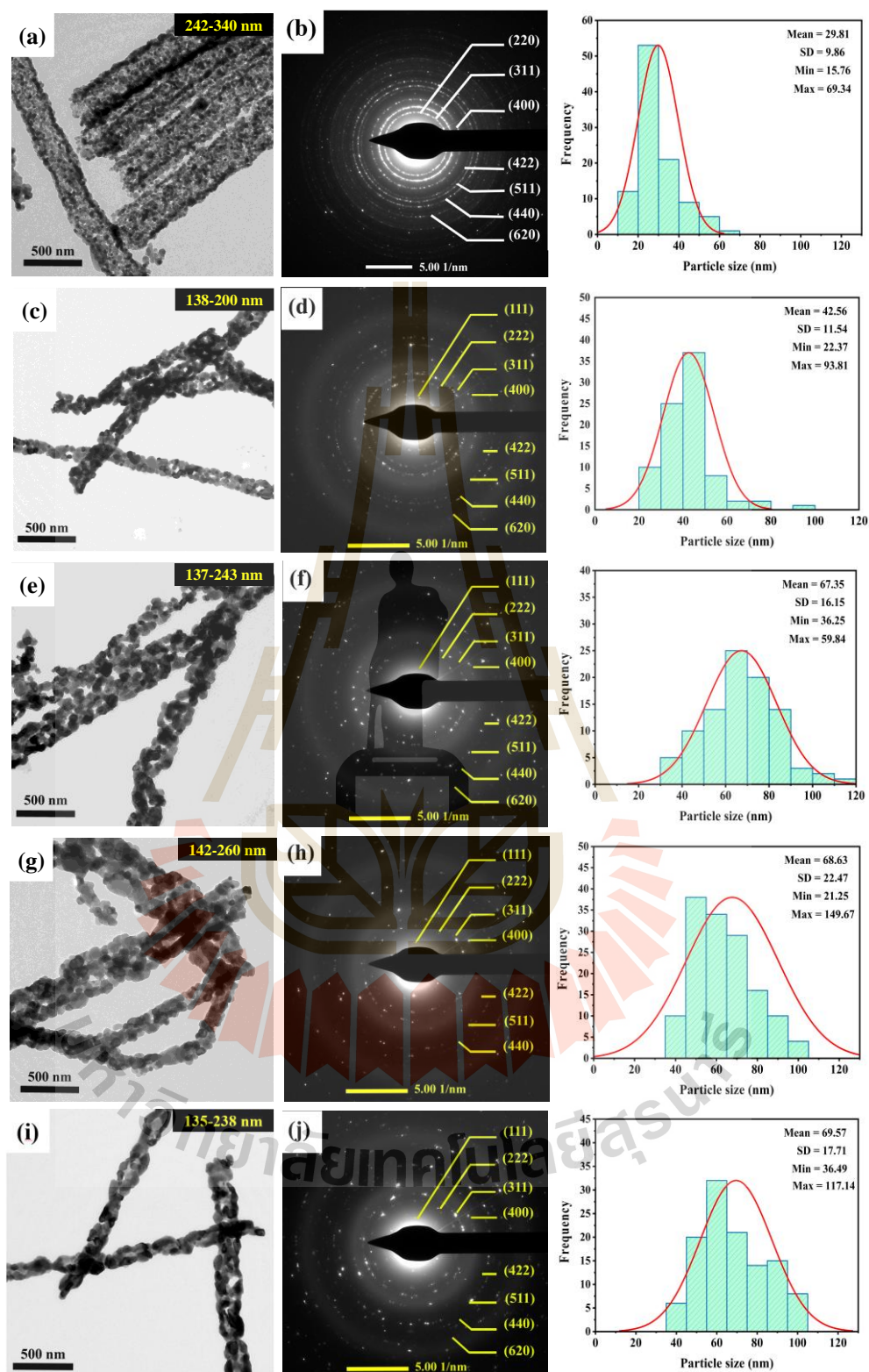


Figure 4.82 TEM images with corresponding SAED of $\text{Mn}_{1-x}\text{Zn}_x\text{Co}_2\text{O}_4$ nanofibers:

(a,b) $x = 0.00$, (c,d) $x = 0.05$, (e,f) $x = 0.10$, (g,h) $x = 0.15$, and (i,j) $x = 0.20$.

4.6.1.3 X-ray absorption spectroscopy study of the Zn-doped MnCo₂O₄ nanofibers

The normalized Co K-edge XANES spectra of all the samples were recorded and compared with Co foil, CoO and Co₂O₃ standards, as shown in Figure 4.83. The Co-edge position of all the samples are very close to Co₂O₃ (Co^{2+/3+}) standards reflecting to the combination oxidation state of Co^{2+/3+}. Figure 4.84 displays the Mn K-edge XANES spectra of Zn-doped MnCo₂O₄ nanofibers as compared with the Mn foil (Mn⁰⁺), Mn₂O₃ (Mn³⁺), and MnO₂ (Mn⁴⁺) standards. The Mn-edge position of all the samples occur between Mn₂O₃ (Mn³⁺) and MnO₂ (Mn⁴⁺) standards corresponding to the combining oxidations state of Mn^{3+/4+}. The Zn K-edge XANES spectra of Zn-doped MnCo₂O₄ nanofibers as compared with the Zn foil (Zn⁰⁺) and ZnO (Zn²⁺) standards is presented in Figure 4.85. The close resemblance between the Zn K-edge XANES spectrum of Mn_{1-x}Zn_xCo₂O₄ nanofibers and ZnO standards compound reveals that the zinc ions in all samples have oxidation state of Zn²⁺. In addition, the oxidation state of Co, Mn, and Zn can be confirmed by the edge energy as presented in the Table 4.22.

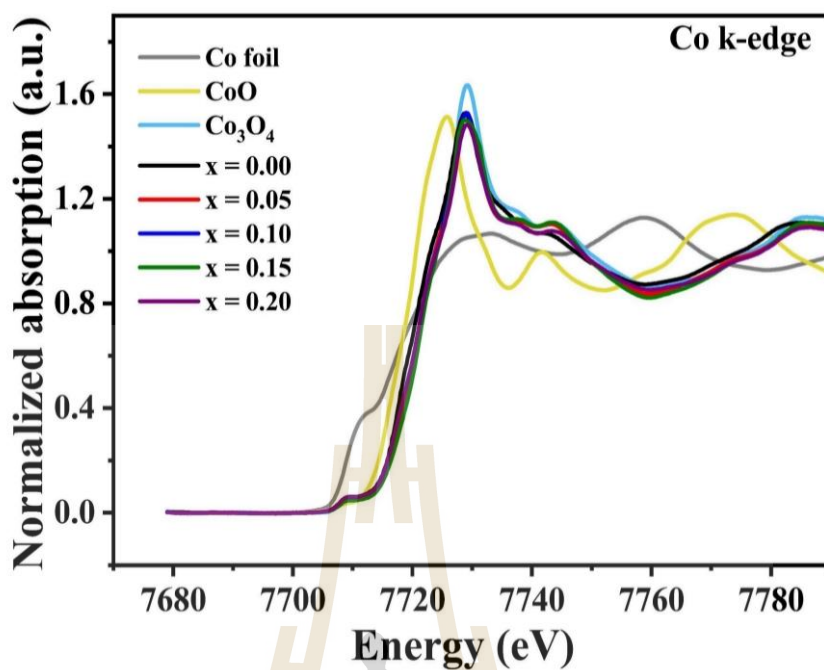


Figure 4.83 Normalized XANES spectra and of $\text{Mn}_{1-x}\text{Zn}_x\text{Co}_2\text{O}_4$ ($x = 0.00, 0.05, 0.10, 0.15,$ and 0.20) nanofibers at Co K-edge.

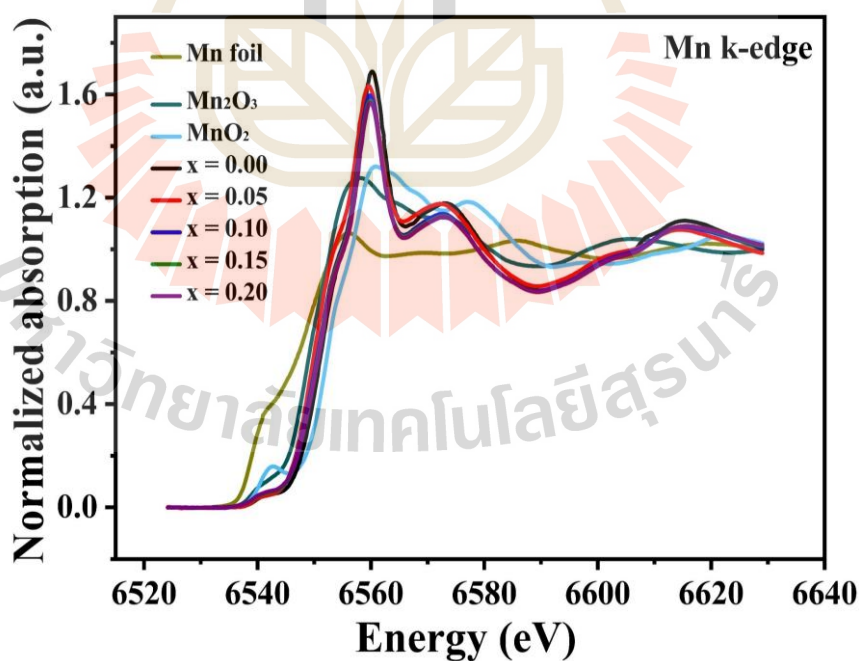


Figure 4.84 Normalized XANES spectra and of $\text{Mn}_{1-x}\text{Zn}_x\text{Co}_2\text{O}_4$ ($x = 0.00, 0.05, 0.10, 0.15,$ and 0.20) nanofibers at Mn K-edge.

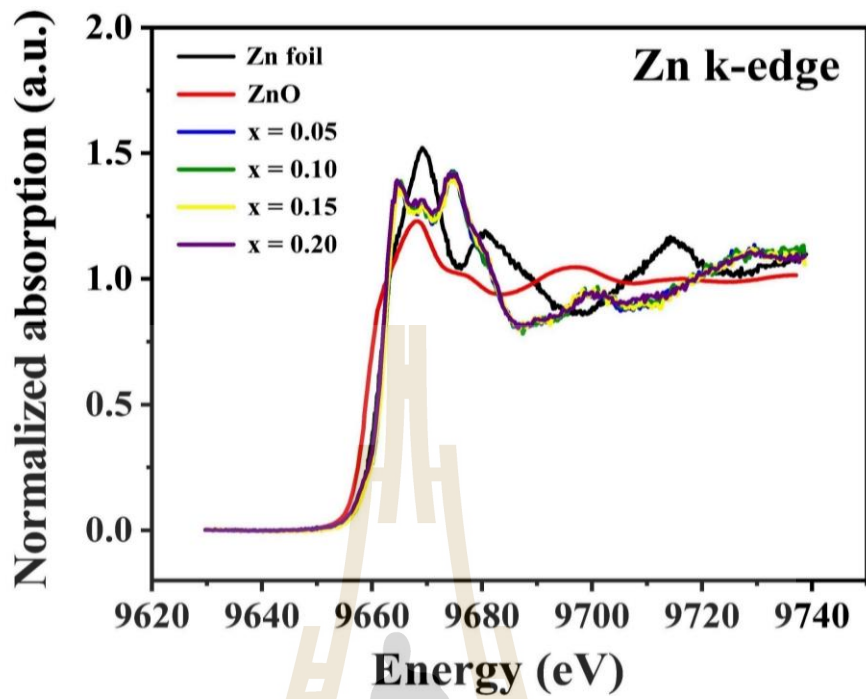


Figure 4.85 Normalized XANES spectra and of $\text{Mn}_{1-x}\text{Zn}_x\text{Co}_2\text{O}_4$ ($x = 0.00, 0.05, 0.10, 0.15,$ and 0.20) nanofibers at Zn K-edge.

Table 4.22 Edge energy and Oxidation state of the standard samples and $Mn_{1-x}Zn_xCo_2O_4$ ($x = 0.00, 0.05, 0.10, 0.15,$ and 0.20) nanofibers.

Samples	Edge element	Absorption Edge (eV)	Oxidation state
CoO	Co	7717.03	+2
Co ₃ O ₄	Co	7719.74	+2, +3
Mn ₂ O ₃	Mn	6548.61	+3
MnO ₂	Mn	6552.07	+4
ZnO	Zn	9661.03	+2
x = 0.00	Co	7719.67	+2, +3
	Mn	6550.76	+3, +4
x = 0.05	Co	7718.45	+2, +3
	Mn	6549.68	+3, +4
	Zn	9661.04	+2
x = 0.10	Co	7718.45	+2, +3
	Mn	6549.93	+3, +4
	Zn	9661.04	+2
x = 0.15	Co	7718.45	+2, +3
	Mn	6550.18	+3, +4
	Zn	9661.04	+2
x = 0.20	Co	7718.45	+2, +3
	Mn	6549.98	+3, +4
	Zn	9661.04	+2

4.6.1.4 X-ray photoelectron spectroscopy (XPS) study of the Zn-doped MnCo₂O₄ nanofibers

X-ray photoelectron spectroscopy (XPS) are employed to understand the elemental composition and oxidation state of Zn-doped MnCo₂O₄ nanofibers. The survey scan XPS spectrums of the Zn-doped MnCo₂O₄ nanofibers in Figure 4.86 suggest the presence of elements Co, Mn, Zn, O and C from the reference and absence of other impurities in all samples. The Co 2p high resolution spectrum of all the samples are shown in Figure 4.87. The two major peaks were observed at binding energy of ~779 (Co 2p_{3/2}) and ~794 eV (Co 2p_{1/2}). After Gaussian fitting, the Co 2p spectra of all the samples can be well-fitted with two spin-orbit doublets and 4 shakeup satellites (denoted as “Sat.”), assigned to the existence of Co²⁺ and Co³⁺ in all the samples. Orbital splitting energy of 15.66 eV and satellite peak are characteristic of the MnCo₂O₄. The first satellite peak at 3.5-6.5 eV above the Co 2p_{3/2} peak is typical of Co²⁺ ions, and second satellite peak at 9-10 eV above the Co 2p_{1/2} main peak is assigned to Co³⁺ ions (Che *et al.*, 2016; Li *et al.*, 2015; Wang *et al.*, 2015; Qiu *et al.*, 2015; Naveen and Selladurai, 2015). By using the Gaussian fitting method, Mn 2p was well-fitted with two spin-orbit doublets (Figure 4.88), which are characteristic of Mn³⁺ and Mn⁴⁺. The fitting peaks at ~642 (Mn 2p_{3/2}) and ~653 eV (Mn 2p_{1/2}) were indexed to Mn³⁺, while the peaks at ~645 (Mn 2p_{3/2}) and ~655 eV (Mn 2p_{1/2}) were indexed to Mn⁴⁺. The Zn 2p XPS spectra of all the samples exhibit major peaks with binding energy of 1022 eV (Zn 2p_{3/2}) and 1045 eV (Zn 2p_{1/2}), indicating that Zn²⁺ is existing in all the Zn-doped MnCo₂O₄ samples, as presented in Figure 4.89. Figure 4.41 shows the high-resolution O 1s XPS spectra for Zn-doped MnCo₂O₄ nanofibers. It reveals that the O 1s spectra of all the samples can be fitted into three components at 530, 532, and 533

eV, which are related to the metal–oxygen bonds, the oxygen in OH^- groups and the oxygen atom of the adsorbed water molecules, respectively. The XPS result are also in well agreeable with the XANES analysis. The coexistence of the Zn^{2+} , $\text{Co}^{2+}/\text{Co}^{3+}$ and $\text{Mn}^{3+}/\text{Mn}^{4+}$ may provide the electrochemical activity that led to an improvement in the electrochemical properties.

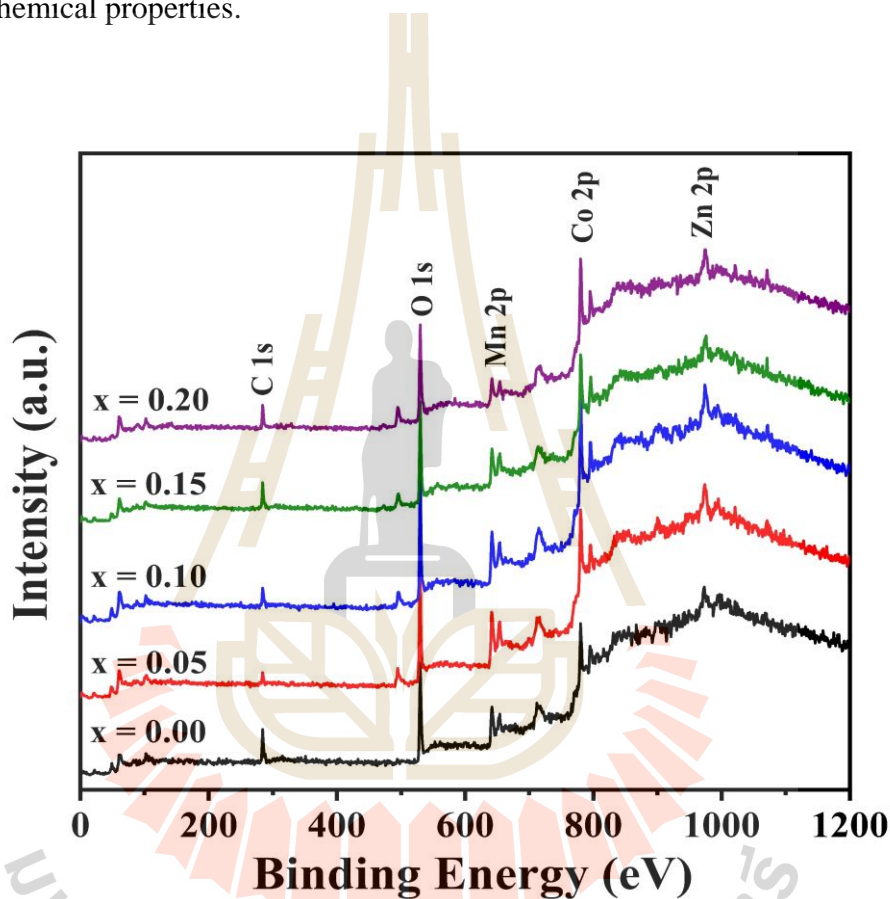


Figure 4.86 XPS survey spectrum of the $\text{Mn}_{1-x}\text{Zn}_x\text{Co}_2\text{O}_4$ ($x = 0.00, 0.05, 0.10, 0.15,$ and 0.20) nanofibers.

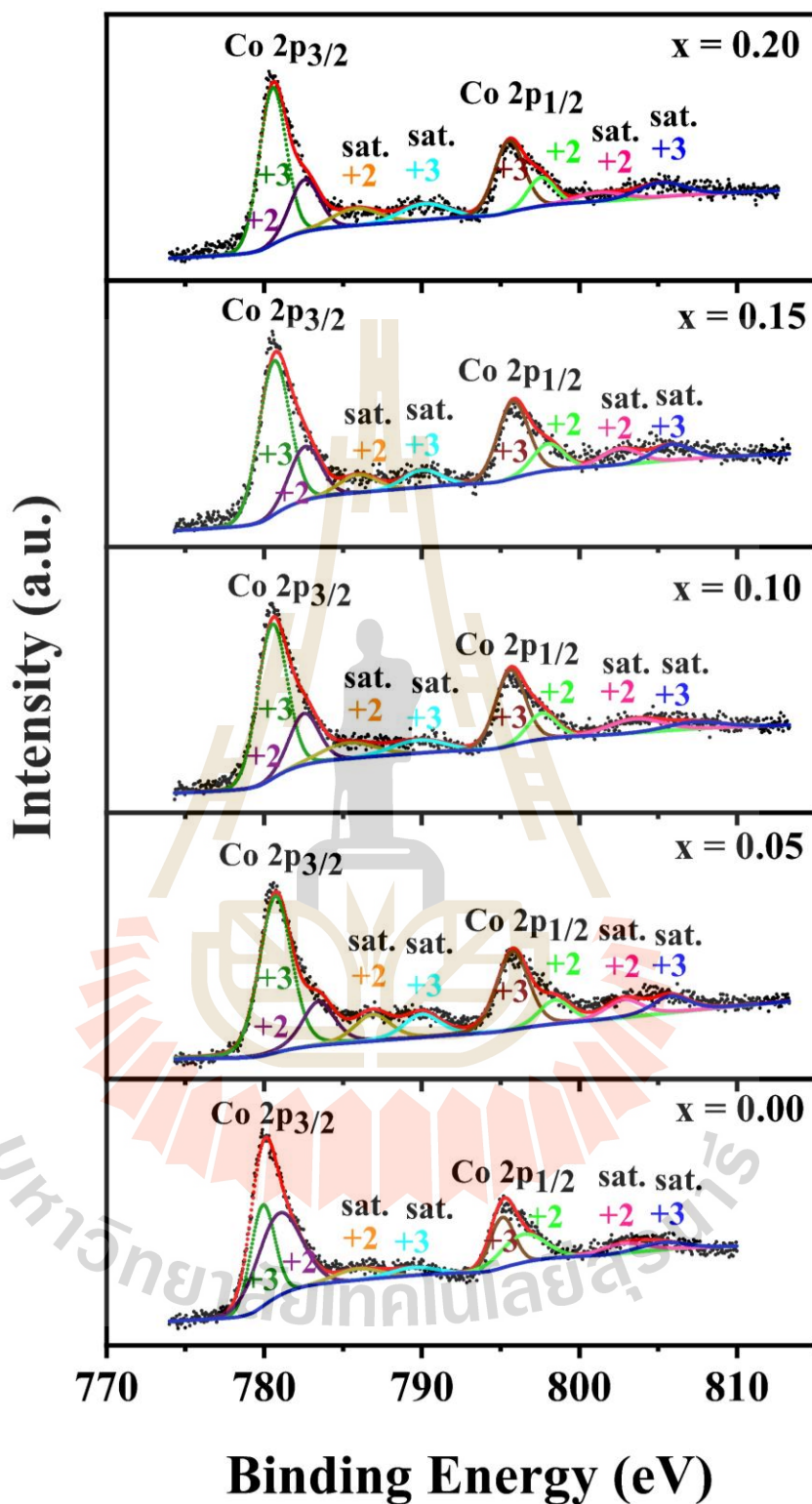


Figure 4.87 XPS spectra at Co 2p of the $\text{Mn}_{1-x}\text{Zn}_x\text{Co}_2\text{O}_4$ ($x = 0.00, 0.05, 0.10, 0.15,$ and 0.20) nanofibers.

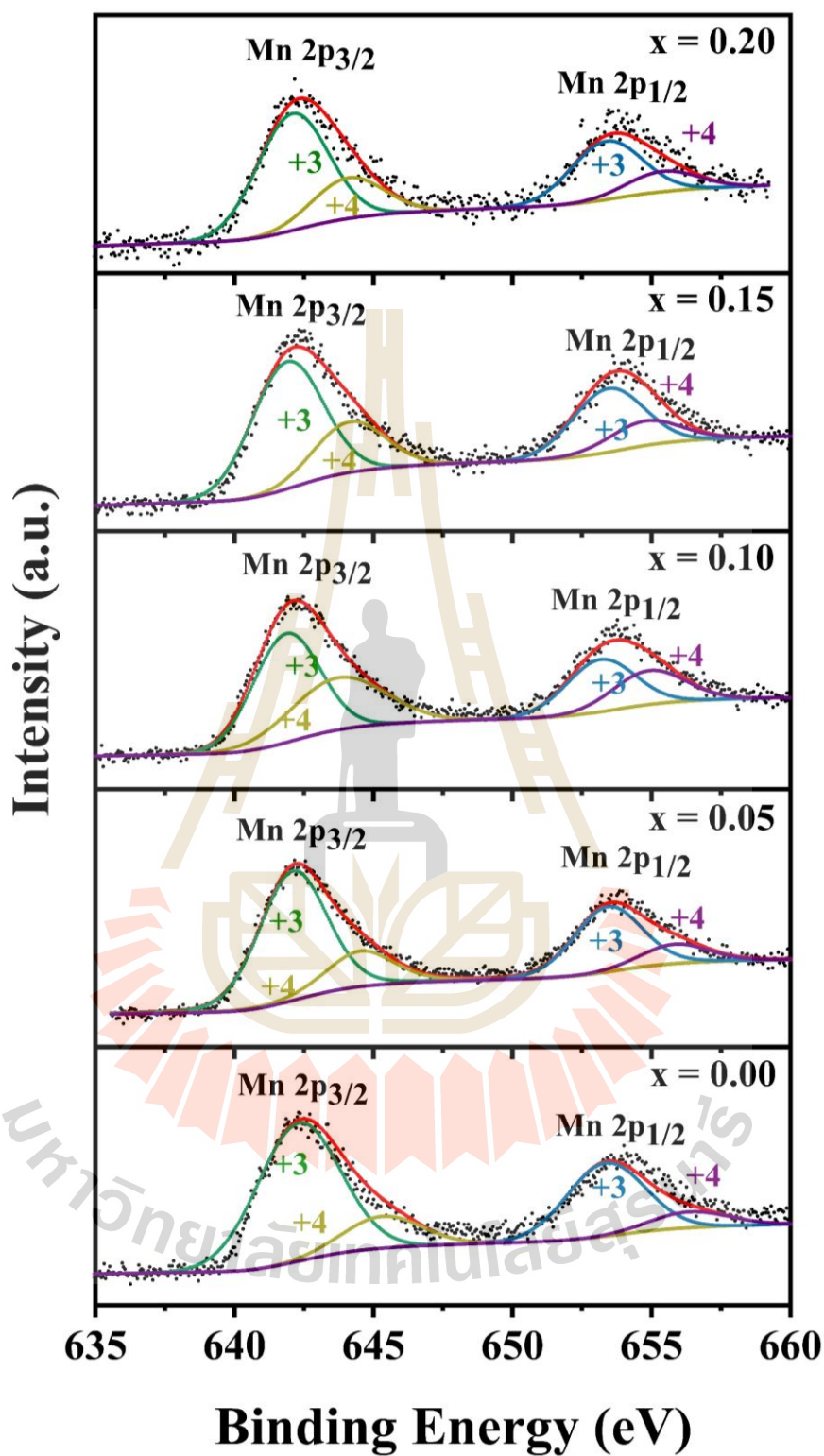


Figure 4.88 XPS spectra at Mn 2p of the $\text{Mn}_{1-x}\text{Zn}_x\text{Co}_2\text{O}_4$ ($x = 0.00, 0.05, 0.10, 0.15,$ and 0.20) nanofibers.

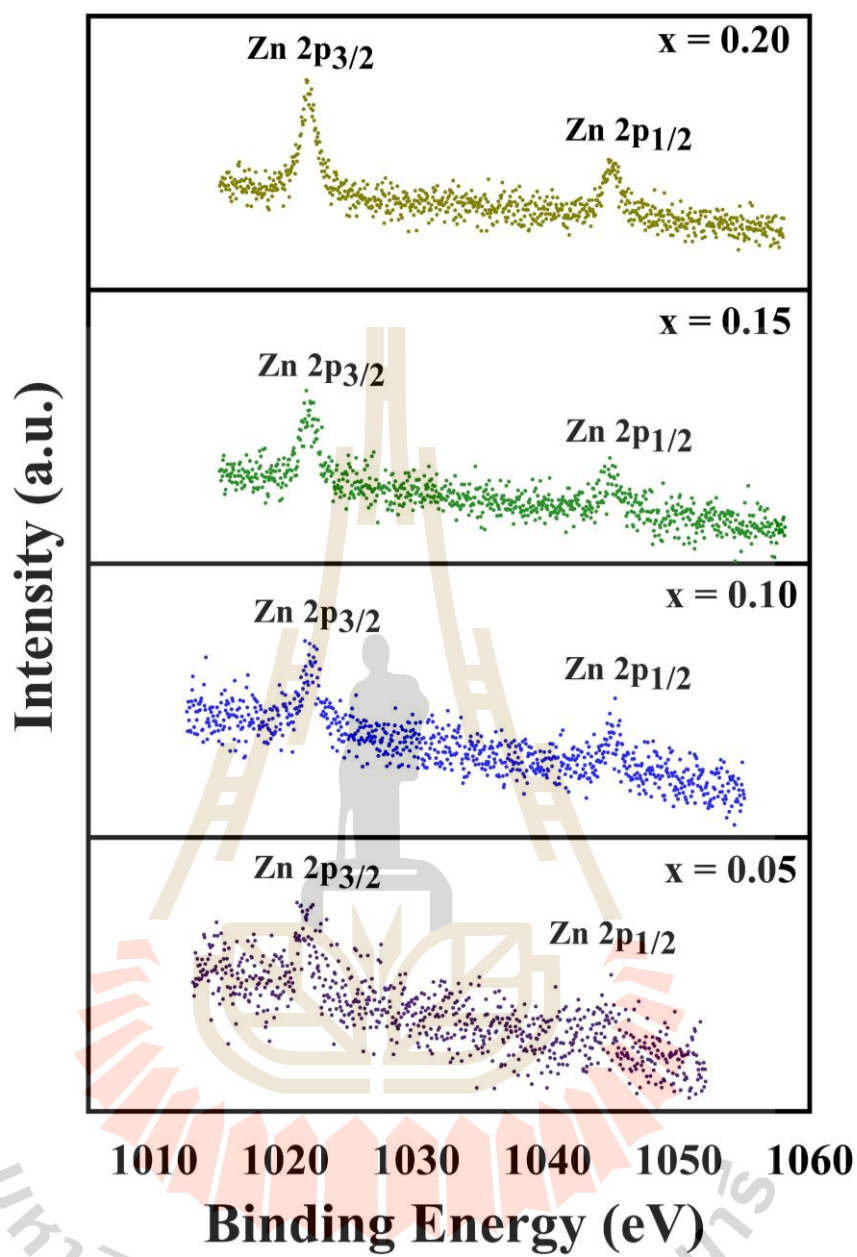


Figure 4.89 XPS spectra at Zn 2p of the $\text{Mn}_{1-x}\text{Zn}_x\text{Co}_2\text{O}_4$ ($x = 0.05, 0.10, 0.15,$ and 0.20) nanofibers.

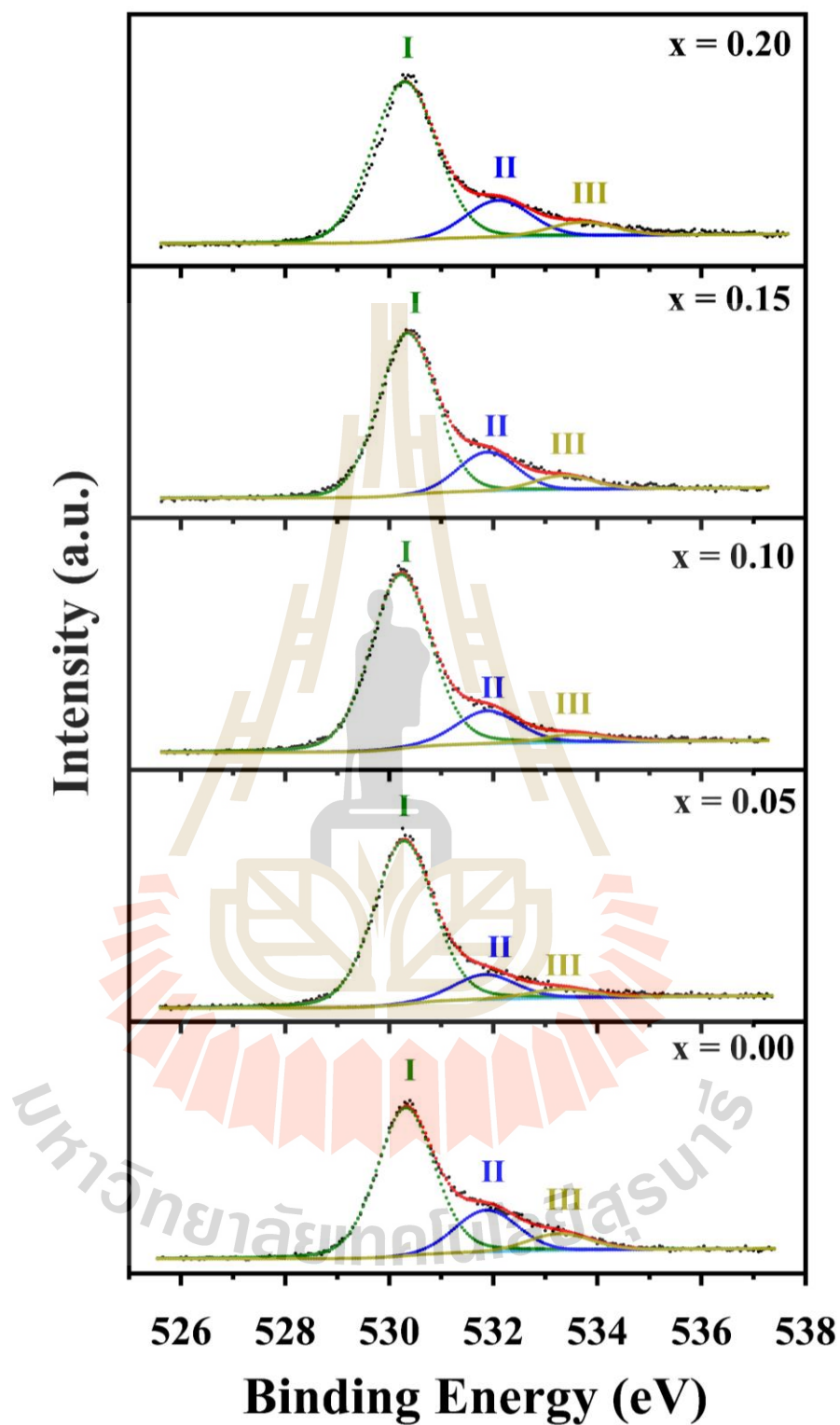
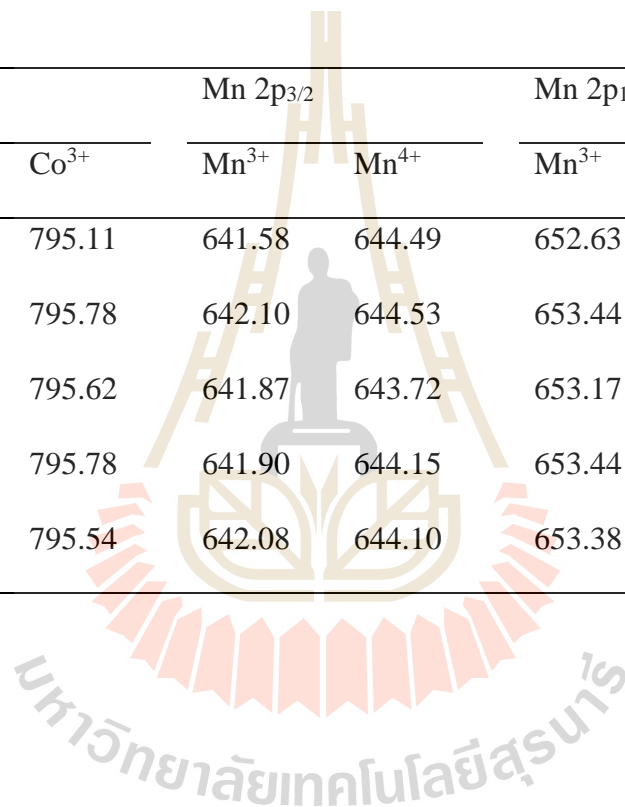


Figure 4.90 XPS spectra at O 1s of the $\text{Mn}_{1-x}\text{Zn}_x\text{Co}_2\text{O}_4$ ($x = 0.00, 0.05, 0.10, 0.15,$ and 0.20) nanofibers.

Table 4.23 XPS data of the $\text{Mn}_{1-x}\text{Zn}_x\text{Co}_2\text{O}_4$ ($x = 0.00, 0.05, 0.10, 0.15,$ and 0.20) nanofibers.

Binding energy position (eV)										
Samples	Co 2p _{3/2}		Co 2p _{1/2}		Mn 2p _{3/2}		Mn 2p _{1/2}		Zn 2p _{3/2}	Zn 2p _{1/2}
	Co ²⁺	Co ³⁺	Co ²⁺	Co ³⁺	Mn ³⁺	Mn ⁴⁺	Mn ³⁺	Mn ⁴⁺	Zn ²⁺	Zn ²⁺
x = 0.00	780.95	779.91	796.43	795.11	641.58	644.49	652.63	654.82		
x = 0.05	783.46	780.73	798.46	795.78	642.10	644.53	653.44	655.83	1022.19	1044.25
x = 0.10	782.53	780.52	797.63	795.62	641.87	643.72	653.17	654.92	1022.15	1044.47
x = 0.15	782.61	780.63	798.03	795.78	641.90	644.15	653.44	654.78	1022.10	1044.98
x = 0.12	782.58	780.54	797.58	795.54	642.08	644.10	653.38	655.40	1022.08	1044.93



4.6.1.5 Characterization of surface area and pore size distribution of the Zn-doped MnCo_2O_4 nanofibers by BET method and BJH method

The pore structural characteristics of Zn-doped MnCo_2O_4 nanofibers were determined by Nitrogen isothermal adsorption/desorption measurements. The N_2 adsorption /desorption isotherms of all the sample in Figure 4.92(a-b) show a typical IV shape with hysteresis loops, indicating a typical mesoporous structure. Moreover, when the relative pressure is close to the saturated vapor pressure, the adsorption/desorption curves still incline to go up, indicating some slit-like pores within the Zn-doped MnCo_2O_4 nanofibers (Lin *et al.*, 2015; Xue *et al.*, 2016). The pore-size distribution of all samples is in the range of 2-10 nm attributed to a typical feature of a mesoporous structure. The specific surface areas of the samples were estimated by the BET equation, as presented in Table 4.24. The sample with Zn doping of $x = 0.05$ shows the highest specific surface area of $37.56 \text{ m}^2/\text{g}$. Moreover, when the concentration of Zn increases with $x = 0.10$ to $x = 0.20$, the specific surface area values decrease and these are smaller than the pure MnCo_2O_4 nanofibers. However, the total pore volume values of the samples with $x = 0.05$ to $x = 0.15$ are larger than the pure MnCo_2O_4 nanofibers. The larger pore volume results in that easy diffusion of electrolyte-ion to active material with less resistance (Cai *et al.*, 2014). The shape of Zn-doped MnCo_2O_4 nanofibers with $x = 0.20$ is strongly destroyed, resulting in the smallest of specific surface area and pore volume values.

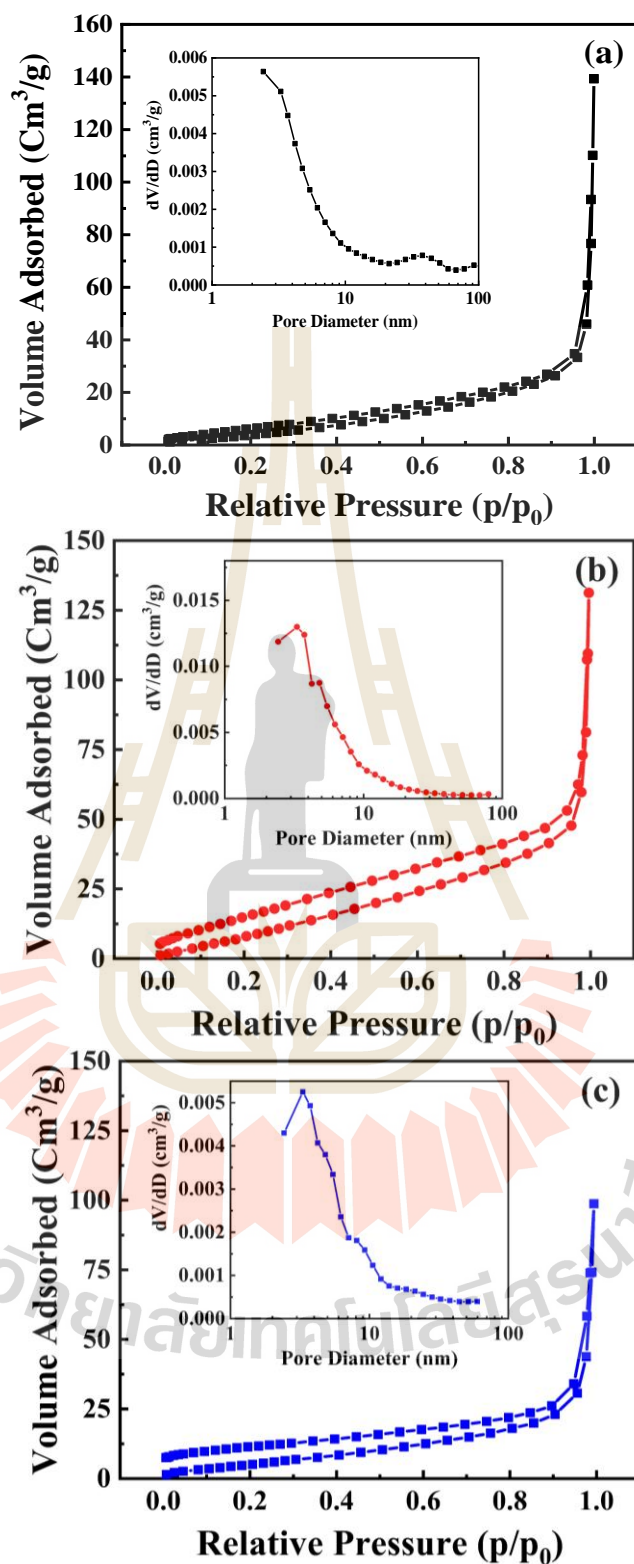


Figure 4.91 Nitrogen adsorption/desorption isotherms and pore size distribution (inset) of $\text{Mn}_{1-x}\text{Zn}_x\text{Co}_2\text{O}_4$ ($x = 0.00, 0.05, 0.10, 0.15,$ and 0.20) nanofibers.

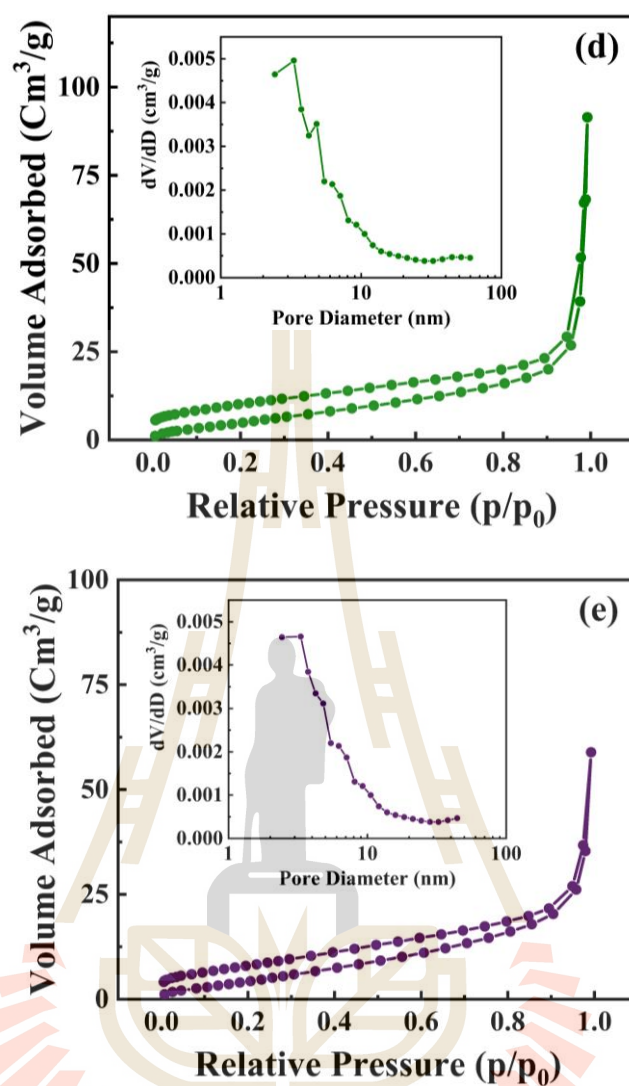


Figure 4.92 (Continued) Nitrogen adsorption/desorption isotherms and pore size distribution (inset) of $\text{Mn}_{1-x}\text{Zn}_x\text{Co}_2\text{O}_4$ ($x = 0.00, 0.05, 0.10, 0.15,$ and 0.20) nanofibers.

Table 4.24 Physical properties of spinel $Mn_{1-x}Zn_xCo_2O_4$ ($x = 0.00, 0.05, 0.10, 0.15,$ and 0.20) nanofibers.

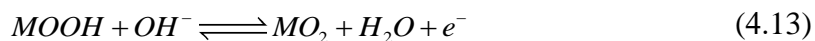
Samples	BET specific surface area (m ² /g)	Total pore volume (cm ³ /g)	Mean pore diameter (nm)
$x = 0.00$	26.56	0.107	16.11
$x = 0.05$	37.56	0.128	13.69
$x = 0.10$	22.16	0.121	21.77
$x = 0.15$	21.28	0.118	22.14
$x = 0.20$	18.99	0.085	17.82

4.6.2 Electrochemical properties

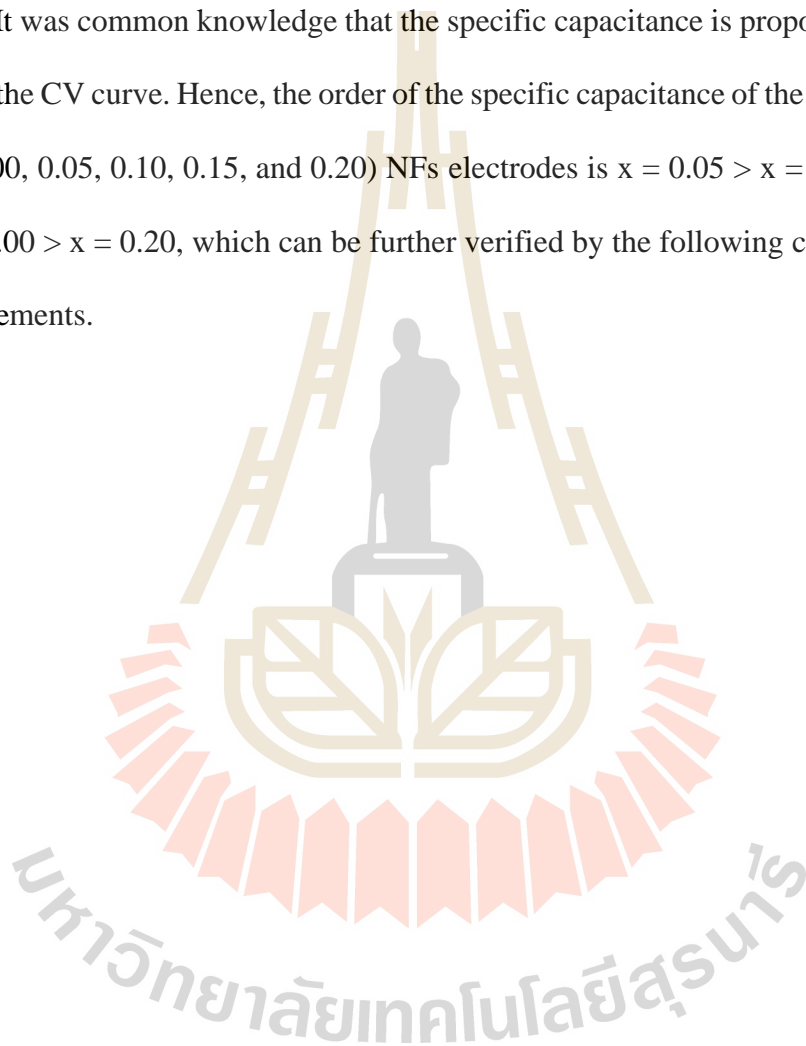
4.6.2.1 Cyclic voltammetry measurement

Cyclic voltammetry measurement was employed to evaluate the electrochemical properties of the $Mn_{1-x}Zn_xCo_2O_4$ ($x = 0.00, 0.05, 0.10, 0.15,$ and 0.20) NFs electrodes. This electrode material was fabricated by electrospinning technique with the different concentration of Zn doping as supercapacitor electrodes, the CV curves are presented in Figure 4.92. The CV curves clearly show the redox peaks, which confirm the pseudocapacitive behavior of the Zn-doped $MnCo_2O_4$ NFs electrodes. The observed redox peaks in the CV curves of the Zn-doped $MnCo_2O_4$ NFs electrodes because of the faradaic reactions that occur in the surface of electrode materials. The faradaic redox reactions in the alkaline electrolyte are based on the following equations (Li *et al.*, 2014; Bai *et al.*, 2016; Hao *et al.*, 2015; Tamboli *et al.*, 2017):





where M is indicative of Co or Mn and Zn. With the increases of the scan rate from 2 to 500 mV/s, the position of redox peaks slightly shifts, suggesting a good electrochemical reversibility and relatively low resistance of the electrode (Zhu *et al.*, 2014). It was common knowledge that the specific capacitance is proportional to under area of the CV curve. Hence, the order of the specific capacitance of the $Mn_{1-x}Zn_xCo_2O_4$ ($x = 0.00, 0.05, 0.10, 0.15, \text{ and } 0.20$) NFs electrodes is $x = 0.05 > x = 0.10 > x = 0.15 > x = 0.00 > x = 0.20$, which can be further verified by the following charge-discharge measurements.



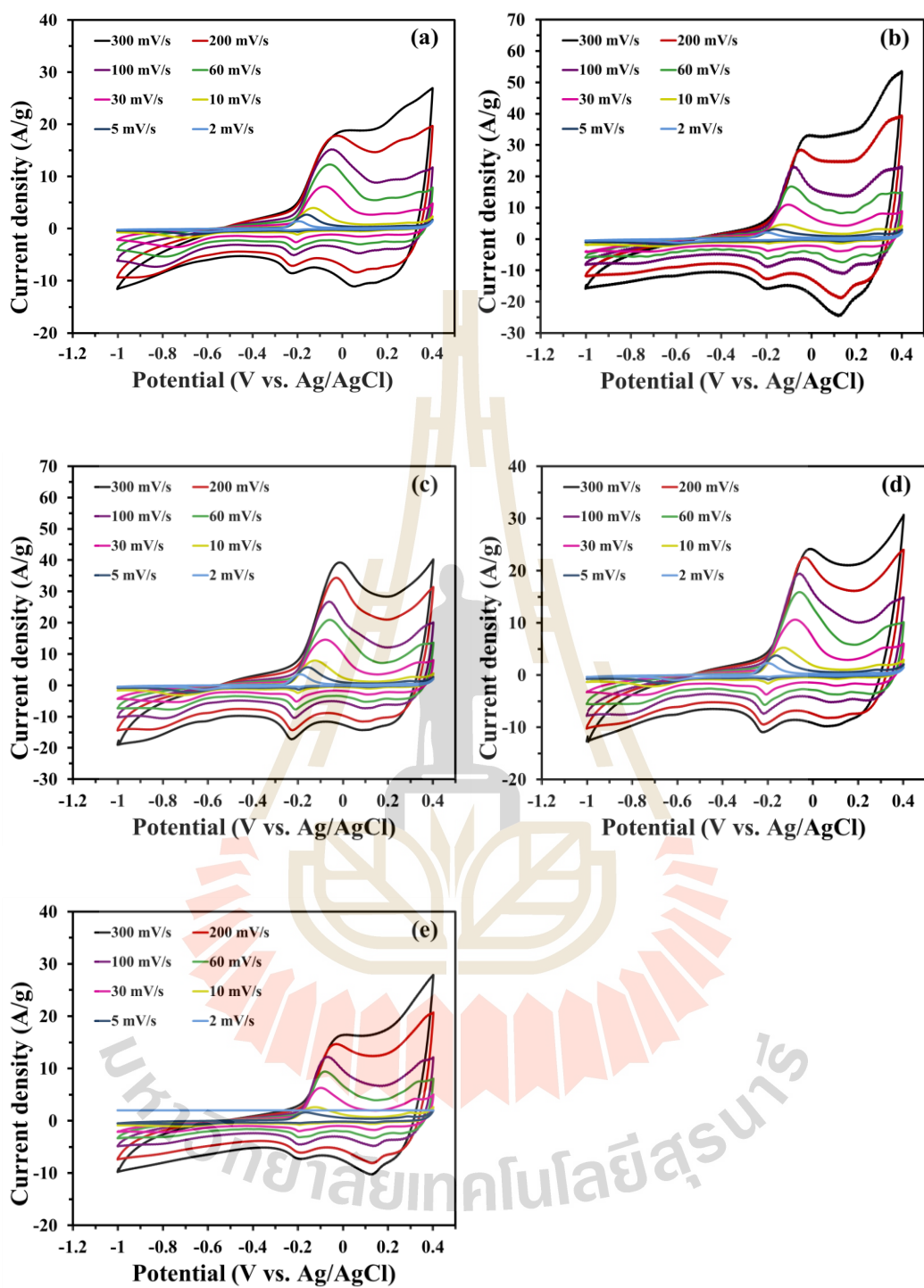


Figure 4.92 CV curves at various scan rates of $\text{Mn}_{1-x}\text{Zn}_x\text{Co}_2\text{O}_4$ nanofibers: (a) $x = 0.00$, (b) $x = 0.05$, (c) $x = 0.10$, (d) $x = 0.15$, and (e) $x = 0.20$.

4.6.2.2 Galvanostatic charge-discharge measurements

Figure 4.93 shows the galvanostatic discharge curves of the $\text{Mn}_{1-x}\text{Zn}_x\text{Co}_2\text{O}_4$ ($x = 0.00, 0.05, 0.10, 0.15,$ and 0.20) NFs electrodes in a potential window between of -1.0 to 0.4 V at various current density. Nonlinear discharge curves are observed, which confirms the pseudocapacitance behavior of the $\text{Mn}_{1-x}\text{Zn}_x\text{Co}_2\text{O}_4$ NFs electrodes. The specific capacitances at a function of a current density of the $\text{Mn}_{1-x}\text{Zn}_x\text{Co}_2\text{O}_4$ NFs electrodes are shown in Figure 4.94. The specific capacitance at current densities of 1 A/g of the samples with the Zn content of $x = 0.00, 0.05, 0.10, 0.15,$ and 0.20 is calculated to be $76, 178, 163, 132,$ and 70 F/g, respectively. The capacity retention rate (Figure 4.95) is $76.9\%, 80.2\%, 76.8\%, 70.4\%$ and 67.7% at current densities of 2 A/g, respectively. The sample with the Zn content of $x = 0.05$ electrode exhibits the highest capacitance and best rate capability which corresponds to the CV curve analysis. This is due to the higher BET specific surface area and larger pore volume, which increase electrolyte/electrode contact areas and hence provide more active sites for fast faradaic redox reactions. From The comparison of the cycling stability, a sample with the Zn content of $x = 0.05$ has more cycling numbers with highest specific capacitance, and this is because the smaller pore size of the $x = 0.05$ electrode needs a longer time to reach the complete activation.

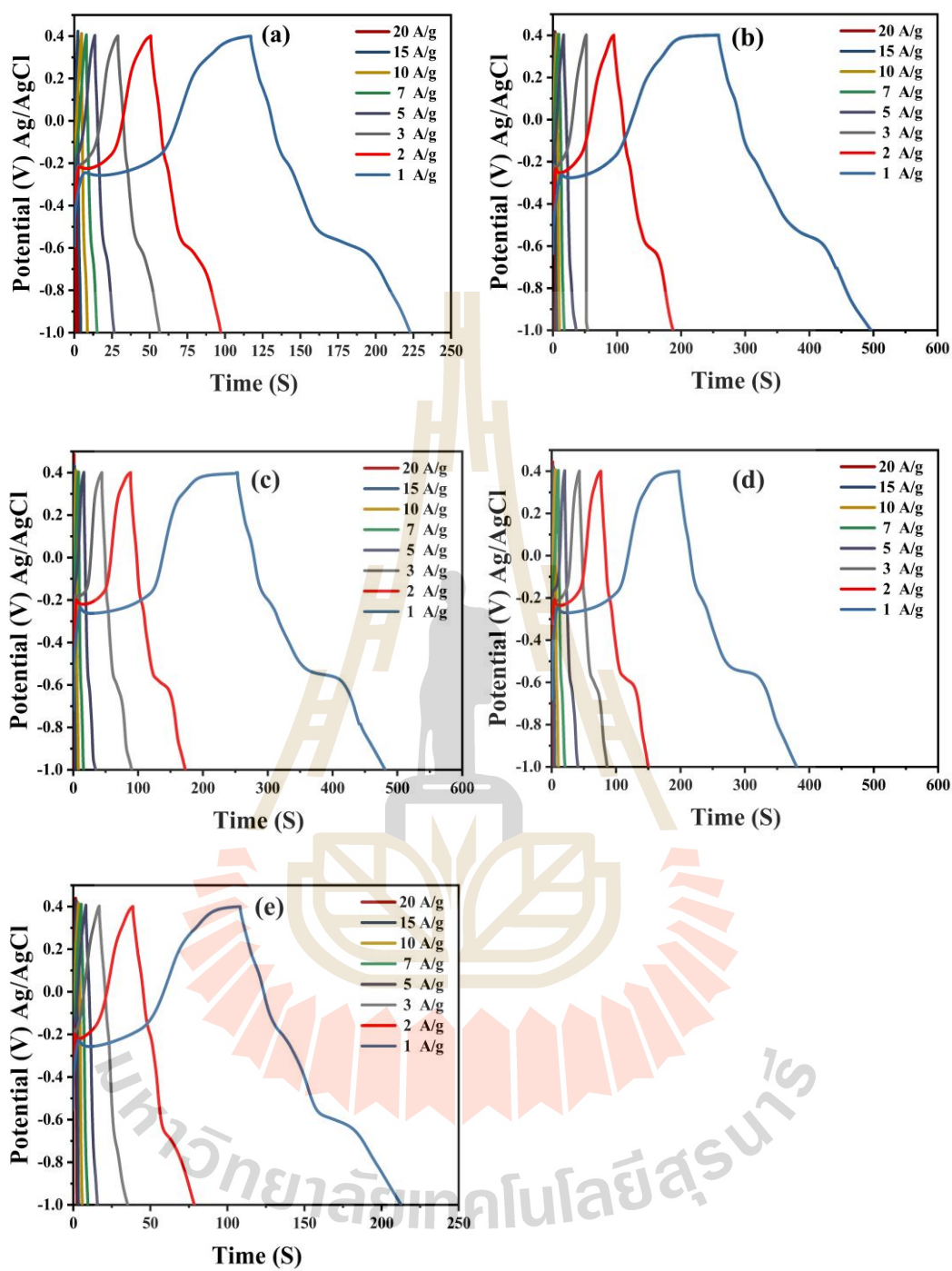


Figure 4.93 Galvanostatic charge-discharge curves at various current densities of $\text{Mn}_{1-x}\text{Zn}_x\text{Co}_2\text{O}_4$ nanofibers: (a) $x = 0.00$, (b) $x = 0.05$, (c) $x = 0.10$, (d) $x = 0.15$, and (e) $x = 0.20$.

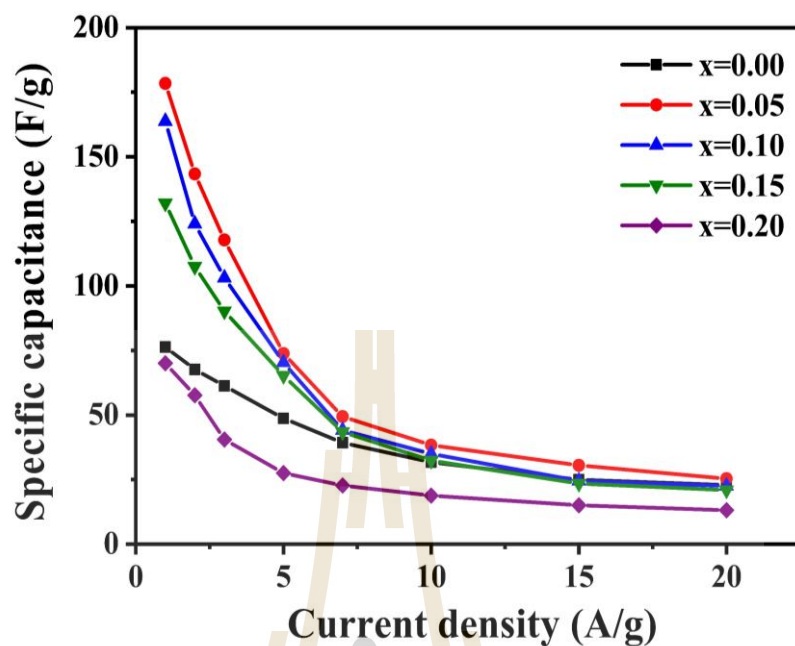


Figure 4.94 Comparison of the specific capacitance at a function of a current density of $\text{Mn}_{1-x}\text{Ni}_x\text{Co}_2\text{O}_4$ ($x = 0.00, 0.05, 0.10, 0.15,$ and 0.20) nanofibers.

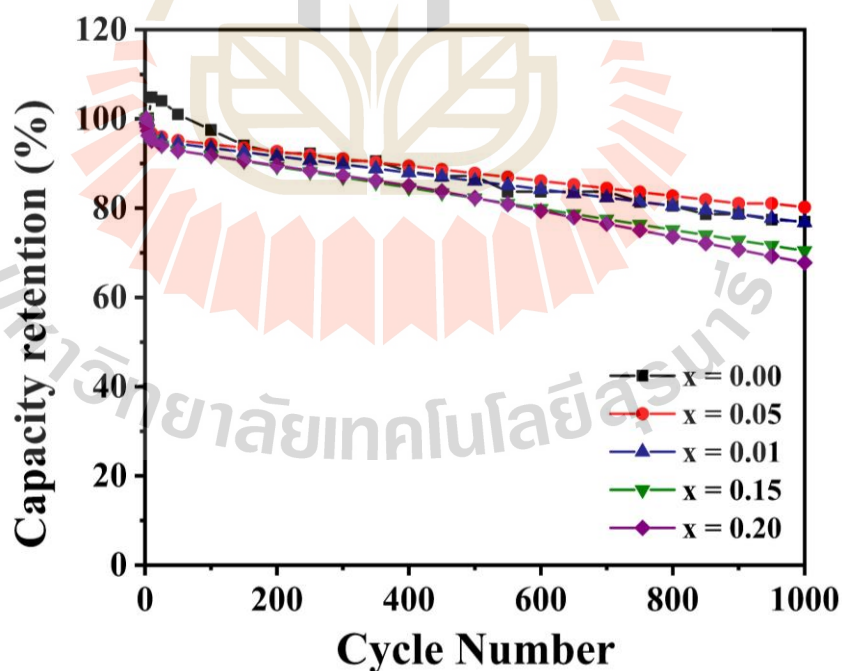


Figure 4.95 Capacity retention (%) of $\text{Mn}_{1-x}\text{Zn}_x\text{Co}_2\text{O}_4$ ($x = 0.00, 0.05, 0.10, 0.15,$ and 0.20) nanofibers and after 1000 cycles at a current density of 2 A/g.

4.6.2.3 Electrochemical impedance spectroscopy (EIS)

The electrochemical impedance spectroscopy (EIS) experiments were performed from the frequency range of 0.1 Hz to 100 kHz with 1 mV (vs. SCE). An incomplete semicircle was observed in the high-frequency region of EIS curves of all the $\text{Mn}_{1-x}\text{Zn}_x\text{Co}_2\text{O}_4$ NFs electrodes which is characteristics of the resistance at the oxide-electrolyte interface as shown in Figure 4.96. The intercept on the real axis at high frequency corresponds to internal resistance. In Nyquist plots, all the electrodes exhibit a low real axis intercept and small semicircle, indicating the low active material resistance, solution resistance, interfacial resistance, and charge transfer resistance. Obviously, the sample with the Zn content of $x = 0.05$ electrode shows lower charge transfer resistance and internal resistance than the other electrodes, resulting in a better rate capability than the other (Zhu *et al.*, 2014). As low frequency area, the slope of the straight line for with the Zn content of $x = 0.05$ electrode is significantly higher than that of the other electrodes, indicating a lower diffusion resistance (Warburg impedance) of the electrolyte ions in host material.

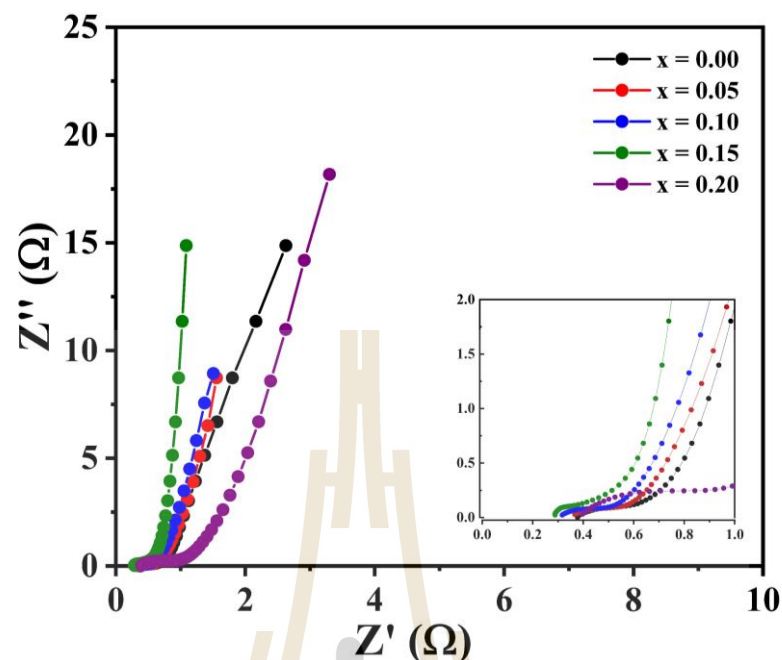


Figure 4.96 The Nyquist plots of the of $\text{Mn}_{1-x}\text{Zn}_x\text{Co}_2\text{O}_4$ ($x = 0.00, 0.05, 0.10, 0.15,$ and 0.20) NFs electrodes at various calcination temperature.

4.7 Conclusion of the effects of calcination temperature on the electrochemical properties of MnCo_2O_4 nanostructures

Figure 4.97 shows the specific surface area values as a function of calcination temperature of MnCo_2O_4 nanoparticles and MnCo_2O_4 nanofibers. It is observed that the MnCo_2O_4 nanoparticles have a larger specific surface area than the MnCo_2O_4 nanofibers, which may be because the structure of the fabricated nanofibers is destroyed severely by calcination temperature. The MnCo_2O_4 nanoparticles calcined at $600\text{ }^\circ\text{C}$ exhibit largest specific surface area. Generally, a high specific surface area can bring about a high specific capacitance because large active sites can provide multiple redox reactions, demonstrating good electrochemical capacitance (Naveen and Selladurai, 2015). Therefore, the MnCo_2O_4 nanoparticles calcined at $600\text{ }^\circ\text{C}$ provide

the higher specific capacitance and longer cycling stability than the other MnCo_2O_4 NPs and MnCo_2O_4 NFs electrodes as shown in Figure 4.98 and Figure 4.99.

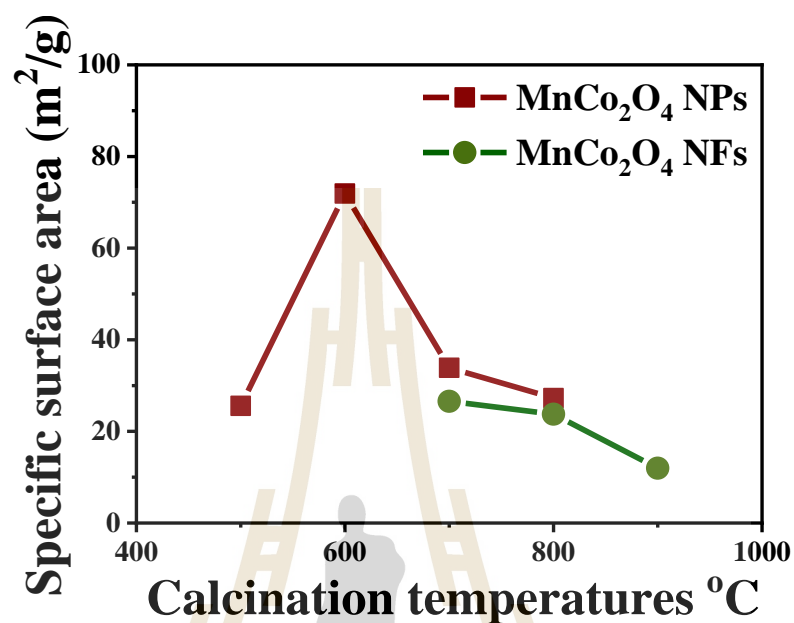


Figure 4.97 The specific surface area as a function of calcination temperature of MnCo_2O_4 nanoparticles and MnCo_2O_4 nanofibers.

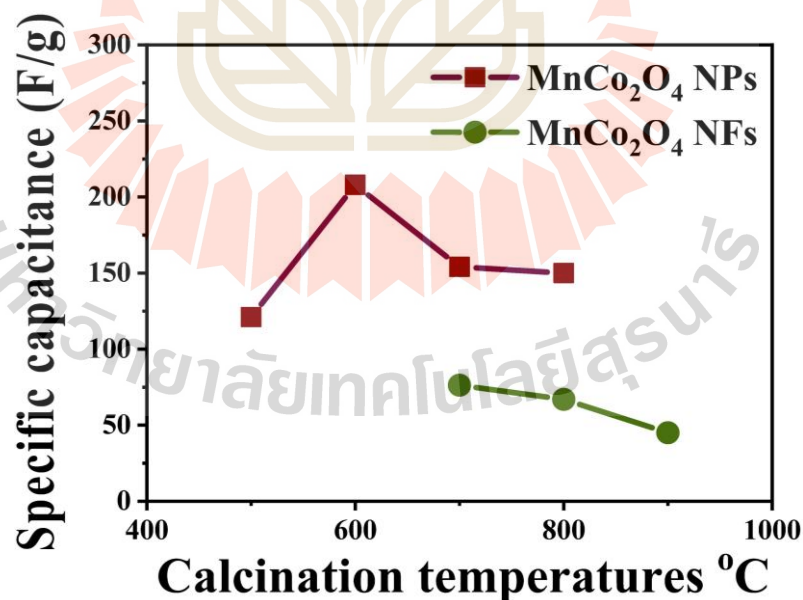


Figure 4.98 The specific capacitance at current density of 1 A/g as a function of calcination temperature of MnCo_2O_4 nanoparticles and MnCo_2O_4 nanofibers.

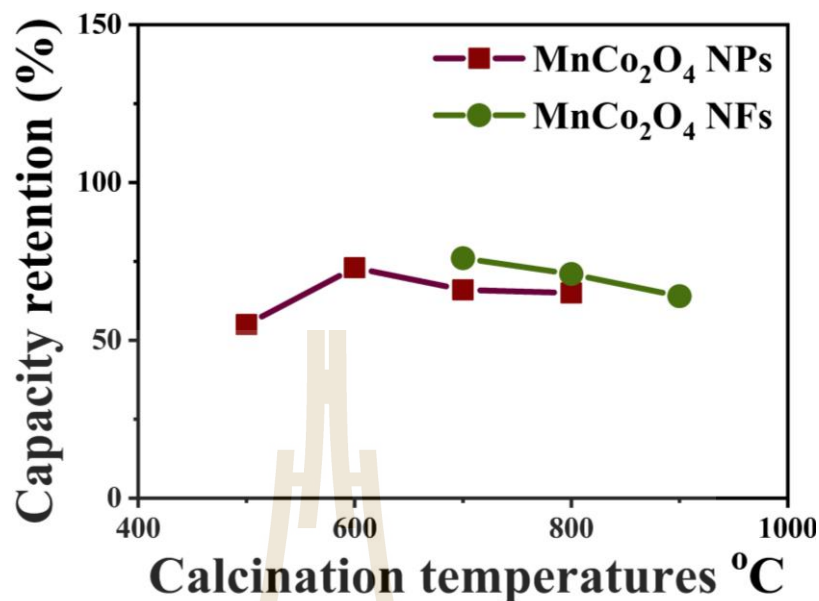


Figure 4.99 Capacity retention after 1000 cycles at current density of 2 A/g as a function of calcination temperature of MnCo₂O₄ nanoparticles and MnCo₂O₄ nanofibers.

4.8 Conclusion of the effects of the nanostructures and various dopants concentration on electrochemical properties

Figure 4.100 presents the specific surface area as a doping content of Ni, Zn-doped MnCo₂O₄ NPs and Ni, Zn-doped MnCo₂O₄ NFs. It is clearly seen that the BET specific surface area of Ni, Zn-doped MnCo₂O₄ NPs tend to increase with increasing Ni content of $x = 0.00$ to $x = 0.15$ owing to the decreasing of the particle size. In contrast, the sample with Ni content of $x = 0.20$ has smallest the BET specific surface area, which may be due to the thick accumulation of nanoparticles. In addition, the increase in BET surface area values with increasing the doping Ni concentration of $x = 0.00$ to $x = 0.15$ was also associated with decreasing of the fiber diameter. However, the BET surface area values decrease in the samples with Ni content $x = 0.20$, which

may be because the fibers are destroyed severely in this sample. Figure 4.101 shows the specific capacitance at current density of 1 A/g as a doping content, and Figure 4.102 presents capacity retention after 1000 cycles as a doping content of Ni, Zn-doped MnCo_2O_4 NPs and Ni, Zn-doped MnCo_2O_4 NFs. Among MnCo_2O_4 -base, the Ni-doped MnCo_2O_4 NPs with Ni content $x = 0.15$ exhibit a highest specific capacitance value and provide a good cycling stability. This sample is well defined smallest particle sizes with a larger specific surface area, which can encourage the supercapacitor performance.

From the overall electrochemical results, MnCo_2O_4 -base prepared by a simple polymer method shows performance than MnCo_2O_4 -base prepared by electrospinning technique because the structure and shape of MnCo_2O_4 -base nanofiber were destroyed with increase the doping concentration owing to smaller BET specific surface area and pore volume. The maximum specific capacitance, capacity retention, BET specific surface area, total pore volume, and mean pore diameter the MnCo_2O_4 -based NFs and MnCo_2O_4 -based NPs electrodes are summarized in Table 4.25. In addition, we made a comparison of electrochemical performance of the MnCo_2O_4 based materials with the different structures, as shown in Table 4.26. It is found that the $\text{Mn}_{0.85}\text{Ni}_{0.15}\text{Co}_2\text{O}_4$ nanoparticles prepared by a simple polymer solution method have a great potential as supercapacitor electrode for next-generation energy storage device.

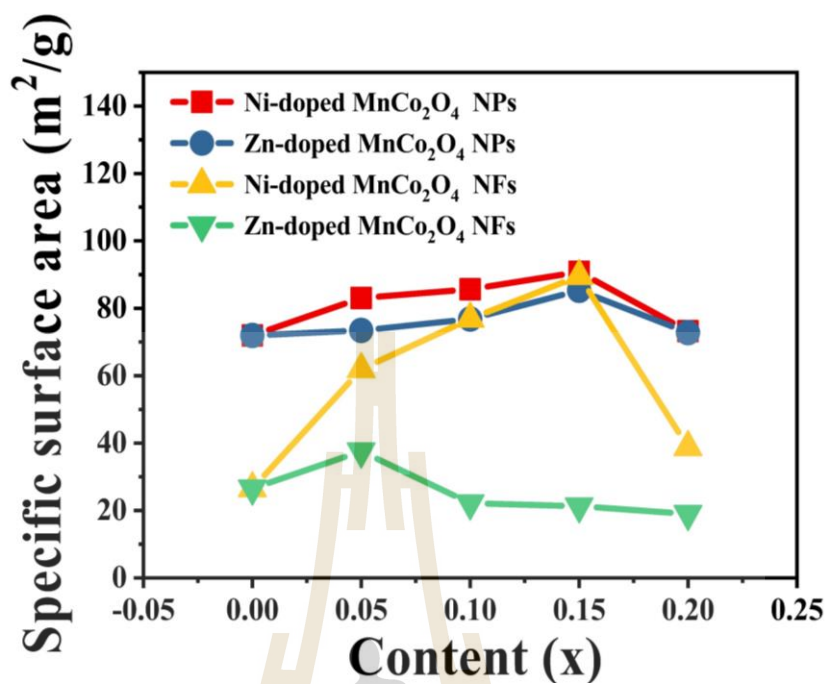


Figure 4.100 The specific surface area as a doping content.

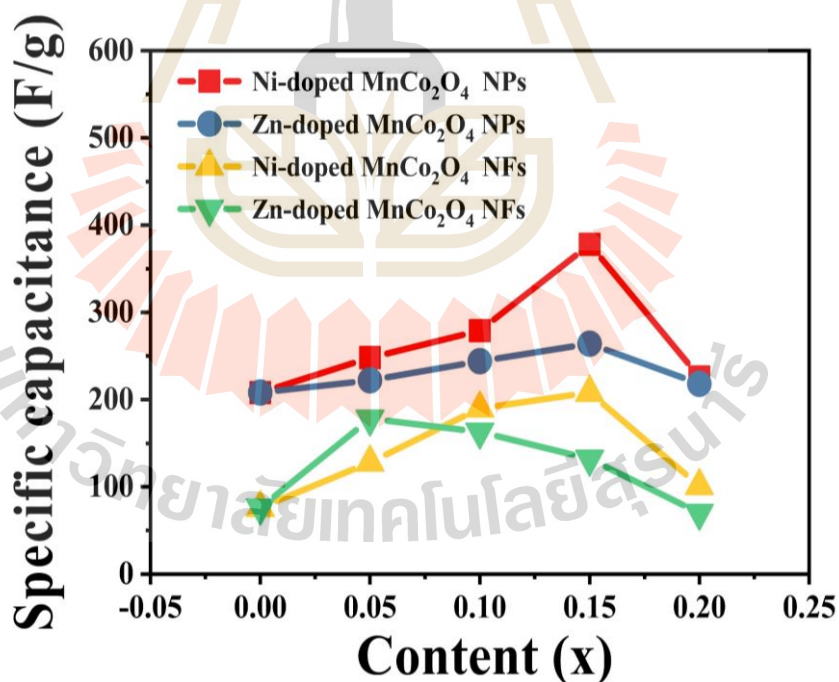


Figure 4.101 The specific capacitance at current density of 1 A/g as a doping content.

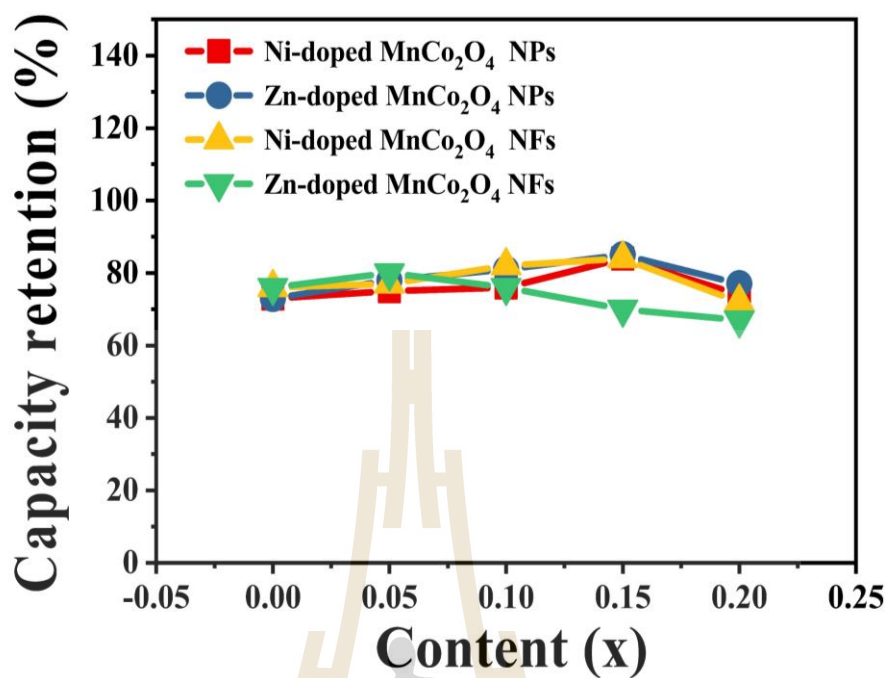


Figure 4.102 Capacity retention after 1000 cycles at current density of 2 A/g as a doping content.

Table 4.25 The maximum specific capacitance of MnCo₂O₄-based NPs and MnCo₂O₄-based NFs electrodes at current densities of 1A/g and BET specific surface area, Total pore volume, and Mean pore diameter.

Samples	Specific capacitance (F/g)	Capacity retention (%) after 1000	BET specific surface area (m ² /g)	Total pore volume (cm ³ /g)	Mean pore diameter (nm)
MnCo ₂ O ₄ NPs	189	73%	71.92	0.079	4.39
Mn _{0.85} Ni _{0.15} Co ₂ O ₄ NPs	373	84%	90.78	0.085	3.74
Mn _{0.85} Zn _{0.15} Co ₂ O ₄ NPs	204	85%	85.30	0.085	3.93
MnCo ₂ O ₄ NFs	76	76%	26.56	0.101	16.11
Mn _{0.85} Ni _{0.15} Co ₂ O ₄ NFs	208	84%	89.55	0.400	12.6
Mn _{0.95} Zn _{0.05} Co ₂ O ₄ NFs	178	80%	37.56	0.128	13.69



Table 4.26 Comparison of supercapacitor performance of the MnCo₂O₄ based materials reported earlier.

Material	Synthesis method	Specific capacitance (F/g)	Reference
1D MnCo ₂ O ₄ nanowire	Hydrothermal	349.8 (at 1 A/g)	(Li <i>et al.</i> , 2014)
MnCo ₂ O ₄ nanoparticles	Hydrothermal	671 (at 5 mV/s)	(Tholkappian <i>et al.</i> , 2015)
Flower-like MnCo ₂ O ₄	Solvothermal	539 (at 1 A/g)	(Che <i>et al.</i> , 2016)
Mesoporous MnCo ₂ O ₄	Solvothermal	346 (at 1 A/g)	(Padmanathan and Selladurai, 2014)
MnCo ₂ O ₄ nanosheet	Electrodeposition	290 (at 1 mV/s)	(Sahoo <i>et al.</i> , 2015)
Mn _{0.4} Ni _{0.6} Co ₂ O ₄ nanowire	Hydrothermal	1762 (at 1 A/g)	(Tamboli <i>et al.</i> , 2017)
MnCo ₂ O ₄ nanoparticles	Polymer–solution	189 (at 1 A/g)	This work
Mn _{0.85} Ni _{0.15} Co ₂ O ₄ nanoparticles	Polymer–solution	378 (at 1 A/g)	This work
Mn _{0.8} Zn _{0.15} Co ₂ O ₄ nanoparticles	Polymer–solution	204 (at 1 A/g)	This work
MnCo ₂ O ₄ nanoparticles	Electrospinning	76 (at 1 A/g)	This work
Mn _{0.85} Ni _{0.15} Co ₂ O ₄ nanoparticles	Electrospinning	208 (at 1 A/g)	This work
Mn _{0.8} Zn _{0.15} Co ₂ O ₄ nanoparticles	Electrospinning	178 (at 1 A/g)	This work

CHAPTER V

CONCLUSIONS AND SUGGESTIONS

In this study, MnCo_2O_4 and $\text{Mn}_{1-x}\text{M}_x\text{Co}_2\text{O}_4$ where $\text{M} = \text{Ni}$ and Zn ($0.0 \leq x \leq 0.2$) nanostructures were successfully prepared by using a simple polymer solution and electrospinning technique. The structure and morphology were investigated by SEM, TEM, XRD, BET, XAS, XPS techniques. The electrochemical properties were studied by CV, GCD, and EIS techniques. From the results and discussion, improving our understandings of the morphology–property relationship for the MnCo_2O_4 and $\text{Mn}_{1-x}\text{M}_x\text{Co}_2\text{O}_4$ where $\text{M} = \text{Ni}$ and Zn ($0.0 \leq x \leq 0.2$) nanostructures are summarized as follows:

5.1 The structure and morphology characterization

The XRD patterns of all samples could be indexed to the spinel structure of MnCo_2O_4 (JCPDS No. 23-1237). However, the impurities phase of MnO_2 with cubic structure can also be seen in the MnCo_2O_4 nanoparticles calcined at 500°C . The crystallite sizes of MnCo_2O_4 nanoparticles are in the range of 26.5-43.4 nm. The crystallite sizes of Ni-doped MnCo_2O_4 and Zn-doped MnCo_2O_4 nanoparticles decrease and increase with increasing of doping content (22.3-19.8 nm and 22.3-48.9 nm, respectively). In the same way, the crystallite sizes of Ni-doped MnCo_2O_4 and Zn-doped MnCo_2O_4 nanofibers decrease and increase with the increasing of doping content (20.8-19.8 nm and 20.8-43.2 nm, respectively). The variation of lattice constant value

of MnCo_2O_4 nanostructures confirms to the doping of Ni, and Zn ions. The decrease in lattice constant values with increasing of the doping content for Ni-doped MnCo_2O_4 nanostructures occur due to Ni^{2+} (0.69 Å) with a small ionic radius substitute in the Mn^{3+} (0.72 Å) site, respectively. Conversely, As a result in substitution of Zn^{2+} (0.74 Å) into Mn^{3+} (0.72 Å) or Mn^{4+} (0.53 Å) leading to the expansion of unit cell. which is in good agreement with oxidation states results from XAS analysis that the oxidation-state of Co and Mn atom in all samples are $\text{Co}^{2+/3+}$ and $\text{Mn}^{3+/4+}$, respectively. The oxidation states of Ni, and Zn atom in Ni-doped MnCo_2O_4 and Zn-doped MnCo_2O_4 nanostructures are the Ni^{2+} and Zn^{2+} respectively. Moreover, the According to the morphology observation, the particle sizes of between 20 to 200 nm and diameters of 200 to 400 nm for MnCo_2O_4 -based nanoparticles and MnCo_2O_4 -based nanofibers, respectively. The HR-TEM shows the lattice fringes with interplanar spacing which correspond to the MnCo_2O_4 structure. Moreover, The SAED patterns of all samples show spotty and ring patterns which indicate the characteristics of nanocrystalline MnCo_2O_4 (JCPDS No. 23-1237). This is in agreement with the XRD results. In this research, we confirm that the samples with concentrations of Ni of $x = 0.15$ show the best morphology of the MnCo_2O_4 nanostructures, which confirms to a larger specific surface area.

5.2 The electrochemical properties

According to the electrochemical property studies, the redox behavior of the all the samples were studied by CV technique between -1.0 V to 0.4 V at different potential scan rates of 2 to 300 mV/s in 6 M KOH solution. This study indicates that all samples exhibit a pseudocapacitive behavior. The presence of redox peaks for all the samples

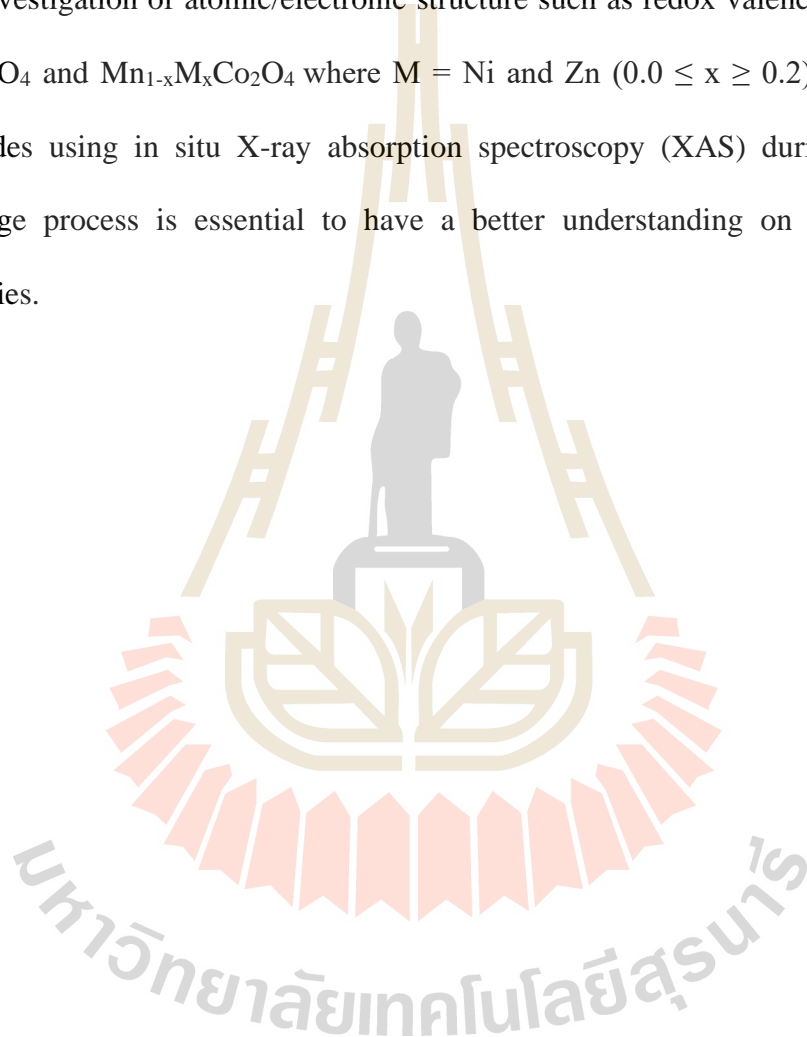
indicates that the redox transitions between different valence states and the capacitance of the electrodes are mainly due to the rapid and faradic reaction on the electrode/electrolyte interface. The anodic and cathodic peak currents in the CV increase with an increasing in potential scan rate. In GCD measurement, all samples show the nonlinear form of curves which exhibit the pseudocapacitive behavior due to internal resistance and a capacitive component. For the doped-MnCo₂O₄ nanoparticles, the Mn_{0.85}Ni_{0.15}Co₂O₄ electrode exhibits the highest specific capacitance of 378 F/g at the current density of 1 A/g. This is due to the higher BET specific surface area and larger pore volume, which increases electrolyte/electrode contact areas and provide more active sites for faradaic redox reactions. Similarly, the Mn_{0.85}Ni_{0.15}Co₂O₄ nanofibers electrode shows the specific capacitance of 208 F/g at the current density of 1 A/g. Furthermore, most of the electrodes showed the imposing cycling capacity retention more than 60% after 1000 cycles. From the overall electrochemical results, MnCo₂O₄- base nanoparticles prepared by a simple polymer method shows performance than MnCo₂O₄- base nanofibers prepared by electrospinning technique because the structure and shape of MnCo₂O₄- base nanofiber were destroyed with increase the doping concentration owing to smaller BET specific surface area and pore volume.

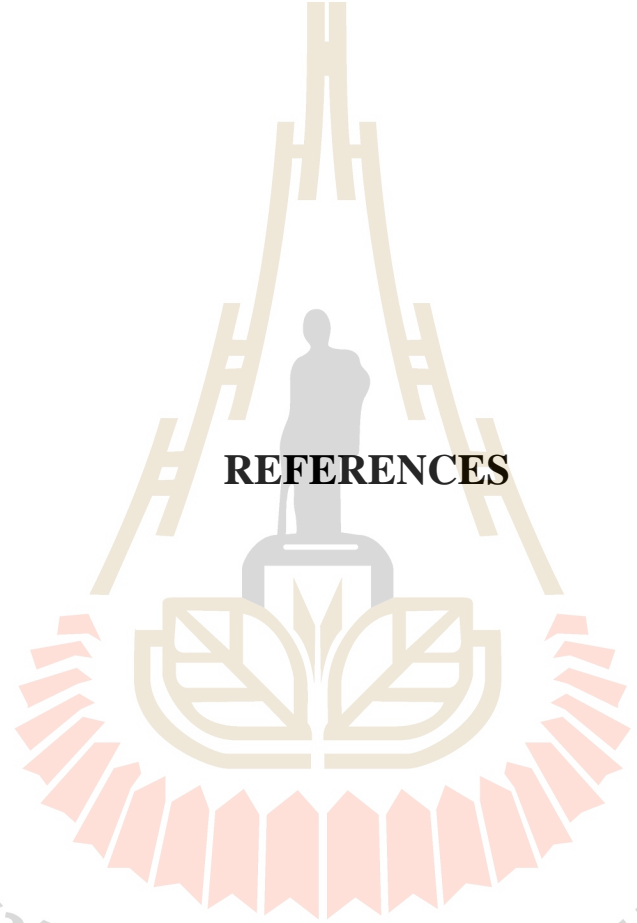
5.3 Suggestions

From the study of the electrochemical properties of MnCo₂O₄ and Mn_{1-x}M_xCo₂O₄ where M = Ni and Zn ($0.0 \leq x \leq 0.2$) nanostructures, we have suggestions for future work to make clear explanation of the results as follows,

(1) Study of electrochemical properties in the MnCo_2O_4 and $\text{Mn}_{1-x}\text{M}_x\text{Co}_2\text{O}_4$ where $\text{M} = \text{Ni}$ and Zn ($0.0 \leq x \leq 0.2$) nanostructures using various electrolytes in different concentrations and various substrate materials is required to confirm the suitable condition for the fabrication of supercapacitor electrodes.

(2) Investigation of atomic/electronic structure such as redox valency change of the MnCo_2O_4 and $\text{Mn}_{1-x}\text{M}_x\text{Co}_2\text{O}_4$ where $\text{M} = \text{Ni}$ and Zn ($0.0 \leq x \leq 0.2$) nanostructures electrodes using in situ X-ray absorption spectroscopy (XAS) during the charge-discharge process is essential to have a better understanding on electrochemical properties.





REFERENCES

มหาวิทยาลัยเทคโนโลยีสุรนารี

REFERENCES

- Bai, Y., Wang, R., Lu, X., Sun, J. and Gao, L. (2016). Template method to controllable synthesis 3D porous NiCo_2O_4 with enhanced capacitance and stability for supercapacitors. **Journal of Colloid and Interface Science**. 468: 1-9.
- Becker, H. I. (1957) Low voltage electrolytic capacitor. (pp. Google Patents).
- Boos, D. L. (1970) Electrolytic capacitor having carbon paste electrodes. (pp. Google Patents).
- Borges, F. M. M., Melo, D. M. A., Câmara, M. S. A., Martinelli, A. E., Soares, J. M., de Araújo, J. H. and Cabral, F. A. O. (2006). Magnetic behavior of nanocrystalline MnCo_2O_4 spinels. **Journal of Magnetism and Magnetic Materials**. 302(2): 273-277.
- Brousse, T., Toupin, M. and Belanger, D. (2004). A hybrid activated carbon-manganese dioxide capacitor using a mild aqueous electrolyte. **Journal of the Electrochemical Society**. 151(4): A614-A622.
- Cai, F., Kang, Y., Chen, H., Chen, M. and Li, Q. (2014). Hierarchical $\text{CNT}@\text{NiCo}_2\text{O}_4$ core-shell hybrid nanostructure for high-performance supercapacitors. **Journal of Materials Chemistry A**. 2(29): 11509-11515.
- Cao, Y. L., Lv, F. C., Yu, S. C., Xu, J., Yang, X. and Lu, Z. G. (2016). Simple template fabrication of porous MnCo_2O_4 hollow nanocages as high-performance cathode catalysts for rechargeable Li- O_2 batteries. **Nanotechnology**. 27(13): 135703.
- Che, H., Liu, A., Mu, J., Wu, C. and Zhang, X. (2016). Template-free synthesis of novel flower-like MnCo_2O_4 hollow microspheres for application in supercapacitors.

Ceramics International. 42(2): 2416-2424.

- Che, H., Wang, Y. and Mao, Y. (2016). Novel flower-like MnCo_2O_4 microstructure self-assembled by ultrathin nanoflakes on the microspheres for high performance supercapacitors. **Journal of Alloys and Compounds.** 680: 586-594.
- Chen, J., Zhu, B., Sun, Y., Yin, S., Zhu, Z. and Li, J. (2018). Investigation of Low-Temperature Selective Catalytic Reduction of NO_x with Ammonia over Mn-Modified $\text{Fe}_2\text{O}_3/\text{AC}$ Catalysts. **Journal of the Brazilian Chemical Society.** 29: 79-87.
- Chen, X., Liu, Y., Yang, Y., Ren, T., Pan, L., Fang, P., Chen, D. and Cen, C. (2017) Modified fly ash from municipal solid waste incineration as catalyst support for Mn-Ce composite oxides. In **IOP Conference Series: Earth and Environmental Science**, (Vol. 81, pp. 012146) IOP Publishing.
- Cheng, J., Lu, Y., Qiu, K., Yan, H., Hou, X., Xu, J., Han, L., Liu, X., Kim, J.-K. and Luo, Y. (2015). Mesoporous ZnCo_2O_4 nanoflakes grown on nickel foam as electrodes for high performance supercapacitors. **Physical Chemistry Chemical Physics.** 17(26): 17016-17022.
- Dong, Y., Wang, Y., Xu, Y., Chen, C., Wang, Y., Jiao, L. and Yuan, H. (2017). Facile synthesis of hierarchical nanocage MnCo_2O_4 for high performance supercapacitor. **Electrochimica Acta.** 225: 39-46.
- Donohue, M. and Aranovich, G. L. (1998). **Classification of Gibbs adsorption isotherms.** 76: 137-152.
- Duan, L., Gao, F., Wang, L., Jin, S. and Wu, H. (2013). Hydrothermal synthesis and characterization of MnCo_2O_4 in the low-temperature hydrothermal process:

Their magnetism and electrochemical properties. **Journal of Advanced Ceramics**. 2(3): 266-273.

Fantauzzi, M., Secci, F., Sanna Angotzi, M., Passiu, C., Cannas, C. and Rossi, A. (2019). Nanostructured spinel cobalt ferrites: Fe and Co chemical state, cation distribution and size effects by X-ray photoelectron spectroscopy. **RSC Advances**. 9(33): 19171-19179.

Fu, W., Li, X., Zhao, C., Liu, Y., Zhang, P., Zhou, J., Pan, X. and Xie, E. (2015). Facile hydrothermal synthesis of flowerlike ZnCo_2O_4 microspheres as binder-free electrodes for supercapacitors. **Materials Letters**. 149: 1-4.

Gao, M., Lu, X., Chi, M., Chen, S. and Wang, C. (2017). Fabrication of oxidase-like hollow MnCo_2O_4 nanofibers and their sensitive colorimetric detection of sulfite and l-cysteine. **Inorganic Chemistry Frontiers**. 4(11): 1862-1869.

Gao, Y., Chen, S., Cao, D., Wang, G. and Yin, J. (2010). Electrochemical capacitance of Co_3O_4 nanowire arrays supported on nickel foam. **Journal of Power Sources**. 195(6): 1757-1760.

Gupta, R. K., Candler, J., Palchoudhury, S., Ramasamy, K. and Gupta, B. K. (2015). Flexible and High Performance Supercapacitors Based on NiCo_2O_4 for Wide Temperature Range Applications. **Scientific Reports**. 5.

Habjanič, J., Jurić, M., Popović, J., Molčanov, K. and Pajić, D. (2014). A 3D Oxalate-Based Network as a Precursor for the CoMn_2O_4 Spinel: Synthesis and Structural and Magnetic Studies. **Inorganic Chemistry**. 53(18): 9633-9643.

Hao, P., Zhao, Z., Li, L., Tuan, C. C., Li, H., Sang, Y., Jiang, H., Wong, C. P. and Liu, H. (2015). The hybrid nanostructure of $\text{MnCo}_2\text{O}_{4.5}$ nanoneedle/carbon

- aerogel for symmetric supercapacitors with high energy density. **Nanoscale**. 7(34): 14401-14412.
- Hu, C.-C., Chang, K.-H., Lin, M.-C. and Wu, Y.-T. (2006). Design and tailoring of the nanotubular arrayed architecture of hydrous RuO₂ for next generation supercapacitors. **Nano letters**. 6(12): 2690-2695.
- Hu, C.-C. and Chen, W.-C. (2004). Effects of substrates on the capacitive performance of RuO_x·nH₂O and activated carbon-RuO_x electrodes for supercapacitors. **Electrochimica Acta**. 49(21): 3469-3477.
- Hu, X., Zhang, S., Li, X., Sun, X., Cai, S., Ji, H., Hou, F., Zheng, C. and Hu, W. (2017). Large-scale and template-free synthesis of hierarchically porous MnCo₂O_{4.5} as anode material for lithium-ion batteries with enhanced electrochemical performance. **Journal of Materials Science**. 52: 5268-5282.
- Huang, T., Liu, B., Yang, P., Qiu, Z. and Hu, Z. (2018). Facile Synthesized NiCo₂O₄ Nanoparticles as Electrode Material for Supercapacitors. **International Journal of Electrochemical Science**. 13: 6144-6154.
- Huang, T., Zhao, C., Wu, L., Lang, X., Liu, K. and Hu, Z. (2017). 3D network-like porous MnCo₂O₄ by the sucrose-assisted combustion method for high-performance supercapacitors. **Ceramics International**. 43(2): 1968-1974.
- Huang, T., Zhao, C., Zheng, R., Zhang, Y. and Hu, Z. (2015). Facile synthesized porous ZnCo₂O₄ rodlike nanostructure for high-rate supercapacitors. **Ionics**. 21(11): 3109-3115.
- Hui, K. N., San Hui, K., Tang, Z., Jadhav, V. and Xia, Q. X. (2016). Hierarchical chestnut-like MnCo₂O₄ nanoneedles grown on nickel foam as binder-free

- electrode for high energy density asymmetric supercapacitors. **Journal of Power Sources**. 330: 195-203.
- Inagaki, M., Konno, H. and Tanaike, O. (2010). Carbon materials for electrochemical capacitors. **Journal of Power Sources**. 195(24): 7880-7903.
- Inkson, B. J. (2016) **2 - Scanning electron microscopy (SEM) and transmission electron microscopy (TEM) for materials characterization**. In *Materials Characterization Using Nondestructive Evaluation (NDE) Methods* (Eds, Hübschen, G., Altpeter, I., Tschuncky, R. and Herrmann, H.-G.) Woodhead Publishing, pp. 17-43.
- Issa, B., Obaidat, I. M., Albiss, B. A. and Haik, Y. (2013). Magnetic nanoparticles: surface effects and properties related to biomedicine applications. **International journal of molecular sciences**. 14(11): 21266-21305.
- Joy, P. A. and Date, S. K. (2000). Unusual magnetic hysteresis behavior of oxide spinel MnCo_2O_4 . **Journal of Magnetism and Magnetic Materials**. 210(1-3): 31-34.
- Karthikeyan, K., Kalpana, D. and Renganathan, N. (2009). Synthesis and characterization of ZnCo_2O_4 nanomaterial for symmetric supercapacitor applications. **Ionics**. 15(1): 107-110.
- Khalid, S., Cao, C., Wang, L. and Zhu, Y. (2016). Microwave Assisted Synthesis of Porous NiCo_2O_4 Microspheres: Application as High Performance Asymmetric and Symmetric Supercapacitors with Large Areal Capacitance. **Scientific Reports**. 6.
- Kim, B. K., Sy, S., Yu, A. and Zhang, J. (2015). Electrochemical supercapacitors for energy storage and conversion. **Handbook of Clean Energy Systems**.

- Kim, I.-H. and Kim, K.-B. (2006). Electrochemical characterization of hydrous ruthenium oxide thin-film electrodes for electrochemical capacitor applications. **Journal of The Electrochemical Society**. 153(2): A383-A389.
- Kim, J. G., Kim, Y., Noh, Y. and Kim, W. B. (2015). MnCo₂O₄ nanowires anchored on reduced graphene oxide sheets as effective bifunctional catalysts for Li-O₂ battery cathodes. **ChemSusChem**. 8(10): 1752-1760.
- Kim, T., Ramadoss, A., Saravanakumar, B., Veerasubramani, G. K. and Kim, S. J. (2016). Synthesis and characterization of NiCo₂O₄ nanoplates as efficient electrode materials for electrochemical supercapacitors. **Applied Surface Science**. 370: 452-458.
- Kong, L. B., Lu, C., Liu, M. C., Luo, Y. C., Kang, L., Li, X. and Walsh, F. C. (2014). The specific capacitance of sol-gel synthesised spinel MnCo₂O₄ in an alkaline electrolyte. **Electrochimica Acta**. 115: 22-27.
- Kötz, R. and Carlen, M. (2000). Principles and applications of electrochemical capacitors. **Electrochimica Acta**. 45(15-16): 2483-2498.
- Krishnan, S. G., Rahim, M. H. A. and Jose, R. (2016). Synthesis and characterization of MnCo₂O₄ cuboidal microcrystals as a high performance pseudocapacitor electrode. **Journal of Alloys and Compounds**. 656: 707-713.
- Li, G., Xu, L., Zhai, Y. and Hou, Y. (2015). Fabrication of hierarchical porous MnCo₂O₄ and CoMn₂O₄ microspheres composed of polyhedral nanoparticles as promising anodes for long-life LIBs. **Journal of Materials Chemistry A**. 3(27): 14298-14306.

- Li, L., Dai, Z., Zhang, Y., Yang, J., Huang, W. and Dong, X. (2015). Carbon@NiCo₂S₄ nanorods: an excellent electrode material for supercapacitors. **RSC Advances**. 5(101): 83408-83414.
- Li, L., Zhang, Y. Q., Liu, X. Y., Shi, S. J., Zhao, X. Y., Zhang, H., Ge, X., Cai, G. F., Gu, C. D., Wang, X. L. and Tu, J. P. (2014). One-dimension MnCo₂O₄ nanowire arrays for electrochemical energy storage. **Electrochimica Acta**. 116: 467-474.
- Li, T., Li, X., Wang, Z., Guo, H., Hu, Q. and Peng, W. (2016). Robust synthesis of hierarchical mesoporous hybrid NiO-MnCo₂O₄ microspheres and their application in Lithium-ion batteries. **Electrochimica Acta**. 191: 392-400.
- Li, W., Xu, K., Song, G., Zhou, X., Zou, R., Yang, J., Chen, Z. and Hu, J. (2014). Facile synthesis of porous MnCo₂O_{4.5} hierarchical architectures for high-rate supercapacitors. **CrystEngComm**. 16(12): 2335-2339.
- Lin, X., Su, J., Li, L. and Yu, A. (2015). Hierarchical porous NiCo₂O₄@Ni as carbon-free electrodes for Lithium-oxygen batteries. **Electrochimica Acta**. 168: 292-299.
- Liu, X. Y., Zhang, Y. Q., Xia, X. H., Shi, S. J., Lu, Y., Wang, X. L., Gu, C. D. and Tu, J. P. (2013). Self-assembled porous NiCo₂O₄ hetero-structure array for electrochemical capacitor. **Journal of Power Sources**. 239: 157-163.
- Liu, Z.-Q., Xu, Q.-Z., Wang, J.-Y., Li, N., Guo, S.-H., Su, Y.-Z., Wang, H.-J., Zhang, J.-H. and Chen, S. (2013). Facile hydrothermal synthesis of urchin-like NiCo₂O₄ spheres as efficient electrocatalysts for oxygen reduction reaction. **International Journal of Hydrogen Energy**. 38(16): 6657-6662.

- Marco, J. F., Gancedo, J. R., Gracia, M., Gautier, J. L., Ríos, E. I., Palmer, H. M., Greaves, C. and Berry, F. J. (2001). Cation distribution and magnetic structure of the ferrimagnetic spinel NiCo_2O_4 . **Journal of Materials Chemistry**. 11(12): 3087-3093.
- Meena, P. L., Pal, S., Sreenivas, K. and Kumar, R. A. (2015). Structural and magnetic properties of MnCo_2O_4 spinel multiferroic. **Advanced Science Letters**. 21(9): 2760-2763.
- Meher, S. K. and Rao, G. R. (2011). Ultralayered Co_3O_4 for high-performance supercapacitor applications. **The Journal of Physical Chemistry C**. 115(31): 15646-15654.
- Mondal, A. K., Su, D., Chen, S., Ung, A., Kim, H. S. and Wang, G. (2015). Mesoporous MnCo_2O_4 with a flake-like structure as advanced electrode materials for lithium-ion batteries and supercapacitors. **Chemistry - A European Journal**. 21(4): 1526-1532.
- Nakayama, M., Kanaya, T. and Inoue, R. (2007). Anodic deposition of layered manganese oxide into a colloidal crystal template for electrochemical supercapacitor. **Electrochemistry Communications**. 9(5): 1154-1158.
- Nam, K.-W., Yoon, W.-S. and Kim, K.-B. (2002). X-ray absorption spectroscopy studies of nickel oxide thin film electrodes for supercapacitors. **Electrochimica Acta**. 47(19): 3201-3209.
- Naveen, A. N. and Selladurai, S. (2015). A 1-D/2-D hybrid nanostructured manganese cobaltite-graphene nanocomposite for electrochemical energy storage. **RSC Advances**. 5(80): 65139-65152.

- Nguyen, T., Boudard, M., Rapenne, L., Chaix-Pluchery, O., Carmezim, M. J. and Montemor, M. F. (2015). Structural evolution, magnetic properties and electrochemical response of MnCo_2O_4 nanosheet films. **RSC Advances**. 5(35): 27844-27852.
- Padmanathan, N. and Selladurai, S. (2014). Mesoporous MnCo_2O_4 spinel oxide nanostructure synthesized by solvothermal technique for supercapacitor. **Ionics**. 20(4): 479-487.
- Pang, S. C., Anderson, M. A. and Chapman, T. W. (2000). Novel electrode materials for thin-film ultracapacitors: comparison of electrochemical properties of sol-gel-derived and electrodeposited manganese dioxide. **Journal of the Electrochemical Society**. 147(2): 444-450.
- Papavasiliou, J., Avgouropoulos, G. and Ioannides, T. (2007). Combined steam reforming of methanol over Cu-Mn spinel oxide catalysts. **Journal of Catalysis**. 251(1): 7-20.
- Patterson, A. (1939). The Scherrer formula for X-ray particle size determination. **Physical review**. 56(10): 978.
- Pendashteh, A., Moosavifard, S. E., Rahmanifar, M. S., Wang, Y., El-Kady, M. F., Kaner, R. B. and Mousavi, M. F. (2015). Highly ordered mesoporous CuCo_2O_4 nanowires, a promising solution for high-performance supercapacitors. **Chemistry of Materials**. 27(11): 3919-3926.
- Peng, S., Li, L., Hu, Y., Srinivasan, M., Cheng, F., Chen, J. and Ramakrishna, S. (2015). Fabrication of spinel one-dimensional architectures by single-spinneret electrospinning for energy storage applications. **ACS nano**. 9(2): 1945-1954.

- Pettong, T., Iamprasertkun, P., Krittayavathananon, A., Sukha, P., Sirisinudomkit, P., Seubsai, A., Chareonpanich, M., Kongkachuichay, P., Limtrakul, J. and Sawangphruk, M. (2016). High-Performance Asymmetric Supercapacitors of MnCo₂O₄ Nanofibers and N-Doped Reduced Graphene Oxide Aerogel. **ACS applied materials & interfaces**. 8(49): 34045-34053.
- Qiu, M., Zhan, S., Yu, H., Zhu, D. and Wang, S. (2015). Facile preparation of ordered mesoporous MnCo₂O₄ for low-temperature selective catalytic reduction of NO with NH₃. **Nanoscale**. 7(6): 2568-2577.
- Sahoo, S., Naik, K. K. and Rout, C. S. (2015). Electrodeposition of spinel MnCo₂O₄ nanosheets for supercapacitor applications. **Nanotechnology**. 26(45): 455401.
- Sawangphruk, M., Srimuk, P., Chiochan, P., Krittayavathananon, A., Luanwuthi, S. and Limtrakul, J. (2013). High-performance supercapacitor of manganese oxide/reduced graphene oxide nanocomposite coated on flexible carbon fiber paper. **Carbon**. 60: 109-116.
- Shanmugavani, A. and Selvan, R. K. (2016). Improved electrochemical performances of CuCo₂O₄/CuO nanocomposites for asymmetric supercapacitors. **Electrochimica Acta**. 188: 852-862.
- Simon, P. and Gogotsi, Y. (2008). Materials for electrochemical capacitors. **Nature materials**. 7(11): 845.
- Srinivasan, V. and Weidner, J. W. (2002). Capacitance studies of cobalt oxide films formed via electrochemical precipitation. **Journal of Power Sources**. 108(1-2): 15-20.
- Sun, D. S., Li, Y. H., Wang, Z. Y., Cheng, X. P., Jaffer, S. and Zhang, Y. F. (2016). Understanding the mechanism of hydrogenated NiCo₂O₄ nanograss supported

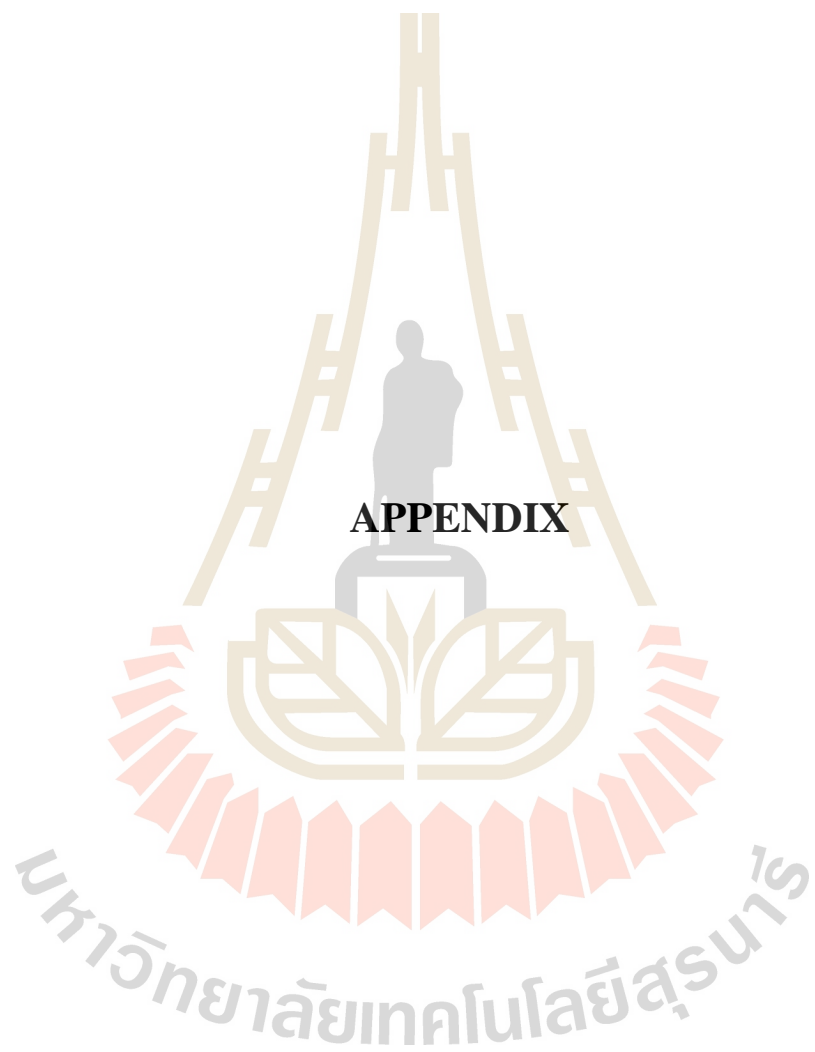
- on Ni foam for enhanced-performance supercapacitors. **Journal of Materials Chemistry A**. 4(14): 5198-5204.
- Tamboli, M. S., Dubal, D. P., Patil, S. S., Shaikh, A. F., Deonikar, V. G., Kulkarni, M. V., Maldar, N. N., Inamuddin, Asiri, A. M., Gomez-Romero, P., Kale, B. B. and Patil, D. R. (2017). Mimics of microstructures of Ni substituted $Mn_{1-x}Ni_xCo_2O_4$ for high energy density asymmetric capacitors. **Chemical Engineering Journal**. 307: 300-310.
- Tholkappian, R., Naveen, A. N., Sumithra, S. and Vishista, K. (2015). Investigation on spinel $MnCo_2O_4$ electrode material prepared via controlled and uncontrolled synthesis route for supercapacitor application. **Journal of Materials Science**. 50(17).
- Vijayakumar, S., Lee, S.-H. and Ryu, K.-S. (2015). Hierarchical $CuCo_2O_4$ nanobelts as a supercapacitor electrode with high areal and specific capacitance. **Electrochimica Acta**. 182: 979-986.
- Waghmode, R. B. and Torane, A. P. (2016). Hierarchical 3D $NiCo_2O_4$ nanoflowers as electrode materials for high performance supercapacitors. **Journal of Materials Science: Materials in Electronics**. 27(6): 6133-6139.
- Wang, M., Chen, K., Liu, J., He, Q., Li, G. and Li, F. (2018). Efficiently enhancing electrocatalytic activity of α - MnO_2 nanorods/N-doped ketjenblack carbon for oxygen reduction reaction and oxygen evolution reaction using facile regulated hydrothermal treatment. **Catalysts**. 8(4): 138.
- Wang, Q., Qin, X., Jiang, P., Dai, J. F., Li, W. and Gao, H. (2018). Core/shell structure $NiCo_2O_4@MnCo_2O_4$ nanofibers fabricated by different temperatures for high-performance supercapacitors. **Materials Research Express**. 5(3).

- Wang, S., Hou, Y. and Wang, X. (2015). Development of a stable MnCo_2O_4 cocatalyst for photocatalytic CO_2 reduction with visible light. **ACS Applied Materials and Interfaces**. 7(7): 4327-4335.
- Wang, X. and Li, Y. (2002). Selected-control hydrothermal synthesis of α - and β - MnO_2 single crystal nanowires. **Journal of the American Chemical Society**. 124(12): 2880-2881.
- Wang, Z., Zhang, X., Zhang, Z., Qiao, N., Li, Y. and Hao, Z. (2015). Hybrids of NiCo_2O_4 nanorods and nanobundles with graphene as promising electrode materials for supercapacitors. **Journal of Colloid and Interface Science**. 460: 303-309.
- Wei, T. Y., Chen, C. H., Chien, H. C., Lu, S. Y. and Hu, C. C. (2010). A cost-effective supercapacitor material of ultrahigh specific capacitances: spinel nickel cobaltite aerogels from an epoxide-driven sol-gel process. **Advanced materials**. 22(3): 347-351.
- Wu, C., Cai, J., Zhang, Q., Zhou, X., Zhu, Y., Li, L., Shen, P. and Zhang, K. (2015). Direct growth of urchin-like ZnCo_2O_4 microspheres assembled from nanowires on nickel foam as high-performance electrodes for supercapacitors. **Electrochimica Acta**. 169: 202-209.
- Wu, M., Gao, J., Zhang, S. and Chen, A. (2006). Comparative studies of nickel oxide films on different substrates for electrochemical supercapacitors. **Journal of Power Sources**. 159(1): 365-369.
- Wu, X., Li, S., Wang, B., Liu, J. and Yu, M. (2015). Controllable synthesis of micro/nano-structured MnCo_2O_4 with multiporous core-shell architectures as

- high-performance anode materials for lithium-ion batteries. **New Journal of Chemistry**. 39(11): 8416-8423.
- Wu, Z.-S., Ren, W., Wang, D.-W., Li, F., Liu, B. and Cheng, H.-M. (2010). High-energy MnO₂ nanowire/graphene and graphene asymmetric electrochemical capacitors. **ACS nano**. 4(10): 5835-5842.
- Xu, C., Kang, F., Li, B. and Du, H. (2010). Recent progress on manganese dioxide based supercapacitors. **Journal of materials research**. 25(08): 1421-1432.
- Xu, K., Li, S., Yang, J., Xu, H. and Hu, J. (2016). Hierarchical MnO₂ nanosheets on electrospun NiCo₂O₄ nanotubes as electrode materials for high rate capability and excellent cycling stability supercapacitors. **Journal of Alloys and Compounds**. 678: 120-125.
- Xu, Y., Wang, X., An, C., Wang, Y., Jiao, L. and Yuan, H. (2014). Facile synthesis route of porous MnCo₂O₄ and CoMn₂O₄ nanowires and their excellent electrochemical properties in supercapacitors. **Journal of Materials Chemistry A**. 2(39): 16480-16488.
- Xue, H., Wu, S., Tang, J., Gong, H., He, P., He, J. and Zhou, H. (2016). Hierarchical Porous Nickel Cobaltate Nanoneedle Arrays as Flexible Carbon-Protected Cathodes for High-Performance Lithium-Oxygen Batteries. **ACS Applied Materials and Interfaces**. 8(13): 8427-8435.
- Yang, X.-h., Wang, Y.-g., Xiong, H.-m. and Xia, Y.-y. (2007). Interfacial synthesis of porous MnO₂ and its application in electrochemical capacitor. **Electrochimica Acta**. 53(2): 752-757.
- Yu, A., Chabot, V. and Zhang, J. (2017). **Electrochemical Supercapacitors for Energy Storage and Delivery: Fundamentals and Applications**. CRC press.

- Yu, A., Davies, A. and Chen, Z. (2012). Electrochemical supercapacitors. **Electrochemical Technologies for Energy Storage and Conversion.** 317-382.
- Yuan, C., Zhang, X., Su, L., Gao, B. and Shen, L. (2009). Facile synthesis and self-assembly of hierarchical porous NiO nano/micro spherical superstructures for high performance supercapacitors. **Journal of Materials Chemistry.** 19(32): 5772-5777.
- Yuan, Y., Bi, H., He, G., Zhu, J. and Chen, H. (2014). A Facile Hydrothermal Synthesis of a MnCo₂O₄@Reduced Graphene Oxide Nanocomposite for application in Supercapacitors. **Chemistry Letters.** 43(1): 83-85.
- Zhai, Y., Mao, H., Liu, P., Ren, X., Xu, L. and Qian, Y. (2015). Facile fabrication of hierarchical porous rose-like NiCo₂O₄ nanoflake/MnCo₂O₄ nanoparticle composites with enhanced electrochemical performance for energy storage. **Journal of Materials Chemistry A.** 3(31): 16142-16149.
- Zhang, J., Kong, L.-B., Li, H., Luo, Y.-C. and Kang, L. (2010). Synthesis of polypyrrole film by pulse galvanostatic method and its application as supercapacitor electrode materials. **Journal of Materials Science.** 45(7): 1947-1954.
- Zhang, L. L. and Zhao, X. (2009). Carbon-based materials as supercapacitor electrodes. **Chemical Society Reviews.** 38(9): 2520-2531.
- Zhang, Y., Xuan, H., Xu, Y., Guo, B., Li, H., Kang, L., Han, P., Wang, D. and Du, Y. (2016). One-step large scale combustion synthesis mesoporous MnO₂/MnCo₂O₄ composite as electrode material for high-performance supercapacitors. **Electrochimica Acta.** 206: 278-290.

- Zhao, D.-D., Bao, S.-J., Zhou, W.-J. and Li, H.-L. (2007). Preparation of hexagonal nanoporous nickel hydroxide film and its application for electrochemical capacitor. **Electrochemistry communications**. 9(5): 869-874.
- Zheng, C., Cao, C., Chang, R., Hou, J. and Zhai, H. (2016). Hierarchical mesoporous NiCo₂O₄ hollow nanocubes for supercapacitors. **Physical Chemistry Chemical Physics**. 18(8): 6268-6274.
- Zhong, C., Deng, Y., Hu, W., Qiao, J., Zhang, L. and Zhang, J. (2015). A review of electrolyte materials and compositions for electrochemical supercapacitors. **Chemical Society Reviews**. 44(21): 7484-7539.
- Zhou, H., Chen, H., Luo, S., Lu, G., Wei, W. and Kuang, Y. (2005). The effect of the polyaniline morphology on the performance of polyaniline supercapacitors. **Journal of Solid State Electrochemistry**. 9(8): 574-580.
- Zhu, J. and Gao, Q. (2009). Mesoporous MCo₂O₄ (M = Cu, Mn, and Ni) spinels: Structural replication, characterization and catalytic application in CO oxidation. **Microporous and Mesoporous Materials**. 124(1): 144-152.
- Zhu, Y., Ji, X., Wu, Z., Song, W., Hou, H., Wu, Z., He, X., Chen, Q. and Banks, C. E. (2014). Spinel NiCo₂O₄ for use as a high-performance supercapacitor electrode material: Understanding of its electrochemical properties. **Journal of Power Sources**. 267: 888-900.



APPENDIX

PUBLICATION AND PRESENTATION

A.1 List of publication

Kalawa, O., Kidkhunthod, P., Chanlek, N., Khajonrit, J. and Maensiri, S. (2020). Synthesis and electrochemical properties of polymer solution prepared MnCo₂O₄ nanoparticles. ***Ionics***. 26(1): 457-469.

A.2 List of oral presentations

Kalawa, O., Nilmoung, S., Pinitsoontorn, S., and Maensiri, S. (2015). Synthesis, magnetic and electrochemical properties of polymer-solution prepared MnCo₂O₄ nanoparticles. **10th Conference on Surfaces, Coatings and Nanostructured Materials**. Manchester, United Kingdom.

Kalawa, O., and Maensiri, S. (2016). Fabrication, Characterization, and Electrochemical Properties of Electrospun MnCo₂O₄ Nanofibers. **The 5th Thailand International Nanotechnology Conference**. Nakhon Ratchasima, Thailand.

Kalawa, O., Kidkhunthod, P., and Maensiri, S. (2017). Synthesis and Electrochemical Properties of Ni-doped MnCo₂O₄ Nanoparticles Prepared by a Simple Polymer Solution Method. **12th International Conference on Surfaces, Coatings and Nanostructured Materials**. Paris, France.

A.3 List of poster presentation

Kalawa, O., Kidkhunthod, P., Chanlek, N., and Maensiri, S. (2016). Synthesis and Electrochemical Properties of Spinel MnCo_2O_4 Nanoparticles Prepared by a Simple PAN-solution Route. **8th International Workshop on Advanced Materials Science and Nanotechnology**. Ha Long City, Vietnam.

Kalawa, O., Kidkhunthod, P., Chanlek, N., and Maensiri, S. (2017). Synthesis and electrochemical properties of polymer–solution prepared MnCo_2O_4 nanoparticles. **The First Materials Research Society of Thailand International Conference**. Chiang Mai, Thailand.

Kalawa, O., Kidkhunthod, P., and Maensiri, S. (2018). Synthesis and Electrochemical Properties of Zn-doped MnCo_2O_4 Nanoparticles. **International Union of Materials Research Societies – International Conference on Electronic Materials 2018**. Daejeon Convention Center, South Korea.

Kalawa, O., Kidkhunthod, P., Chanlek, N., and Maensiri, S. (2018). Synthesis and electrochemical properties of polymer–solution prepared MnCo_2O_4 nanoparticles. **International Union of Materials Research Society – International Conference in Asia**. Bali, Indonesia.

CURRICULUM VITAE

Name	Miss Ornuma Kalawa
Date of Birth	August 16, 1990
Place of Birth	19 Moo 6, Tambol Kutwa, Kuchinarai District, Kalasin Province, 46110, Thailand.
Education	
2013-2019	Ph.D. Thesis in Physics (For B.SC. Holder) School of Physics, Institute of Science, Suranaree University of Technology.
2009-2012	B.Sc. (Physics) Department of Physics, Faculty of Science, Ubon Ratchathani University.
Awards	Young Student Award , Synthesis and Electrochemical Properties of Polymer–Solution Prepared MnCo_2O_4 Nanoparticles, International Union of Materials Research Society – International Conference in Asia, Bali – Indonesia, Oct. 31 – Nov 2, 2018
Grants and Fellowships	Science Achievement Scholarship of Thailand (SAST)

